Università degli Studi del Molise

DIPARTIMENTO DI BIOSCIENZE E TERRITORIO

DOTTORATO DI RICERCA XXXI CICLO

The Slow Control and the Calibration Systems of the E989 Experiment at Fermilab

PhD Thesis

Antonio GIOIOSA

SSD:INF01

PhD Coordinator:

Prof. Gabriella Stefania SCIPPA

Tutor:

Prof. Fausto FASANO

Co-Tutor:

Prof. Giovanni Maria PIACENTINO

TRIENNIO 2016-2018

To My Mother Lucia

To My Family

Acknowledgments

The successful implementation of an experiment demanding as the a_μ measurement required strong effort from a lot of people to coordinate the work in the construction. At the time of the redaction of this Thesis, the collaboration included:

- Brookhaven National Laboratory: J. Crnkovic, W.M. Morse, V. Tishchenko;
- Budker Institute of Nuclear Physics: A. Anisenkov, I. Logashenko, Y.M. Shatunov;
- Center for Axion and Precision Physics (CAPP) / Institute for Basic Science (IBS): S. Haciomeroglu, Y.I. Kim, M.J. Lee, S. Lee, Y.K. Semertzidis;
- China University of Geosciences (Wuhan): D. Li;
- Cornell University: R. Bjorkquist, A. Chapelain, C.J.R. Duncan, L.K. Gibbons, S.C. Kim, A.A. Mikhailichenko, Y. Orlov, N.T. Rider, D.L. Rubin, D.A. Sweigart;
- Fermi National Accelerator Laboratory: D. Allspach, K. Badgley, E. Barzi, B. Casey, S. Chappa, M. Convery, B. Drendel, H. Friedsam, C. Johnstone, J.A. Johnstone, B. Kiburg, I. Kourbanis, A. Lucà, A. L. Lyon,

W. Merritt, J.P. Morgan, H. Nguyen, J.-F. Ostiguy, C. Polly, E. Ramberg, M. Rominsky, J. Stapleton, D. Still, C. Stoughton, D. Stratakis, T. Walton, L. Welty-Rieger, C. Yoshikawa;

- INFN Sezione di Napoli: P. Di Meo, R. Di Stefano, O. Escalante-Aguirre, M. Iacovacci, S. Marignetti, S. Mastroianni, A. Nath;
- INFN Laboratori Nazionali di Frascati: S. Ceravolo, G. Corradi, S. Dabagov, D. Hampai;
- INFN Sezione di Pisa: A. Basti, F. Bedeschi, S. Di Falco, C. Ferrari, A. Fioretti, C. Gabbanini, M. Incagli, A. Lusiani, G. Pezzullo, M.W. Smith, G. Venanzoni;
- INFN Sezione di Roma Tor Vergata: G. Di Sciascio, A. Gioiosa, D. Moricciani, G.M. Piacentino;
- INFN Sezione di Trieste: G. Cantatore, D. Cauz, A. Driutti, M. Karuza, G. Pauletta, L. Santi;
- Istituto Nazionale di Ottica - Consiglio Nazionale delle Ricerche: C. Ferrari, A. Fioretti, C. Gabbanini;
- James Madison University: K.L. Giovanetti;
- Joint Institute for Nuclear Research: V.A. Baranov, V.N. Duginov, N.V. Khomutov, V.A. Krylov, N.A. Kuchinskiy, V.P. Volnykh;
- Korea Advanced Institute of Science and Technology (KAIST): S. P. Chang, O. Kim, Y.K. Semertzidis;
- Lancaster University: I. Bailey, M. Korostelev;

- Lebedev Physical Institute and NRNU MEPhI: S. Dabagov;
- Michigan State University: M. Berz, R. Hipple, K. Makino, D. Tarazona, E. Valetov;
- North Central College: P. Bloom;
- North Central College: M. Rominsky;
- Northern Illinois University: M. Eads, A. Epps, N. Pohlman, M.J. Syphers;
- Novosibirsk State University: A. Anisenkov, I. Logashenko;
- Oak Ridge National Lab, S. Baessler;
- Regis University: F. Gray;
- Scuola Normale Superiore di Pisa: A. Lusiani;
- Shanghai Key Laboratory for Particle Physics and Cosmology: C. Fu, L. Li;
- Shanghai Jiao Tong University: C. Fu, B. Li, D. Li, L. Li, H. Yang;
- Technische Universität Dresden: D. Stöckinger;
- The Cockcroft Institute of Accelerator Science and Technology: I. Bailey, A.T. Herrod, M. Korostelev, A. Wolski;
- Università del Molise: A. Gioiosa, G.M. Piacentino;
- Università di Cassino: R. Di Stefano, S. Marignetti;
- Università di Messina: A. Anastasi;
- Università di Napoli: O. Escalante-Aguirre, M. Iacovacci, A. Nath;

- Università di Trieste: G. Cantatore;
- Università di Udine: D. Cauz, A. Driutti, G. Pauletta, L. Santi;
- University College London: S. Al-Kilani, R. Chislett, M. Lancaster, G. Lukicov, E. Motuk, T. Stuttard, M. Warren;
- University of Illinois at Urbana-Champaign: P.T. Debevec, S. Ganguly, K.T. Pitts, C. Schlesier;
- University of Kentucky: R. Fatemi, W. Gohn, T. Gorringe, F. Han, L. Kelton, B. Plaster;
- University of Liverpool: T. Albahri, T. Bowcock, J. Carroll, S. Charity, T. Halewood-Leagas, A.T. Herrod, A. Keshavarzi, B. King, S. Maxfield, J. Price, D. Sim, A. Smith, T. Teubner, K. Thomson, W. Turner, M. Whitley, A. Wolski, M. Wormald;
- University of Massachusetts: A. Conway, D. Flay, D. Kawall;
- University of Michigan: T.E. Chupp, M. Farooq, A.E. Tewsley-Booth;
- University of Mississippi: J.L. Holzbauer, B. Quinn, W. Wu;
- University of Rijeka: M. Karuza;
- University of Texas at Austin: J. George. J.L. Ritchie, A. Schreckenberger;
- University of Virginia: S. Baessler, E. Frlez, J. Fry, D. Pocanic;
- University of Washington: H.P. Binney, M. Fertl, A.T. Fienberg, N.S. Froemming, A. Garcia, J. Hempstead, D.W. Hertzog, P. Kammel, J. Kaspar, K.S. Khaw, B. MacCoy, R. Osofsky, H.E. Swanson.

I want to thank all of the members of the Laser Calibration Group for all the support given in these years and the lessons learned from them.

I am deeply grateful to my supervisor Prof. Giovanni Maria Piacentino, for all the time spent with me in these three years, for the lesson learned from him and for trusting me since the beginning.

I am incredibly grateful also to Dr. Graziano Venanzoni for all the help and the teaching given in these years and for all grate time spent together.

I would also like to thank all the graduate students and post-doc of the collaboration met in these years for the useful discussion and helps on every aspect of the experiment, analysis, hardware and for special time spent with them.

Contents

Introduction

One of the more persistent hints of new physics is the deviation between the measured muon anomalous magnetic moment, $a_\mu = (g-2)/2$, and its Standard Model expectation, where both are determined to a precision of about 0.5 parts per million. This fundamental measurement has been pursued for decades with increasing precision. The discrepancy has been interpreted to point toward several attractive candidates for Standard Model extensions: supersymmetry, extra dimensions, or a dark matter candidate. The Large Hadron Collider (LHC) is now delivering on its promise to explore physics at the highest mass ranges to date, although no new physics has yet been found. A new and more precise muon $g-2$ experiment offers a strategic opportunity to search for new physics through alternative means, which could lead to a more coherent picture of the underlying physics.

After the impressive result obtained at Brookhaven National Laboratory in 2001 with a total accuracy of 0.54 ppm (540 ppb), a new experiment E989 is working at Fermilab, motivated by the difference of $a_\mu^{exp} - a_\mu^{SM} \sim 3\sigma$.

In fact the current muon $g-2$ measurement is used as a benchmark for new physics and has been used as input into the parameter space explored in almost all model dependent searches for new physics at the LHC, but the current discrepancy between the muon $g-2$ measurement and the theoretical prediction could be also explained as a statistical fluctuation at the three-sigma

level and has only been observed by one experiment. The discrepancy needs to be confirmed and established above the accepted discovery threshold of five standard deviations.

The purpose of the E989 experiment is a fourfold reduction of the error on a_μ, with a goal of 140 ppb, improving both the systematic and statistical uncertainty. With the use of the Fermilab beam complex, a statistics of 21 times with respect to the BNL experiment will be attained in almost 2 years of data taking improving the statistical uncertainty to 100 ppb. Improvement on the systematic error involves the measurement technique of ω_a and ω_p, the anomalous precession frequency of the muon and the Larmor precession frequency of the proton respectively. The measurement of ω_p involves the magnetic field measurement and improvements on this sector related to the uniformity of the field should reduce the systematic uncertainty with respect to BNL from 170 ppb to 70 ppb. A reduction from 180 ppb to 70 ppb is also required for the measurement of ω_a; new DAQ, a faster electronics and new detectors and calibration system are implemented with respect to E821 to reach this goal. In particular, the laser calibration system will reduce the systematic error due to gain fluctuations of the photodetectors from 120 to 20 ppb. The 20 ppb limit on systematic requires a system with a stability of 10^{-4} on a short time scale (700 μs) while on a longer time scale the stability is at the percent level. The 10^{-4} stability level required is almost an order of magnitude better than the existing laser calibration system in particle physics, making the calibration system a very challenging item. In addition to the high level of stability a particular environment, due to the presence of a 14 m diameter storage ring, a highly uniform magnetic field and the detector distribution around the storage ring, set specific guidelines and constraints. This thesis will focus on the Laser Calibration System, developed for the E989 experiment

and installed at Fermilab, its Slow Control System, on the capability of the Calibration System to reduce the systematics and on the analysis of the gain corrections and other effect in the ω_a determination.

Chapter 1 introduces the subject of the anomalous magnetic moment of the muon; Chapter 2 discusses the Standard Model prediction and possible new physics scenario. Chapter 3 presents previous measurements of $g-2$ and Chapter 4 describes the E989 experiment. In this Chapter the experimental technique will be described and also will be presented the experimental apparatus focusing on the improvements necessary to reduce the statistical and systematic errors. The main subject of the thesis is discussed in the last four chapters: Chapter 5 is focused on the Laser Calibration System; Chapter 6 presents performances and calibration procedures of the E989 Laser Calibration System installed at Fermilab and describes two Test Beams performed at the Beam Test Facilities of Laboratori Nazionali di Frascati, Italy and at SLAC National Accelerator Laboratory, Menlo Park California, United States, as a final test for the full calibrations system before the installation at Fermilab and Chapter 7 describes the slow controls system of the E989 experiment and specifically the developing of the Slow Control and the Data Quality Monitor of the Laser Calibration System. The last Chapter 8 regards the contribution of the Calibration System in the determination of anomalous frequency ω_a that will be measured in the E989 experiment, particularly significant in the reduction of the systematic uncertainties. The results obtained on the reduction of the systematic uncertainties due to lost muons will be presented.

Chapter 1

Introduction to the magnetic moment

This Chapter introduces the "anomalous magnetic moment" and sets out the motivation for measuring it.

As will be described in more detail later, the magnetic moment of the muon can be measured by placing a muon in a magnetic field and measuring the rate at which the muon's spin vector precesses in the field.

1.1 Classical Magnetic Dipole Moment

The vector potential of a magnetic field can be expressed as a multipole expansion, in the same way of a scalar potential of a continuous electric charge distribution [1] (in natural units $\frac{h}{2\pi} = c = 1$):

$$\mathbf{A} = \sum_{n=0}^{\infty} \frac{1}{r^{n+1}} \int (r') P_n(\cos\theta') \mathbf{J}(\mathbf{r}') d^3\mathbf{r}' = I \left[\frac{1}{r} \oint d\boldsymbol{\ell} + \frac{1}{r^2} \oint r' \cos\theta' d\boldsymbol{\ell} + ... \right], \tag{1.1}$$

where the differences are the replacement of the charge distribution $\rho(\mathbf{r}')$

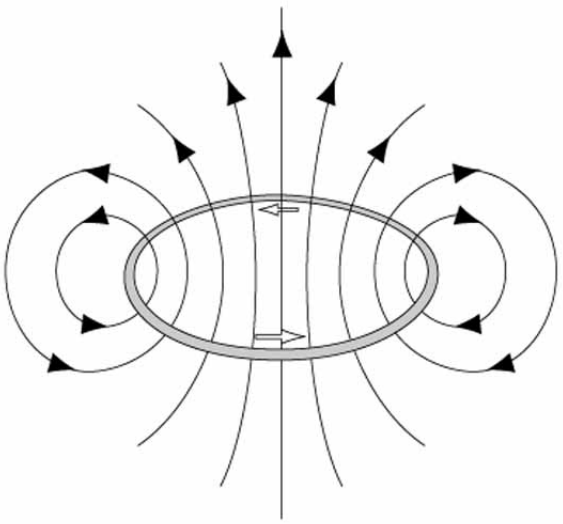

Figure 1.1: Current loop generating a dipole magnetic field.

with the current distribution $\mathbf{J}(\mathbf{r}')$, because magnetic fields are generated by moving charges [1] and the integral over space that is written as a simple line integral over all the infinitesimal elements I$d\boldsymbol{\ell}$

The first term of the Legendre polynomials P_n expansion is zero because of the non-existence of the magnetic monopole and the first non-vanishing term is the second order term, a magnetic dipole consisting of a current loop as in Fig. 1.1.

The second order term can be written as:

$$\mathbf{A}_{dip} = I\left[-\frac{1}{2}\hat{\mathbf{r}} + \oint(\mathbf{r}\times d\boldsymbol{\ell})\right] = \frac{\boldsymbol{\mu}\times\hat{\mathbf{r}}}{r^2} \tag{1.2}$$

where we can define the value of the *magnetic dipole moment*

$$\boldsymbol{\mu} = \frac{I}{2}\oint(\mathbf{r}\times d\boldsymbol{\ell}) \tag{1.3}$$

[1] $V = \sum_{n=0}^{\infty}\frac{1}{r^{n+1}}\int(r')^n P_n(\cos\theta')\rho(\mathbf{r}')d^3\mathbf{r}'$ where V indicates the potential observed at any point with an integral over the charge distribution $\rho(\mathbf{r}')$.

which can be simplified to

$$\mu = IA \tag{1.4}$$

in the case of a current loop confined in a plane, where A is the total area enclosed by the current loop.

This quantity represents the strength and the direction of the torque experienced by a current distribution placed in an external magnetic field

$$\boldsymbol{\tau} = \boldsymbol{\mu} \times \mathbf{B} \tag{1.5}$$

with a potential energy

$$U = -\boldsymbol{\mu} \cdot \mathbf{B}. \tag{1.6}$$

This is a specific example used to introduce the quantity μ; the most general expression of the magnetic moment is given by:

$$\boldsymbol{\mu} = \frac{1}{2} \int (\mathbf{r}' \times \mathbf{J}(\mathbf{r}')) d^3\mathbf{r}'. \tag{1.7}$$

Now considering the current as a series of i point-like particles each with a velocity $\mathbf{v}_i$ and charge q_i, it could be written as a sum $\mathbf{J} = \sum_i q_i \mathbf{v}_i \delta(\mathbf{r}' - \mathbf{r}_i)$; substituting this into Eq. 1.7 yields

$$\boldsymbol{\mu} = \frac{1}{2} \sum_i q_i (\mathbf{r}_i \times \mathbf{v}_i) = \frac{1}{2} \sum_i \frac{q_i}{m_i} (\mathbf{r}_i \times \mathbf{p}_i) = \frac{1}{2} \sum_i \frac{q_i}{m_i} \mathbf{L}_i. \tag{1.8}$$

where velocities are written in terms of the momentum of the individual particles. Considering particles to be identical, the magnetic dipole moment is simply proportional to the total angular momentum of the system $\mathbf{L} = \sum_i L_i$ and can be written as

$$\boldsymbol{\mu} = \frac{q}{2m} \mathbf{L}. \tag{1.9}$$

Eq. 1.9 shows the direct proportionality between the magnetic moment $\boldsymbol{\mu}$ and the angular momentum $\mathbf{L}$.

1.2 Quantum determination

1.2.1 From classical to quantum mechanics

In 1922 the famous experiment by Stern and Gerlach showed that a beam of identical silver atoms, electrically neutral, passing through a magnetic field [2] emerged from it physically separated into two different bands along the axis of the magnetic field. Given Equation 1.5, what should be inferred by this result is that the silver atoms have two possible magnetic moments, equal in magnitude but pointing to opposite directions.

The silver atom is a complex system with a large nucleus and many shells of orbiting electrons, so in 1927, to simplify the interpretation, Phipps and Taylor repeated the experiment at the University of Illinois (Urbana) using hydrogen atoms and found same results [3].

One possible source to this magnetic moments could be the electric charge of the nucleus that implies, from Equation 1.9 a scaling factor of $1/m_N$, where m_N is the mass of the nucleus. This scaling is not observed in silver and hydrogen experiments.

This moved the interest to the orbiting electron in the atom as the possible explanation.

From spectroscopy experiment what came out was that a fourth quantum number, in addition to n, m and l introduced by quantum mechanics, was necessary to remove all the degeneracies in the experimental data. There was a big effort to explain data using different models (e.g Sommerfeld and Lande's *Ersatzmodel*), which were only able to describe just some specific situation. The first solution to this problem, even if only qualitatively, was given by two young physicists, Samuel Goudsmith and George Uhlenbeck, where the idea of the *spin* with its value of $\pm\frac{1}{2}$ came out [4].

Quantitatively the classical equation of the magnetic moment[2], Eq. 1.9, underestimates the result of experiments like the Stern-Gerlach of a factor 2. The common practice to solve this problem was to incorporate this factor via the Lande *g-factor* or *gyromagnetic ratio*

$$\boldsymbol{\mu} = g\frac{q}{2m_e}\mathbf{S} \tag{1.10}$$

where g=1 for a classical system and g=2 referring to the electron. The rigorous mathematical description of spin came out from Dirac in 1928 and his effort to create the relativistic variant of Schrödinger's equation. Existence of spin was predicted together with the existence of anti-particles. The Dirac's equation also predicts exactly the correct value of the magnetic moment for the electron with g=2 even when is not in the relativistic limit [5]

$$\left(\frac{1}{2m_e}(\mathbf{P}\cdot q\mathbf{A})^2 + \frac{q}{2m_e}\boldsymbol{\sigma}\cdot\mathbf{B} - qA^0\right)\Psi_A = (E - m_e)\Psi_A. \tag{1.11}$$

Indeed recognizing the correspondence between the term proportional to $\mathbf{B}$ in Eq. 1.11 and the classical potential energy

$$U = -\boldsymbol{\mu}\cdot\mathbf{B} = \frac{q}{2m}\boldsymbol{\sigma}\cdot\mathbf{B}, \tag{1.12}$$

and solving for the magnetic moment shows that the g-factor for the electron is in fact 2,

$$\boldsymbol{\mu} = -\frac{q}{2m_e}\boldsymbol{\sigma} = -2\frac{q}{2m_e}\mathbf{S} = -g\frac{q}{2m_e}\mathbf{S}. \tag{1.13}$$

Foldy has shown that this result holds even in a fully relativistic treatment [6].

[2]Considering the electron a point particle executing uniform circular motion in a microscopic radius r then it has an angular momentum $L = m_e v r$. From Equation 1.4 we have $\boldsymbol{\mu} = \frac{e}{2m_e}\mathbf{L}$, the Eq. 1.9 for electron, where $g = 1$ in contrast with experiments.

1.2.2 The anomalous magnetic moment

For some years, the experimental situation remained the same. The electron had $g = 2$, and the Dirac equation seemed to describe nature, then a surprising and completely unexpected result was obtained. In 1933, after discoveries of the neutron [7] and the positron [8], against the advice of Pauli who believed that the proton was a pure Dirac particle [9], Stern and his collaborators [10, 11] showed that the g-factor of the proton was ~ 5.5, not the expected value of 2. Even more surprising was the discovery in 1940 by Alvarez and Bloch [12] that the neutron had a large magnetic moment.

1.2.3 The Quantum Field Theory approach

The transition from quantum mechanics to quantum field theory adds another level of insight into the gyromagnetic ratio. Table 1.1 shows the gyromagnetic ratios for various particles. It is apparent that g is approximately 2 for the charged leptons–that is, the electron, muon, and tau. Indeed, the Dirac equation predicts that g is exactly 2 for a pointlike particle. The small discrepancy is caused by corrections from higher-order interactions described by quantum field theories that consider the vacuum filled with a continuous flux of virtual particles which influence ordinary matter. Composite particles such as the proton and neutron show large differences from 2, which are indications of their rich internal structure.

The gyromagnetic ratios of stable and nearly-stable particles can be measured experimentally to extremely high precision. Indeed, the electron g factor, known to a precision of 4×10^{-12}, is the physical quantity with the smallest quoted uncertainty in the current CODATA table [19]. The lepton g factors can also be calculated very precisely in the context of the standard model, and

Particle	Experimental value	Relative precision	Ref.	Theoretical prediction	Ref.
Electron	2.0023193043738(82)	4×10^{-12}	[1]	2.00231930492(29)	[2]
Muon	2.0023318406(16)	8×10^{-10}	[3]	2.0023318338(14)	[4]
Tau	2.008(71)	4×10^{-2}	[5]	2.0023546(6)	[6]
Proton	5.585694674(58)	1×10^{-8}	[1]	5.58	[7]
Neutron	-3.8260854(10)	3×10^{-7}	[1]	-3.72	[7]

Table 1.1: Gyromagnetic ratios (g) for various subatomic particles.

a comparison of the experimental and theoretical values provides a sensitive test of the theory.

The electron magnetic anomaly $\mathbf{a}_e$

In 1947, motivated by measurements of the hyperfine structure in hydrogen, that obtained splittings larger than expected from the Dirac theory [13, 14, 15, 16], with a very small error, Schwinger [17] showed that from a theoretical viewpoint these "discrepancies can be accounted for by a small additional electron spin magnetic moment" that arises from the lowest-order radiative correction to the Dirac moment,

$$\frac{\delta\mu}{\mu} = \frac{1}{2\pi}\frac{e^2}{\hbar c} = 0.001162. \tag{1.14}$$

within the quoted error of the experiments.

It is useful to break the magnetic moment into two terms:

$$\mu = (1+a)\,\frac{e\hbar}{2m}, \quad \text{where} \quad a = \frac{(g-2)}{2}. \tag{1.15}$$

The first term is the Dirac moment, 1 in units of the appropriate magneton $e\hbar/2m$. The second term is the anomalous (Pauli) moment [18], where the dimensionless quantity a (Schwinger's $\delta\mu/\mu$) is sometimes referred to as the *anomaly*.

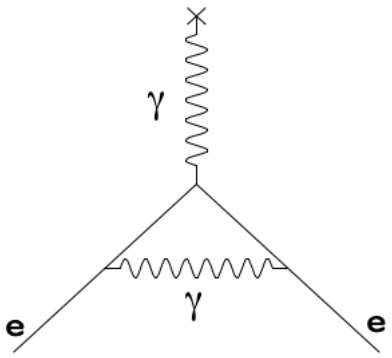

Figure 1.2: Feynman diagram for the lowest order self-interaction term.

Pictorially, the lowest-order electron self-interaction responsible for the Schwinger term is shown by the Feynman diagram inThe Fig. 1.2.

The anomaly can be written as an expantion in terms of the fine structure constant $\alpha = 2\pi q^2/hc$ and the uncertainty in the theory is dominated by the precision to which α is known.

The best measurement of α comes from the comparison of the experimental value of the electron anomaly a_e^{exp} [20, 21, 22] and the theoretical evaluation of a_e^{SM}, where $\alpha^{-1} = 137.035999046(27)[0.20\text{ ppb}]$ [23].

The most recent calculation of a_e comes from the computation of the fourth order in α [24, 25, 19, 26, 27]

$$a_e^{theor} = \frac{\alpha}{2\pi} - 0.32847844400255(33)\left(\frac{\alpha}{\pi}\right)^2 + 1.181234016816(11)\left(\frac{\alpha}{\pi}\right)^3 + \tag{1.16}$$

$$-1.9113213917(12)\left(\frac{\alpha}{\pi}\right)^4 + 1.70(2)\times 10^{-12} = 0.00115965218160(1)(1)(23).$$

The experimental measurement on α_e has reached an incredible precision of 4 ppb even compared to the amazing precision obtained in the theoretical calculation of 20 ppb. The experimental setup used at Washington, by H. Dehmelt and his group [28, 29], consists of a Penning trap and they were able

to obtain the values of

$$a_{e^-}^{exp} = 0.00115965218073(28). \tag{1.17}$$

with a difference between the theoretical and the experimental value of the electron anomaly at the 2.4 σ level.

1.3 The Muon

The muon was first observed in a Wilson cloud chamber by Kunze [30] in 1933, where it was reported to be "a particle of uncertain nature." In 1936 Anderson and Neddermeyer [31] reported the presence of "particles less massive than protons but more penetrating than electrons" in cosmic rays, which was confirmed in 1937 by Street and Stevenson [32], Nishina, Tekeuchi and Ichimiya [33], and by Crussard and Leprince-Ringuet [34]. The Yukawa theory of the nuclear force had predicted such a particle, but this "mesotron" as it was called, interacted too weakly with matter to be the carrier of the strong force. Today we understand that the muon is a second generation lepton, with a mass about 207 times the electron one. Like the electron, the muon obeys quantum electrodynamics, and can interact with other particles through the electromagnetic and weak forces. Unlike the electron which appears to be stable, the muon decays through the weak force predominantly by $\mu^- \rightarrow e^- \nu_\mu \bar{\nu}_e$. The muon's long lifetime of $\simeq 2.2$ μs (microseconds) permits precision measurements of its mass, lifetime, and magnetic moment.

1.3.1 The muon magnetic moment

The magnetic moment of the muon played an important role in the discovery of the generation structure of the Standard Model (SM). As described in

more details in the Chapter 3 the pioneering muon spin rotation experiment at the Nevis cyclotron observed parity violation in muon decay [84], and also showed that g_μ was consistent with 2. Subsequent experiments at Nevis [35] and CERN [97] showed that $a_\mu \simeq \alpha/(2\pi)$, implying that in a magnetic field, the muon behaves like a heavy electron. Two additional experiments at CERN required that contributions from higher-order QED [36], and then from virtual hadrons [37] be included into the theory in order to reach agreement with experiment.

1.3.2 The muon magnetic anomaly a_μ

As shown before a lepton ($\ell = e,\ \mu,\ \tau$) has a magnetic moment which is along its spin, given by the relationship

$$\boldsymbol{\mu}_\ell = g_\ell \frac{Qe}{2m_\ell}\mathbf{s}\,, \qquad \underbrace{g_\ell = 2}_{\text{Dirac}}(1 + a_\ell), \qquad a_\ell = \frac{g_\ell - 2}{2} \tag{1.18}$$

where $Q = \pm 1$, $e > 0$ and m_ℓ is the lepton mass.

The muon's magnetic moment is illustrated as a Feynman diagram in Fig. 1.3a.

This diagram shows the muon coupling directly to a photon from the external magnetic field; it corresponds to the Dirac equation's prediction that $g = 2$. However, there is a large set of radiative corrections; these couplings to virtual fields lead to an anomalous part a_μ of the magnetic moment

$$a_\mu = \frac{g - 2}{2}. \tag{1.19}$$

These corrections are represented symbolically by the "blob" in Fig. 1.3b; any allowed intermediate state may be inserted in its place. The dominant correction arises from a coupling to a single virtual photon, as shown in Fig. 1.3c, the leading-order contribution was first evaluated by Schwinger [17].

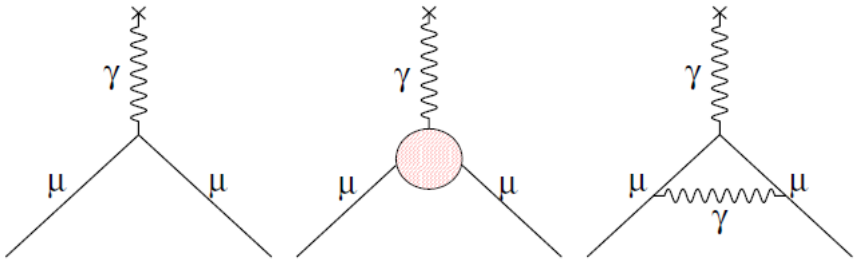

(a) (b) (c)

Figure 1.3: Feynman diagrams for (a) the magnetic moment, corresponding to $g = 2$, (b) the general form of diagrams that contribute to the anomalous magnetic moment a_μ, and (c) the Schwinger term.

Many higher-order processes lead to additional perturbations; contributions are included from all known particles and interactions. Aoyama, Hayakawa, Kinoshita and Nio calculated more than 12,000 diagrams to evaluate the tenth-order (five loop) contribution [23]. Relevant contributes will be discussed in detail in Chapter 2.

Both the electron [20, 21, 22], as shown before, and muon [103] anomalies have been measured very precisely:

$$a_e^{exp} = 1\,159\,652\,180.73\,(28) \times 10^{-12} \quad \pm 0.24\,\text{ppb} \tag{1.20}$$

$$a_\mu^{exp} = 1\,165\,920\,89\,(63) \times 10^{-11} \quad \pm 0.54\,\text{ppm} \tag{1.21}$$

While the electron anomaly has been measured to $\simeq 0.3$ ppb (parts per billion) [22], it is significantly less sensitive to heavier physics, because the relative contribution of heavier virtual particles to the muon anomaly goes as $(m_\mu/m_e)^2 \simeq 43000$. Thus the lowest-order hadronic contribution to a_e is [38]: $a_e^{\text{had,LO}} = (1.875 \pm 0.017)\ 10^{-12}$, 1.5 ppb of a_e. For the muon the hadronic contribution is $\simeq 60$ ppm (parts per million). With much less precision, when compared with the electron, the measured muon anomaly is sensitive to mass

scales in the several hundred GeV region. In addition a discrepancy, over 3σ, remaining between the experimental and theoretical values of the a_μ, shown in Chapter 2 could be the result of new physics: particles and interactions that are not included in the standard model. The muon therefore provides an excellent compromise between mass and stability (reasonable decay time) and the search for such a difference provides the motivation for new experiments.

Chapter 2

Standard-Model contributions to the muon $(g-2)$

As discussed in Chapter 1, the muon anomaly a_μ arises from quantum corrections. This Chapter describes the calculation of the theoretical value of a_μ in the context of the Standard Model (SM). The calculation is divided into contributions that arise from Quantum electrodynamics (QED), electroweak interactions (EW), and hadronic contribution or term (HAD).

$$a_\mu^{SM} = a_\mu^{QED} + a_\mu^{EW} + a_\mu^{QCD}. \tag{2.1}$$

2.1 Overview of the Standard-Model cotribution to a_μ

The Standard Model (SM) prediction of a_μ (a_μ^{SM}) can be split in the following terms

$$a_\mu^{SM} = a_\mu^{QED} + a_\mu^{EW} + a_\mu^{HVP} + a_\mu^{HOHVP} + a_\mu^{HLbL} \tag{2.2}$$

where the hadronic contribution has been further divided into three distinct classes:

- The lowest-order contribution arising from hadronic vacuum polarization diagram (HVP);
- Higher-order contributions (HOHVP) containing an HVP "blob" along with an additional loop. The additional loop can be a photon that is emitted and reabsorbed, a leptonic pair, or a second HVP insertion;
- Higher-order hadronic contributions, known as hadronic light-by-light (HLBL) scattering.

The determination of the SM value can be obtained using:

- The recent QED calculation from Aoyama [23];
- The electroweak EW contribution from Ref. [48];
- Lowest-order hadronic contribution from Davier, et al., [52], or Hagiwara et al., [53];
- The higher-order hadronic contribution from Ref. [53];
- The hadronic light-by-light contribution from the "Glasgow Consensus" [62].

A summary of these values is given in Table 2.1.

By Table 2.1 is clear that although the dominant contribution comes by far by QED, the error on the Standard Model comes entirely from the hadronic terms.

This SM value is compared with the combined a_μ^+ and a_μ^- values from E821 experiment [103], corrected for the revised value of $\lambda = \mu_\mu/\mu_p$ from Ref [19],

$$a_\mu^{\mathrm{E821}} = (116\,592\,089 \pm 63) \times 10^{-11} \quad (0.54\,\mathrm{ppm}), \tag{2.3}$$

	Value ($\times 10^{-11}$)
a_μ^{QED}	116584718.95±0.08
a_μ^{EW}	154 ±1
a_μ^{HVP}(lo) [52]	6923 ± 42
a_μ^{HVP}(lo) [53]	6949 ± 43
a_μ^{HVP}(ho) [53]	-98.4 ± 0.7
a_μ^{HLbL}	105 ±26
Total SM [52]	$116591802 \pm 42_{HLO} \pm 26_{HHO} \pm 2_{other}$ ($\pm 49_{tot}$)
Total SM [53]	$116591828 \pm 43_{HLO} \pm 26_{HHO} \pm 2_{other}$ ($\pm 50_{tot}$)

Table 2.1: Standard model contribution to a_μ.

which give a difference of

$$\Delta a_\mu(\text{E821} - \text{SM}) = (287 \pm 80) \times 10^{-11} \text{ [52]} \quad (2.4)$$

$$= (261 \pm 80) \times 10^{-11} \text{ [53]} \quad (2.5)$$

depending on which evaluation of the lowest-order hadronic contribution that is used.

2.2 The QED contribution

The largest contribution to a_μ comes from interactions described by QED, which involve only leptons and photons. As a dimensionless quantity, it can be cast in the following general form:

$$a_\mu^{QED} = A_1 + A_2\left(\frac{m_\mu}{m_e}\right) + A_2\left(\frac{m_\mu}{m_\tau}\right) + A_3\left(\frac{m_\mu}{m_e}, \frac{m_\mu}{m_\tau}\right) \quad (2.6)$$

where m_e, m_μ and m_τ are the masses of the electron, muon and tau leptons respectively. The mass dependent terms A_2 and A_3 are associated with Feynman graphs (see Feynman diagrams in Fig. 2.1) containing closed fermion loops

where the fermion differs from the external one; for the muon as the external lepton there are two possibilities:

- An additional electron-loop (light-in-heavy), $A_2(m_\mu/m_e)$: it is proportional to large logarithms $\propto ln(m_\mu/m_e)^2$, thus it's a huge correction;
- An additional τ-loop (heavy-in-light), $A_2(m_\mu/m_\tau)$: it produces, because of the decoupling of heavy particles in QED, only small effects of order $\propto (m_\mu/m_\tau)^2$ [40].

The renormalizability of QED guarantees that the function A_μ can be expressed as a power series expansion of $\frac{\alpha}{\pi}$ that means,as showed before, an increasing number of loops in the Feynman diagrams. The QED contribution has been calculated out to terms of order $\left(\frac{\alpha}{2\pi}\right)^5$ yielding [39],

$$a_\mu^{QED} = \frac{\alpha}{2\pi} + 0.765857425(17)(\frac{\alpha}{2\pi})^2 + 24.05050996(32)(\frac{\alpha}{2\pi})^3 + \\ +130.8796(63)(\frac{\alpha}{2\pi})^4 + 753.3(1.0)(\frac{\alpha}{2\pi})^5 = 116584718.95(0.08) \times 10^{-11} \quad (2.7)$$

The overall relative error is $\sim$ 1 ppb, which is entirely insignificant compared to the new experimental goal of 140 ppb uncertainty. This small error results mainly from the uncertainty in α. The value of α^{-1} used for this calculation is

$$\alpha^{-1} = 137.035999049(90) \quad (2.8)$$

obtained [41] from the precise measurement of the recoil velocity of Rubidium (^{87}Rb) h/m_{Rb} [42], the Rydberg constant and m_{Rb}/m_e [41], with 0.66 ppb precision.

2.3 The EW contribution

The leading contribution to the anomalous magnetic moment of the muon from the electroweak Lagrangian of the Standard Model originates at the one-

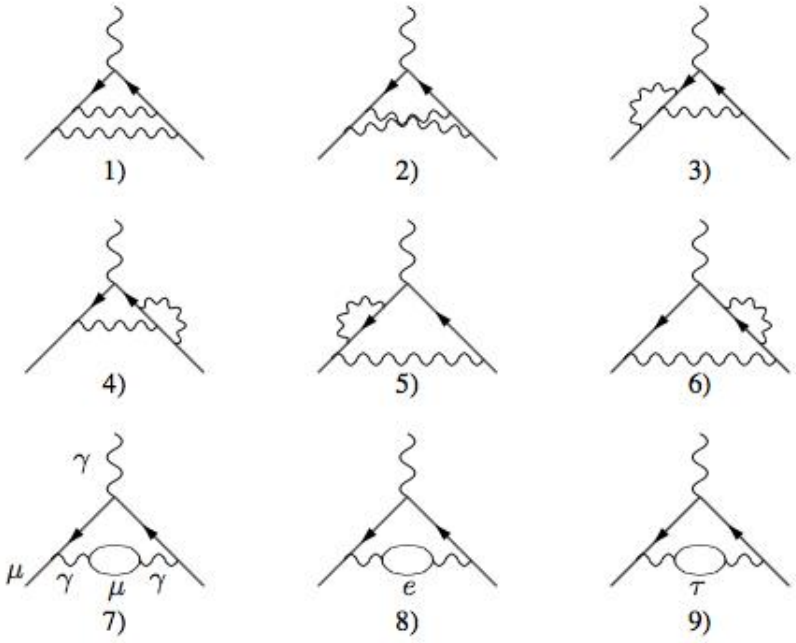

Figure 2.1: Feynman diagrams 1-7 represent the universal second order contribution to a_μ^{QED}, diagram 8 yields the "light", diagram 9 the "heavy" mass dependent corrections.

loop level. The relevant Feynman diagrams are topologically similar to the Schwinger diagram in QED, but they contain virtual $W^{\pm}$, Z, and Higgs bosons rather than photons. These diagrams are shown in Fig. 2.2.

The single loop contribution was calculated by several authors starting from Jackiw and Weinberg in 1972 [43]. Since the Fermi coupling constant $G_F \propto 1/m_W^2$, the electroweak terms are suppressed by (m_μ/M_W). Relative to the entire QED-dominated anomaly a_μ , the perturbation from single-loop W exchange is of ~ 3.3 ppm. The single loop Z-exchange reduces the overall EW contribution with a negative fractional value of -1.6 ppm while the single-loop Higgs contribution has an additional suppression of (m_μ/M_W) not contributing significantly to the single-loop calculation. The final calculations yields

$$\begin{aligned} a_\mu^{\mathrm{EW}(1)} &= \frac{G_F}{\sqrt{2}}\frac{m_\mu^2}{8\pi^2}\left\{ \underbrace{\frac{10}{3}}_{W} + \underbrace{\frac{1}{3}(1-4\sin^2\theta_W)^2 - \frac{5}{3}}_{Z} \right. \\ &+ \left. \mathcal{O}\left(\frac{m_\mu^2}{M_Z^2}\log\frac{M_Z^2}{m_\mu^2}\right) + \frac{m_\mu^2}{M_H^2}\int_0^1 dx \frac{2x^2(2-x)}{1-x+\frac{m_\mu^2}{M_H^2}x^2} \right\} \\ &= 194.8 \times 10^{-11}\,, \end{aligned} \tag{2.9}$$

where [44] $G_\mu = 1.16638(1)x10^{-5}GeV^{-2}$, $sin^2 \equiv 1$, $m_W^2/m_Z^2 \simeq 0.231$, $m_\mu = 105.658MeV/c^2$, $m_Z = 91.188GeV/c2$, $m_W = 80.385GeV/c^2$ and $m_H = 125.6GeV/c^2$.

The two-loop electroweak contribution (see Fig. 2.2(c-e)), which is negative [46], has been re-evaluated using the LHC value of the Higgs mass and consistently combining exact two-loop with leading three-loop results [48]. Taking into account also this higher order contributions to the electroweak sector the total contribution is

$$a_\mu^{\mathrm{EW}} = (153.6 \pm 1.0) \times 10^{-11} \tag{2.10}$$

where the error comes from hadronic effects in the second-order electroweak

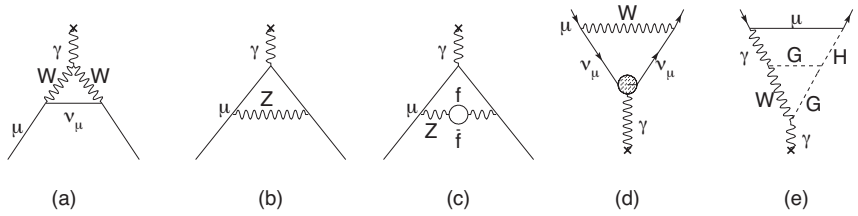

Figure 2.2: Weak contributions to the muon anomalous magnetic moment. Single-loop contributions from (a) virtual W and (b) virtual Z gauge bosons. These two contributions enter with opposite sign, and there is a partial cancellation. The two-loop contributions fall into three categories: (c) fermionic loops which involve the coupling of the gauge bosons to quarks, (d) bosonic loops which appear as corrections to the one-loop diagrams, and (e) a new class of diagrams involving the Higgs where G is the longitudinal component of the gauge bosons. See Ref. [45] for details. The $\times$ indicates the photon from the magnetic field.

diagrams with quark triangle loops, along with unknown three-loop contributions [47, 49]. The leading logs for the next-order term have been shown to be small [48]. The weak contribution is about 1.3 ppm of the anomaly, so the experimental uncertainty on a_μ of ± 0.54 ppm now probes the weak scale of the Standard Model.

2.4 The hadronic contribution

Hadronic vacuum polarization processes provide the second-largest contribution to a_μ. It is about 60 ppm of the total value. The lowest-order diagram shown in Fig. 2.3a dominates this contribution and its error, but the hadronic light-by-light contribution Fig. 2.3b is also important.

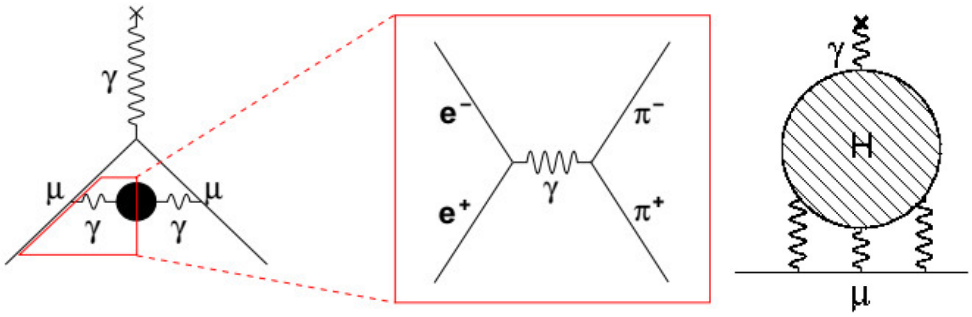

(a) (b)

Figure 2.3: (a) Feynman diagrams on the left shows the lowest-order HVP contribution to the muon anomaly, where the "blob" in the middle indicates any possible contribution of quarks. This contribution can be related to the cross section for hadron production from e^+e^- where the dominant hadron production process is the $e^+e^- \to \pi^+\pi^-$ annihilation [53]. (b) The hadronic light-by-light contribution.

2.4.1 Hadronic vacuum polarization

The energy scale for the virtual hadrons is of order $m_\mu c^2$, well below the perturbative region of QCD. In this case, the hadronic contribution cannot be calculated analytically as a perturbative series, but it can be expressed in terms of the cross section of the reaction $e^+e^- \to hadrons$, which is known from experiments, using analyticity and unitarity (the optical theorem) [50]. The leading Hadronic Vacuum Polarization (HVP) process is determined via the dispersion relation [40]:

$$a_\mu^{\mathrm{had;LO}} = \left(\frac{\alpha m_\mu}{3\pi}\right)^2 \int_{m_\pi^2}^{\infty} \frac{ds}{s^2} K(s) R(s), \tag{2.11}$$

where $R \equiv \frac{\sigma_{\mathrm{tot}}(e^+e^- \to \mathrm{hadrons})}{\sigma(e^+e^- \to \mu^+\mu^-)}$ and $K(s)$ is a kinematic factor ranging from 0.4 at $s = m_\pi^2$ to 0 at $s = \infty$ (see Ref. [45]). Because the integrand contains a factor of s^{-2}, the values of $R(s)$ at low energies (the ρ resonance) dominate the determination of $a_\mu^{\mathrm{had;LO}}$ as shown in Fig. 2.4. At the level of precision needed, more than 90 percent of the entire contribution comes from energies

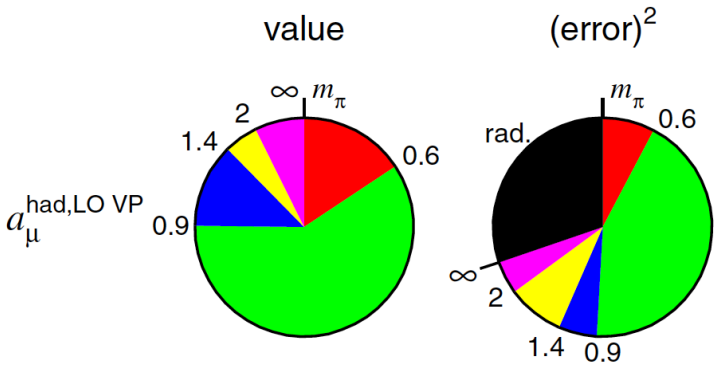

Figure 2.4: Contributions to the dispersion integral for different energy regions, and to the associated error (squared) on the dispersion integral in that energy region. Taken from Hagiwara et al. [53].

$\sqrt{s}$ ¡ 1.8 GeV. The contribution is dominated by the two-pion final state, but other low-energy multi-hadron cross sections are also important.

Two recent analyses [52, 53] using the $e^+e^- \to hadrons$, the same data set with different data treatment, see Figures 2.5 and 2.6:

$$a_\mu^{\text{had;LO}} = (6\ 923 \pm 42) \times 10^{-11}\,, \tag{2.12}$$

$$a_\mu^{\text{had;LO}} = (6\ 949 \pm 43) \times 10^{-11}\,, \tag{2.13}$$

respectively.

Higher-order contributions (HOHVP), the next-to-leading order, contain an HVP insertion along with an additional loop. The additional loop can be a leptonic pair, a photon that is emitted and reabsorbed or a second HVP insertion, as shown in Fig. 2.7.

The calculation can also be determined from a dispersion relation and is similar to the first-order HVP in that it requires experimental input from

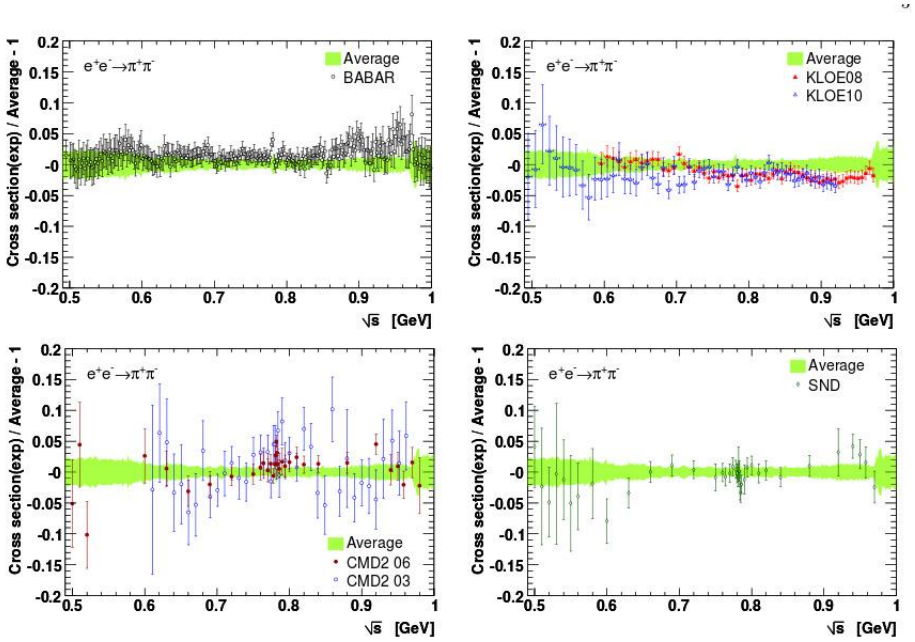

Figure 2.5: Comparison between individual $e^+e^- \to \pi^+\pi^-$ cross sections measurement from BABAR, KLOE08, KLOE10, CMD2 03. CMD2 06, SND and the HVPTools average. The error bars shows statistical and systematic errors added in quadrature. Taken from Ref. [52, 54].

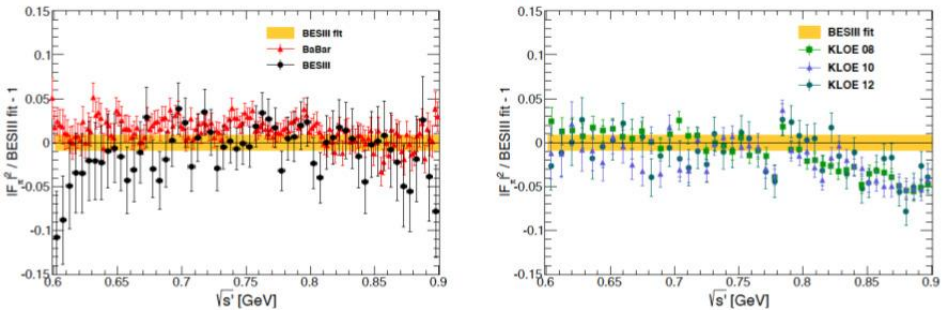

Figure 2.6: Recent results from BESIII collaboration [55].

(a) (b) (c)

Figure 2.7: HOHVP Feynman diagrams: (a) leptonic pair, (b) photon emitted and reabsorbed, (c) second HVP insertion.

$R(s)$ [40] and also knowledge of the kernel $K^{(2)}(s)$ for higher-order loops [56]:

$$a_\mu^{\text{had;NLO}} = \frac{2}{3}\left(\frac{\alpha}{\pi}\right)^2 \int_{4m_\pi^2}^{\infty} \frac{ds}{s} K^{(2)}(s/m_\mu^2) R(s), \tag{2.14}$$

The most recent evaluation of the next-to-leading order hadronic contribution is [53]

$$a_\mu^{\text{had;NLO}} = (-98.4 \pm 0.6_{\text{exp}} \pm 0.4_{\text{rad}}\ ) \times 10^{-11}\,. \tag{2.15}$$

Very recently, also the next-to-next-to-leading order hadronic contribution has been evaluated [57], with a result of the order of the expected future experimental uncertainty. This result will be included in future evaluations of the full SM theory prediction.

2.4.2 Hadronic light-by-light scattering

The hadronic light-by-light contribution (HLbL), where four photons couple to a hadronic intermediate state as shown in Fig. 2.8a, cannot at present be determined from data, but rather must be calculated using hadronic models that correctly reproduce properties of QCD. The dominant subdiagram is shown in Fig. 2.8b, the long-distance contribution, where there are two distinct vertices at which a π^0 couples to two photons. Consequently, the most

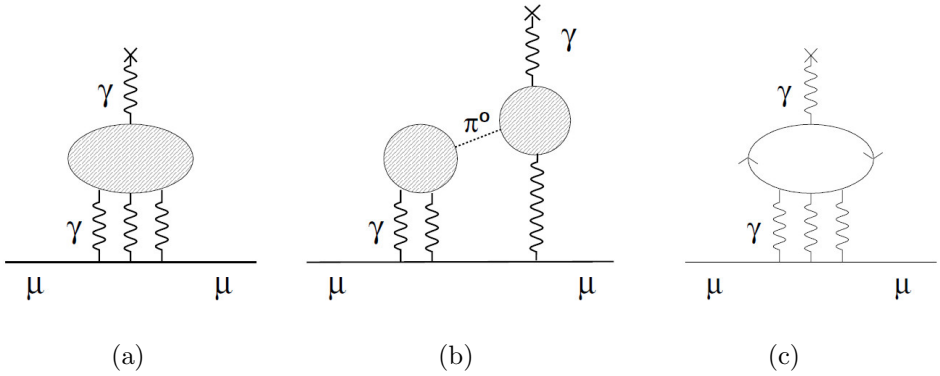

Figure 2.8: Feynman diagrams for (a) the general case of hadronic light-by-light scattering, (b) interaction involving two three-point loops connected by exchange of a pseudoscalar such as π^0, and (c) four-point loop interaction, where the particle in the loop may be a free quark or a meson.

important part of the calculation is the determination of the form factor $F_{\pi\gamma\gamma}$. There are, however, additional contributions from similar diagrams with other intermediate states and also from four-point loop diagram topologies as shown in Fig. 2.8c.

The low-energy long-distance contribution of the hadronic light-by-light scattering term has been evaluated, using the Extended Nambu-Jona-Lasinio (ENJL) model [58], for energies below $0.5GeV$. This model integrates out gluonic degrees of freedom in QCD, replacing gluon exchange interactions with local four-quark scattering diagrams. It also expands the Lagrangian as a power series in the inverse of the number of colors $\frac{1}{N_c}$. In the so-called chiral limit, where the mass gap between the pseudoscalars (Goldstone-like) particles and the other hadronic particles (the ρ being the lowest vector state in Nature) is considered to be large, it preserves the chiral symmetry structure of QCD as well as its spontaneous breaking, though it does not naturally include confinement.

The choice of the ENJL model is validated by its prediction of a_μ^{HVP}, which was calculated [59] by de Rafael. More recently evaluation of this contribution has been calculated analytically [60] and provides a long-distance constraint to model calculations.

Also a high-energy short-distance contribution of the HLbL scattering term has been evaluated. The short-distance constraint from the operator product expansion (OPE) of two electromagnetic currents, in specific kinematic conditions, relates the light-by-light scattering amplitude to an Axial-Vector-Vector triangle amplitude for which one has a good theoretical understanding [61].

Unfortunately, the two asymptotic QCD constraints mentioned above are not sufficient for a full model independent evaluation of the HLbL contribution. Most of the last decade calculations found in the literature are compatible with the QCD chiral and large-N_c limits. They all incorporate the π^0-exchange contribution modulated by $\pi^0\gamma^*\gamma^*$ form factors correctly normalized to the Adler, Bell-Jackiw point-like coupling. They differ, however, on whether or not they satisfy the particular OPE constraint mentioned above, and in the shape of the vertex form factors which follow from the different models.

A synthesis of the model contributions, which was agreed to by authors working in this field, known as the Glasgow Consensus, can be found in [62]

$$a_\mu^{HLbL} = +105(26) \times 10^{-11} \tag{2.16}$$

A different evaluation [51] leads the same central value but with a larger uncertainty (102 ± 39).

2.5 Contributions to a_μ beyond the Standard-Model

The Standard Model is a very well established theory which is able to successfully describe, in an unified way, three of the four fundamental forces: electromagnetic, weak and strong interactions but fails to explain a number of problems that are still unresolved. First, it does not incorporate the fourth fundamental force of gravity. Moreover it doesn't provide insight into the nature of the invisible matter or field, in order of 26%, that is holding galaxies together and the nature of (69%) dark energy. The SM lead to a mismatch of 120 orders of magnitude when attempts to explain dark energy in terms of vacuum energy. Therefore the SM explains about only the 5% of the energy present in the universe.

It fails also to explain why in our universe there seems to be a predominance of matter over antimatter (the matter-antimatter asymmetry problem). The Standard Model predicts CP violation which leads to a matter-antimatter asymmetry however the asymmetry predicted by the SM is smaller than what has been observed so far.

New physics can manifest itself through states or interactions which have not been seen by experiments so far because of either a lack of sensitivity or because the new state was too heavy to be produced at the existing experimental facilities. The muon $(g-2)$, together with searches for charged lepton flavor violation, electric dipole moments, and rare decays, belongs to a class of complementary low-energy experiments. In fact, the muon magnetic moment has a special role because it is sensitive to a large class of models related and unrelated to electroweak symmetry breaking (EWSB) and because it combines several properties in a unique way: it is a flavour- and CP-conserving, chirality-

flipping and loop-induced quantity. In contrast, many high-energy collider observables at the LHC and a future linear collider are chirality-conserving, and many other low-energy precision observables are CP or flavour-violating. These unique properties might be the reason why the muon $(g-2)$ is the only among the mentioned observables which shows a significant deviation between the experimental value and the SM prediction.

In this context, the new measurement of the anomalous magnetic moment of the muon at Fermilab will provide one of the most precise tests of Quantum Field Theory and will be able to place tighter constraints in the physics beyond the SM. The comparison of theoretical and experimental values for a_μ, Eq. 2.5, is very important, regardless of the outcome. If the values differ, then the comparison provides evidence for Physics beyond the Standard Model. If they agree, then the result constrains any proposed speculative extension, assuming that there are no fine-tuned cancellations between different varieties of New Physics.

Three beyond SM (BSM) models examples of interesting New Physics probed by $a_\mu^{EXP} - a_\mu^{SM}$, see Eq. 2.5, are described in this section, analyzing the effect that each would have on a_μ: muon compositeness, and supersymmetry. Those BSM models are not the only possible new physics scenario; For further reading the reader is referred to refer [69].

2.5.1 Muon compositeness

Fundamental "preons" [63] might be able to account for the existence of multiple generations of leptons, in the same way as the spectrum of hadrons is explained by the quark model. Therefore, it could be expected that a perturbation to a_μ is due to some constituents of the muon. An initial model is represented by the three-level Feynman diagram in Fig. 2.9a.

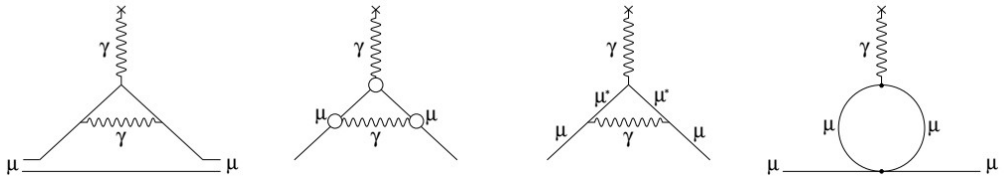

Figure 2.9: Feynman diagrams [64] for (a) the leading-order effect of compositeness, which must be canceled out in a workable model; (b) a form factor at each $\mu\gamma$ interaction vertex; (c) exited lepton states; (d) four fermion contact interactions.

The associated contribution to a_μ is linear [65] in the ratio of the muon mass to the characteristic scale $\Lambda = \frac{1}{r}$, which must be canceled out in a workable model.

Once the linear contribution has been removed, substructure affects a_μ in three ways:

1. Each vertex at which a muon interacts with another particle is multiplied by a form factor $(1 + \frac{q^2}{\Lambda^2})$ to account for the spatial extent of the charge distribution; see Feynman diagram in Fig. 2.9b;

2. The muon may enter excited states in which the constituents have acquired relative orbital angular momentum; see Feynman diagram in Fig. 2.9c;

3. There may be contact interactions among the constituents that do not correspond to the usual exchange of gauge bosons; see Feynman diagram in Fig. 2.9d.

The numerical results are clearly dependent on the details of the model; however, the contribution to a_μ is always proportional [64] to $(\frac{m_\mu}{\Lambda})^2$. Likely

the order of the coefficients, after the summation of all the diagrams, is 1. Consequently,

$$a_\mu^\Lambda = O[(\frac{m_\mu}{\Lambda})^2], \tag{2.17}$$

a measurement of a_μ to 14 ppb is capable of constraining Λ at energies of the orders of TeV.

2.5.2 Supersymmetry

The most promising theoretical scenarios for New Physics are supersymmetric extensions of the SM, in particular, the Minimal Supersymmetric Standard Model (MSSM) [40]. Inside the SM, masses of fundamental particles and couplings associated with interactions are free parameters, determined by spontaneous symmetry breaking. However, they appear conspiring to give a dramatic cancellation in their effects on the Higgs boson mass. This problem is known as the "gauge hierarchy problem". Supersymmetry (SUSY) implements a symmetry mapping

$$boson \leftrightarrow fermion$$

between bosons and fermions, by changing the spin by $\pm\frac{1}{2}$ units [67]. Every boson has a fermion partner, and every fermion has a boson partner. There is no experimental evidence for the partner particles. The symmetry must therefore be broken by the addition of "soft" terms to the Lagrangian; otherwise, the masses of the paired fermions and bosons would be the same, and the partners would have been seen long ago. SUSY associates with each SM state X a supersymmetric "s-state" $\tilde{\mathrm{X}}$ where sfermions are bosons and sbosons are fermions. This new partner particles are labeled using and *s-* as a prefix for fermions having *squarks* and *sleptons*; the suffix *-ino* is used for bosons: so photon becomes *photino* and so on.

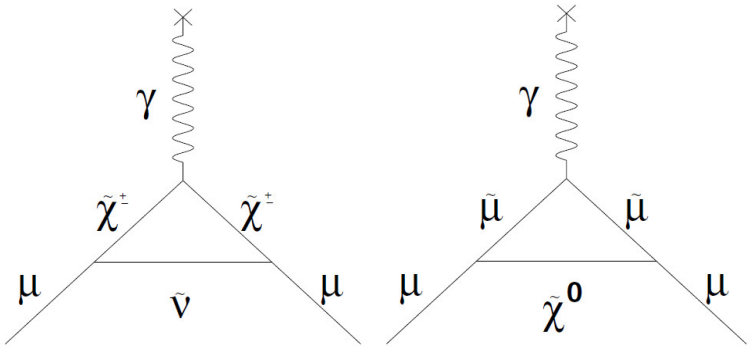

Figure 2.10: Feynman diagrams for the lowest-order supersymmetric contributions to a_μ.

Another effects of supersymmetry is that this theory leads to two Higgs doublets: one gives mass to the upper half of each generation (u, c and t quarks) and the other gives mass to the lower half (d, s and b quarks). Of this four states, two are electrically neutral, one is positive and the other is negative. The ratio $tan\beta = \frac{v_2}{v_1}$ of the vacuum expectation values of the Higgs doublets is an important parameter describing the nature of supersymmetry and its scale is related to the ratio of top and bottom quark and is of the order of 40.

In Fig. 2.10 are shown the lowest-order contributions to a_μ. The first thing to note is that these contributions are identical to the dominant standard model electroweak contribution. The $\tilde{\mu}$ represents the smuon and the $\tilde{\nu}$ the sneutrinos. The $\tilde{\chi}^0$ and $\tilde{\chi}^\pm$ are called neutralino and chargino respectively: these are the mass eigenstates whose linear combinations give photino, wino, zino and Higgsinos which clearly here are not mass eigenstates.

The contributions to a_μ from a supersymmetric mass can be expressed as to be degenerate at m yielding [70]:

$$a_\mu^{SUSY} \approx sign(\mu)130 \times 10^{-11} tan\beta \left(\frac{100GeV}{m}\right)^2, \tag{2.18}$$

with $tan\beta$ is as large as 40, then a_μ is sensitive to mass scales m of up to 800 GeV. The formula still approximately applies even if only the smuon and chargino masses are of the order of m.

The Minimal Supersymmetric Standard Model (MSSM) describes a very general form of supersymmetric breaking and do not assume to have degenerate masses. It has 105 independent parameters as masses, phases and mixing angles beyond those of the ordinary Standard Model [66]. But if we consider the leading contribution on a_μ only a small number of those parameters are involved in the calculation. This set of parameters can be reduced just postulating a mechanism responsible for supersymmetry breaking. As an example, assuming unification with the gravitational force at the Planck scale, is possible to construct a supergravity model, in which only four relevant parameters remain [68].

a_μ determination versus LHC data

The LHC is sensitive to virtually all proposed weak-scale extensions of the standard model, ranging from supersymmetry, extra dimensions and technicolor to little Higgs models, unparticle physics, hidden sector models and others. However, even if the existence of physics beyond the Standard Model is established, it will be far from easy for the LHC alone to identify which of these alternatives is realized. Qualitatively different SUSY models which are in agreement with current LHC data. Muon $g-2$ would predict a tiny effect to a_μ [71, 72], while SUSY effects are often much larger.

If the LHC finds no physics beyond the standard model but the a_μ measurement establishes a deviation, might be a signal for dark sector models [73].

Next, if New Physics is realized in the form of a non-renormalizable theory, a_μ might not be fully computable but depend on the ultraviolet cutoff. In such

a case, the a_μ measurement will not only help to constrain model parameters but it will also help to get information on the ultraviolet completion of the theory.

The complementarity between a_μ and LHC can be exemplified quantitatively within general SUSY, because this is a well-defined and calculable framework. Fig. 2.11 illustrates the complementarity in selecting between different models. The points in the plot in Fig. 2.11a show the values of possible SUSY contributions to a_μ [74, 76, 77], where the current (yellow band) and an improved (blue band) measurement of a_μ is also reported. Within SUSY, the very different a_μ predictions, can resolve such LHC degeneracies, which cannot be distinguished at the LHC alone (see also Ref. [75] for the LHC inverse problem). Therefore, a precise measurement of $g-2$ to $\pm 1.6 \times 10^{-10}$ will be a crucial way to rule out a large fraction of models and thus determine SUSY parameters.

The plot of Fig. 2.11b illustrates that the SUSY parameter $\tan\beta$ can be measured more precisely by combining LHC-data with a_μ. It is based on the assumption that the deviation $\Delta a_\mu = 255 \times 10^{-11}$. The plot compares the LHC $\Delta\chi^2$ parabola with the ones obtained from including a_μ,

$$\Delta\chi^2 = \left[\frac{a_\mu^{\mathrm{SUSY}}(\tan\beta) - \Delta a_\mu}{\delta a_\mu}\right]^2$$

with the errors $\delta a_\mu = 80 \times 10^{-11}$ (dark blue) and 34×10^{-11} (light blue). As can be seen from the Fig. 2.11b, using today's precision for a_μ would already improve the determination of $\tan\beta$, but the improvement will be even more impressive after the future a_μ measurement.

In summary, the anomalous magnetic moment of the muon is sensitive to contributions from a wide range of physics beyond the standard model. It will continue to place stringent restrictions on all of the models, both present and yet to be written down. If physics beyond the standard model is discovered

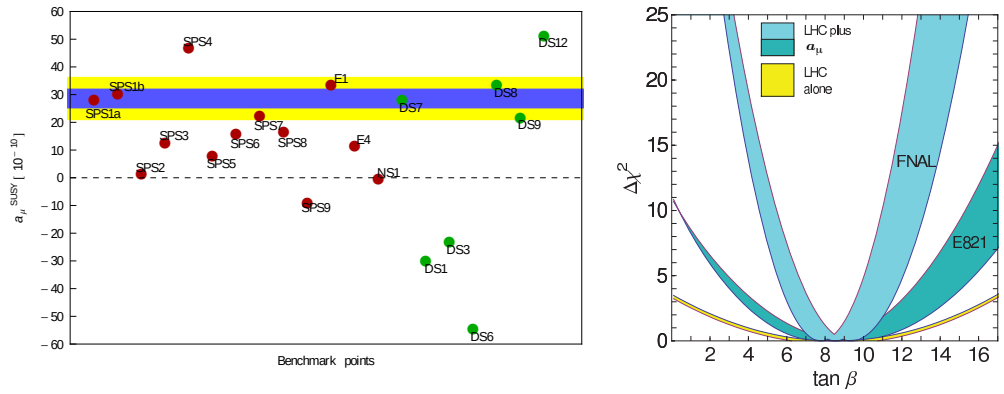

(a) (b)

Figure 2.11: (a) SUSY contributions to a_μ for the SPS and other benchmark points (red), and for the "degenerate solutions" from Ref. [78]. The yellow band is the ± 1 σ error from E821, the blue is the projected sensitivity of E989. (b) Possible future tan β determination. The bands show the $\Delta\chi^2$ parabolas from LHC-data alone (yellow) [79], including the a_μ with current precision (dark blue) and with prospective precision (light blue). The width of the blue curves results from the expected LHC-uncertainty of the parameters (mainly smuon and chargino masses) [79].

at the LHC or other experiments, a_μ will constitute an indispensable tool to discriminate between very different types of new physics, especially since it is highly sensitive to parameters which are difficult to measure at the LHC. If no new phenomena are found elsewhere, then it represents one of the few ways to probe physics beyond the standard model. In either case, it will play an essential and complementary role in the quest to understand physics beyond the standard model at the TeV scale.

Chapter 3

The evolution of muon $g-2$ experiments

This Chapter provides a brief history of previous measurements of the anomalous magnetic moment of the muon and a sense of the evolution of the experimental precision with time.

From the discovery of parity violation in 1957 [82, 83], was understood that muons produced from pion decay are naturally polarized, providing a natural source of polarization for the experiment with muons. In fact, pions decay as following:

$$\pi^+ \to \mu^+ \nu_\mu$$
$$\pi^- \to \mu^- \overline{\nu}_\mu$$

exchanging a $W^\pm$ boson. Pions have $S_\pi = 0$, so daughter particles will have opposite spin in order to conserve the angular momentum. Considering as example π^+ decays, neutrinos are lefthanded, so high energy muons (those produced with momentum parallel to the one of the pion) will be produced with spin parallel to their momentum (see Fig. 3.2). For more discussion on

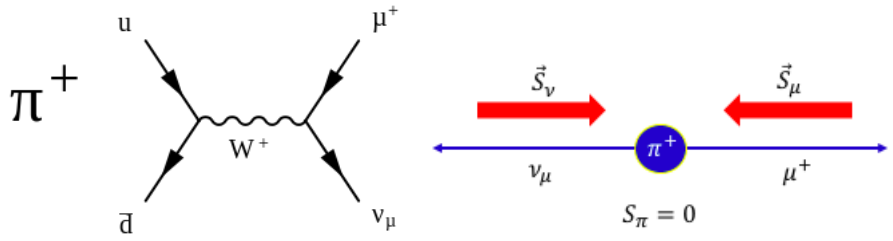

(a) (b)

Figure 3.1: (a) Feynman diagram for $\pi^+ \to \mu^+\nu_\mu$ decay (equally valid in the laboratory frame). (b) Spin configuration in the π^+ decay. Muon have their momentum opposite to the neutrino's one; neutrino is lefthanded ($m_\nu \approx 0$), for angular momentum conservation, the two spin have to be opposite.

parity violation in pion decay see [1, 80, 81].

As another consequence of parity violation, the decaying of high energy electrons from a polarized muon source is preferentially in the same direction of the muon spin. As an example, considering μ^+ decay, high energy positrons are most likely produced with momentum opposite to the one of the two neutrinos due to kinematic considerations. Also, neutrinos, due to helicity consideration are produced with opposite spins (one is lefthanded, the other, $\overline{\nu}_\mu$, is righthanded), therefore the total spin of the neutrino system is zero. In order to conserve the angular momentum the positron's spin has to be aligned with the spin of the muon (see Fig. 3.2). Highly relativistic positrons are most likely produced as righthanded particles: high energy positrons behave like massless particles (E $\gg$ m_e) and for a massless particle helicity eigenstates match the chiral eigenstates, so the antiparticles are produced righthanded. In this case, high energy positrons have the spin parallel to their momentum. Therefore there is a strong correlation between the high energy e^+ momentum direction and the muon's spin.

Due to above correlation, if a polarized muon source is stopped in a mag-

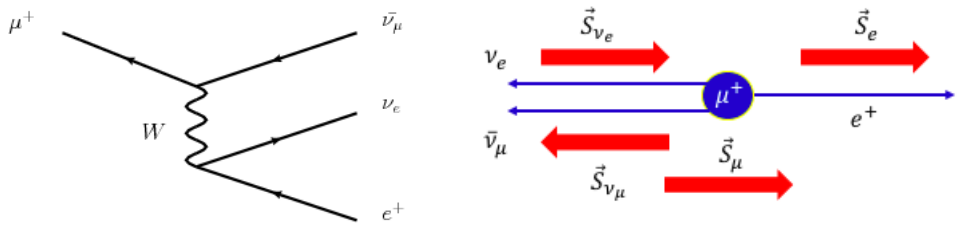

(a) (b)

Figure 3.2: (a) Feynman diagram for $\mu^+ \rightarrow e^+\nu_e\overline{\nu_\mu}$ decay. (b) Spin configuration for μ^+ decay. High energy positrons are produced opposite to neutrino. Neutrino spins are opposite due to helicity considerations, so $\vec{S}_e \| \vec{S}_\mu$. High energy positron behaves almost like righthanded particle, so $\vec{p}_e \| \vec{S}_e$.

netic field, a fixed counter with a threshold on the decay electron energy will measure a time distribution of the following form:

$$N(t) = N_0 e^{-\frac{t}{\tau_\mu}}[1 + A\cos(\omega_s t + \phi)], \tag{3.1}$$

where N_0 is total population at time t=0, τ_μ is the muon lifetime, the asymmetry A is determined by the threshold on the energy of decaying particle and the phase ϕ depends on the initial polarization of the muon ensemble. ω_s represents the *Larmor precession frequency* that is referred to the torque, manifested as a rotation of the spin direction of the muon dipole about the magnetic field B where it is placed:

$$\omega_s = g\frac{eB}{2mc}, \tag{3.2}$$

3.1 Early muon experiments

The first muon experiment was performed in 1957 by Garwin and collaborators at the Nevis cyclotron of the Columbia University [84]. Muons formed in flight from pion decays were stopped in a carbon target after passing one at

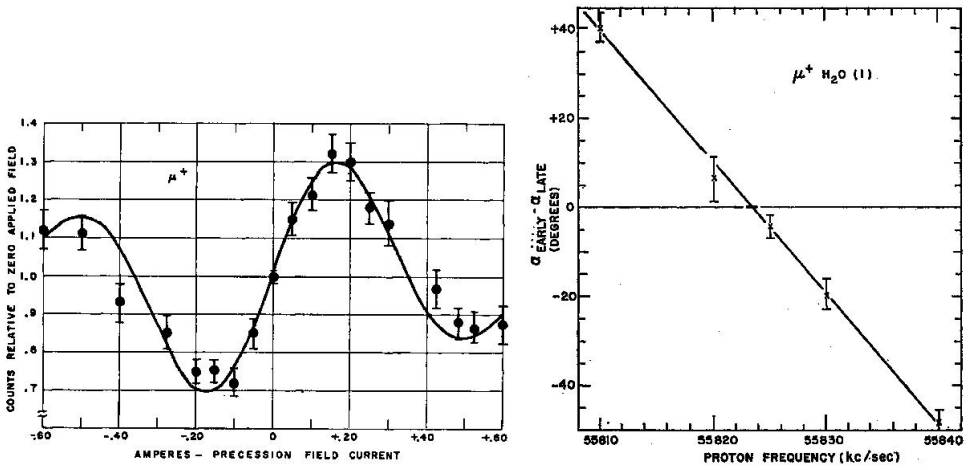

(a) Garwin data (b) Hutchinson data

Figure 3.3: Historical plots showing Larmor precession data from the Garwin (a) and Hutchinson (b) experiments [84, 85] used to determine the muon *g-factor*.

time through an entrance counter. An external magnetic field applied to the target region causes the spin of the muon to precess. The precession could be increased or decreased tuning the magnitude of the external field. This experiment was able to determine a value for $g = 2.00 \pm 0.10$ for the muon, plotting the counts measured from the fixed counter as a function of the magnetic field following Eq. 3.2 as shown in Fig. 3.3a.

Muons have a lifetime, in the rest frame, $\tau_\mu \simeq 2$ microseconds (μs) which makes difficult to store them and analyze their spin. In this short period of time, the muons have to be created, stored in a magnetic field, and their spins analyzed. The precision obtained with this experiment was not sufficient to measure anomaly contribution to g. Similar experiments continued during the next five years with the aim to improve the precision of this measurement. The highest precision was obtained by Hutchinson and collaborators in 1963 [85] by stopping muons in a magnetic field and measuring the early-to-late phase difference between a standard reference and peaks in the decay electron distri-

bution (Eq. 3.1). In Fig. 3.3b it is shown the final result of the measurement of the *Larmor* precession frequency plotting the phase difference, at a fixed time interval, as a function of the reference clock and fitting for the zero crossing. In this experiment the magnetic field was measured via nuclear magnetic resonance (NMR) in terms of the Larmor precession frequency of protons in a polarized water sample, so it easier to express the results as a ratio λ of the two frequencies or magnetic moments obtaining:

$$\lambda = \frac{\omega_\mu}{\omega_p} = \frac{\mu_\mu}{\mu_p} = 3.18338(4). \tag{3.3}$$

Hutchinson and his group measured the Larmor precession frequency and the magnetic field to a 10 ppm precision [1].

3.2 CERN experiments

Several years before Hutchinson published his results on the Larmor precession frequency a new experimental procedure was studied at CERN to increase the precision of the $g-2$ measurement, following the principles used in the determination of the electron's anomalous magnetic moment [86]. A charged particle moving in a uniform magnetic field B it will execute a circular motion with a cyclotron frequency:

$$\omega_c = \frac{eB}{mc}. \tag{3.4}$$

Taking the ratio between ω_s/ω_c and the definition of a_μ, by Eq. 1.19, follow that:

$$\frac{\omega_s}{\omega_c} = 1 + a_\mu. \tag{3.5}$$

[1] Using this result of the *Larmor* precession frequency is possible to obtain a direct test with the QED prediction substituting ω_s into Eq. 3.2 and then solving for g.

Therefore, the spin precession of muons moving into this magnetic field develops $1 + a_\mu$ times faster than the momentum vector. Taking the difference between the two frequencies the result is the *anomalous precession frequency* defined as:

$$\begin{aligned} \omega_a &= \omega_s - \omega_c, \\ &= \frac{eB}{mc}\left(\frac{g}{2} - 1\right), \\ &= \frac{eB}{mc}\frac{g-2}{2}, \\ &= a_\mu \frac{eB}{mc}, \end{aligned} \tag{3.6}$$

which is proportional to a_μ. Uncertainties on a_μ incorporates uncertainties on the magnetic field determination or in the muon mass determination but because $a_\mu \sim 1/800$ of g, measuring directly the anomaly increase the precision of almost three order of precision.

Looking at Fig. 3.4 it is possible to understand the spin precession concept. The figure shows the spin and momentum vectors for an initially forward polarized muon beam, moving along a circular orbit in a magnetic field. If the value of g is exactly 2, the situation is the one of the left panel, where the spin vector is locked to the momentum direction. Since g is a little larger than 2, the spin vector slightly rotates more than 2π during each cyclotron period, as shown on the right panel.

Considering as example the μ^+ decay, parity violation in the weak interaction allows the spin direction to be measured as a function of time. Eventually, essentially every muon decays by $\mu^+ \to e^+ \nu_\mu \overline{\nu}_e$. In the rest frame of the muon, the differential probability for the positron to emerge with a normalized energy

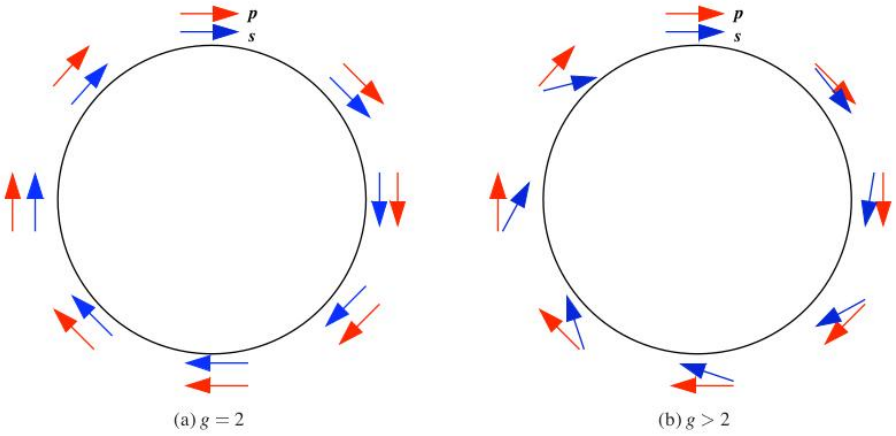

Figure 3.4: Illustration of the muon spin and momentum vectors for a muon orbiting in a magnetic field when $g = 2$ (a) and $g > 2$ (b).

$y = E/E_{max}$ at an angle *theta* with respect to the muon spin is [87]:

$$\frac{dP}{dyd\Omega} = n(y)[1 + A(y)cos\theta s] \tag{3.7}$$

$$with\ n(y) = y^2(3 - 2y) \tag{3.8}$$

$$and\ A(y) = \frac{2y - 1}{3 - 2y}. \tag{3.9}$$

The quantities *n(E)* and *A(E)*,in the muon rest frame, are plotted in Fig. 3.5, normalized to $E_{max} = 52.8$ MeV. Positrons with $y > 0.5$ are most likely to be emitted in the direction of the muon spin, and those with lower energy are most likely to be emitted opposite it. Because more positrons are emitted with $y > 0.5$ and because their asymmetry is higher, the overall effect is that the decay positrons tend to go in the direction of the muon spin. If a nonzero energy threshold is established, then the asymmetry is even higher than 1/3. Because the spin appears to rotate at the frequency ω_a, so does the distribution of decay positrons.

In the laboratory frame, the stored muons are highly relativistic so that

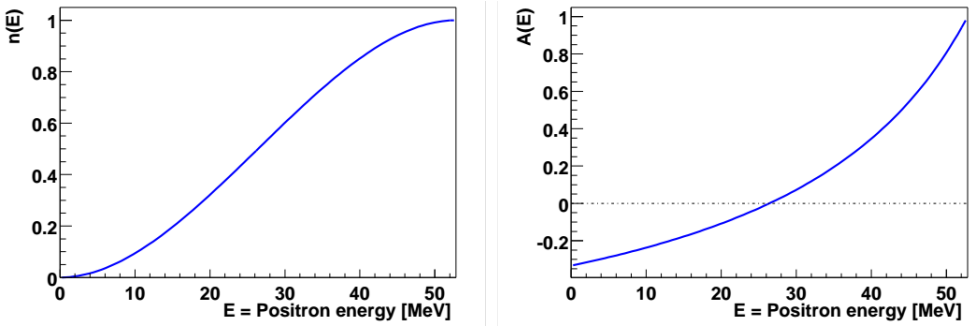

(a) n(E) (b) A(E)

Figure 3.5: Number density and asymmetry distributions for decay positrons in the muon rest frame.

the range of observed decay angles is extremely compressed; the effect of the Lorentz boost is illustrated in Fig. 3.6. Compared to the angle subtended by a practical detector, all decays are forward. The energy of the positron in the laboratory frame is given by:

$$E_{lab} = \gamma(E* + \beta p * cos\theta*). \tag{3.10}$$

The positron energy E∗ is also high enough, in general, to justify a fully relativistic treatment, so

$$E_{lab} = \gamma E * (1 + cos\theta*). \tag{3.11}$$

The laboratory energy clearly depends strongly on the decay angle $\theta*$. To have a high energy in the laboratory frame, a positron must have a high energy in the CM frame and also be emitted at a forward angle there. Setting a laboratory energy threshold therefore selects a range of angles in the muon rest frame. Consequently, the number of particles detected above such a threshold as a function of time is modulated with the frequency ω_a.

This procedure developed at CERN permits to improve the experimental precision and from this concept a series of experiments with increasing precision

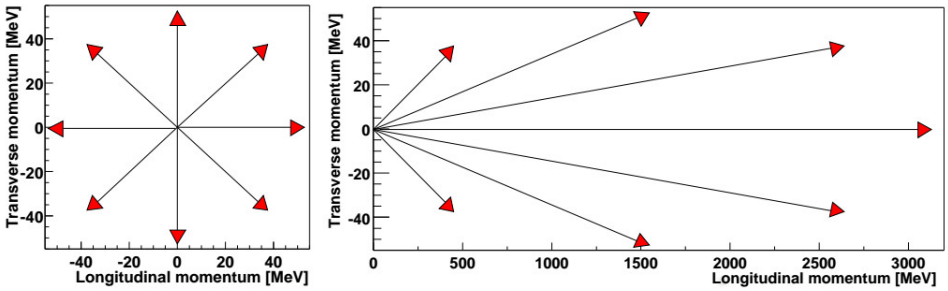

(a) CM frame (b) Laboratory frame

Figure 3.6: Illustration of the Lorentz boost of the decay positron from the muon rest frame to the laboratory frame.

come out; three were performed at CERN, which will be referred as CERN I, CERN II and CERN III, one at the Brookhaven National Laboratory (BNL) and a new one at Fermilab (FNAL).

3.2.1 The CERN I experiment

In the first experiment at CERN a forward polarized muon beam, using muons created from a 600 MeV Synchro-cyclotron, is injected into a 6 m long magnet, with a magnetic field of 1.5 T. The magnetic field causes the muon beam to move in a spiraling orbit. To create this kind of motion is important to shim carefully the magnetic field in order to be parabolic in the vertical direction

$$B(y) = B_0(1 + ay + by^2), \tag{3.12}$$

where the radius of the orbit is determined by the value of B_0, the linear term a causes each orbit to advance along the magnet and the term b produces a quadratic field providing vertical focusing. Increasing gradually the value of a increases the step size of orbital 'walking'. At the end of the magnet this gradient is large enough to allow the muons to escape from the field.

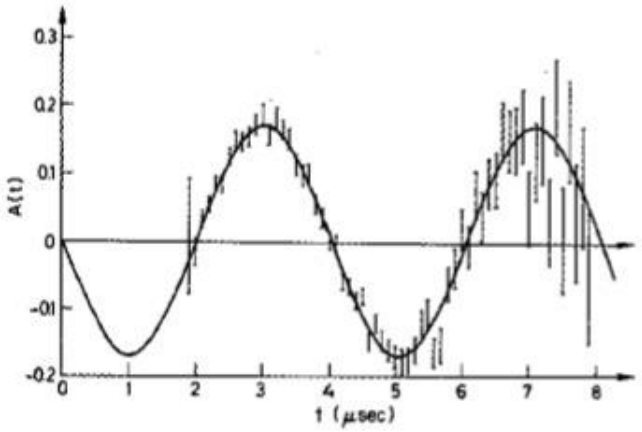

Figure 3.7: CERN I data.

A methylene-iodide target stops the beam and from the asymmetry of the decay electrons the polarization is extracted. To determine the spin precession relative to the momentum is necessary to determine the amount of time spent by the muon beam in the magnetic field. To avoid the use of a forward and backward detector, with different efficiencies for each, the magnetic field is pulsed to alternately rotate the muon spin by $\pm 90^\circ$ before injection. Data from CERN I don't appear to be more precise than Garwin data, as shown in Fig. 3.7, but they represent a direct measurement of the anomaly. Therefore, the precision of 5×10^{-3} on a_μ

$$a_\mu^{exp}(1965) = 0.001162(5) \rightarrow 4300\ ppm, \tag{3.13}$$

implies a precision of ~ 5 ppm on the determination of g.

The muon mass and the constants in Eq. 3.2 were known at the time of the CERN I experiment with an adequate precision to extract a_μ. But using different techniques for extracting a_μ like Hutchinson's, provide a measurement independent on the muon mass. This technique gains importance as the precision of the anomalous precession experiments improves, since Eq. 3.2, using

Eq. 1.19 and Eq. 3.2, can be written as

$$\frac{\omega_a}{\omega_s} = \frac{a_\mu}{a_\mu + 1}. \tag{3.14}$$

Multiplying and dividing the left side of the equation for the Larmor precession frequency of proton ω_p in the same magnetic field, the ratio can also be written as

$$\frac{\omega_a}{\omega_s} = \frac{\omega_a \omega_p}{\omega_p \omega_s} \tag{3.15}$$

The factor ω_p/ω_s in Eq. 3.15 is the inverse of the ratio λ (Eq. 3.3) measured by Hutchinson independently. Frequencies in nominator and denominator of Eq. 3.15 are individually B dependent, but the ratio is not. This permits to take the value of λ and the ratio $\mathrm{Re} = \omega_a/\omega_p$ from different experiments to extract the value of a_μ. In fact solving Eq. 3.15 for a_μ considering λ and Re one obtains

$$a_\mu = \frac{\mathrm{Re}}{\lambda - \mathrm{Re}} \tag{3.16}$$

With an accurate knowledge of λ, the value of a_μ can be extracted from experiments which measure the anomalous precession frequency ω_a and the proton Larmor frequency ω_p in the same apparatus. CERN I results were surprising due to the agreement with the prediction for the electron (see Eqs. 1.2.3, 3.13). It was expected a noticeable deviation because of the moun mass, as in the proton and neutron case, but the result was the proof that in terms of QED the muon behaves just as an heavier electron. This result, together with the idea of a CERN II experiment, led theorists to improve the QED calculation to second order in α, with the new result [88]

$$a_\mu^{theor}(1965) = 0.00116552(5) \rightarrow 42\ ppm, \tag{3.17}$$

where the error of 5×10^{-8} is due to the uncertainty in the virtual loops containing hadronic processes. This value can be improved to 1×10^{-8} with a first estimation of a third order QED calculation and by the knowledge of α.

Uncertainties in the result of the CERN I experiment was dominated by statistical error, so the main obstacle for a new experiment was to find a method of increasing the statistical power. The prospects for improving a_μ can be understood by examining the terms of the expression used to fit data:

$$N(t) = N_0 e^{-\frac{t}{\tau_\mu}}[1 + A\cos(\omega_a t + \phi)], \tag{3.18}$$

This is the same functional form as used in a spin precession experiment where the muon is at rest, see Eq. 3.1, only now the frequency corresponds to the anomalous precession frequency ω_a and the lifetime τ_μ has been time dilated in the lab frame.

The fractional error on ω_a is [89]

$$\frac{\delta\omega_a}{\omega_a} = \frac{\sqrt{2}}{\omega_a A \tau \sqrt{N}}. \tag{3.19}$$

In addition to the obvious improvement in statistical power gained through increasing N, the precision can be improved by increasing any of the other factors in the denominator:

- The anomalous precession frequency ω_a is proportional to the magnetic field, so one option is to increase the field strength, thus generating more cycles to be fit;
- Another possibility is to use higher-energy muons so that the lifetime τ has been relativistically enhanced;
- The asymmetry of the signal A can be improved by using better detectors and choosing an appropriate energy level to maximize the imbalance in the parity violating decay electrons [105].

In 1959, while the CERN I experiment was just starting to take data, the CERN Proton Synchotron (PS) came online. The new machine was capable

of producing 28 GeV protons, which could then in turn be used to generate a highly relativistic source of muons with a luminosity much higher than the Synchro-cyclotron. Immediately after. The advent of the PS at CERN provided a more energetic muon source with a luminosity higher than the Synchro-cyclotron giving the idea to the same group of physicist of CERN I to exploit the possibility to perform a measurement of a_μ.

3.2.2 The CERN II experiment

The CERN II experiment had a 5 m diameter storage ring with a C-shaped cross section. The polarized muon source was obtained by injecting a 10.5 GeV proton beam onto a target placed inside the storage ring. Forward-going pions of momentum $p = 1.27\ GeV/c$ was captured in the 1.7 T field in the storage ring. As the pion decays, a beam of longitudinally polarized muons with a relativistic factor $\gamma = 12$ were captured in the storage ring. This injection process was inefficient, creating a large background, due to protons and the large amount of pion momenta produced a less than optimal initial muon polarization. However, the luminosity of the PS and the factor of 12 in the dilated lifetime, more than CERN I, made up for the inadequacies associated with the injection. The decay electrons from the stored muons bend radially inward with respect to the muon orbit because of their lower momentum. Therefore, detectors had to be placed around the inner radius of the ring to detect the decayed electrons. In Fig. 3.8 the experimental setup is shown. The CERN II experiments was able to measure for a_μ (Fig. 3.9)

$$a_\mu^{exp}(1968) = 0.00116616(31) \rightarrow 270\ ppm, \tag{3.20}$$

which is almost 2σ from the theoretical prediction. This level of discrep-

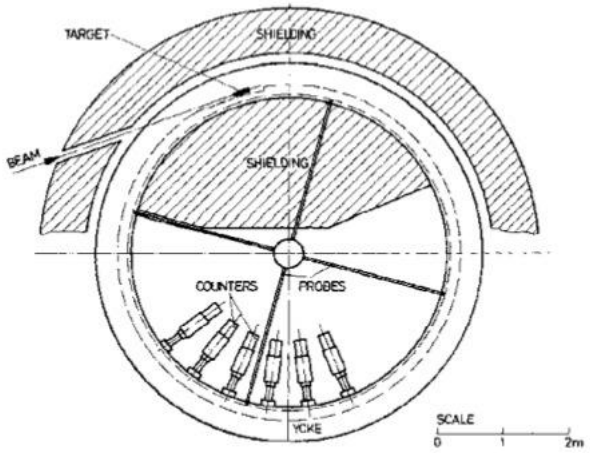

Figure 3.8: CERN II setup.

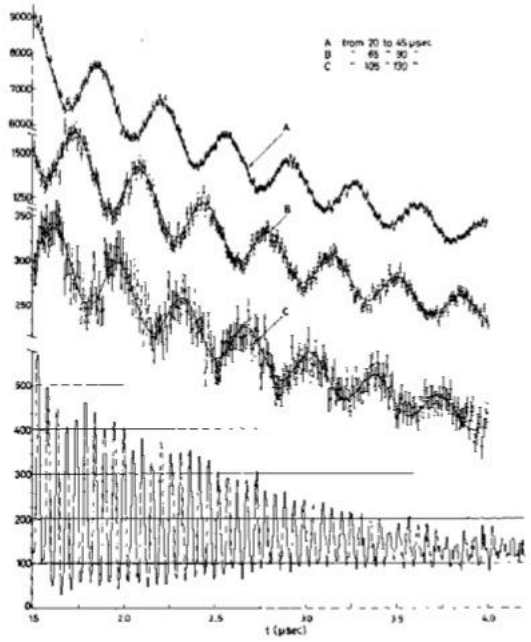

Figure 3.9: CERN II data.

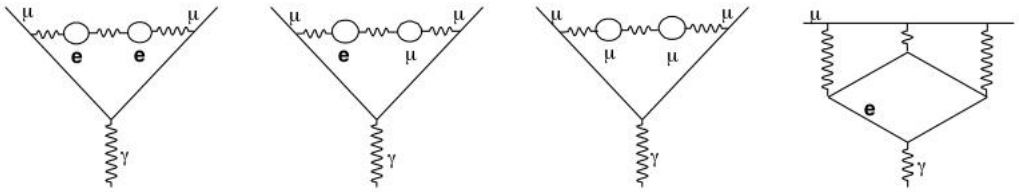

Figure 3.10: Feynman diagrams for the 3rd order QED calculation.

ancy between the two values was resolved by Aldins and collaborators [91] examining QED contribution arising from light-by-light scattering, Fig. 3.10. This contribution was assumed to be negligible but, in 1969, was confirmed a 200 ppm contribution to the theoretical value of a_μ, leading to a new determination:

$$a_\mu^{theor}(1969) = 0.0116587(3) \rightarrow 25\ ppm, \tag{3.21}$$

confirming the agreement between the experimental and theoretical values.

The increased precision of the experimental procedure required to start considering the hadronic contributions to vacuum polarization in the theoretical calculation of a_μ. Quantum chromodynamics does not provide a method to calculate hadronic loops at low energies, associated with the muon's vacuum polarization. A way out is to take the electromagnetic coupling of hadrons from experimental data using the dispersion relation [92]

$$a_\mu^{HVP} = \frac{1}{3}(\frac{\alpha}{\pi})^2 \int_{4m_\pi^2}^{\infty} \frac{R(s)}{s} K(s) ds, \tag{3.22}$$

where $R(s)$ is given by:

$$R(s) = \frac{\sigma(e^+e^- \rightarrow hadrons)}{\sigma(e^+e^- \rightarrow \mu^+\mu^-)} \tag{3.23}$$

A more precise determination of the cross section data, obtained at Novosibirsk and Orsay [93, 94] experiments, were included as first in the paper of Gourdin and de Rafael [92], where they present a contribution to a_μ of

$65.(0.5)\times10^{-8}$, with the error calculated solely from the uncertainty in the cross section measurements. At this point, from the experimental point of view, physicists started again to search a way to improve the precision of the measurements, considering that the CERN II experiments ended with a statistical error of 2.3 $\times10^{-7}$ and a systematic error of 1.9 $\times10^{-7}$.

3.2.3 The CERN III experiment

The systematic uncertainty coming from the CERN II experiment was entirely due to the radial variation in the magnetic field required to provide vertical confinement. A possible solution was to use a quadrupole electric field to prevent the stored muons from oscillates up and down into the magnet yoke. A relativistic muon see this quadrupole electric field in the lab frame as a magnetic field in its rest frame; so the anomalous precession frequency can be derived as

$$\vec{\omega_a} = \frac{e}{m}\left[a_\mu \vec{B} - \left(a_\mu - \frac{1}{\gamma^2 - 1}\right)(\vec{\beta}\times\vec{E})\right]. \tag{3.24}$$

In the Eq. 3.24 the last term introduces a dependence of the spin frequency on the electric field; while NMR probes provides an extremely precise way to determine the magnetic field, there's no way to measure electric field at the same level of precision. Even if the option of electric quadrupoles seems not a practicable option, if the coefficient in front of the term $(\vec{\beta}\times\vec{E})$ can be made zero, the measurement of the electric field is not required. It comes out that for the correct relativistic enhancement

$$\gamma = \sqrt{\frac{1}{a_\mu} + 1} \tag{3.25}$$

this coefficient is precisely zero. The related muon momentum, called magic momentum p_μ, is 3.09 GeV/c which corresponds to a momentum that was eas-

ily reachable at the PS. For the goals established for the CERN III the Hutchinson error of 13 ppm in the determination of λ was not sufficient anymore, so most scientist undertook the endeavor to have a better λ measurement, with the most precise determination obtained by Ken Crowe and collaborators [95]

$$\lambda = \frac{\omega_\mu}{\omega_p} = \frac{\mu_\mu}{\mu_p} = 3.1833467(82). \tag{3.26}$$

The experience obtained with CERN II was used to revisit the whole scheme and improve the experimental setup:

- Background was reduced by not injecting protons directly into the ring, but placing the target outside and using an inflector to inject pions into the storage region. This allowed also to place detectors all around the circumference, increasing statistics, because the shielding block were not necessary as in CERN II;

- Using a beamline to transport pions permitted to select a very narrow range of pion momenta increasing the polarization of stored muons;

- The magic momentum meant that the relativistic lifetime of the muons is precisely 64.4 μs, which is more than a factor of two than CERN II.

Therefore, almost all the factors in the denominator of Eq. 3.19 were improved as can be seen easily from Fig. 3.11.

The final result obtained after combining data for both positive and negative muon was

$$a_\mu^{exp}(1979) = 0.001165924(8.5) \rightarrow 7\ ppm, \tag{3.27}$$

where the fact that the 7 ppm error is dominated by statistical uncertainty proved the robustness of the new magic momentum technique. With a total uncertainty in theoretical prediction of 11 ppm the CERN III results did not

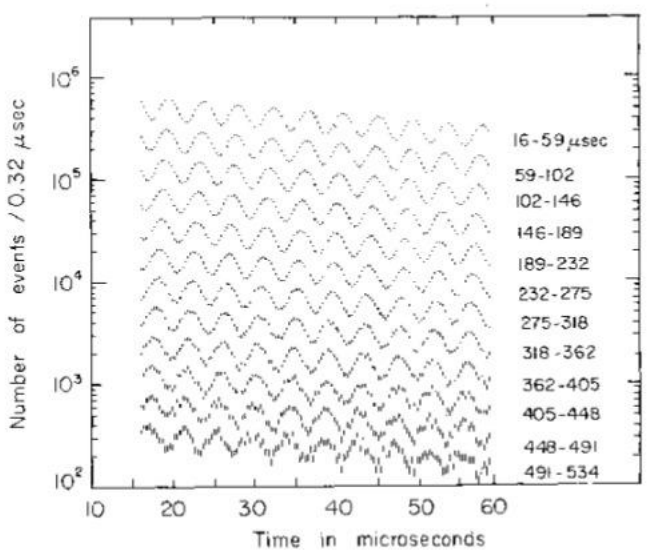

Figure 3.11: CERN III data. As can be easily seen the wiggles are visible up to 500 μs w.r.t the CERN II data of Fig. 3.9 which are up to 130 μs.

discover the origin of the muon mass but proved the importance of the hadronic vacuum polarization contribution to the 5σ level.

3.3 The Brookhaven experiment

After the CERN III result, the theoretical progress on the determination of a_μ slowed down to the point that an immediate experiment pushing forward the precision was no longer justifiable. It was only after the calculation of the α^4 order QED term, by Kinoshita and collaborators [96] and improvements on the measurement of *R(s)* cross sections in the hadronic sector, that a group of physicists of the CERN experiments started to think about a possible experiment to be performed at the Alternate Gradient Synchrotron (AGS) at BNL. Despite the 4 ppb precision of the electron $g-2$ experiments, at that time the sensitivity to heavy particles due to the muon with respect of electrons

compensate adequately the factor 100 in precision. Thanks to this reason an experiment to measure a_μ to 0.35 ppm was established at BNL. The experimental method of the storage ring was not yet exhausted so the first step of the experiment was to reach a factor 20, a factor 400 in the muon flux, of overall improvement with respect to the CERN III. A first factor comes from the AGS itself which is capable to delivery a beam which is almost a factor 20 more intense than the PS at CERN; the second step comes from a better method of injection. In the CERN experiments a flux of pion was injected inside the storage ring and the decaying muons were captured while for this experiment was found that let decay the pions outside the storage ring and injecting the resulting muon beam increase the flux dramatically. To avoid interference of this muon beam with the inflector magnet after the first orbit a series of kicker should be implemented shifting the muon orbit after injection.

Together with this, below are listed some other improvements on the systematics effects:

- The storage ring is constructed with three continuously wound superconductors, as opposed to the series of 40 independent conventional bending magnets used in CERN III;

- The inflector incorporates a superconducting shield to minimize the disruption of the field in the storage region, and unlike the CERN inflector, allows it to operate in DC mode;

- A NMR system capable of making *in situ* measurement of the field in the storage ring was designed, which unlike CERN III, does not require cycling the magnet power;

- In the BNL experiment, the decay electron signals from the calorimeters are recorded by waveform digitizers and stored for later analysis instead

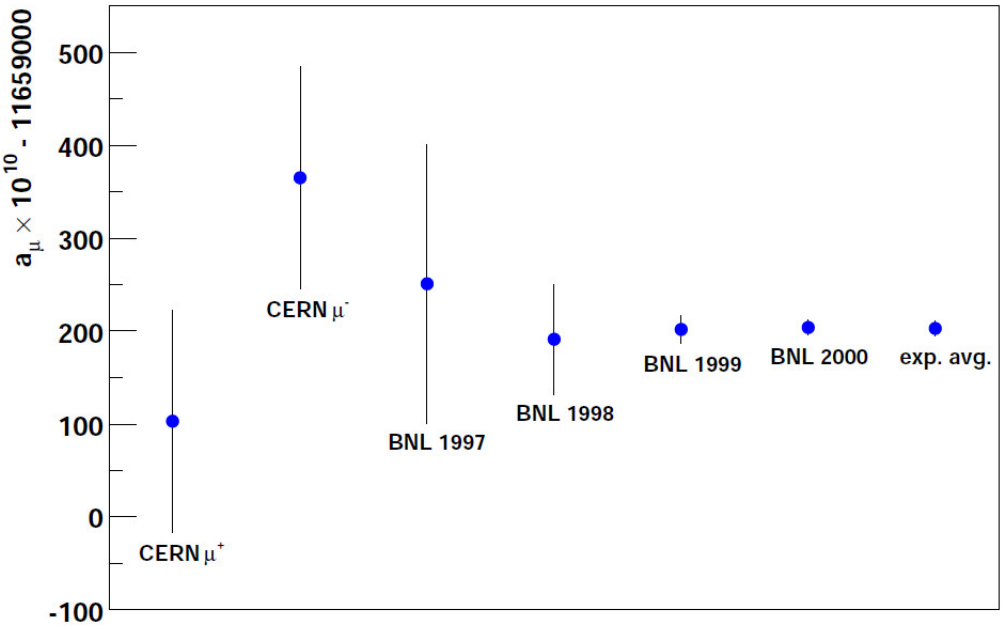

Figure 3.12: Progression of the experimental precision from CERN through the 2000 BNL data set [104].

of relying on a hardware trigger.

It took almost 15 year of developments before starting data taking in 1997, and the first years of runs were just some test of the new improvements and subsystems. Nevertheless they were useful and gave also interesting results as shown in Fig. 3.12.

In the years 1999 and 2000 were taken data on the positive muon obtaining a precision on a_μ of 0.7 ppm (Fig. 3.13) and then was decided to switch to the negative muon.

The switching procedure was a success and combining data from both measurement the BNL experiment ended with a total result of [106]:

$$a_\mu^{\mathrm{E821}} = 116\,592\,089(54)_{stat}(33)_{syst}(63)_{tot} \times 10^{-11} \quad (\pm 0.54\,\mathrm{ppm}), \tag{3.28}$$

That resulted in a difference with the theoretical value of the time of 2.7σ.

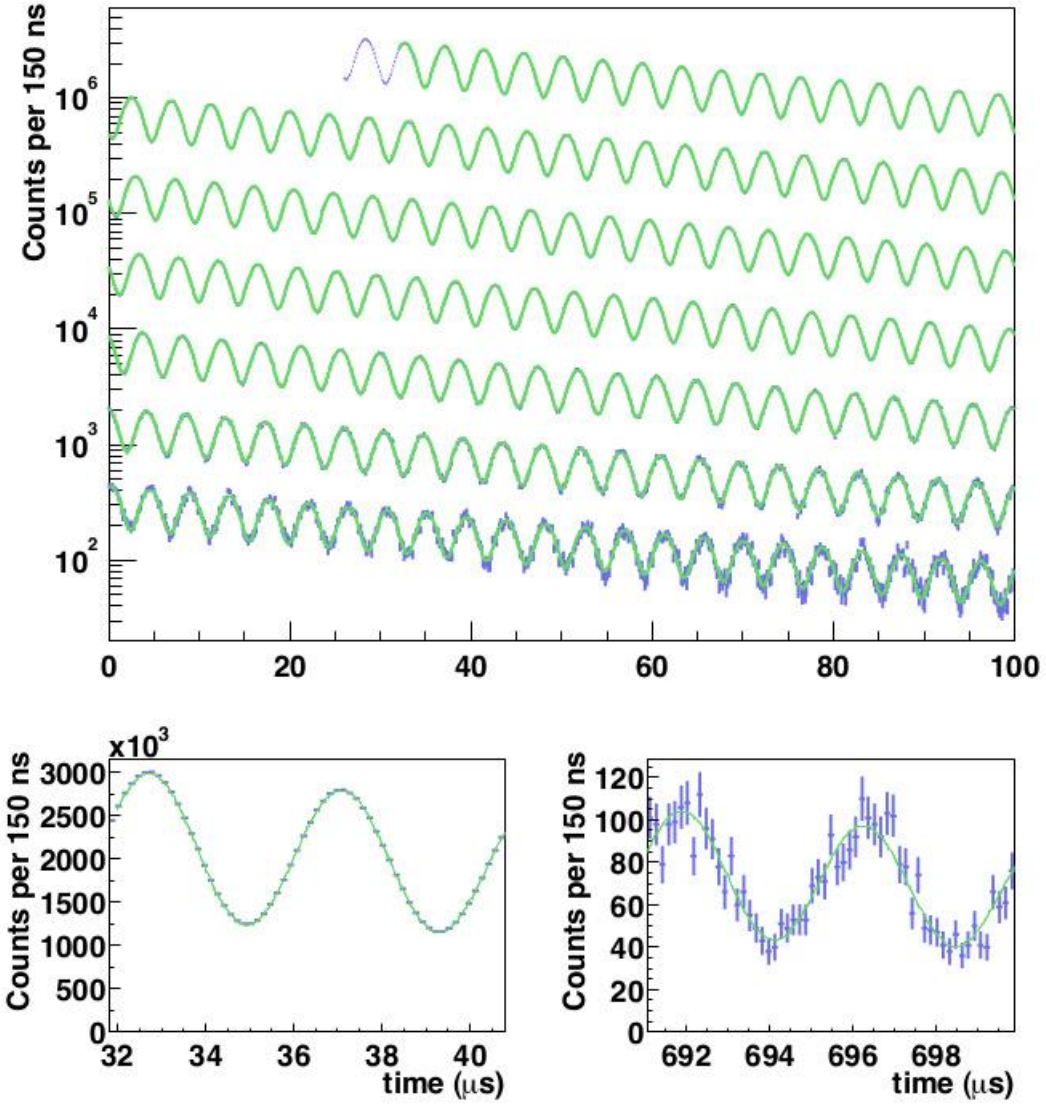

Figure 3.13: Decay electron data from 2000 positive muon data set. As can be seen easily with respect to Fig. 3.11 the improved statistics make the signal clearly visible up to 700 μs [105].

Experiment	years	Polarity	$a_\mu \times 10^{10}$	Precision [ppm]	Reference
CERN I	1961	μ^+	11 450 000(220 000)	4300	[97]
CERN II	1962-1968	μ^+	11 661 600(3100)	270	[98]
CERN III	1974-1976	μ^+	11 659 100(110)	10	[99]
CERN III	1975-1976	μ^-	11 659 360(120)	10	[99]
BNL	1997	μ^+	11 659 251(150)	13	[100]
BNL	1998	μ^+	11 659 191(59)	5	[101]
BNL	1999	μ^+	11 659 202(15)	1.3	[102]
BNL	2000	μ^+	11 659 204(9)	0.7	[103]
BNL	2001	μ^-	11 659 214(8)(3)	0.7	[105]
Average			11 659 208 (6)	0.5	[105, 106]

Table 3.1: Summary of a_μ results from various experiments and data sets, showing the evolution of experimental precision over time.

The results of the CERN and BNL experiments are also summarized in Table 3.1.

Chapter 4

The E989 experiment at Fermilab

The greater than 3σ difference found by E821 with respect to the theoretical prediction, does not meet the 5σ threshold for claiming a discovery, so a more precise measurement was desirable.

4.1 Introduction to the E989 experiment

The goal of the new g-2 experiment at Fermilab (E989) is a four-fold improvement in the experimental precision thereby reducing the error on a_μ down to 140 ppb which should be compared to the 400 ppb uncertainty of the most accurate Standard Model prediction [107].

BNL E821 experiment improved on the CERN III experiment in a significant manner, primarily by the invention of direct muon injection into the storage ring. The FNAL E989 experiment introduces, in add, a broad suite of refinements focused on optimizing the beam purity and rate, the muon storage efficiency, and modernizing the instrumentation used to measure both ω_a and

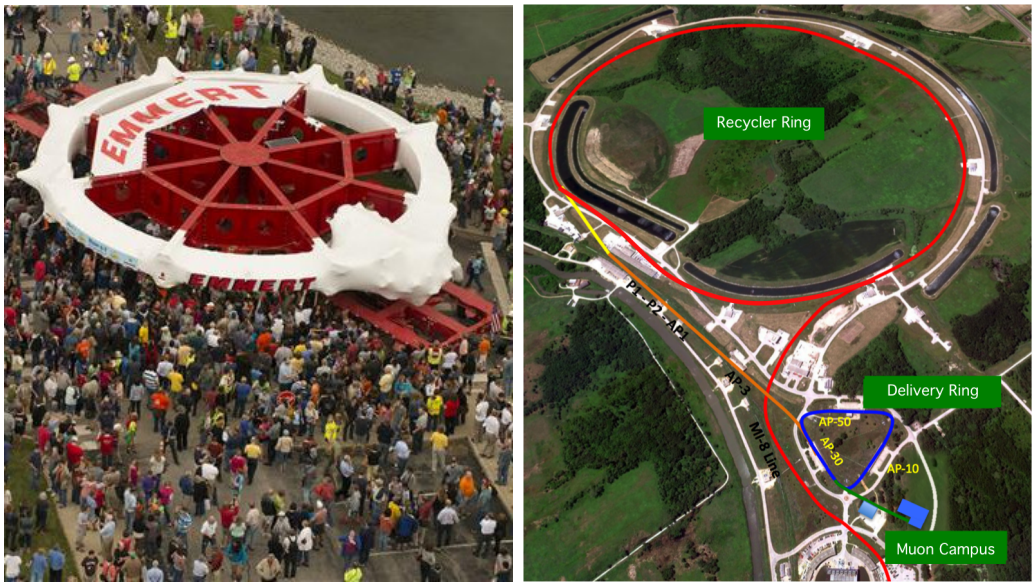

(a) (b)

Figure 4.1: (a) Hundreds crowd around the Muon $g-2$ magnet during the celebration on Friday, July 26, 2013 commemorating the end of the "Big Move" from BNL. (b) Aerial view of Muon Campus in relation to accelerator complex Credit: Fermilab.

ω_p [108]. E989 uses the same muon storage ring of E821, with a diameter of 14 meters, which has been relocated at Fermilab in a new building characterized by mechanical stability and controlled temperature. These options were not available at BNL [109]. In the Fig. 4.1 are shown the Muon $g-2$ magnet when arrived at Fermilab, during the celebration on Friday, July 26, 2013 and an aerial view of Muon Campus, where is placed the E989 $g-2$ experiment building with storage ring, in relation to accelerator complex.

The E989 experiment is measuring a_{μ^+} during the first run, due to the enhanced cross section for producing π^+ at the target and due the fact that negative muons tend to be captured in matter more often than positive muons; a_{μ^-} could be measured in a second run. Measuring both provides a test of CPT theorem. Since the values measured for a_{μ^+} and a_{μ^-} in the E821 experiment

were consistent, the E821 Collaboration averaged the two values to produce their final experimental value for a_μ [106]. The total uncertainty of 140 ppb expected for the E989 experiment is subdivided into $(100_{stat} \oplus 100_{sist})$ ppb. The 100 ppb statistical uncertainty is a factor 21 improvement on muon rate with respect to the previous experiment.

To reach this value the Fermilab accelerator complex has been upgraded to have:

- Higher proton rate with less protons per bunch: the Fermilab beam complex which is expected to annually deliver $2.3 \cdot 10^{20}$ 8 GeV protons on an Inconel[1] core target; at this rate, the desired statistics of 1.8×10^{11} detected positrons with energy greater than 1.8 GeV, will be achieved in less than two years of running [109];

- 6-12 times larger muon yield per proton and a $\times 3$ fill higher rate; the muon storage ring is filled at a repetition rate of 12 Hz, which is the average rate of muon spills that consists of sequences of successive 700 microseconds (μs) spills with 11 milliseconds spill-separations, compared to 4.4 Hz at BNL [109].

The 100 ppb systematic uncertainty is also challenging and some specific improvements are:

- A longer pion decay line: a limiting factor at BNL was the 120 m beam-line between the pion production target and the storage ring; because the decay length of a 3.11 GeV/c pion is $\approx$ 173 m, the beam injected into the storage ring contained both muons and a significant number of undecayed pions, the latter creating an enormous burst of neutrons when

[1]Inconel is an alloy, composed of a metal and other elements, specially designed to withstand high beam stresses.

intercepting materials: their subsequent capture in scintillator-based detectors impacted detector performance adversely [108]; this background is reduced by a factor of 20 in E989 due to a pion decay line of ∼2000 m;

- Improved detectors and new electronics: the detectors and electronics are all newly constructed to meet the demands of measuring the anomalous spin precession frequency ω_a to the 70 ppb level; this is a substantial improvement over the E821 experiment where the total systematic error on ω_a was 180 ppb [107]. Better gain stability and corrections for overlapping events in the calorimeters are crucial improvements addressed in the new design.

  A new tracking system allows for better monitoring of the stored muon orbit, thus improving the convolution of the stored muon population with the magnetic field volume, and establishing corrections to ω_a that arise from electric field and pitch corrections, which are related to vertical particle oscillations (pitch effect): the vertical undulation of the muons means $\mathbf{p}_{\boldsymbol{\mu}}$ is not exactly perpendicular to $\mathbf{B}$, thus a small "pitch" correction is necessary at the current and proposed levels of experimental precision [111];

- Better shimming to reduce B-field variations: the storage ring magnetic field, and thus ω_p, will be measured with an uncertainty of 70 ppb, that is approximately 2.5 times smaller by placing critical Nuclear Magnetic Resonance (NMR) probes at strategic locations around the ring and shimming the magnetic field to achieve a high uniformity, in addition to other incremental adjustments [112];

- A continuous monitoring and re-calibration of the detectors, whose re-

ω_a			ω_p		
Category	E821 [ppb]	E989 [ppb]	Category	E821 [ppb]	E989 [ppb]
Gain changes	120	20	Absolute field calibration	50	35
Pileup	80	40	Trolley probe calibrations	90	30
Lost muons	90	20	Trolley measurements of B_0	50	30
CBO	70	<30	Fixed probe interpolation	70	30
E and pitch	50	30	Muon distribution	30	10
			Time dependent external B fields	-	5
			Others[2]	100	30
Total	180	70	Total	170	70

Table 4.1: Total systematics error on ω_a and ω_p of E821 and expected values of E989.

sponse may vary on both the short timescale of a single fill, and the long time scale of an entire run, is required: a high-precision laser calibration system that monitors the gain fluctuations of the calorimeter photodetectors at 0.04 % accuracy [110] is used and described in the Chapter 5;

- A new slow controls system encompasses an array of functionality, including monitoring various environmental conditions to be stored and used if needed later for determining data quality, monitoring diagnostics for various subsystems, setting alarms to alert control room operators of problems, and providing automated controls to interface with various subsystems. It will be described in the Chapter 7.

4.2 Overview of the experimental technique

The experimental technique was briefly presented in Chapter 3 following the historical development of the experiment. Here a more focused and detailed

description is given.

As it will shown after, the measurement of a_μ requires the determination of the muon spin frequency ω_a and the magnetic field $\vec{B}$ averaged over the muon distribution.

The concept of the measurement in the experiment is based on the following points:

1. Production of an appropriate pulsed proton beam by an accelerator complex;

2. Production of pions using the proton beam that has been prepared;

3. Collection of polarized muons from pion decay $\pi^+ \rightarrow \mu^+\nu_\mu$;

4. Transporting the muon beam to the $g-2$ storage ring;

5. Injection of the muon beam into the storage ring;

6. Kicking the muon beam onto storage orbits;

7. Measuring the arrival time and energy of positrons from the decay $\mu^+ \rightarrow e^+\bar{\nu}_\mu\nu_e$;

8. Precise mapping and monitoring of the precision magnetic field.

4.2.1 Production injection and vertical focusing of the Muon beam

The E989 experiment brings a bunched beam from the 8 GeV Booster to a pion production target located where the antiproton production target was during Tevatron runs. Pions of 3.11 GeV/c $\pm$ 5% are collected and sent into

a large-acceptance beamline. Muons [3] are produced in the weak pion decay

$$\pi^+ \rightarrow \mu^+ + \nu_\mu. \tag{4.1}$$

The neutrino is left-handed and the pion is spin zero. Thus the muon spin must be anti-parallel to the neutrino spin, so it is also left-handed. A beam of polarized muons can be obtained from a beam of pions by selecting the highest-energy muons or lowest-energy muons, obtaining a beam with a polarization greater than 90%. Pions and daughter muons are injected into the Delivery Ring, where after several turns the remaining pions decay. The pion decay line is ∼2 km long while the one of Brookhaven was only 120 m. The layout of the beamlines is shown in Fig. 4.2.

The Storage Ring Magnet and the Inflector

The surviving muon beam are extracted and brought to the muon storage ring built for E821 at Brookhaven in Fig. 4.3.

The storage ring magnet, of 14 meters diameter, is energized by three superconducting coils. The continuous "C" magnet yoke is built from twelve 30° segments of iron, which were designed to eliminate the end effects present in lumped magnets. This construction eliminates the large gradients that would make a precision determination of the average magnetic field $\langle B \rangle$ very difficult. Furthermore, a small perturbation in the yoke can effect the field at the ppm level at the opposite side of the ring. Thus every effort is made to minimize holes in the yoke, and other perturbations. The only penetrations to the yoke are to permit the muon beam to enter the magnet as shown in Fig. 4.4a, and to connect cryogenic services and power to the inflector [107] magnet and the outer radius coil, Fig. 4.4b.

[3] The term muon is used in general for muons and also for anti-muons.

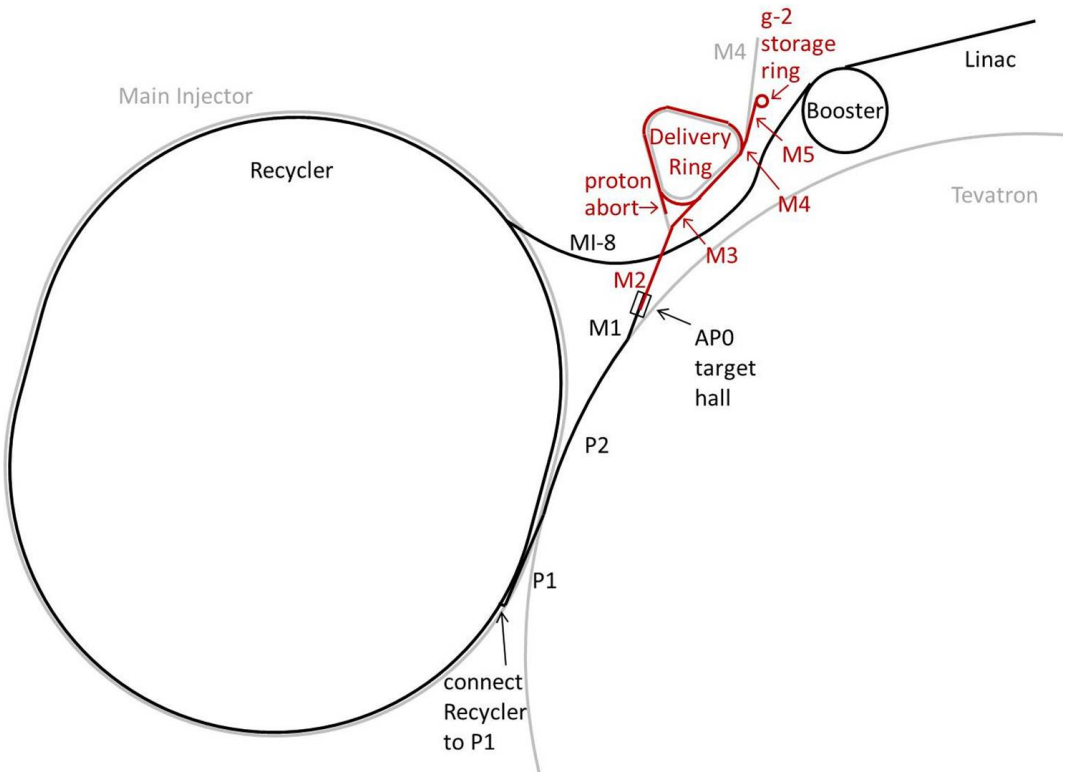

Figure 4.2: Path of the beam to $g-2$. Protons (black) are accelerated in the Linac and Booster, are re-bunched in the Recycler, and then travel through the P1, P2, and M1 lines to the AP0 target hall. Secondary beam (red) then travels through the M2 and M3 lines, around the Delivery Ring, and then through the M4 and M5 lines to the muon storage ring.

Figure 4.3: The E821 ring magnet in the MC-1 building at Fermilab. Courtesy of Fermi National Accelerator Laboratory.

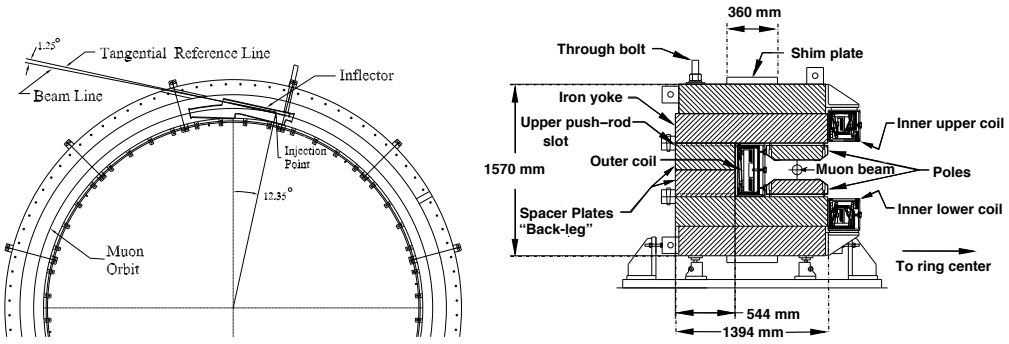

(a) (b)

Figure 4.4: (a) Plan view of the beam entering the storage ring. (b) View of the storage ring cross section.

The beam enters through a hole in the "back-leg" of the magnet and then crosses into the inflector magnet, which provides an almost field free region, delivering the beam to the edge of the storage region.

Kickers

Once that the beam is injected it requires to be kicked otherwise it impacts against the inflector after one turn. The kick required to put magic momentum muons onto a stable orbit centered at the magic radius is on the order of 10 mrad. There are strictly requirements on the muon kicker:

1. Since the magnet is continuous, any kicker device has to be inside the precision magnetic field region;

2. The kicker hardware cannot contain magnetic elements such as ferrite, because they affects the precision uniform magnetic field;

3. Any eddy currents produced in the vacuum chamber, or in the kicker electrodes by the kicker pulse must be negligible by 10 to 20 μs after injection, or must be well known and corrected for in the measurement;

4. Any kicker hardware has to fit within the real estate that was occupied by the E821 kicker. The available space consists of three consecutive 1.7 m long spaces;

5. The kicker pulse should be shorter than the cyclotron period of 149 ns.

Vertical Focusing with Electrostatic Quadrupoles

The storage ring acts as a weak-focusing betatron, with the vertical focusing provided by electrostatic quadrupoles. The ring is operated at the magic

momentum, so that the electric field does not contribute to the spin precession. However there is a second-order correction to the spin frequency from the radial electric field, which is discussed below. There is also a correction from the vertical betatron motion, since the spin equations in the previous section were derived with the assumption that $\vec{\beta} \cdot \vec{B} = 0$.

A pure quadrupole electric field provides a linear restoring force in the vertical direction, and the combination of the (defocusing) electric field and the central (dipole) magnetic field (B_0) provides a net linear restoring force in the radial direction. The important parameter is the field index, n, which is defined by

$$n = \frac{\kappa R_0}{\beta B_0}, \tag{4.2}$$

where κ is the electric quadrupole gradient and R_0 is the storage ring radius. For a ring with a uniform vertical dipole magnetic field and a uniform quadrupole field that provides vertical focusing covering the full azimuth, the stored particles undergo simple harmonic motion called betatron oscillations, in both the radial and vertical dimensions.

4.2.2 Muons precession in the ring magnet

Injecting a beam of polarized muons into a uniform magnetic field and measuring the rate at which the spin precess respect to the momentum gives $\vec{\omega_a} = \vec{\omega_S} - \vec{\omega_C}$, where $\vec{\omega_S}$ and $\vec{\omega_C}$ stands for the spin precession frequency and the cyclotron frequency. In absence of any external fields the spin and cyclotron frequencies are given by:

$$\omega_S = -g\frac{Qe}{2m}B - (1-\gamma)\frac{Qe}{\gamma m}B; \tag{4.3}$$

$$\omega_C = -\frac{Qe}{\gamma m}B. \tag{4.4}$$

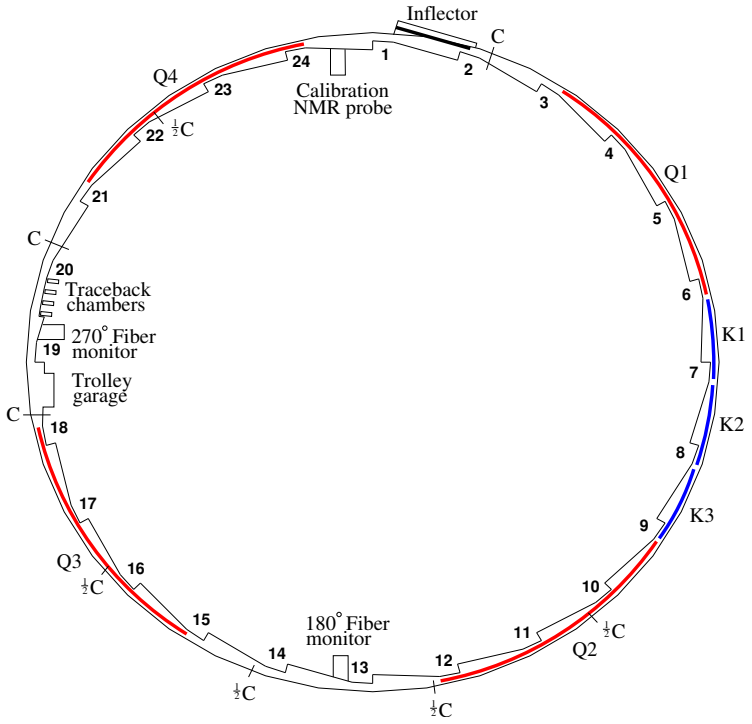

Figure 4.5: The layout of the storage ring, as seen from above, showing the location of the inflector, the kicker sections (labeled K1-K3), and the quadrupoles (labeled Q1-Q4). The beam circulates in a clockwise direction. Also shown are the collimators, which are labeled "C", or "$\frac{1}{2}$C" indicating whether the C collimator covers the full aperture, or half the aperture. The collimators are rings with inner radius: 45 mm, outer radius: 55 mm, thickness: 3 mm. The scalloped vacuum chamber consists of 12 sections joined by bellows. The chambers containing the inflector, the NMR trolley garage, and the trolley drive mechanism are special chambers. The other chambers are standard, with either quadrupole or kicker assemblies installed inside. An electron calorimeter is placed behind each of the radial windows, at the position indicated by the calorimeter number.

As a result the difference ω_a is

$$\omega_a = \omega_S - \omega_C = -(\frac{g-2}{2})\frac{Qe}{m}B = -a_\mu \frac{Qe}{m}B, \tag{4.5}$$

which is the same as Eq. 3.2. From this simple equations is important to note two features which makes the experiment work:

- ω_a depends on the anomaly and not on the full magnetic moment;
- It depends linearly on the applied magnetic field.

From these two simple considerations it follows that to determine the anomaly, is necessary to measure only ω_a and the magnetic field B. Actually the quantity that is relevant is the average of B over the muon distribution, $\langle B \rangle$ [107],

$$\langle B \rangle = \int M(r,\theta)B(r,\theta)rdrd\theta \tag{4.6}$$

where $B(r,\theta)$ and $M(r,\theta)$ are expressed respectively as

$$B(r,\theta) = \sum_{m=0}^{\infty} r^n(c_n \cos n\theta + s_n \sin n\theta), \tag{4.7}$$

and the muon distribution is expressed in terms of moments

$$M(r,\theta) = \sum_{m=0}^{\infty}(\xi_m(r)\cos m\theta + \sigma_m(r)\sin m\theta). \tag{4.8}$$

The harmonic terms $\sin n\theta \sin m\theta$, etc., in Eqs. 4.7, 4.8 are orthogonal, it means they vanish for each term with $n \neq m$, so the only contribution is for products of the same moment/multipole. The way to determine the value of $\langle B \rangle$ to ppm precision is to have a very excellent knowledge of all the moment and multipole distributions or to take care to minimize the number of terms participating, making the first term to be large, in order to have just a few multipoles contributing. Actually the second option is the one involved.

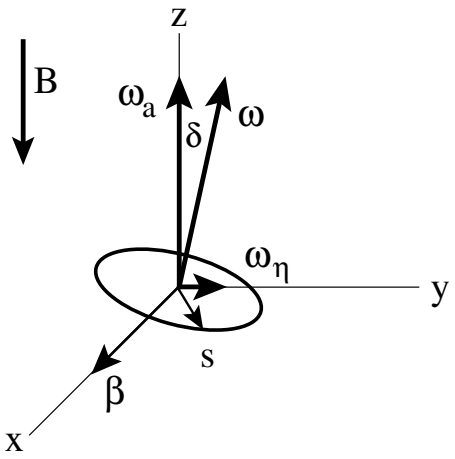

Figure 4.6: The vectors $\vec{\omega}_a$ and $\vec{\omega}_\eta$ showing the tipping of the precession plane because of the presence of an electric dipole moment.

This option obviously seems to forbid any kind of confinement and vertical focusing of the muon beam because no magnetic gradients are permitted. In a presence of E field, a relativistic particle feels a motional magnetic field proportional to $\vec{\beta} \times \vec{E}$, changing Eq. 4.5 to [113, 114]:

$$\vec{\omega_a} = -\frac{Qe}{m}\left[a_\mu \vec{B} - \left(a_\mu - \frac{1}{\gamma^2 - 1}\right)\frac{\vec{\beta} \times \vec{E}}{c}\right]. \tag{4.9}$$

Fortunately working with the *"magic" momentum* $p_{\text{magic}} = m/\sqrt{a} \simeq 3.09\,\text{GeV/c}$ ($\gamma_{\text{magic}} = 29.3$), the second term vanishes and no electric field contributes to the beam motion, making the measurement possible. The same treatment could be done if is taken into account the possibility to have an Electric Dipole Moment of the muon (EDM)[4]. The net effect of an EDM is to tip the plane of polarization precession out of the ring plane by the angle $\delta = \tan^{-1}\frac{\eta\beta}{2a_\mu}$[5], (see Fig. 4.6), and increase the magnitude of the precession frequency according to $\omega = \sqrt{\omega_a^2 + \omega_\eta^2} = \sqrt{\omega_a^2 + \left(\frac{e\eta\beta B}{2m}\right)^2}$.

[4] A possible new physics effect.

[5] The symbol η plays the same role for EDM as g plays for the magnetic moment.

One of the features of the E989 experiment is that it is equipped with three tracking stations that are useful for determining the properties of the stored muon beam, having the up-down oscillating EDM signal for free. The experiment should be able to improve the muon EDM limit with respect to E821 [115] of two or more orders of magnitude.

$$d_\mu < 1.8 \times 10^{-19} e \cdot cm (95\% CL). \tag{4.10}$$

4.2.3 Measurement of the arrival time and energy of positrons from the muons decay

The way to measure ω_a is related to the muon decay properties. The dominant muon decay mode is

$$\mu^\mp \rightarrow e^\mp + \nu_\mu(\bar{\nu}_\mu) + \bar{\nu}_e(\nu_e) \tag{4.11}$$

which violates parity. The muon beam is produced from a beam of pions which traverse a straight beam channel constituted by a set of focusing and defocusing elements (FODO), selecting the forward an backward decay in order to ensure polarization. The experiment uses forward muons which are the one produced with the highest laboratory momenta. Their polarization is directed along (μ^-) or opposite (μ^+) their laboratory momenta. The (V-A) three body weak decay of the muon provides information on the muon spin orientation thanks to a correlation between the decay of high energy electrons[6] and the spin itself. Taking the approximation that the energy of the decay electron $E' >> m_e c^2$ the differential decay distribution is given by [116]

$$dP(y', \theta') \propto n'(y')[1 \pm A(y') \cos\theta'] dy' d\Omega' \tag{4.12}$$

[6]The word electron will be used both for electron and positron in this Section.

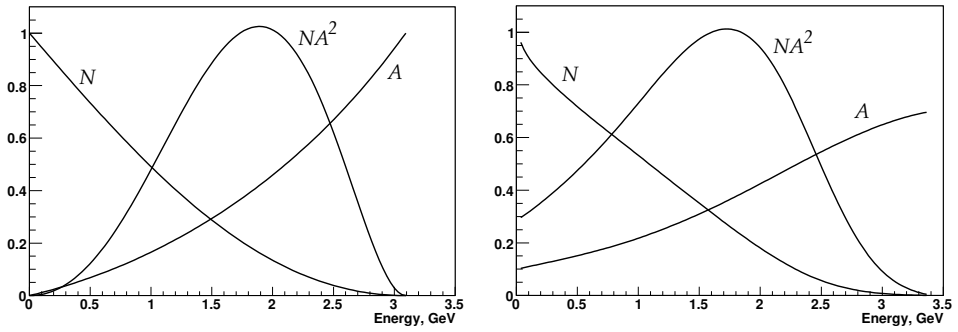

(a) No detector acceptance or energy resolution included

(b) Detector acceptance and energy resolution included

Figure 4.7: The integral N, A, and NA^2 in arbitrary units for a single energy-threshold as a function of the threshold energy in the laboratory frame. (a) Not including the detector acceptance and energy resolution of the E821 experiment; (b) including all this effects.

where $y' = p'_e/p'_{emax}$, $d\Omega'$ is the solid angle and θ' is the angle between the muon spin and $\vec{p}'_e$. This definition is valid until we refer to the muon rest frame. Moving to the laboratory frame we can have directly the electron oscillation number as a function of the emitted electron energy above the energy threshold

$$N(t, E_{th}) = N_0(E_{th}) \exp^{-\frac{t}{\tau_\mu}} [(1 + A(E_{th}) \cos(\omega_a t + \phi(E_{th}))]. \tag{4.13}$$

Eq. 4.13 is the same of Eq. 3.1. As already discussed N is the number of electrons, N_0 the number of electrons at t=0, A is the asymmetry, τ_μ is the muon dilated life time and ϕ is the phase.

In Fig. 4.7 together with the distribution for N and A, is also shown the statistical figure of merit (FOM) NA^2 according to Eq. 3.19.

The energy threshold is needed because if *all* the decay electrons are counted, the number detected as a function of time will be a purely exponential; therefore is important to apply cut on the energy in the laboratory frame in order to select only the electrons emitted in the same direction of the muon spin, it means the ones whose number oscillates at the precession fre-

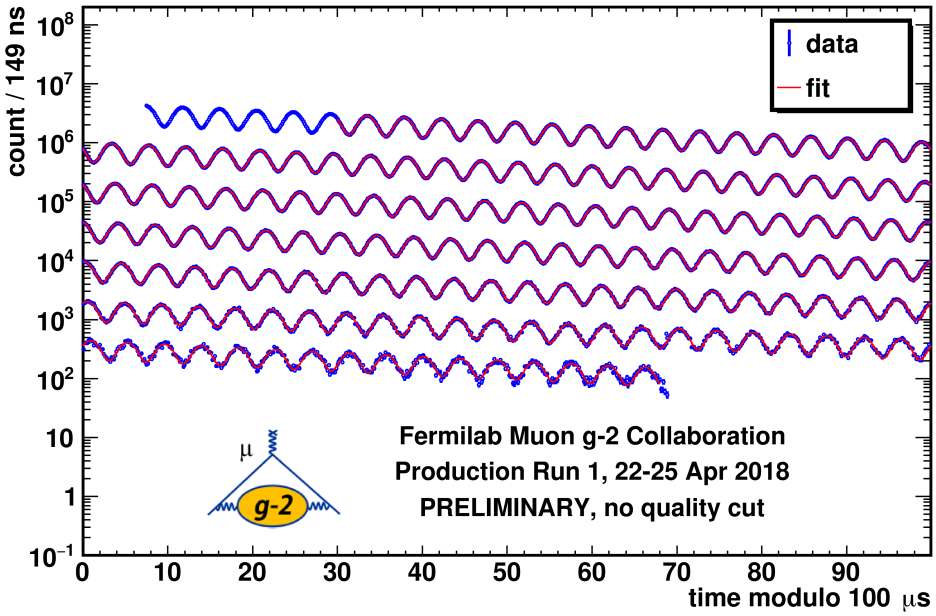

Figure 4.8: Histogram, modulo 100 μs, of the number of detected electrons above 1.8 GeV for the E989 2018 Run1 data set as a function of time, summed over detectors, with a least-squares fit to the spectrum superimposed. The data are in blue, the fit in red.

quency, which are the most energetic ones. The value of the energy threshold comes directly maximizing the FOM and is $\sim$ 1.8 GeV.

The decay electrons have a smaller momenta than the muon parents, curling inward and going out the magic orbit being detected from the various calorimeter stations placed around the storage ring.

The resulting arrival-time spectrum of electrons with energy greater than 1.8 GeV from the E989 data of Run1 is shown in Fig. 4.8. While this plot clearly exhibits the expected features of the five-parameter function, a least-square fit to these events gives an unacceptably large chi-square. A number of small effects must be taken into account to obtain a reasonable fit, which will be discussed in Chapter 8.

Besides the measurement of ω_a is important to measure the knowledge of the magnetic field through the frequency ω_p. To obtain a_μ we use Eq. 3.16 which requires precise knowledge of the muon mass.

4.2.4 Magnetic field measurement

The high level of precision needed to determine a_μ reflects on the determination of ω_a and $\langle B \rangle$. The muon beam once injected is confined to a cylindrical region with a radius of 9 cm and 44.7 m in length. The scale for the magnetic field measurement and its control is set by the total volume of this region which is ~ 1.14 m^3. The goal of the experiment is to know the magnetic field averaged over time and the muon distribution to an uncertainty of $\pm$ 70 ppb.

This problem can be divided into 5 different aspects:

1. Producing as uniform magnetic field as possible by shimming the magnet;

2. Stabilizing B in time at the sub-ppm level by feedback, with mechanical and thermal stability;

3. Monitoring B to 20 ppb level at the storage ring during data collection;

4. Periodically mapping the field throughout the storage region and correlating the field map to the monitoring information without turning off the magnet between data collection and field mapping. It is essential to not turn off the magnet unless it is absolutely necessary;

5. Obtaining an absolute calibration of the B field relative to Larmor frequency of the free proton.

There is only one possibility to measure the magnetic field to the required accuracy by using nuclear magnetic resonance (NMR) as in E821 experiment.

The measurement in the E989 experiment is done using a $\pi/2$ RF pulse to rotate the proton spin and than the resulting free-induction decay is detected by a pick-up coil around the sample. There are three different kind of probes: a spherical water probe that provides the absolute calibration to the free proton; cylindrical probes that monitor the field during data collection, and also in an NMR trolley to map the field; a smaller spherical probe which can be plunged into the muon storage region by means of a bellows system to transfer the absolute calibration to the trolley probes. A collection of 378 cylindrical probes placed in symmetrically machined grooves on the top and bottom of the muon beam vacuum chamber provide a point-to-point measure of the magnetic field while beam is in the storage ring. Probes at the same azimuthal location but different radii gave information on changes to the quadrupole component of the field at that location.

The field mapping trolley contains 17 cylindrical probes arranged in concentric circles as shown in Fig. 4.9a. Every 2-3 days during the running periods, the beam is turned off, and the field mapping trolley is driven around the inside of the evacuated beam chamber measuring the magnetic field with each of the 17 trolley probes at 6000 location around the ring. One of the resulting E821 field maps, averaged over azimuth, is shown in Fig. 4.9b.

The absolute calibration uses a probe with a spherical water sample [117]. The Larmor frequency of a proton in a spherical water sample is related to that of the free proton through [118, 119]

$$\omega_L(sph - H_2O, T) = [1 - \sigma(H_2O, T)]\omega_L(free) \tag{4.14}$$

where $\sigma(H_2O, 34.7°C)$=25.790(14) $\times 10^{-6}$ comes from the diamagnetic shielding of the proton in the water molecule, determined in Ref. [120].

An alternate absolute calibration explored for the E989 experiment consist of an optically pumped ^{3}He NMR probe [121]. This solution has several advan-

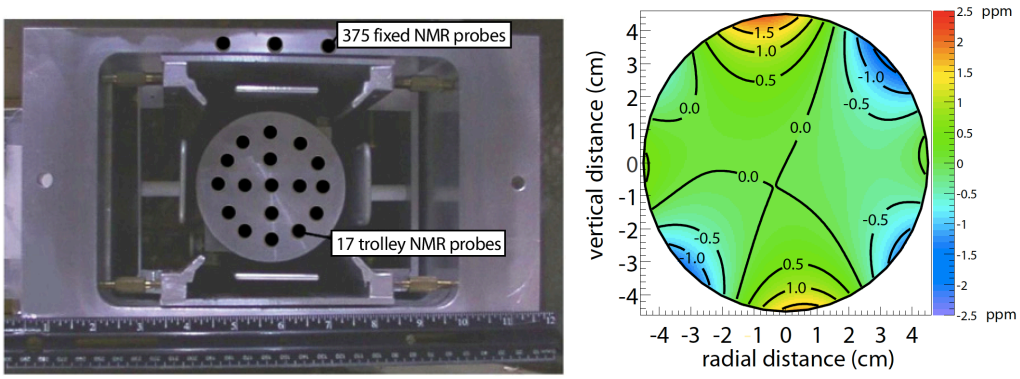

(a) (b)

Figure 4.9: (a) The electrostatic quadrupole assembly inside a vacuum chamber showing the NMR trolley sitting on the rails of the cage assembly. Seventeen NMR probes are located just behind the front face in the places indicated by the black circles. The inner (outer) circle of probes has a diameter of 3.5 cm (7 cm) at the probe centers. The storage region has a diameter of 9 cm. The vertical location of three of the 180 upper fixed probes is also shown. Additional 180 probes are located symmetrically below the vacuum chamber. (Copyright 2006 by the American Physical Society.) (b) A contour plot of the magnetic field averaged over azimuth, 0.5 ppm intervals.

tages: the sensitivity to the probe shape is negligible and also the temperature dependence is negligible. Test on the different solution is performing to choose the best option.

4.2.5 a_μ determination

The calibration procedure described in the previous paragraph permits the magnetic field to be expressed in terms of the Larmor frequency of a free proton, ω_p. The magnetic field is weighted by the muon distribution, and also averaged over the running time weighed by the number of stored muons to determine the value of ω_p which is combined with the average ω_a to determine a_μ. The reason for the use of these two frequencies, rather than B measured in tesla can be understood from Eq. 4.9. To obtain a_μ from this relationship requires precise knowledge of the muon charge to mass ratio.

To determine a_μ from the two frequencies ω_a and ω_p, it uses the relationship

$$a_\mu = \frac{\omega_a/\omega_p}{\lambda_+ - \omega_a/\omega_p} = \frac{\mathcal{R}}{\lambda_+ - \mathcal{R}}\,, \tag{4.15}$$

where the ratio

$$\lambda_+ = \mu_{\mu^+}/\mu_p = 3.183\,345\,137\,(85) \tag{4.16}$$

is the muon-to-proton magnetic moment ratio [122] measured from muonium (the μ^+e^- atom) hyperfine structure [123]. Of course, to use λ_+ to determine a_{μ^-} requires the assumption of *CPT* invariance, *viz.* ($a_{\mu^+} = a_{\mu^-}$; $\lambda_+ = \lambda_-$). The comparison of $\mathcal{R}_{\mu^+}$ with $\mathcal{R}_{\mu^-}$ provides a *CPT* test. In E821

$$\Delta\mathcal{R} = \mathcal{R}_{\mu^-} - \mathcal{R}_{\mu^+} = (3.6 \pm 3.7) \times 10^{-9} \tag{4.17}$$

4.3 Detector system

4.3.1 Calorimeter system

The detector system of the E989 experiment consists of 24 calorimeter stations along the inner radius of the storage ring. To arrive at the required systematic uncertainty of 70 ppb for ω_a, a timing resolution better than 100 ps, for positrons with kinetic energy greater than 100 MeV, and an energy resolution better than 5% at 2 GeV are required [107]. Differently from the E821 experiment, where each calorimeter was 4 monolithic block of PbW/SciFi readout by PMTs through light guides, this experiment has a block of 54 PbF_2 crystals, 6 height by 9 wide, readout by fast large area silicon-photomultipliers (SiPM). Each crystal is a $2.5 \times 2.5 \times 14$ cm^3 pure Cerenkov with a density of 7.77 g/cm^3. The 14 cm length corresponds to $15X_0$ radiation lengths with a Moliére radius of 2.2 cm. The choice of a pure Cerenkov material is driven by the almost instantaneous signal produced when an electron strikes a crystal. This improves a lot the time resolution of the experiment also contributing to pile-up events recognition. Pile-up recognition is also improved thanks to high granularity of the calorimeter. The PbF_2 crystals have a very low magnetic susceptibility, perfect for working in a magnetic environment without perturbing the magnetic field itself. Several test beams have been performed[7] to verify all the properties of the crystals together with an intense simulation work, see for example Fig. 4.10 and the reference [124].

[7] Some of them will be described in the Chapter 6 of the Thesis.

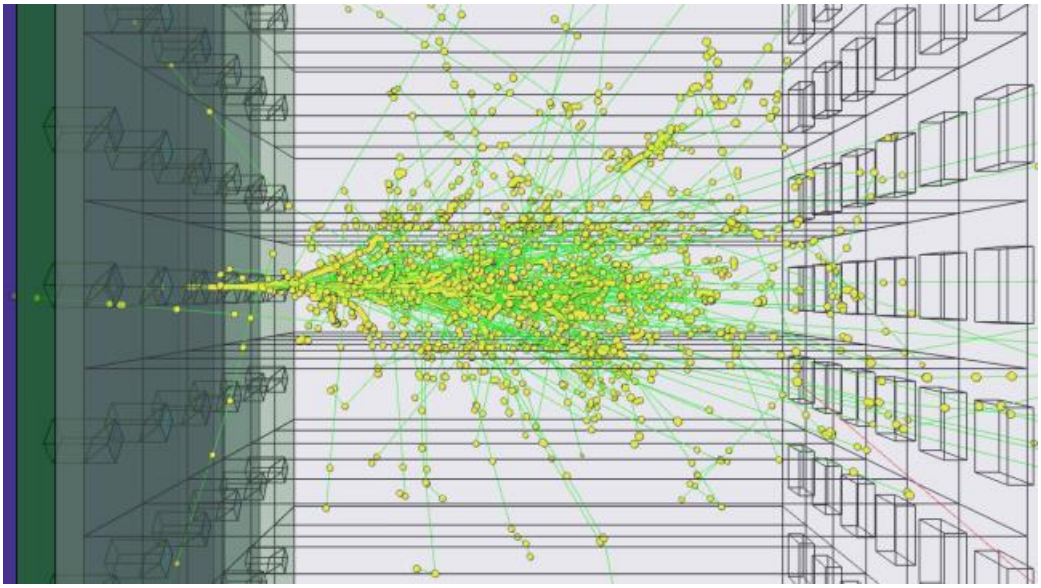

Figure 4.10: The shower of secondary particles in PbF 2 crystal hit by 2 GeV positron. Green tracks are trajectories of neutral particles, such as X-ray and gamma photons (visualization of Cherenkov photons is turned off) [124].

One of the result of the test performed on the crystals was the choice of the wrapping material. The wrapping that is used is a black-tedlar absorptive material which, even if it has a light yield lower than a reflective one, ensures a faster response of the crystal to a radiation. In Tab. 4.2 is available a summary of crystal properties [107].

The fast nature of these crystals will be useless if not coupled with an appropriate photo-detector. SiPMs satisfy all the requirements needed for the experiment. SiPM works as a pixelated Geiger-mode counter, with 57600 50 μm-pitch pixels on a 1.2×1.2 cm^2 device. Quenching resistors are intrinsic to the device to arrest the avalanche and allow the device to recover with a recovery rime constant typically of 10's ns. The selection of SiPMs over PMTs is pragmatic. They can be placed inside the storage ring fringe field without perturbation, avoiding the long light guides that would be needed for remote

Crystal cross section	2.5×2.5 cm^2
Crystal length	14 cm ($> 15X_0$)
Array configuration	6 rows, 9 columns
Density of material	7.77 g/cm^3
Magnetic susceptibility	-58.1$\times 10^{-6}$ cm^3/mol
Radiation length	0.93 cm
Moliére radius R_M	2.2 cm
Moliére R_M (Cerenkov only)	1.8 cm
$E_{threshold}$ for Cerenkov light	102 keV

Table 4.2: Properties of led fluoride crystals.

PMTs as in E821. They have also an high-photodetection efficiency and can be mounted directly to the rear face of the PbF_2 crystals. Another aspect is that these device are cheaper than same size-PMTs. Some of the challenging features of SiPM are their high sensitivity to temperature and bias voltage. The calorimeter design is prepared to handle the temperature dependence together with temperature control of the MC-1 building. Regarding bias voltage control a custom low-voltage power supply is used with a 1 mV accuracy. Each power supply serves 5-6 SiPM in order to minimize common fluctuation of all the 1300 due to bias voltage.

To ensure the high level of stability requested for the experiment a high performance calibration system is required for the on-line monitoring of the output stability of each individual calorimeter station. All the 1296 channel must be calibrated during data taking and the proposed solution is based on the method of sending simultaneous light calibration pulses close as much as possible to the signal produced by a positron, directly to the photo-detectors through the active sections of the calorimeter. More detail about this calibra-

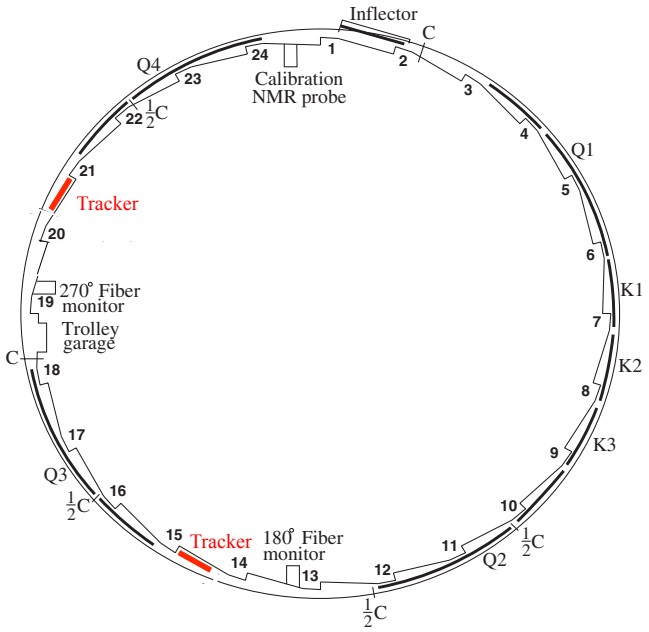

Figure 4.11: Placement of the tracking detectors in the muon storage ring. The detectors can be seen in red in front of calorimeter stations 3, 15, and 21.

tion system will be discussed in the next Chapter.

4.3.2 Tracking system

Three tracking stations are located around the internal radius of the storage ring as shown in Fig. 4.11. Each station is composed by 32 planes of drift tubes arranged in 8 modules, each module has 4 straw planes as shown in Fig. 4.12). The straws are arranged in a stereo pattern, with an angle of $\pm 7.5^{\circ}$ from the vertical direction. This arrangement provides both the x and y position of the track. The tubes are filled with a 50 : 50 mixture of Argon and Ethane.

The primary physics goal of the tracking detectors, also called straw trackers, is to measure the muon beam profile at multiple locations around the ring

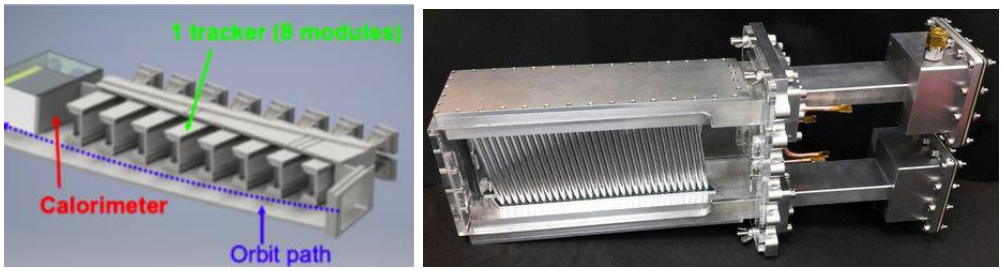

(a) Tracker (1 station) Scheme. The beam goes from right to left.

(b) Single module of the straw tracker.

Figure 4.12: The Tracker detector.

as a function of time throughout the muon fill, without affecting the beam itself. This information is used to determine several parameters associated with the dynamics of the stored muon beam [106]. It is required for the following reasons:

- Momentum spread and betatron motion of the beam lead to ppm level corrections to the muon precession frequency associated with the fraction of muons that differ from the magic momentum and the fraction of time muons are not perpendicular to the storage ring field;
- Betatron motion of the beam causes acceptance changes in the calorimeters that must be included in the fitting functions used to extract the precession frequency;
- The muon spatial distribution must be convoluted with the measured magnetic field map in the storage region to determine the effective field seen by the muon beam.

The secondary physics goal of the tracking detectors involves understanding systematic uncertainties associated with the muon precession frequency

measurement derived from calorimeter data. In particular, the tracking system isolates time windows that have multiple positrons hitting the calorimeter within a short time period and provides an independent measurement of the momentum of the incident particle. This allows an independent validation of techniques used to determine systematic uncertainties associated with calorimeter pileup, calorimeter gain, and muon loss based solely on calorimeter data.

The tertiary physics goal of the tracking detectors is to determine if there is any tilt in the muon precession plane away from the vertical orientation. This would be indicative of a radial or longitudinal component of the storage ring magnetic filed or a permanent electric dipole moment (EDM) of the muon [125]. Any of these effects directly biases the precession frequency measurement. A tilt in the precession plane leads to an up-down asymmetry in the positron angle that can only be measured with the tracking detectors.

The goals for the systematic uncertainties that can be directly determined or partially constrained using tracking information are listed in Table 4.3.

4.3.3 Other Detectors

Several other detectors give informations on the beam and on the ring itself. These side quantities are important for the corrections and the systematics studies.

T0 detector is a scintillating paddle read by two PMTs. It's placed right after the inflector and it's used to precisely measure the beam injection time (this is important for the kickers' timing). Integrating the pulse waveform is also possible to know the total number of injected particles into the storage ring.

IBMS (Inflector Beam Monitoring Station) is a detector made of a series

Uncertainty	E821 value	E989 goal	Role of tracking
Magnetic field seen by muons	30 ppb	10 ppb	Measure beam profile on a fill by fill basis ensuring proper muon beam alignment
Beam dynamics corrections	50 ppb	30 ppb	Measure beam oscillation parameters as a function of time in the fill
Pileup correction	80 ppb	40 ppb	Isolate time windows with more than one positron hitting the calorimeter to verify calorimeter based pileup correction
Calorimeter gain stability	120 ppb	20 ppb	Measure positron momentum with better resolution than the calorimeter to verify calorimeter based gain measurement
Precession plane tilt	4.4 μRad	0.4 μRad	Measure up-down asymmetry in positron decay angle

Table 4.3: Systematic uncertainty goals for the tracker system of the Muon $g-2$ experiment. Information from the tracking detectors are used to constrain these in several ways as indicated in the final column. The first two rows are associated with the tracker's primary physics goal. The second two are associated with the secondary physics goal of the tracker and the main role played by the tracker is in validating the reductions in the uncertainties provided by the new calorimeters. The final row ia associated with the tertiary physics goal and the improvements are entirely from increased acceptance and statistics in the new experiment.

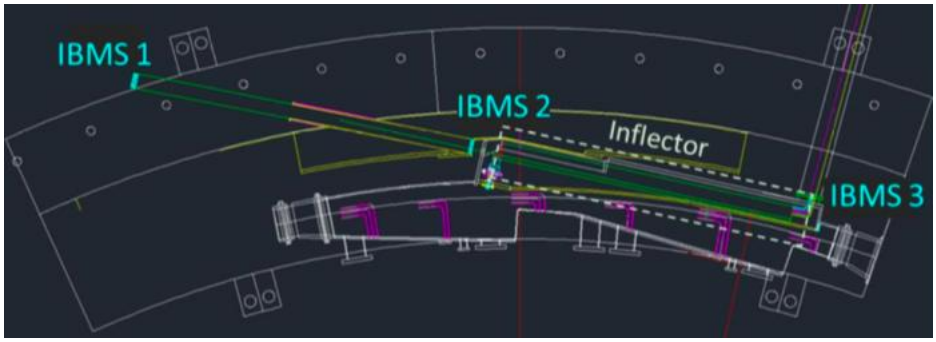

Figure 4.13: Drawing of the IMBS detectors position. IBMS3 may be installed in future.

of scintillating hodoscopes used to measure the beam profile. There are two of them placed before the inflector, one before the hole in the yoke, one right before the inflector (Fig. 4.13). The aim of these detectors is to keep monitoring the beam profile after the final focussing. A third detector, also shown in Fig. 4.13, may be installed in future right after the inflector.

Fiber Harps are planes of vertical and horizontal scintillating fibers that can be placed in the path of the muon beam in two different locations, at $\sim$ 180° and $\sim$ 270°, along the ring. They can destructively measure the beam xy profile and therefore provide a direct measure the betatron oscillations to perform the fast rotation analysis. They are used only in dedicated runs and not during normal data taking. Fig. 4.14 shows an example of y fiber harp detector.

4.3.4 DAQ System and Data Acquisition Framework

The Data acquisition system (DAQ) permits the acquisition of deadtime-free, continuously digitized waveforms from the electromagnetic calorimeter and the laser systems at rates of roughly 10 Hz, the "fill" structure of the Muon $g-2$ experiment.

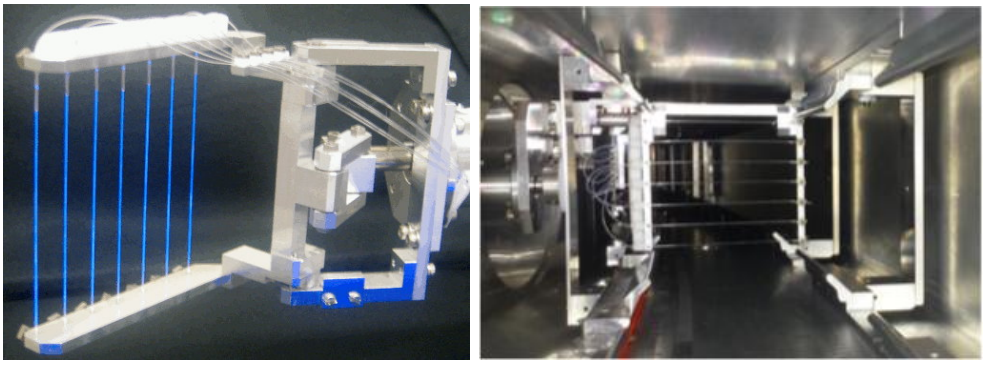

(a) (b)

Figure 4.14: (a) The 180° x-profile monitor, glowing under ultraviolet illumination in the laboratory. (b) Fiber harp (y direction) along the beamline. During normal data-taking this detector is rotated out of the beam path.

The SiPM signals were digitized using custom μTCA AMCs built at Cornell University [126], shown in Chapter 4. Each AMC is a 5-channel, 12-bit, 800 mega samples per second (MSPS) waveform digitizer (WFD) [127] with an average readout rate of 4 Gbit/s (see Fig. 4.15). Upon receiving a trigger signal from the FC7 [128], the 40 MHz master experimental clock, trigger and control signals via the CERN's timing, trigger and control (TTC) protocol [129, 130], the data from the WFDs were transmitted through the μTCA backplane to the AMC13 control card [131, 132] in the μTCA shelf and then to the DAQ machine (frontend) via a 10 Gbit/s optical link.

The acquisition software was based on the *MIDAS* [133] data acquisition framework developed at PSI and TRIUMF and reported in Chapters 4 and 5. The frontend readout consists of: a TCP_thread that receives and reassembles the raw data from the AMC13 controller, a GPU_thread that manages the GPU-based data processing into various derived datasets, and a *MIDAS*_thread that handles the transfer of *MIDAS*-formatted events to the

Figure 4.15: μTCA with 12 waveform digitizers, part of DAQ system used in $g-2$ experiment at Fermilab.

backend computer event builder. Mutual exclusion (Mutex) locks are used to synchronize the execution of threads and ensure the integrity of data. The GPUs were used to construct two distinct types of derived data, the so-called T and Q-method datasets. The T-method first identifies all digitized samples that exceeded a programmable threshold. These above-threshold trigger samples, together with programmable values of required pre and post-samples, determine the T-method regions (islands) of ADC samples for data storage. By comparison the Q-method builds histograms from the raw digitized samples over the entire 700 μs digitization period for each calorimeter segment. Programmable parameters determine a "flush" rate at which the histograms are sent to data storage and a "rebinning" factor by which the histograms are rebinned in time. Together the flush rate and rebinning factor are set to achieve the necessary compression of Q-method data. The GPU processing was implemented on NVIDIA K40 GPUs using the NVIDIA CUDA programming platform [135]. The *MIDAS* tools for event building, data storage and

run control were all hosted on the backend computer. *MIDAS* also provided an online database (ODB) used both for saving the experimental conditions for each run and configuring the detectors, electronics and other sub-systems.

Offline data analysis was performed using the *art*-based framework [136] developed at Fermilab. It handles the raw data coming from *MIDAS* DAQ and converts them into useful information for data analysis. The raw data stored in *MIDAS*-format file are decoded into decimals and are stored as branches in a *art* file, which is very similar to a *ROOT* [134] file. Then the pulses are fitted to extract pulse integrals, timings and pedestals. The fit results are calibrated and the gain corrections are applied using laser response of the crystals. Then we apply clustering algorithm to cluster the crystal hits to form a physics object.

Chapter 5

The E989 Laser Calibration System

The goal of the E989 experiment is to measure the muon anomaly with a total error of 140 ppb, at least a factor four better than the previous E821 experiment. To reach this level of accuracy a state-of-art Laser Calibration System has been developed.

5.1 Physics motivation

The importance of the Laser Calibration System (LCS) is related to the control of the response of the photodetectors. In fact one of the main sources of systematics is the gain stability of the calorimeters, which detect the positrons from muon decays and measure their energy. Specifically, since the measurement is based on fitting the positron rate variation as a function of time for positrons above a given energy threshold, any gain change can vary this threshold and affect the final result. The aim of the LCS is to monitor the gain fluctuations of the photodetectors (SiPM) allowing for a total systematic un-

E821 Error	Size[ppb]	Plan for E989 experiment	Goal[ppb]
Gain changes	120	Better laser calibration and low-energy threshold	20
Lost muons	90	Better collimation in ring	20
Pileup	80	Low-energy samples recorded calorimeter segmentation	40
CBO	70	Higher n value (frequency) Better match of beamline to ring	30
E and pitch	50	Improved tracker and precise storage ring simulations	30
Total	180	Quadrature sum	70

Table 5.1: Comparison of the E821 systematic errors with the requirements for the E989 experiment.

certainty of 20 ppb as described in Tab. 5.1. To reach the required accuracy, the system should guarantee a stability during the muon fill time window, of 700 microsenconds (μs), at few $\times 10^{-4}$. This level of stability is almost one order of magnitude better than the existing calibrations system in particle physics.

Ideally the gain function should be $G(t) = 1$ at all times. If is taken into account the possibility to have small gain changes the fluctuations is simply defined as $\Delta G(t) = G(t) - 1$; this possible fluctuation affects each parameter of Eq. 4.13: in fact at a first order Taylor expansion

$$N(t) = N_0(1 + \left(\frac{1}{N}\frac{dN}{dG}\right)\Delta G(t)) \tag{5.1}$$

$$NA(t) = NA_0(1 + \left(\frac{1}{NA}\frac{d(NA)}{dG}\right)\Delta G(t)) \tag{5.2}$$

$$\Delta\phi(t) = \frac{d\phi}{dG}\Delta G(t) \tag{5.3}$$

Following previous equations is clear that each possible gain drift should be corrected because affects directly the parameters of the fit function used to obtain ω_a from the data set. For these reasons a high performance calibration system is required for the on-line monitoring and calibration of the detectors, whose response may vary on both a short timescale of a single beam fill or more less, and a long one of accumulated data over a period of more than one year.

5.2 Laser source and light distribution system

The LCS operative at Fermilab allows to send simultaneous light calibration pulses onto each of 1296 crystals of the electromagnetic calorimeter. These light pulses must be stable in intensity and time to correct for systematic effects due to drifts in the response of the crystal readout devices that must be calibrated during data taking. To reach this goal the stability of the laser intensity is monitored with a suitable photo-detector system, included in the calibration system, that monitors any possible fluctuation in time and intensity of the calibration light source and laser beam pointing as well as any kind of fluctuation of the transmitted light along the optical path of the light distribution system, due to mechanical vibrations or aging of optics.

Crucial points of this system are: i) the light source; 2) the distribution system that distributes the light to the calorimeters with adequate intensity and homogeneity;3) Monitoring system. The light wavelength must be in the range of the calorimeter photodetector sensitivity and the light source must have an adequate power to deliver an appropriate amount of light to all crystals.

The geometry adopted which fulfills all these requirements is shown in

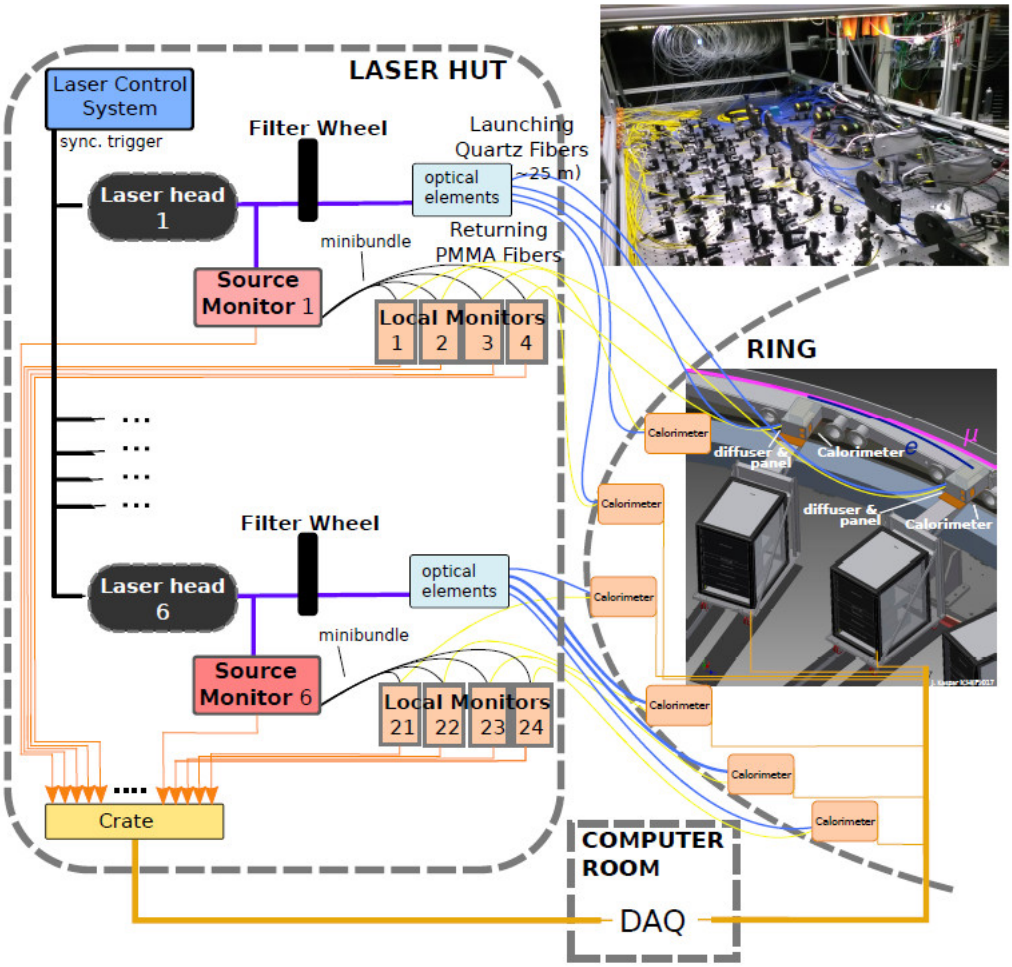

Figure 5.1: A schematic view of the laser calibration system.

Fig. 5.1. The light generated by the laser head is divided into 4 parts, each coupled into a launching fiber and sent to a secondary distribution points located near each calorimeter station.

More detailed, inside a laser hut, with temperature control, placed near the ring, as shown in Fig. 5.2, six independent laser heads (pulsed diode lasers), together with optical distribution, are located onto an optical table. Each laser light is divided into four beams and sent to 4 calorimeters (for a total of

24 calorimeters), using 25 m-long quartz optical fibers. For each calorimeter the laser beam is coupled into a bundle of 60 PMMA optical fibers by means of an engineered diffuser. The light pulses are delivered into the 54 SiPMs through 54 PMMA fibers, kept in place on a 10 mm thick Delrin plate placed between the vacuum chamber of the ring and the calorimeter. On the plate, the pulses are deflected by 54 right-angle prisms into the crystals and reach the photosensors (SiPMs) at the end of the PbF2 crystals.

The laser fluctuation is monitored by a source monitor system (SM) that measures promptly the laser power, using PIN diode photodetectors and a photomultiplier that simultaneously also measures the energy releases of a $Am - 241$ source in a NaI crystal.

A second monitoring system (local monitor or LM) is provided by bringing one of the optical fibers, for each calorimeter, back to the laser hut, by means of 24 PMMA fibers. The LM monitors light power variations over time. LM PMT gains are calibrated by a laser pulse extracted from the SM in the same PMT, separated in time by 250 nanoseconds (ns) respect to the distributed one.

The following list summarizes the main hardware components of the Muon $g - 2$ LCS:

1. Laser control system;
2. 6 laser heads;
3. 6 source monitors to measure the laser intensity stability and provide the fast pulse to the local monitor PMTs;
4. Optical distribution system from laser heads to calorimeters:
    - Optical components and collimators;

- 24 x 25 m-long quartz fibers for light distribution (one per calorimeter);
- In the near of each calorimeter a beam expander incorporating an engineered diffuser to distribute uniformly the laser light to the 54 transport fibers;
- 24 bundles, 62 fibers each (54 corresponding to the 54 crystals of a calorimeter module, 6 spare and 2 for LM), to transport the light from the diffusers to the calorimeters;
- 24 light distribution plates made with Delrin in front of the calorimeter crystals, which host 54 rightangle prisms to deflect by 90° the output of the optical fibers into the crystals;

5. 24 local monitors to measure the stability of the light distribution system.

5.2.1 Laser source

The light source is composed by 6 synchronized laser. The choice of more than one laser was due to the necessary intensity needed to illuminate all the crystals.

The choice of the best light source and the design of the laser calibration system architecture are based on some guidelines, on the basis of several tests with different light distribution schemes [110]. For the light source were used the following criteria [107]:

- Light wavelength must be in the spectral range accepted by the detector and determined by the convolution of the spectral density of the Cerenkov signal produced by electrons in PbF_2 crystals with the spectral transmission of the crystals, and with the spectral Q.E. of the photodetector;

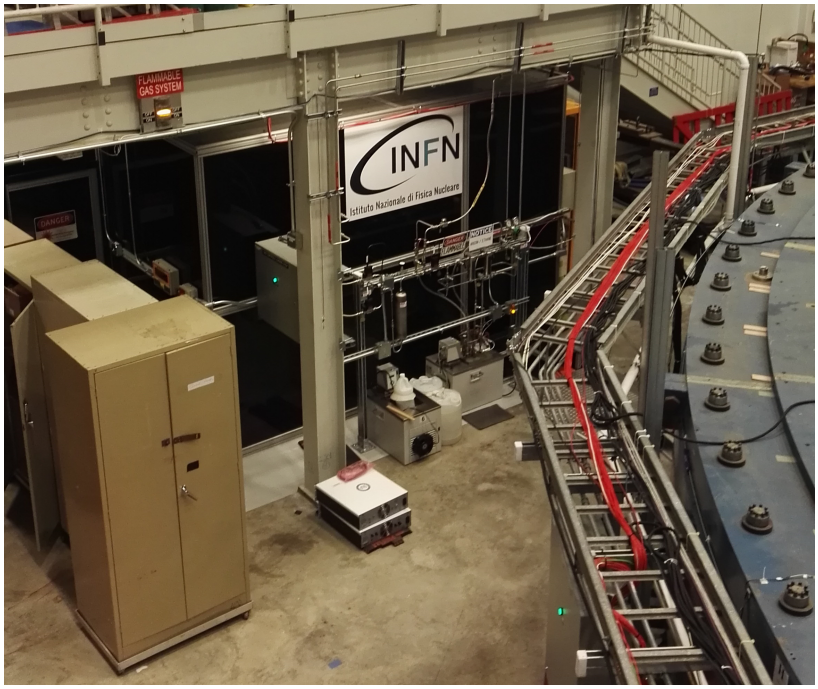

Figure 5.2: The laser hut placed inside the MC-1 building.

- The luminous energy of the calibration pulses must be in the range of the electron deposit in the crystal, typically 1-2 GeV; this corresponds to a luminous energy on each tower of about 0.01 pJ at 2 GeV;

- The pulse shape and time width must be suitable to infer on the readout capability in pile-up event discrimination; pulse rise/trailing time must be of the order of some hundreds of picoseconds, the total pulse width should not exceed 1 ns. This implies a peak power per pulse at the source of some Watts, assuming the conservative value $0.001 < T < 0.01$ for the total intensity transmission factor of the laser calibration system;

- The pulse repetition rate must be of the order of 10 kHz; this value is obtained searching the best compromise between the need of having enough calibration statistics and the need to avoid saturation of the DAQ

Figure 5.3: The LDH-P-C-405M laser head by Picoquant.

bandwidth and perturbation of data due to the laser pulses. If necessary this value can be tuned to improve this optimization.

There is a number of commercial laser that cope with the above criteria. After several test between different kind of lasers the one chosen is the LDH-P-C-405M [143] from Picoquant Fig. 5.3 with the following characteristics:

- Wavelength: 405 nm ± 10 nm;
- Pulse FWHM: <600 picoseconds;
- Average Power (@400MHz): 20 mW;
- Energy/pulse: 500 pJ.

The Picoquant lasers heads chosed are very stable (1% RMS over 12 hours and 3% peak-to-peak for $\Delta T(amb) < 3K$), and the SM is able to monitor laser power changes at the per-mil level.

5.2.2 Optical distribution system

Below are listed the guidelines followed for the light distribution chain:

- High sensitivity monitors of the transmitted light at the end point of each individual section of the distribution chain must be used to ensure online control of the system stability and to have information for applying feedback corrections to the source parameters, if needed;

- The optical path must be minimized in order to limit the light loss due to self-absorption in the optical fibers. The number of cascade distribution points must also be minimized to reduce the unavoidable loss in the coupling between different sections;

- The laser source and its control electronics should be located outside the muon ring in order to avoid perturbation of the local fringe field induced by the current flow used to excite the laser;

- Optical fiber selection: for long distances fibers with high robustness against solarization or other aging effects due the large values of transmitted light intensity. For shorter distance these requirements are less severe so cheaper fibers could be used also for budget reason.

Optical components, collimators and fibers

Each of the six laser beams is split into 4 beams by three 50:50 cubic splitters and sent to a total of 24 adjustable collimators placed in front of 24 optical fibers (launching fibers) Fig. 5.4. The light losses in these steps are of the order of 7% for each cube and 20% for the collimator. In order to minimize the beam attenuation, we chose launching optical fibers made of silica (5 dB/km), with 0.4 mm-diameter. A 12-position filter wheel will be placed at the output of each laser head, to be able to vary the amount of light sent to the calorimeters and perform absolute photoelectron calibration, as shown in Fig. 5.5.

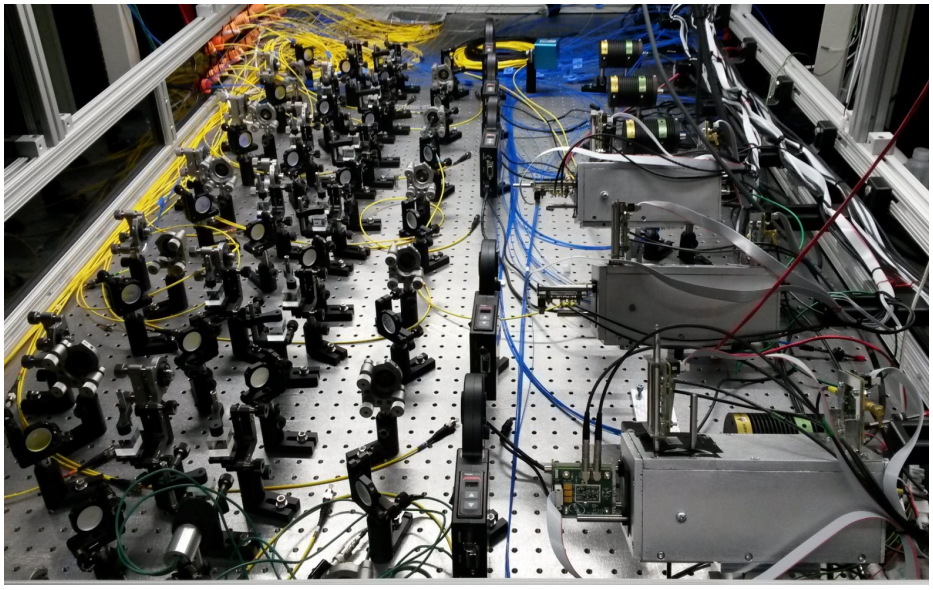

Figure 5.4: The optical table of the Laser Calibration System at Fermilab.

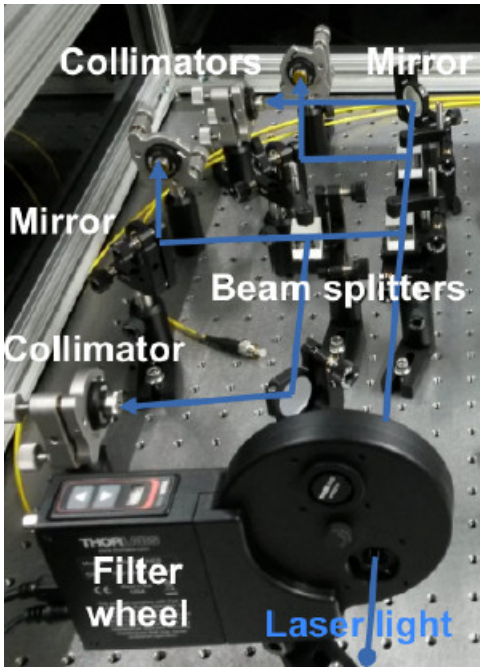

Figure 5.5: Part of the optical table: filter wheel, beam splitters and collimators.

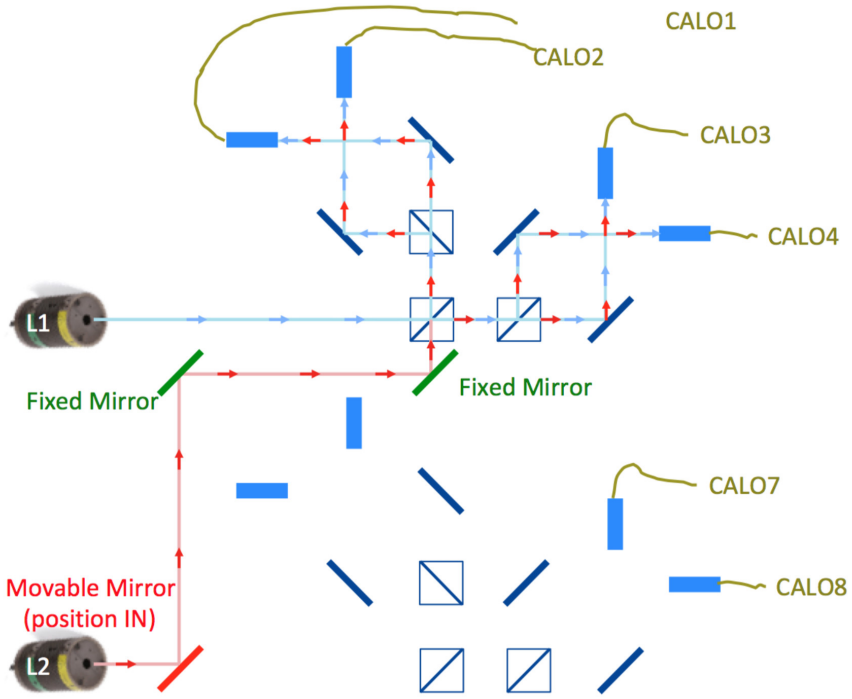

Figure 5.6: Optical hardware setup of Double Pulse System. One set of lasers is reflected onto a different optical path with a movable mirror, and the reflected laser receives a trigger delayed with respect to the non-reflected laser trigger. In this way, two pulses are delivered with a tunable time separation which can be used to explore pileup effects on the gain.

A set of six mouvable mirrors are installed on the laser table and are used for double pulse procedures: By inserting a movable mirror in the light path of laser 2, the light is re-directed, through a set of fixed mirrors, into the first splitter cube of laser 1, as shown in Fig. 5.6. In this way, 2 pulses from 2 different lasers reach each launching fiber. In a similar way, the light of laser 1 can be re-directed into the light path of laser 2 and the same happens to the other pairs: 3-4 and 5-6.

Calorimeter coupling

Out of the laser hut 24 silica fibers, one per calorimeter, 25 m long, route the light to secondary distribution point located close to the calorimeter, as shown in the scheme 5.7.

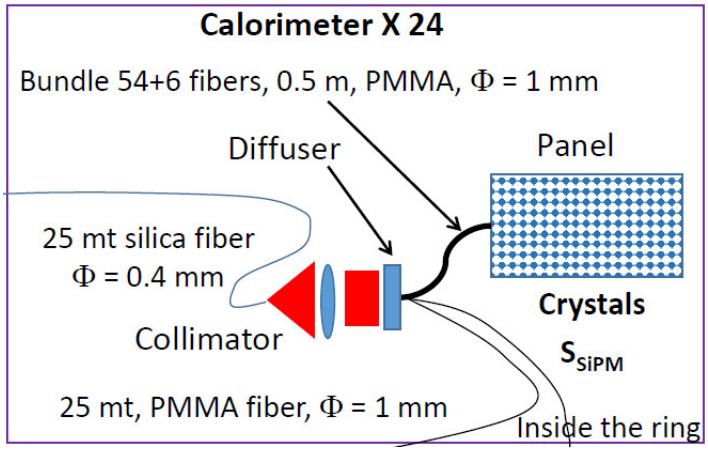

Figure 5.7: Scheme of the fiber to calorimeter coupling.

Several test were performed to find the best solution for the distributors that should be placed near the calorimeter. The requirements are uniformity and stability of the light output without a significant drop in intensity. Studies were performed comparing the performances of the integrating sphere and diffuser [137]. The intrinsic properties of the integrating sphere permit a very high level of uniformity of the light output as can be seen in Fig. 5.8a. The drawback of the sphere is a very low value of the transmitted light, which is almost 10^{-4} times the intensity of the input per single fiber. Comparison with the diffuser, in Fig. 5.8b, shows that the sphere has a better level of uniformity but the diffuser, shown in Fig. 5.9, with its good uniformity and a very high level of the output light intensity, was the solution adopted.

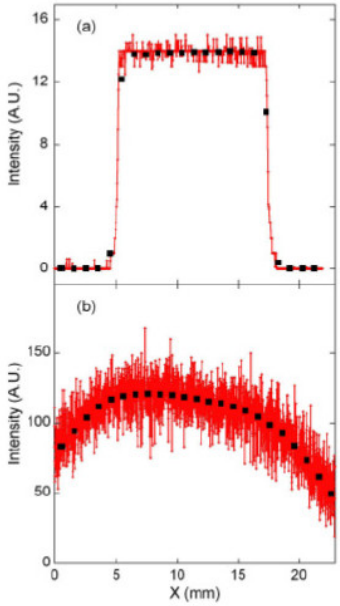

Figure 5.8: Experimental luminance profiles of a single pixel row (daggers) and average 900 pixels (squares), for sphere (a) and diffuser (b).

Diffusers and bundles

To expand the beam exiting the optical fibers and create a beam profile as uniform as possible, an engineered diffuser by Thorlabs was chosen (Mod. ED1-S20). The optical fibers bundle, been see in Fig. 5.11, in front of the diffuser, located 50 mm away, collects about 10% of the light exiting the launching fiber.

The tests showed an excellent uniformity between the fibers of the bundle and its dependence on the distance of the bundle from the launching fiber, see Figures 5.12, 5.13, 5.14. The solution we chose is a light-tight tube, with the quartz launching fiber as input and the fiber bundle as output. Inside the tube we placed both a lens for collimating the beam exiting the launching fiber and a diffuser in front of the fiber bundle, as shown in Fig. 5.9.

For the bundle, shown in Fig. 5.10 and in Fig. 5.11, we chose a large 1 mm-

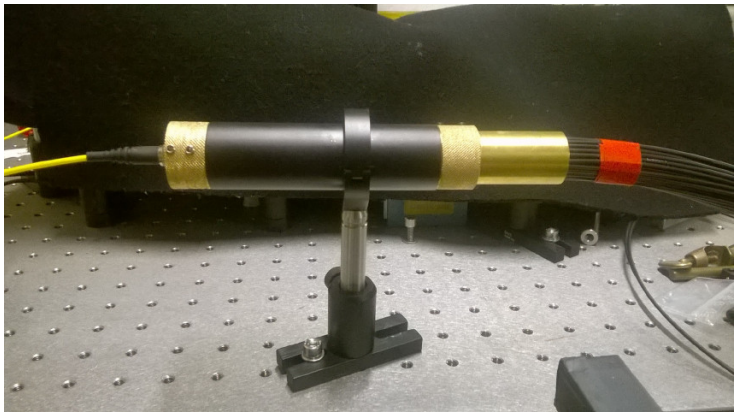

Figure 5.9: Picture of the diffuser used for the calibration system of the E989 experiment.

diameter PMMA fiber, with improved mechanical characteristics (Mitsubishi Eska GK-40). The large diameter is required to be insensitive to the spatial non-uniformity of the flat top beam created by the diffuser placed in front of the bundle. PMMA was chosen because its Minimum Bend Radius is lower than for quartz: the GK-40 model tolerates bending radii down to 20 mm. This small curvature radius is necessary.

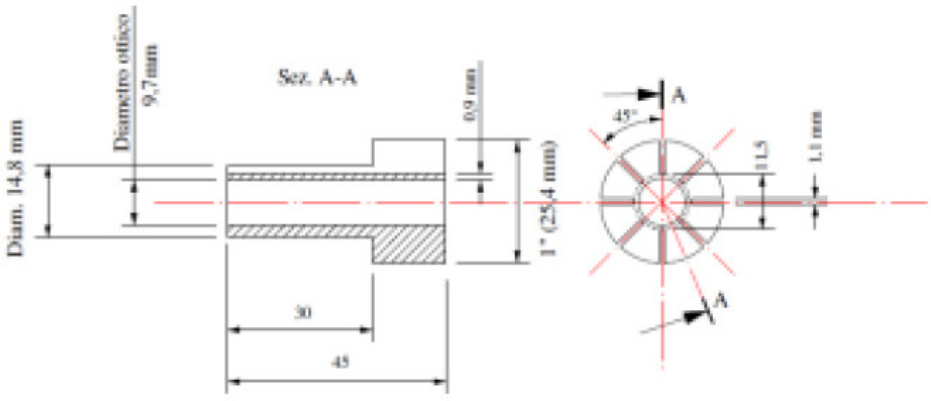

Figure 5.10: Optical fiber bundle: ferrule with housing for removable local monitor optical fibers.

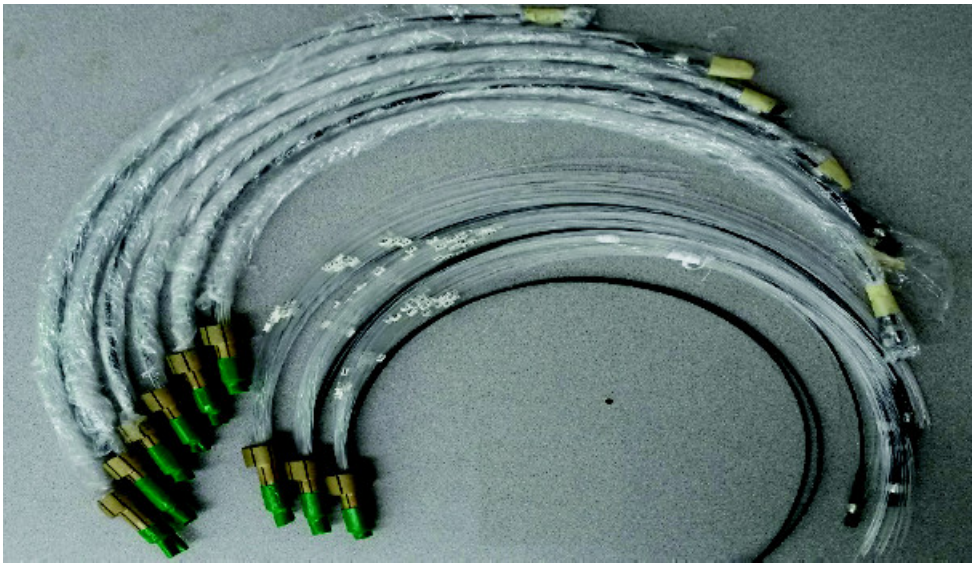

Figure 5.11: Fiber bundles before the installation in calibration boxes.

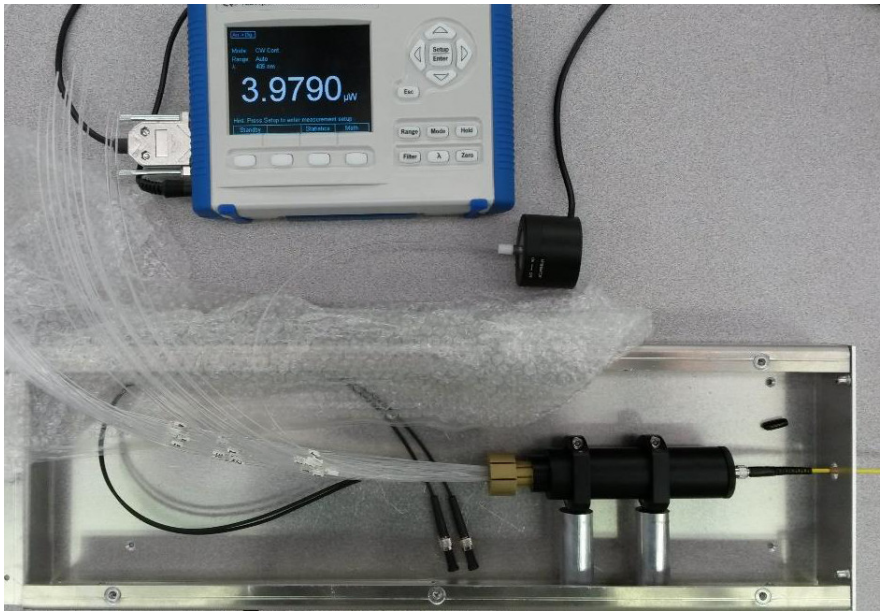

Figure 5.12: Quality check operatin of a bundle with a power meter.

Light distribution plates and mechanics

The coupling of the laser calibration system with each calorimeter requires special care; all the fibers of the bundle must be locked properly to guarantee

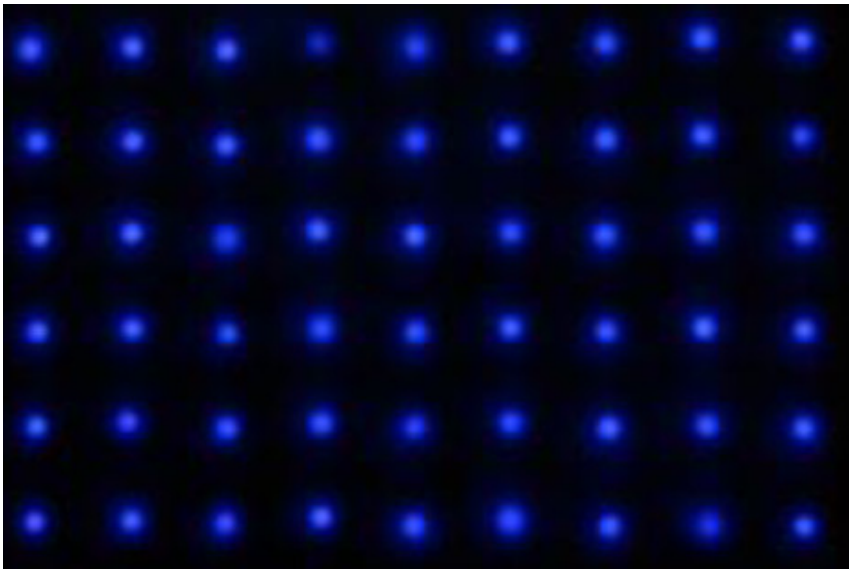

Figure 5.13: Output of the plate (scattered by white paper).

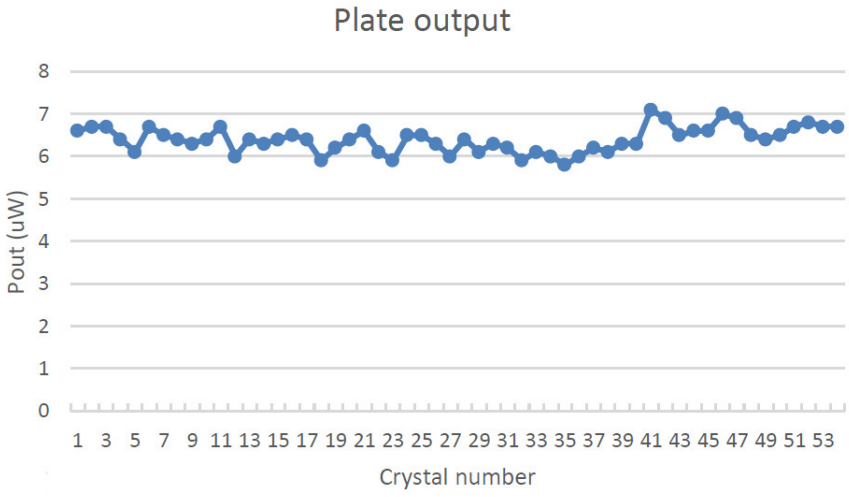

Figure 5.14: Output of the plate measured using light power meter.

the correct light-path to the crystal. Moreover all the system should be in a light tight environment to avoid external light noise. Because of the limited available between the ring wall and the calorimeters, the optical fibers carrying the optical calibration signal to the crystals and SiPMs, cannot deliver the light

normally to the crystals' front faces. In order to deliver the light normally to the crystals, the fibers arrive perpendicular to the crystals and the light is deflected into the crystals with right-angle optical prisms (8 mm X 8 mm). The prisms and the fibers are fixed together by means of a Delrin plate (10 mm thick) with 54 holes, shown in Fig. 5.15, placed in front of the crystals. The plate is quite stiff but has a low interaction cross section for the positrons originating from the decay of muons. Each fiber is routed to an individual prism (accommodated in a through square hole) via a groove which has a curved end part, with a bending radius of about 40 mm. Groves permit to place the fibers in the right position ending to an hole where is placed a 45° prism for each hole, which permits to deflect the light coming from the fibers of 90 degrees without bending the fibers. A PVC plate is placed in front of the front-panel to ensure light tightness of the laser calibration box and subsequently to the calorimeter system to which the box is coupled with.

In Fig. 5.16 is shown how the laser calibration box installed, containing the diffuser, the fiber bundle and the front panel to route the fibers to the crystals, is positioned with respect to the calorimeter box.

A laser calibration box, before the installation on a E989 calorimeter station, is shown in Figures 5.17 and 5.18: Laser light comes from the right through the 25 m long silica fiber coupled to the diffuser placed inside the box. From the diffuser a bundle of fibers drive the light to the crystals, as already explained.

5.3 Monitors

A small fraction of the light exiting each laser source and each light distributors is detected by dedicated detectors used to monitor the intensity of

Figure 5.15: Picture of the front panel. Each hole in the delrin plate house a 5 mm 45° prism which deflects the light coming from the fiber placed inside the grove.

the calibration light. Signals from these "monitors" are sent back to the DAQ system for both online checking of the system stability and further offline monitoring of the calibration signal. The monitoring system consists of 6 Source Monitors (SM) and 24 Local Monitors (LM), as shown in the Fig. 5.19.

5.3.1 Source Monitors

The SM monitors the variations of the intensity of the laser light source, providing the information to correct for them in the calibration procedure (see Chapter 6).

The guidelines followed to optimize the design of the monitor are:

- Zero gain PIN diodes are used which are much more stable than SiPMs to variations in bias voltage and temperature;

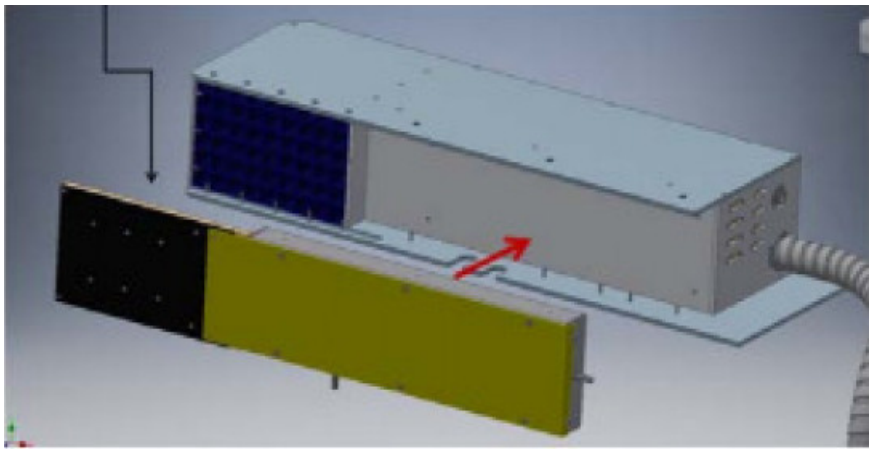

Figure 5.16: Laser calibration box and calorimeter box.

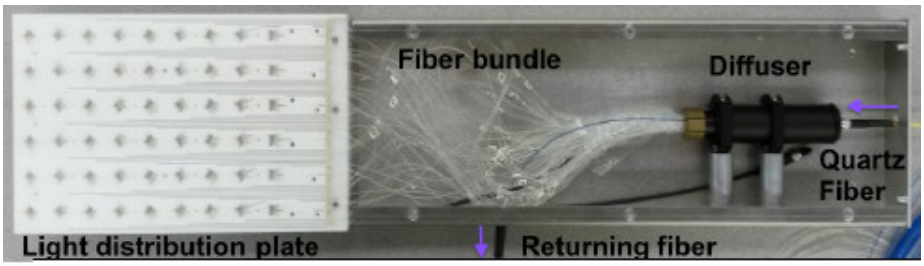

Figure 5.17: Details of the laser calibration box mechanics.

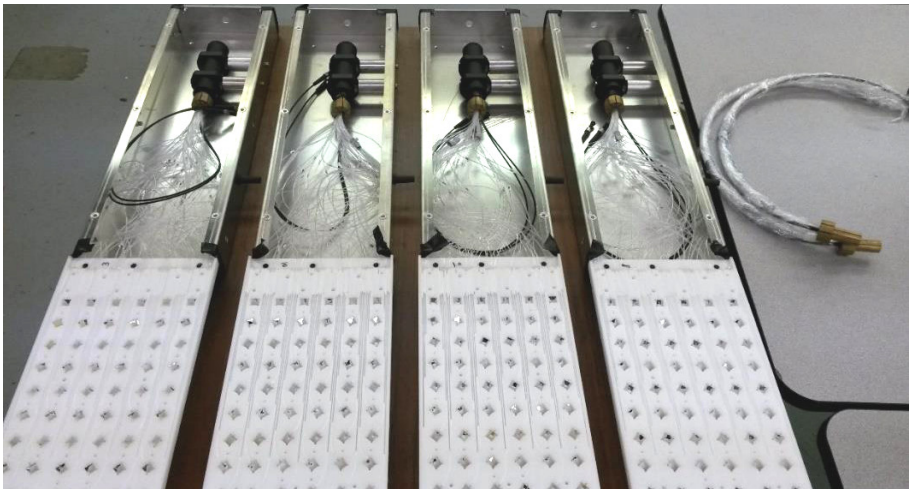

Figure 5.18: Laser calibration boxes before the installation on relatives calorimeter boxes.

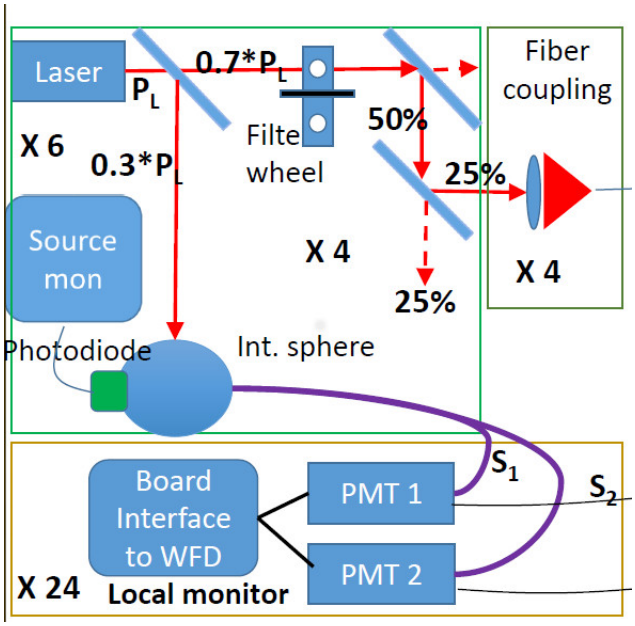

Figure 5.19: Schematic illustration of a monitor geometry.

- The system is exposed to high light level ($\sim$ 30% of the laser light) to minimize photostatistics fluctuations;
- Dedicated electronics specifically designed to get high stability;
- Use of a redundant system with three photodetectors for each monitor;
- Minimize pointing fluctuations incorporating diffusion and mixing elements;
- Use a radioactive source inside the monitor for absolute calibration.

SM are placed inside the laser hut, on the optical table, near laser heads as shown in Fig. 5.20

In the SM, engineered following the above criteria, the laser light is mixed in the SM and viewed by a redundant system of 2 large-area (10 mm x 10 mm) PIN diodes (Hamamatsu S3590-18) and an other monitor photodetector:

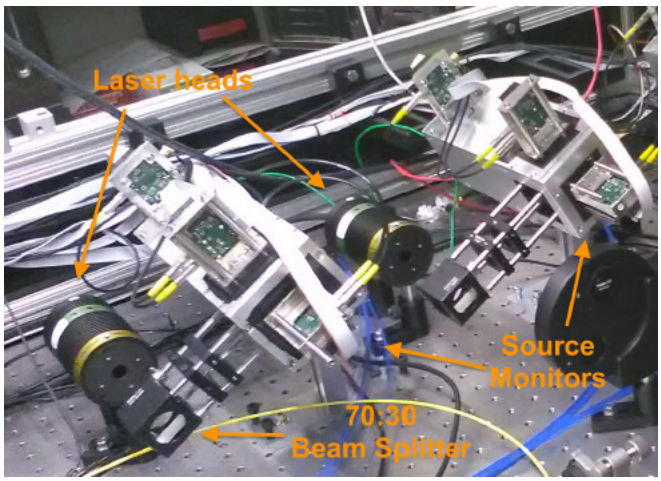

Figure 5.20: Source Monitor placed on the optical table.

a photomultiplier (PMT) (Hamamatsu H5783). The PMT is also illuminated by an absolute reference signal provided by a low-activity (about 6 Hz) Americium radioactive source coupled to a NaI crystal. The SM, by A 70/30 beam splitter, uses 30% of the laser light in order to quickly get a high statistical precision, and requires a longer time to achieve the same precision when measuring the absolute energy reference provided by the ^{241}Am+NaI source. The system is characterized by a large thermal inertia so as to minimize the effect of temperature. In order to ensure uniform distribution of light on the detectors and insensitivity to "beam pointing" fluctuations, a commercial diffusing sphere was used (Thorlabs, mod. IS200). The task of this device is to mix the light with multiple reflections inside. With this procedure the light that comes out from the sphere ports has an high level of uniformity.

Fig. 5.21 shows a schematic illustration of a monitor geometry. The other 2 fibers go to the LM, as reference signal.

The base criteria to use SM signals to correct the calorimeter responce is the follow: To assuming the laser-induced signals, from all calorimeters elements

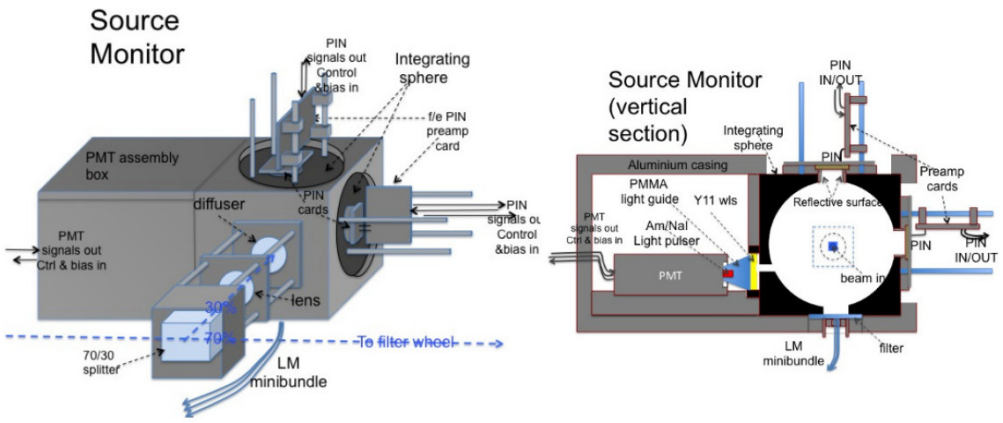

Figure 5.21: Schematic illustration of a monitor geometry.

(*Sci*) and the monitors (*Sm*), are subject to the same laser fluctuations, these kind of fluctuations are cancelled in the ratio *Sci/Sm*. These ratios should then reveal fluctuations in the calorimeter response, provided other fluctuations in *Sm* are stable to degree required.

5.3.2 Local Monitors

To correct for possible gain fluctuations induced by the passive elements of the distribution chain, due to aging effect or mechanical vibrations, a local monitor system is required to keep the systematic error under the required value of 20 ppb. This monitor is designed to serve each calorimeter. It detects the same light of the crystals in the calorimeter, see Figures 5.1, 5.19 and 5.17; this value is orders of magnitude lower than the light that reaches the source monitor and therefore it doesn't allow the use of PIN diodes.

Several test were performed to chose an appropriate photodetector; the best solution is to use PMTs, because of their high level of gain and their intrinsic stability. The only drawback is the high current produced which forbids placing the local monitor close to the calorimeter because it perturbs

Figure 5.22: Mini bundle of fibers drives the light collected by the Source Monitor to Local Monitors. Are used 6 mini bundles, each used for 1 SM and 4 LM are used.

the fringe field even shielded. The adopted solution is to place the two PMTs for each calorimeter in the laser hut, Fig. 5.25.

The Local Monitor consists of a PMT (Photonics XP2982) that receives two optical signals. The first signal is the reference from the Source Monitor, collected from a port of the integrating sphere, and is used to calibrate the gain of the PMT. The second signal comes from the fiber bundle in the vicinity of the calorimeter and is representative of the calibration signal sent to the SiPM, see Figures 5.19 and 5.17. The two optical signals are separated in time by 250 ns, since the first signal travels a distance of approximately 2 meters, through a minibundle of fibers, shown in Fig. 5.22, while the second of about 50 m (25 m one way in the quartz fiber, 25 m return in the PMMA fiber). In order to study and compensate for any fluctuations due to temperature of the transmission coefficient of the local monitor optical fibers, we use two types of fibers: quartz and PMMA. The system is redundant, and allows to monitor any solarizing effect of the PMMA fibers.

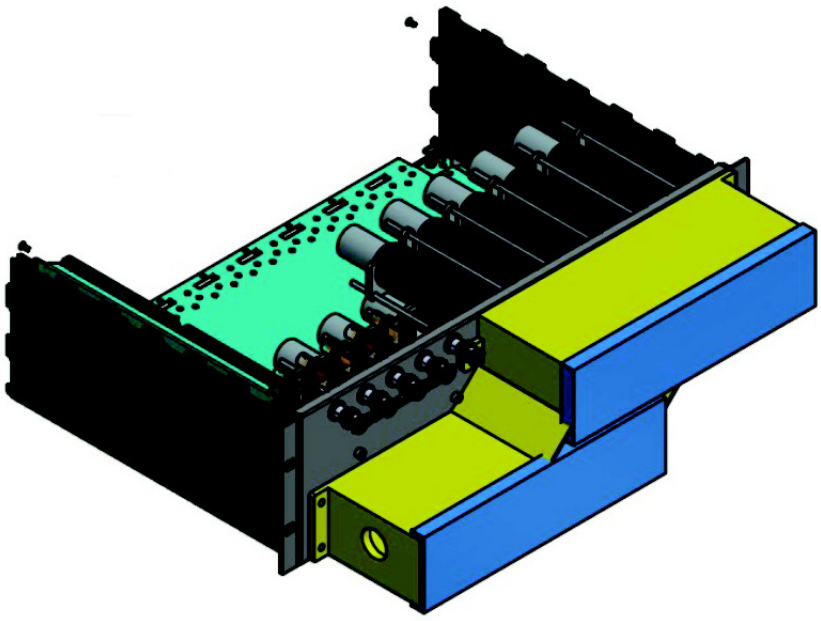

Figure 5.23: Scheme of the local monitor box.

Figures 5.23, 5.23, 5.23 and 5.23 show a schematic illustration of a local monitor box, the construction and the installation in the laser hut at Fermilab. IT contains 10 LM PMT tubes. Totally we use 24 LM placed in 3 local monitor boxes.

The LM signals allow to correct for the gain fluctuation, due to the distribution chain elements, by comparing the signal coming from the distribution chain to the reference one.

5.4 Monitoring electronics

Specific devices and devoted designed electronics have been used to read, process and digitize the corresponding signals. Also, these electronics provide the supply voltage to the photodetectors, read the different temperatures

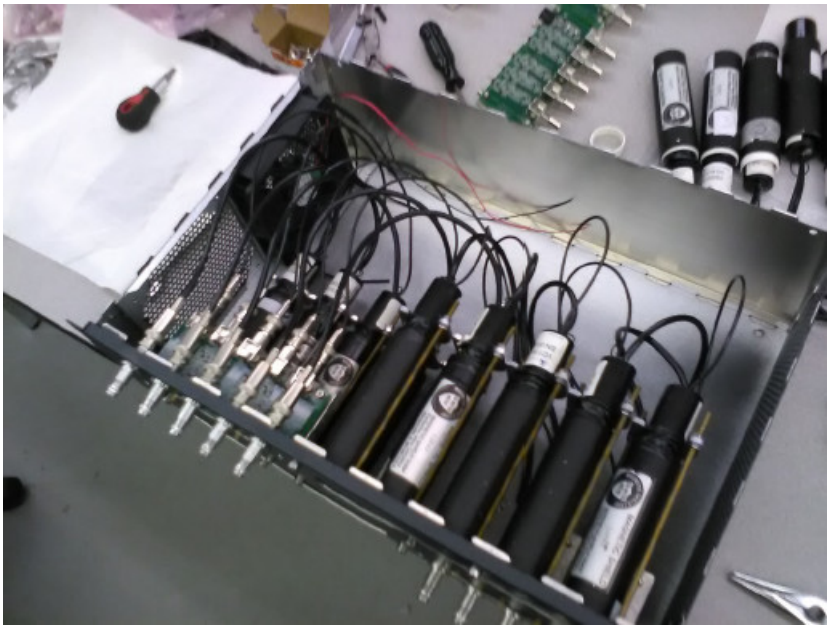

Figure 5.24: the local monitor box under custruction before installation in laser hut.

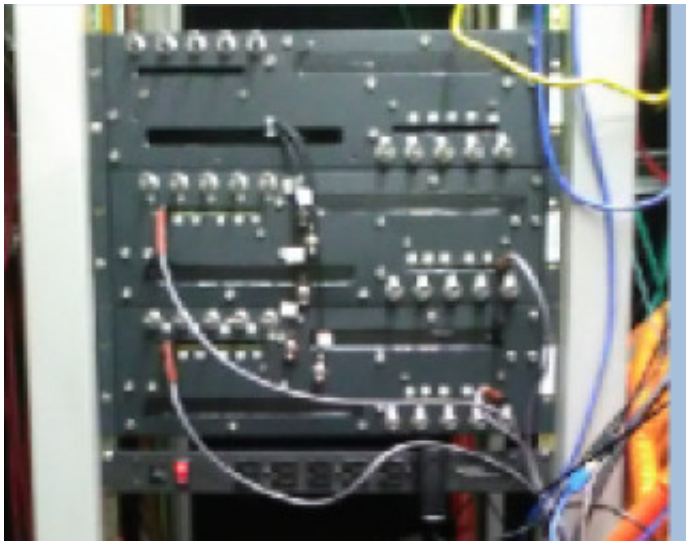

Figure 5.25: the local monitor box installe in the laser hut at Fermilab.

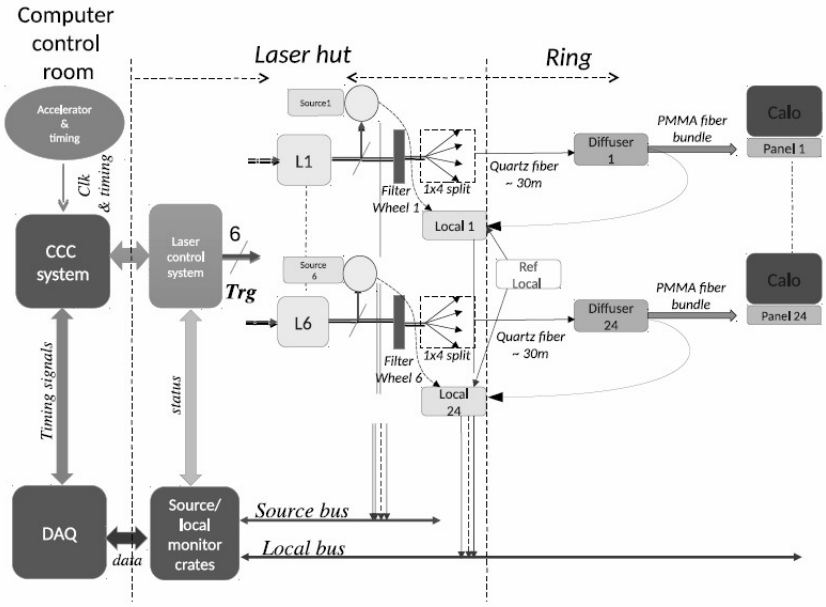

Figure 5.26: Schematic drawing of the laser calibration System and electornics. The light pulses are managed and monitored through electronics at the source, at laser output, Source Monitor, and at the end of the distribution system, Local Monitor.

(environmental, on the preamplifier and on the board itself) and, eventually, stabilize the performance of the readout channel. Moreover the designed electronics is able to self generate pulses of known amplitude and to send them at the input of the readout channel, meaning that it has capability of self-calibration.

5.4.1 Laser Control System

At beginning of the Laser system chain there is the Laser Control System (LCS). It permits:

- Laser operations in two distinct modes. The first is enabled, during physics runs, to correct for systematic gain variation of the SiPMs caused by the high muon decay rate at the beginning of the muon fill. The second

is used for test runs, without beam, in order to exercise detectors and DAQ with specific laser pulse time sequences and to study the SiPM responce to double pulses;

- Time alignment of the SiPMs in a calorimeter and between calorimeters.

The LCS is composed by:

- Laser Control Borad;
- Trigger fan out;
- Laser driver;
- Delay generator system.

Laser Control Board

the Laser Control Board (LCB), a custom electronics made by INFN, manages the interface between the beam cycle and the calibration system itself [144]. It generates laser pulses and distributes the time reference signals to the monitoring electronics Fig. 5.27.

The core of the LCB is a pulse generator with two different implementations (the first fully realized in an FPGA and the second utilizing an ARM processor to control the final generation of pulses) which allow both a high level of flexibility, due to software benefits, and a high level of performance typical of hardware solutions. The time resolution of the pulse generator is 10 ns.

The experiment's synchronous control system, the Clock and Control Center (CCC), provides the triggers to the LCB timed appropriate to delivery of the muon beam. The LCB decodes the trigger mode and generates the suitable laser pulse sequence. The LCB operation is driven by the beam arrival;

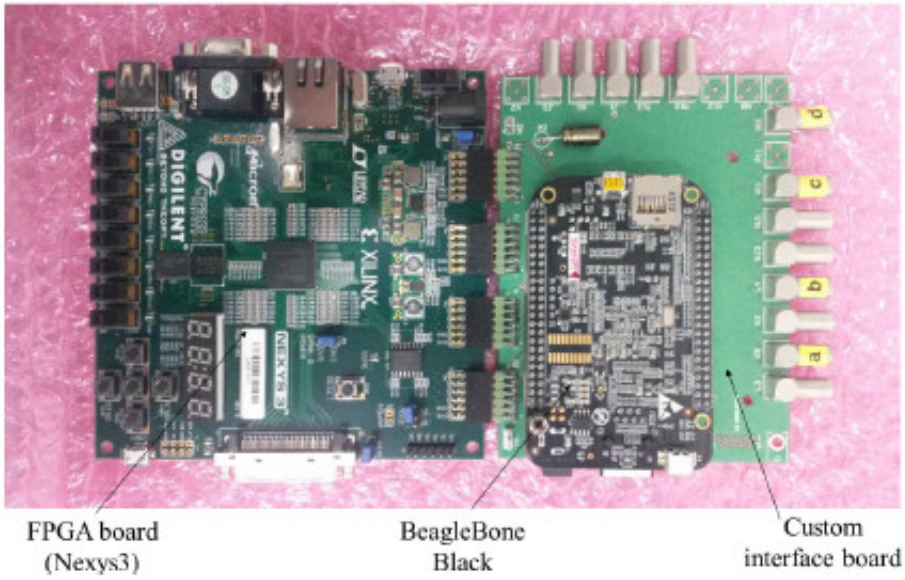

Figure 5.27: The laser control board.

a simplified scheme of the laser pulse sequences is shown in Fig. 5.28 with respect the muon beam structure of the E989 experiment. Nonetheless the same system could accommodate widly different schemes from what we have in the muon $g-2$ experiment at Fermilab. The main cycle of the accelerator machine is represented by 16 repetitions of muon fill and decay windows (700 μs long, represented by the square signal in Fig. 2, or "in-fill phase") typically separated by 10 millisseconds (ms) (or "out-of-fill phase"). Actually there are two bunches of 8 filling-decay windows separated by about 200 ms and 1000 ms. The injection cycle repeats every 1.3 seconds. Moreover the LCB checks the status of the monitoring electronics boards (SM and LM) and if no error flag is active, the LCB initiates the laser patterns.

The LCB implements the following main features:

- *Calibration mode*, or generation of pulse trains, at programmable frequencies, superimposed on the physics data provided in a 700 μs muon

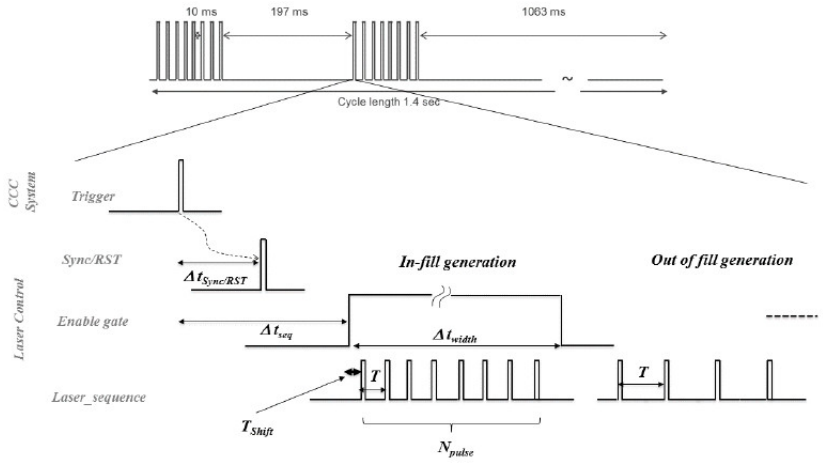

Figure 5.28: The main cycle of the accelerator machine is represented by 16 repetitions of muon fill and decay windows (700 μs long, represented by the square signal in figure, or "in-fill phase") typically separated by 10 ms (or "out-of-fill phase"). Actually there are two bunches of 8 filling-decay windows separated by about 200 ms and 1000 ms. In the lower part is shown the laser pulse sequence, which is structured according to many self-explaining parameters.

fill. The pattern is shifted by a fixed time in order to have the 700 μs sampled in 140 points. The number of samples at each point is determined by the calibration goal of a 10^{-4} relative error. Considering the number of photons in each pulse, the muon fill repetition rate and the rate of calibration pulses within the 700 μs window, we expect that a few thousand samples at each point will be sufficient to reach the needed accuracy. This translates into a capability of calibrating the entire detector in one to two hours;

- *Physics event simulation*, or operation in "flight simulator" mode, entails triggering the laser according to the exponentially decreasing time function, $e^{-t/\tau}$, as expected in the experiment due to muon decay. In fact, an essential feature of the LCB is the capability of generating pulses, or

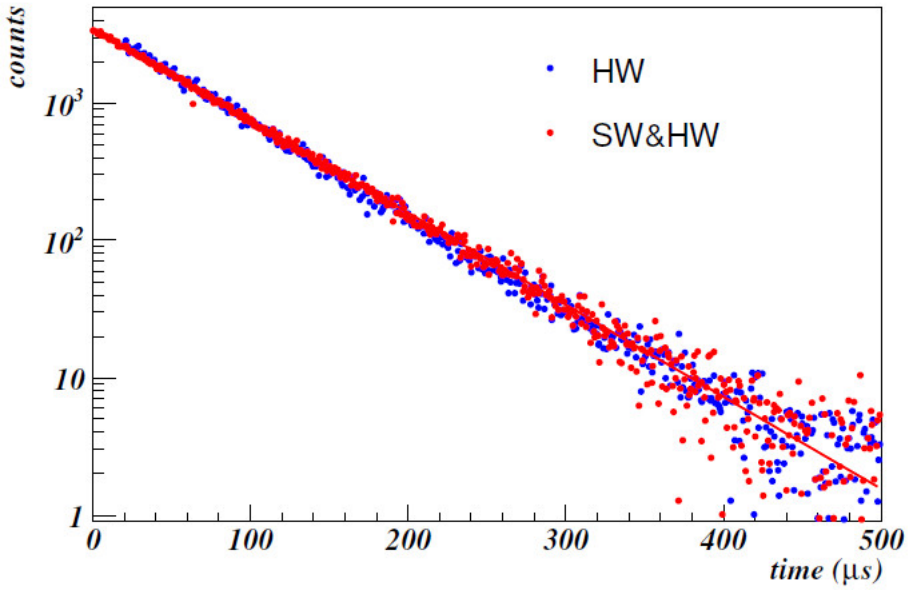

Figure 5.29: Time distribution of pulses generated according to an exponentially decreasing function "flight simulator".

triggering the laser, according to any time distribution. As the arrival times of decay positron in the experiment are exponentially distributed with a decay time of 64.4 μs, the simulation mode envisages a time generation according to an exponentially decreasing function. This mode provides flexible testing of the SiPMs to determine, for example, their response linearity and gain stability, see Fig. 5.29;

- *Fully realistic tests* of the readout electronics, DAQ and data processing;
- *Synchronization* of detectors and electronics by providing a reference pulse on request, or in connection to an accelerator machine signals;
- *Programming of the Prescaling*: pulses light only a predefined times of the CCC trigger occurrences.

The interface with the laser driver and the LCB is a fan-out moduel that

Figure 5.30: Laser crate "Sepia". Each laser head LDH-P-C-405M will be coupled to its driver (the crate contains up to 8 drivers).

provide 6 trigger channels to the laser driver device.

Laser driver

With the scheme reported before and shown in Fig. 5.1, is important synchronization. This will be ensured using a single laser crate "Sepia II" from Picoquant [146] which has the capability to control up to 8 laser synchronizing them up to some picoseconds with its internal trigger Fig. 5.30.

Double Pulse System

The Double Pulse System is implemented to characterize the response of the Fermilab Muon $g-2$ calorimeters to two or more consecutive particles using the laser system. Two pulses separated each other in time by 10 ns (short term double pulse) or by to hundreds ns (long time double pulse). The expectation is that the first pulse causes a systematic reduction in the size of the second pulse due to SiPM response and charge depletion in the capacitive components of the system's electronics.

The hardware setup requires the use of a delay generator as well as remotely controllable mirrors, see Fig. 5.6.

The movable mirrors are mounted on motorized flipflop stands Thorlabs

Figure 5.31: SRS DG645, The delay generator used by the Double Pulse System.

MFF101/M. The stand has 2 positions, at 90 degrees rotation one from the other, allowing for a beam stability better than 0.1 μrad. They are remotely controlled through 6 USB to TTL-232RG cables by a computer located in the Laser Hut. A C++ program talks with the mirror stand through the PC-USB port allowing the possibility to remotely control the mirror positions.

An external delay generator (DG) SRS DG645 [147] is used to send prompt and delayed signals, see Fig. 5.31. The input to the DG is a replica of the Master Clock sent by the Laser Control Board. Two of the four DG outputs are connected to the ODD and EVEN lasers, respectively. This allows to send to the same calorimeter two pulses with a relative delay programmable in the range [0, 1] seconds in steps of 10 picoseconds. The ranges which are relevant for the calorimeter response are $[0 - 100]$ ns, in steps of ~ 1 ns, and $[0 - 100]$ μs, in steps of ~ 1 μs. The DG allows also to send bursts of equally spaced pulses, thus mimicking the flash of particles which illuminate the calorimeters during beam injection. An additional feature of the DG, which turns out to be very useful in signal normalization, is the prescale option: each DG output can be indipendently prescaled by a factor $N = 1 - 10000$, such that only 1 signal every N triggers is actually issued.

5.4.2 High voltage and power supply units

The hardware that requires specific power supply units are:

- Laser Sources;
- Source Monitors;
- Local Monitors.

Laser sources are directly powered by the described laser Driver Sepia.

Source Monitors's Pin Diodes and PMTs are powered by a customized electronics, called Monitoring Board (MB) [145], that manages the complete signal processing, data readout and configuration/control for three channels of Source elements of the Calibration system. A control section provides high voltage to the Source Monitors photodetectors by means of an 12 bit DAC with the possibility to read back the set values, see Fig. 5.34.

Local Monitors PMTs are powered by a commercial high voltage generator CAEN SY5527, remotely controlled, that provides a range of 500 - 1000 high voltage tensions, stable enter 0.1% Fig. 5.32.

5.4.3 DAQ systems

the Laser Calibration System have two different Data acquisition systems (DAQ) to collect data from SM and LM photodetectors.

One custom DAQ system, the same kind used to acquires data from 24 calorimeters, contains an array of 12 Riders (Waveform Digitizers WFDs), each with five channels, that continuously digitized waveforms from the laser system monitors [107].

The other is a custom monitoring system, Monitoring Boards (MBs) [145],developed

Figure 5.32: The HV CAEN sy5527 privide power supplyes to PMTs of Local Monitor system.

by INFN, that collect integrated signals from SMs and monitoring temperatures of the SM electronics and of the optical table hut.

MBs system also provide SM shaped signals at input channels of WFDs.

Waveform Digitizers

The DAQ WFDs hardware [127] is based around the μTCA standard, which was developed for telecommunication applications. At a basic level, this is simply a standard that describes a system where you can plug cards into a crate and have ways for them to talk to each other [126].

Each Rider, responsible for converting waveforms from analog to digital, is developed to retaining the signal fidelity necessary to meet the calorimetry requirements on energy resolution and pileup differentiation and works well also to digitize photodetectors pulses of the Laser Calibration System Monitors [107]. The Rider design has five digitization channels, labelled Channel $0 - 4$, each with its own ADC and DDR3 memory to buffer the data. The logic to acquire and then readout each set of data is controlled by a Channel FPGA. As illustrated in Fig. 5.33, a Master FPGA then serves as the inter-

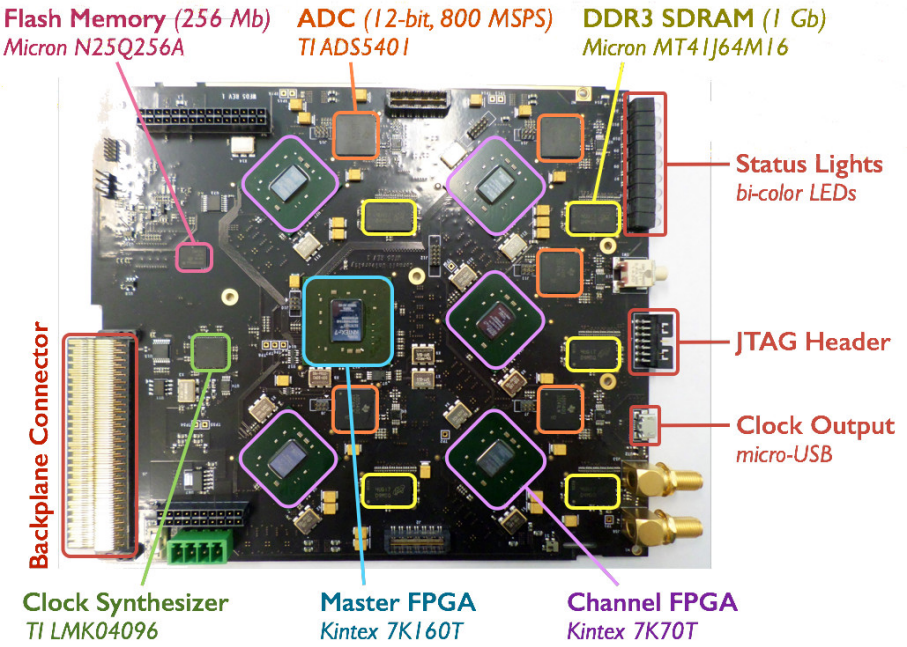

Figure 5.33: Rider baseboard shown with the main components labelled.

face between the five channels and the outside world. The Rider has a clock synthesizer that take in the 40 MHz experiment clock from the AMC13 card and upconverts it into an 800 MHz sampling clock, which is sent on to each ADC. In addition, there is a EEPROM chip connected to the Master FPGA that will be used to store the IP and MAC addresses for the Rider.

The AMC13 card [131, 132], has in imput the TTC signal [129, 130], which encodes the clock, trigger, and control signals and does three major jobs:

1. Distribute triggers to the Riders;

2. Distribute the clock signal across the backplane to all of the Riders;

3. Receive raw ADC data from each Rider, merge the data from all the Riders, and send them to the DAQ system via an optical data link.

The DAQ system also comprised a frontend computers, responsibles for the

read out and the preprocessing of the continuously digitized waveforms from the detector systems, and a backend computers, responsibles for the event assembly, data storage and run control. Each frontend read out the raw data from the μTCA crate over a point-to-point 10 GbE fiber-optic links and preprocessed the raw data into derived datasets using a hybrid system comprising the computer's eight-core processor and two general purpose graphical processing units (GPUs). The raw data rate from the readout electronics was approximately 2 GB/s. The preprocessing is neccessary to reduce of enormous rate of continuously-digitized waveforms to a manageble rate of stored datasets.

Monitoring board

The monitoring system consists of 7 MBs hosted in two custom crates; in each one the master board (Controller) [145] manages the complete data collection, operates as event-builder and transfers data to the online farm through a gigabit ethernet connection. Data acquisition protocol between Controller and MBs (up to 12) is accomplished by a custom backplane, through which each board is connected by means of two unidirectional serial links. The readout cycle is based on a trigger-driven algorithm where all MB boards and Controller share the same trigger signal coming from the Laser Control System [144]. When a trigger arrives, each MB board performs the data assembling by collecting all the sub-frames from the three buffer FIFOs and then transfers them to the Controller which in turn performs the event building at crate level. It processes all the sub-frames from MBs pertaining to the same trigger number, checks the data integrity, adds control and monitoring words and stores the frame in a FIFO accessible via a high speed USB device managed by an embedded processor inside the board. Several specialized tasks running on the Controller are the core of the software architecture for data readout and

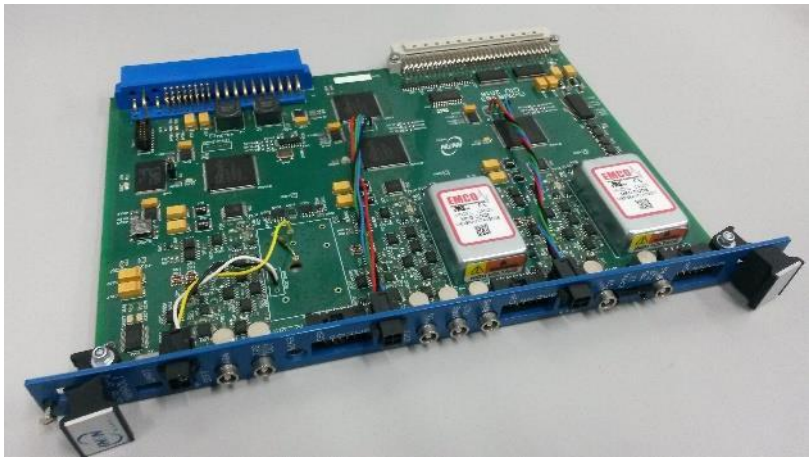

Figure 5.34: The custom electronics, monitoring board, that manages the complete signal processing, data readout and configuration/control for three channels of Source elements of the Calibration system.

monitoring of detectors and DAQ modules. The event building at crate level is fully realized in hardware, while the final event building is managed by an online farm.

Others important facilities of the MB are:

- The use of a test capacitance to inject charge on the line controlled by a 14 bit DAC that allows the self-calibration of each channel; the stability needs to be controlled at a sub-permil level;
- Several temperature measurements are carried out with an accuracy of 0.1°C.

DAQ control software

WFDs are managed by *MIDAS* [133], the data acquisition framework of the E989 $g-2$ Experiment, shown in the Chapter 4. The frontend readout already consists of: a TCP thread that receives and reassembles the raw data from the AMC13 controller, a GPU thread that manages the GPU-based

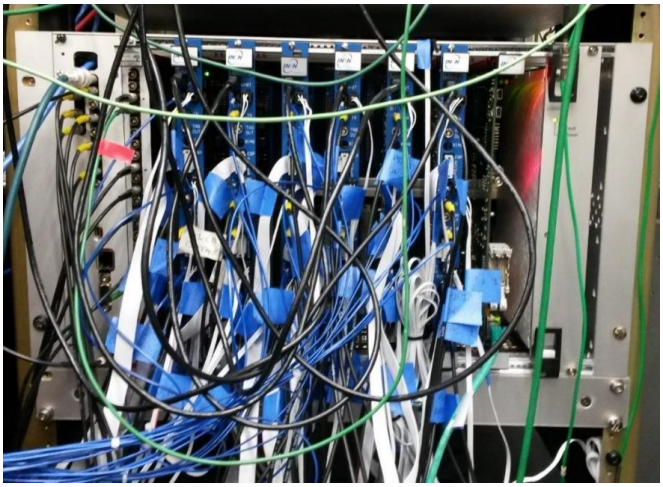

Figure 5.35: The crate and the six MBs installed at Fermilab.

data processing into various derived datasets, and a *MIDAS* thread that handles the transfer of *MIDAS*-formatted events to the backend computer event builder. Mutual exclusion (Mutex) locks are used to synchronize the execution of threads and ensure the integrity of data. Source Monitors MB are managed by custom c++ software developed by INFN.

Chapter 6

Tests and performances of the Laser Calibration System

6.1 Tests at DAΦNE and SLAC accelerator beam Facilities

Two test beams, with a progressive improved design, were performed during 2016 to evaluate the calorimeter prototypes. The test were performed:

1. From 29^{th} February to 7^{th} March at the Beam Test Facility (BTF) [139] at Laboratori Nazionali di Frascati (LNF), Italy [141, 150];

2. In June 2016 at the End Station Test Beams (ESTB) at SLAC, California USA.

The test at BTF, planned and organized by the Laser Calibration group as a final test of the laser calibration system, made possible to evaluate all the different components of the system developed in different laboratories in Italy, coupled together, i.e. the effective operation of the full laser calibration

system on a small calorimeter prototype.

In the second test the full instrumentation for measuring the ω_a for the Muon $g-2$ experiment was evaluated using an electron beam at (ESTB). The tested system includes a PbF_2 calorimeter, the laser calibration system [141], the 800 MSPS custom waveform digitizers [127], the hybrid CPU-GPU DAQ system [155], the *MIDAS*-based [133] data acquisition, the event builder and finally the *art*-based [136] offine data analysis framework.

6.1.1 Experimental setup at DAΦNE beam Facility

The Frascati BTF provides a highly collimated electron beam with a 50 Hz repetition rate and a maximum energy of 500 MeV. The BTF can run in electron or positron mode depending on the user choice. Its duty cycle is dependent on the DAΦNE collider [142] working condition. For this test beam has been chosen an extremely low intensity beam (in average only one electron /pulse). The electron beam has a transverse dimension of about 250μm and a mean position stable in time 6.1. The setup is illustrated schematically in Fig. 6.2.

Calorimeter

The calorimeter consist of a small scale prototype of the calorimeter that will be used for the E989 experiment described in Chapter 4. It was composed of only five elements[1] arranged in a cross-like configuration with four additional mock Plexiglas crystals to create a 3 × 3 array. The sensitive elements used are 2.5 × 2.5 × 14 cm^3 high-quality PbF_2 crystals [140]. Four of them were wrapped in black absorbing Tedlar, while the remaining one was wrapped in reflective white Millipore paper, Fig. 6.3.

[1]Considering crystal and its associated photodetector a single element.

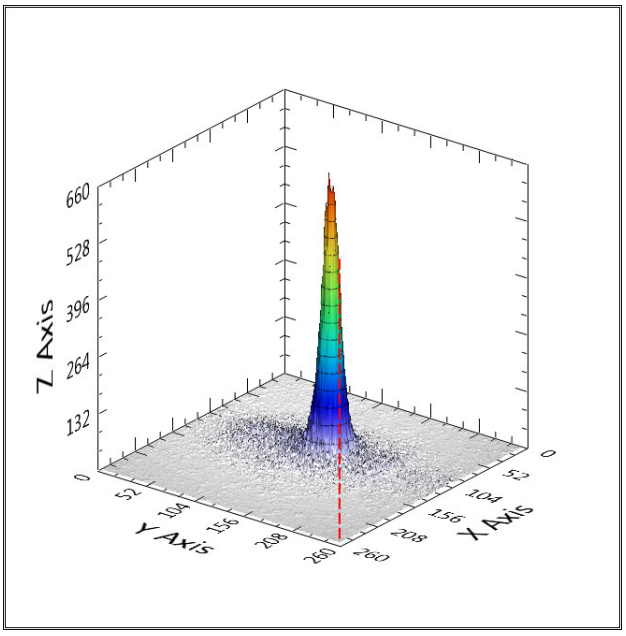

Figure 6.1: Tipical 450MeV electron beam profile registered during the test beam.

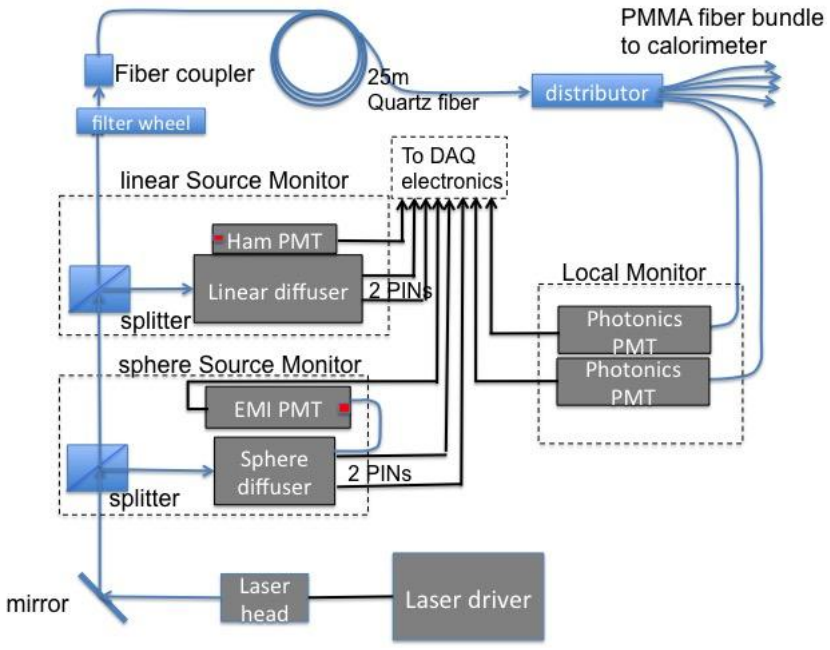

Figure 6.2: Schematic representation of the experimental layout.

(a) (b)

Figure 6.3: (a) A front view of the calorimeter. Different crystal wrappings can be observed (top crystal in white wrapping). Is possible to recognize the real crystal from the fake Plexiglas ones, looking at the SiPM image reflected on the rear side. (b) The box of the calorimeter was made by Università degli Studi del Molise e IPIA Institute of Campobasso.

A 16 channel Hamamatsu SiPM [154, 152] was glued to the rear face of each crystal. The five SiPMs detect both the Cerenkov light generated by the 500 MeV electron beam and the calibration photon pulses. Laser calibration pulses were guided to the front face of each calorimeter element by means of optical fibers, each ending on a reflective right angle prism so as to inject the light in a direction parallel to the crystal axis. The prisms and the terminal of the fibers are held by a Delrin panel manufactured by the Laboratori Nazionali di Frascati mechanic workshop, Fig. 6.4, that is positioned in front of the calorimeter.

At end the calorimeter was positioned on a movable bench in order to match the position of the electron beam.

Each SiPM has two connectors: a PIN connector and an HDMI one. A custom PIN-to-MCX cable is used to connect the SiPM to the digitizer; the HDMI cable provides the bias Voltage through a custom breakout board developed at the University of Washington. This breakout board has 16 channel

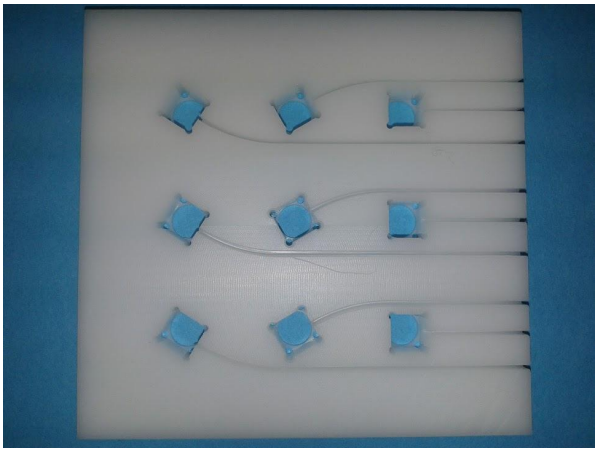

Figure 6.4: Picture of the front panel prototype used. This is a small scale prototype of the front panel that will be used for the full calorimeter in the experiment. Each hole houses a 45° prism and the grooves drive the fiber to the prisms.

for each different SiPM. The bias voltage could be provided in two different ways: a single voltage to all the 16 channels or two different bias via two different lines of 8 channels each. The breakout board is also linked to a beagleboard microprocessor [149] which is used to run control procedures and set parameters of the SiPM frontend electronics, e.g. set gain values and read temperatures. SiPM are very sensitive to temperatures, and is important to have a continuous monitoring of this parameter together with a cooling system. For this test beam was sufficient to maintain an acceptable temperature, stable in time, with a simple system composed by a fan unit.

Laser source and control system

The laser source is a LDH-P-C-405M pulsed laser by PicoQuant [143], as described in the previous Chapter. The repetition rate was varied from from 2.5 MHz to 40 MHz using the PDL 800-B laser driver by PicoQuant. A custom electronic boards, the laser control board described in the previous Chapter 5,

permitted to select also specific values of the repetition rate down to few Hz.

Laser distribution system

Part of the laser light is driven by beam splitter cubes to the monitoring system. The laser beam is then coupled and focused into a 400 μm diameter and 25 m long fused silica fiber, with an attenuation of 20 dB/km at 400 nm. This fiber was used to simulate the running condition of the E989 experiment. The light output of the fibers is collimated and transmitted through an engineered diffuser produced by RPC Photonics, consisting of a structured microlens arrays, which transform a gaussian input beam into a flat top one [137]. The light from the diffuser is then driven to the calorimeter through a fiber bundle made of 1 mm diameter and 3 m long PMMA. Five fibers of this bundle are connected to the light distribution panel faced to the 45° prisms; two other fibers are coupled to the two corresponding PMTs of the local monitor. To complete the system a motorized filter wheel is placed before the silica fiber to change and modulate the light intensity of the laser pulse reaching the calorimeter.

Monitors

A local monitor (LM) system and two different design of the source monitor system (SM) were available for this test. The alternative design of the monitor consisted in a different mixing element: a mixing chamber was used instead of the integrating sphere as shown in Fig. 6.5.

For two different SMs the working idea is the same as well as the kind of signal produced shown in Fig. 6.6.

For the LM the design used in the test beam has been already described in Chapter 5; two PMTs by Photonics will be used, which receive a fiber coming

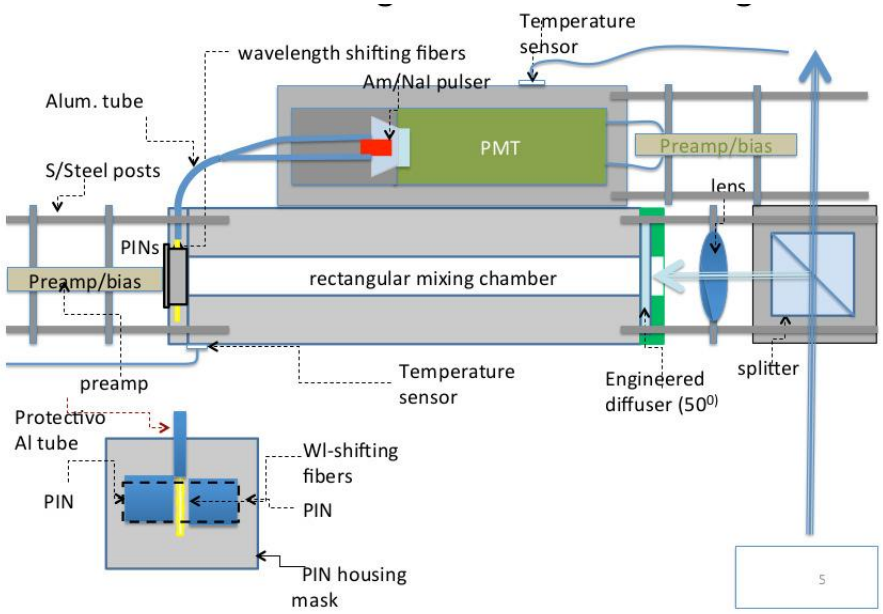

Figure 6.5: Schematic illustration of the alternative design of the source monitor used during the test beam.

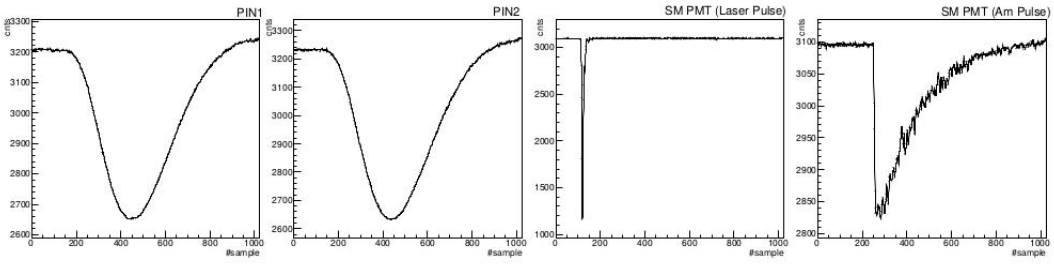

Figure 6.6: Signal produced by the source monitors. Starting from left: Laser signal in output from the pin diodes, laser pulse signal in output from the PMT, and americium pulse signal in output from the PMT.

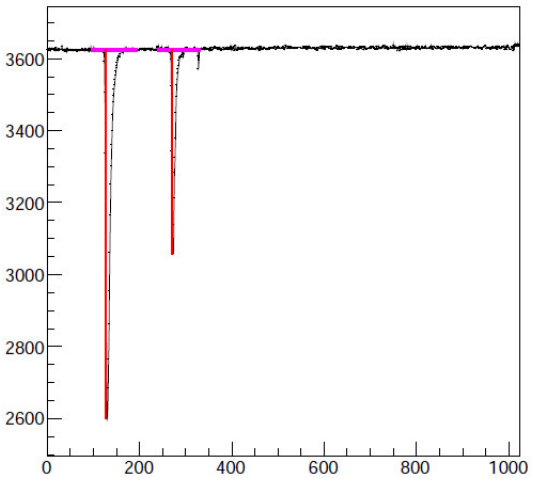

Figure 6.7: Display of a typical LM event. The first signal comes from the SM while the second is the return signal from the calorimeter. Horizontal scale is in nanoseconds.

from the bundle that feeds the calorimeter and a reference signal coming from a source monitor. The two pulses were well separated in time by 120 ns, as shown in Fig. 6.7.

DAQ

For this test 18 digitizers channel has been used to process all the signals from the different devices. For that a CAEN DT5742, 16 channel 5 GS/s, and a CAEN DT5730B, 8 channel 500 MS/s, were used. Four separate triggers could initiate digitization and readout by the DAQ: a beam trigger, a laser trigger and an Americium trigger from each of the two SM being tested. Fig. 6.8 describes the trigger scheme and its configuration. In the data stream also temperatures from SiPM and environment were acquired.

Offline data analysis framework

Offline data analysis hase been performed using the *ROOT* framework developed at CERN [134].

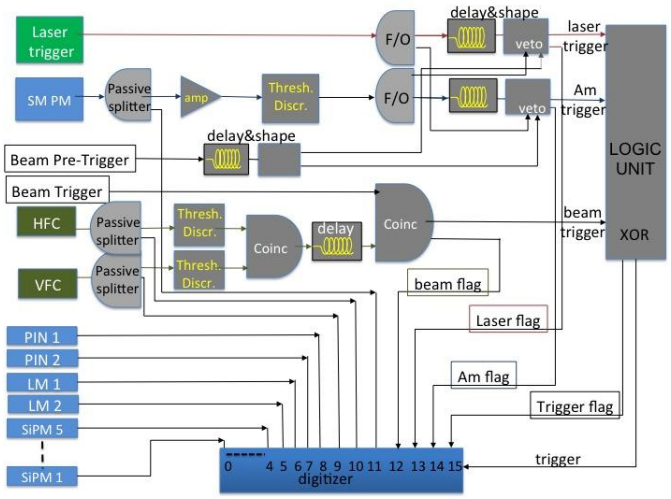

Figure 6.8: A scheme of the trigger used for the test beam.

6.1.2 Experimental setup at SLAC beam Facility

The ESTB facility at SLAC provides a well-collimated beam of electrons at a typical rate of 5-10 s^{-1} . In each precisely timed beam pulse, a Poisson distribution of electrons is delivered. When well tuned, the single-electron beam pulses will be most likely, with the probability of 37%. The Accelerator was also running in a two-bunch mode and that gave sets of runs with particles separated by various bucket numbers where bucket numbers are quantized at 350 ps. The beam radial extent when exiting the last vacuum pipe is expected to be ≈ 1-2 mm and its position is stable, thus avoiding the need for external wire chambers or start counters. Energies from 2 to 5 GeV were used in evaluating the performance of the calorimeter system. At each setting the beam energy was known to about 10% and stable to better than 1%.

An overview of the experiment setup is shown in Fig. 6.9. The calorimeter system is located inside the tunnel, the Laser System is located just outside of it and the DAQ backend and analysis machines are located in the control room several floors above the tunnel. Detailed description of each sub-system

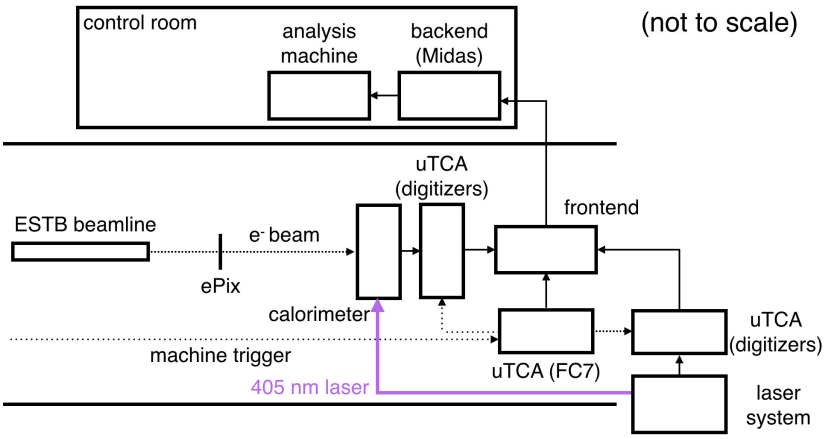

Figure 6.9: Overview of the experimental setup at SLAC. Electron beam from the ESTB beamline is moving from the left to right before hitting the calorimeter. The SiPM pulses resulting from the EM shower are digitized and then processed by the frontend and backend machines to be ready for data analysis.

is given in the subsequent sections.

Calorimeter

The Muon $g-2$ calorimeter is consisted of fifty four $25 \times 25 \times 140$ mm 3 SICCAS [151] PbF2 Cherenkov crystals in a 9×6 array, with each crystal readout by a 12×12 mm 2 Hamamatsu MPPC [152] (SiPM) glued onto it on the rear face. Detailed descriptions of the PbF 2 and SiPMs used here can be found in [140, 154]. The bias supplies of the SiPMs are provided by commercial BK Precision 9124 and the low voltage supplies for the electronics on the SiPM pre-amplifer boards are given by TE HY3003-3 DC power supply. The SiPM pre-amplifer boards are controlled using HDMI cables that connect each to a breakout board mounted within the box service compartment. The boards distribute the bias voltage levels and route the communication information which is controlled by an on-board BeagleBone computer. The housing around

Figure 6.10: Calorimeter sitting on top of the table at SLAC. The electron beam is coming from the long tube is heading towards here.

the crystal SiPM ends is cooled from the bottom by air fans and a duct-work corridor internal to the box. Signals from the SiPMs are connected using pentapus cables to the waveform digitizers. Subsequent connections are discussed in the next sub-Section. Pictures of the setup are shown in Fig. 6.10.

Laser Calibration System

The Laser System setup, togheter with laser source and laser control, was the same used in the test beam at Frascati and with only one SM configured with a mixing chamber used instead of the integrating sphere. For details see previous Fig. 6.5.

DAQ system

The Data acquisition system (DAQ) was a small-scale prototype of the data acquisition designed for the Muon $g-2$ experiment, reported in Chapters 4

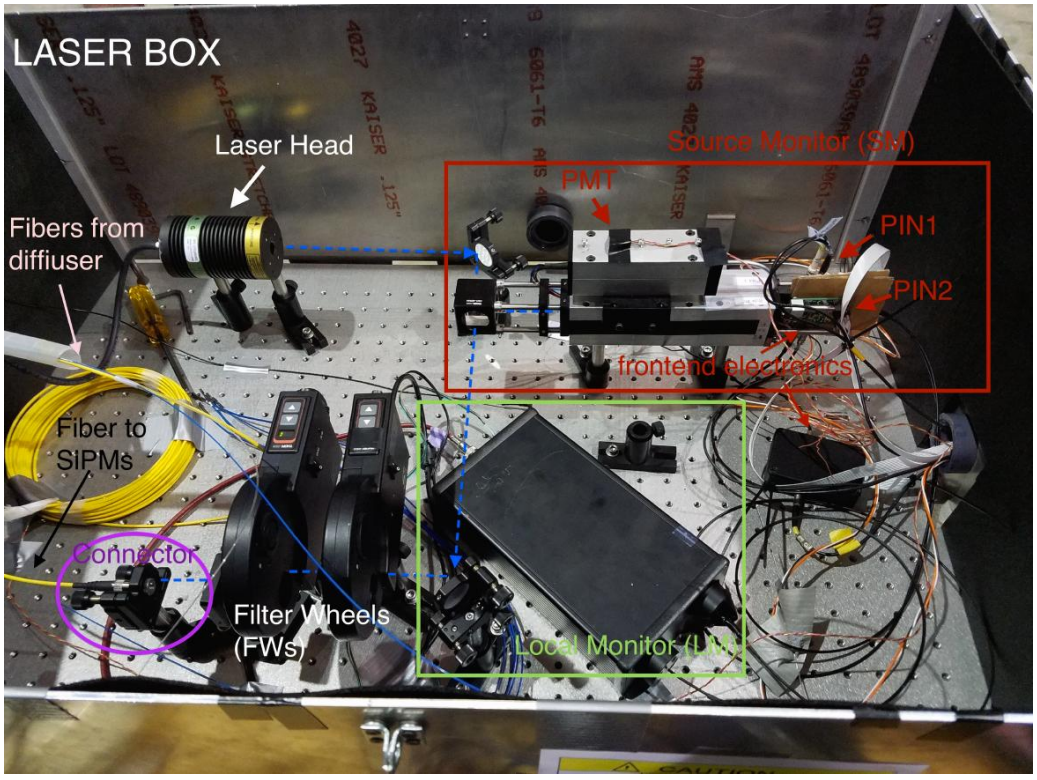

Figure 6.11: The Laser System setup used al SLAC: Laser head with 2 filter wheels, source monitor, optical fibers for sending the calibration pulses to the calorimeter and back to local monitor.

and 5. The system permitted the acquisition of deadtime-free, 700 microseconds (μs) duration, continuously digitized waveforms from the electromagnetic calorimeter and the Laser System at rates of roughly 10 Hz (thus mimicking the "fill" structure of the Muon $g-2$ experiment).

The SiPM signals were digitized using custom μTCA AMCs built at Cornell University [126], shown in Chapter 4.

The acquisition software was based on the *MIDAS* [133] data acquisition framework developed at PSI and TRIUMF and reported in Chapters 4 and 5.

Also a first prototype of the INFN laser DAQ monitoring system, described in previus Chapter 5, was tested.

Offline data analysis framework

Offline data analysis was performed using the art-based framework developed at Fermilab [136]. It handles the raw data coming from *MIDAS* DAQ and converts them into useful information for data analysis. In Fig. 6.12, the raw data stored in *MIDAS*-format file are decoded into decimals and are stored as branches in a art file, which is very similar to a *ROOT* [134] file. Then the pulses are fitted to extract pulse integrals, timings and pedestals. The fit results are calibrated and the gain corrections are applied using laser response of the crystals. Then we apply clustering algorithm to cluster the crystal hits to form a physics object.

Also was needed to combine informations from Riders and the INFN DAQ tested systems, developing a custom *ROOT*-framework based software shown in Fig. 6.13 and in Fig. 6.14, able to collect and compare data, from WFDs as well as from Source Monitor and temperature INFN monitoring system.

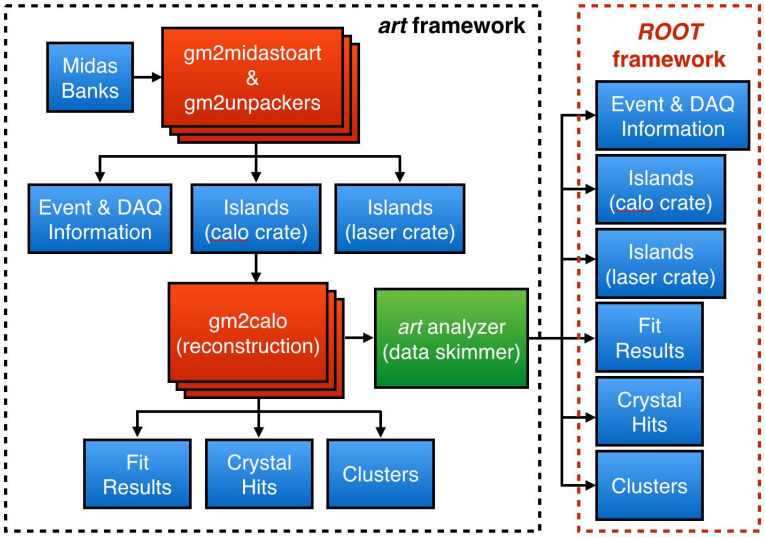

Figure 6.12: art-based offline data analysis framework. The raw data is first converted to decimals using *gm2midastoart* and *gm2unpackers* packages in the *art*-framework. Subsequent data processing is done using the *gm2calo* package. A data skimmer is implemented to provide simplified data file to the users.

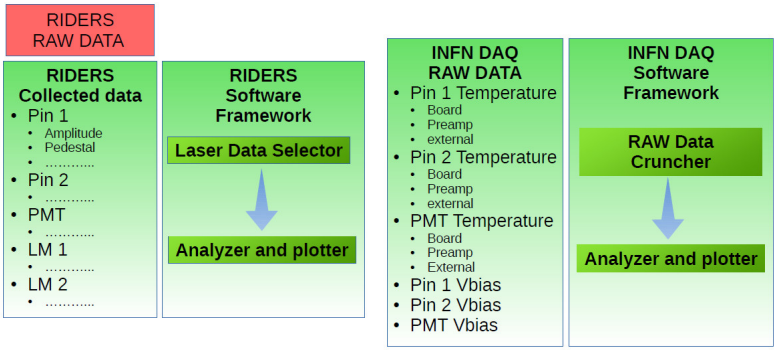

Figure 6.13: Second level offline data analysis art-framework and INFN DAQ data processing and analysis framework, both based on *ROOT*-framework.

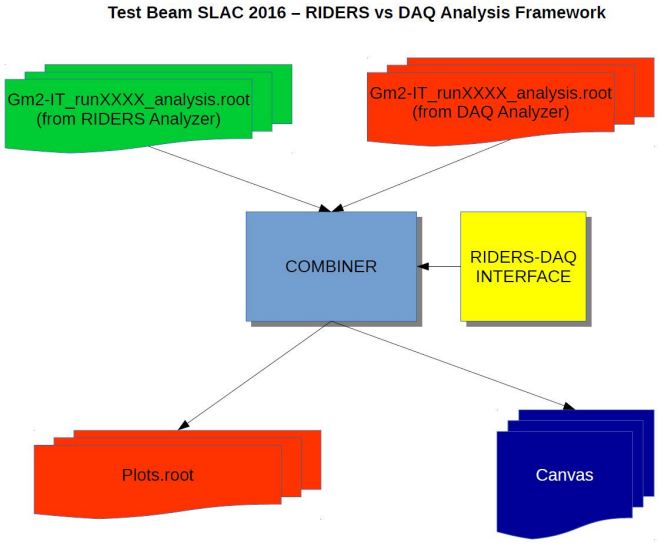

Figure 6.14: Third level offline data analysis framework based on *ROOT*-framework, analyze both informations from WFDs and INFN DAQ.

6.1.3 Results

Pulse fitting and event reconstruction

Before any other trace processing is need to extract the pulse-integral (pulse area) and hit time from a digitized trace. We used a pulse-fitter algorithm. The pulse-integral is an effective measure of the number of pixels fired. The pulse-fitter used in these tests was based on custom pulse templates, for each individual SiPM, to be robust against small fluctuations in pulse shape.

Data-driven templates (also known in literature as "system functions") were built by averaging more than 10,000 digitizer traces and interpolating between digitized samples within a trace using a cubic spline. Templates $T(t')$ were normalized such that $\int T(t')\,dt' = 1$, and aligned in the time domain so that $t' = 0$ corresponds to the pulse maximum, which was interpolated by a parabolic curve across 3 samples—the peak sample and its two neighbors. We have constructed templates for the electron beam and also for the laser beam

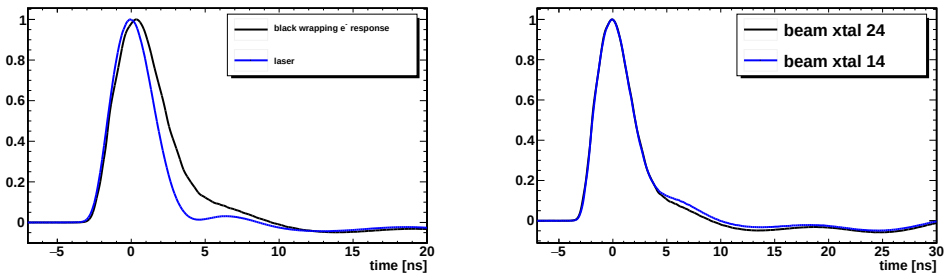

(a) (b)

Figure 6.15: (a) The figure shows an evident difference between the pulse shape originated by an electron (black line) and the pulse originated by a laser pulse (blue line). (b) The figure shows that a small difference in the pulse shape exists also between different crystals, so it is important to build different templates for different crystals.

as shown in Fig. 6.15.

The function used for fitting traces was of the following form:

$$f(t) = s \cdot T(t - t_0) + P \quad . \tag{6.1}$$

The three free parameters of this fit are an overall scale factor (s), the peak time (t_0) and the pedestal (P). Finally, the pulse-integral is extracted as s. The eigen [153] linear algebra library is utilized in the fitting process for its computing performance. This procedure allowed for pulse processing at a rate of approximately 65,000 pulses per second per cpu, which exceeds the expected data rate for a single calorimeter in the $g-2$ experiment.

Template fit χ^2 minimization for n pulses is given by

$$\chi^2 = \sum_{i=0}^{m} \sigma_i^{-2} \left(D_i - \sum_{j=0}^{n} s_j T(t_i - t_{0,j}) - P \right)^2 . \tag{6.2}$$

Here, σ is the uncertainty on sample i, D_i the digitizer sample i, s_j the scale of pulse j, t_i the time of sample i, $t_{0,j}$ the time of pulse j, P the pedestal (baseline), m the number of samples and n the number of pulses.

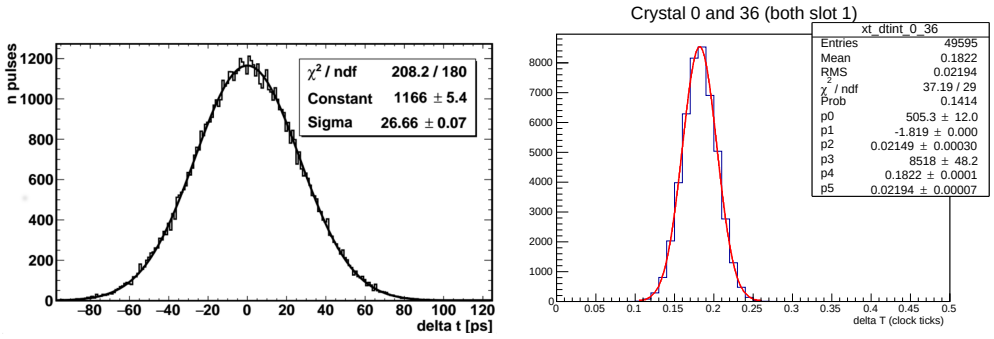

(a) (b)

Figure 6.16: Time difference in ps for two SiPMs each illuminated from the same laser shot. (a) previous test [154]. (b) 2016 SLAC test beam. Two results are comparable.

Timing resolution

Given the stable pulse shape and accurate template fitting procedure, the timing resolution, in picoseconds (ps), can be deduced from either the laser or beam events. The controlled response with the laser is more straightforward because nearly equal amplitude light pulses are injected simultaneously into all crystals. The difference between the fitted time of two SiPMs recorded within the same digitizer module is shown in Fig. 6.16. The width implies that the individual channels have a timing resolution of ∼26 ps / $\sqrt{2}$ ≈18 ps.

In order to identify the cluster produced by the electrons as they hit the calorimeter we can look at the hit times and sum together the energy of those pulses whose hit time differ by ∼1 ns from that of the highest-energy crystal.

Time reference and synchronization with Laser System

At the beginning of each trigger, a laser pulse (sync pulse) in each channel was fired for timing alignment purpose. The time difference plot, of 2 clock ticks, for crystals 40 and 39 is shown in Fig. 6.17. This peak is exactly 2 clock ticks (1 clock tick = 1.25 ns). Because the master TTC clock runs at 40 MHz

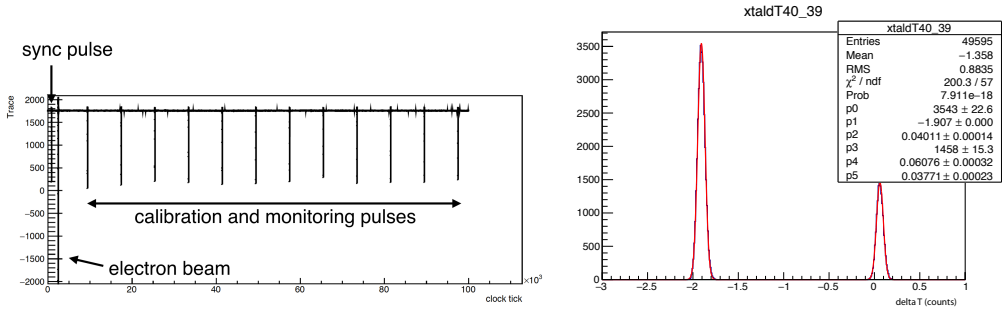

(a) (b)

Figure 6.17: (a) Event topology at SLAC: A laser sync pulse, in each channel, was fired for timing alignment purpose. (b) The time difference plot for crystals 40 and 39 for the same sync laser pulse, where peak is exactly 2 clock ticks.

while the digitizers are running at 800 MHz, there can be small differences in the exact digitizer clock tick on which a given ADC will begin digitizing. That demonstrates the importance of Laser System for time synchronization in the E989 experiment.

Calibration of the digitized signal to photoelectrons

Calibration tests were taken to investigate all the functionality of the laser calibration system and also measured the equivalence between the ADC counts of the SiPM and the number of photelectrons. To ensure a uniform response across calorimeters used during tests, the SiPM gains was equalized as well as possible. The equalization process is iterative and consists of alternating laser calibrations and adjustments to the gains and bias voltages. After several iterations, equalization on the level of 10% was achieved. Calibration runs consisted in a series of consecutive run with 6 different setting of the filter wheel and performed after every change in the setup configuration and before every electron run. About five thousand events per run were taken at a frequency of 50 Hz taking only some minutes per run [141]. For each setting it was measured

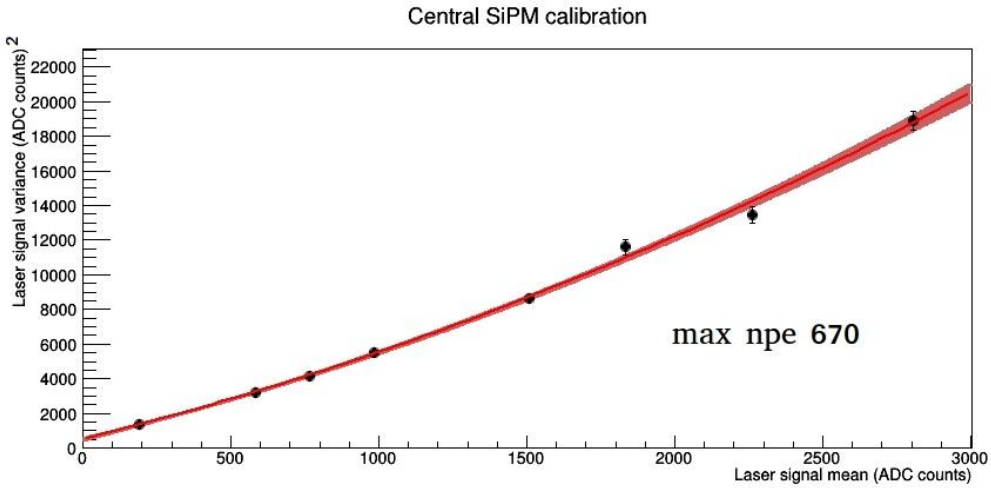

Figure 6.18: Calibration signal of a SiPM width with fitted curve.

the mean μ and the standard deviations σ of the distribution of each of the five SiPM used. In general the signal L observed by each SiPM is given by $L = k\nu$, where k is the proportionality constant and ν is the number of pixels fired. The width of the signal L is given mainly by three main contributions: 1) the electronic noise σ_N, 2) the Poisson statistics of the pixel fired $\sigma_P = k\sqrt{\nu}$, 3) the intrinsic laser pulse fluctuations $\sigma_L = \alpha k\nu$, where α is the average relative laser intensity variation, which has been measured to be less than 1%. Other factors contributes to L proportionally that come from the statistical variation in the number of photons incident on the SiPM photocatodes and from fluctuations in the amplification mechanism. Based on this model and assuming statistical independence of the sources of fluctuation, can be obtained the dependence of σ^2 as a function of the measured light intensity

$$\sigma^2 = \sigma_N^2 + kL + \beta L^2 \tag{6.3}$$

where the factor β includes all the contributions proportional to L. In Fig. 6.18 is shown a typical fit of the variance versus signal strength [141].

Values measured were between 600 and 800 fired pixels, depending on SiPM, bias voltage and SiPM temperatures, in open position of the filter wheel. Considering the total number of pixels of a single SiPM of ~ 57600 these values are about 1% of the total [140], applying a correction about saturation of the order of 0.05%, which are negligible for these calibration results.

Calibration of the light yield to electron energy

In the electron runs the laser was also pulsed at the same rate of the electron beam, at 50 Hz. This was done in order to exercise both Source and Local monitors, providing a reference to stabilize the SiPM response over the time needed to complete the data taking. In the test at Frascati the calorimeter response was calculated as the sum of all the SiPMs normalized to response of the central one after correcting for the laser calibrations. This was guided by the fact that the beam is strongly focused on the central crystal, which receives $\geq 90\%$ of the beam energy and because the light transmitted to the dummy diagonal mock crystals is expected to be very small.

In the test at SLAC, with the full size, 54 crystals, calorimeter prototype, the energy distribution for single electron beam across the calorimeter was compared with the MC simulation. The recorded energy distribution is shown in Fig. 6.19. On average, the central crystal has 85% of the total energy.

Fig. 6.20 shows the calorimeter response, at Frascati BTF, with the single and multiple electron spill; the fit is performed with a sum of Gaussian distributions for the different electron peaks where the means are assumed to be linearly related to the number of electrons and the widths with their square root. The assumption on the widths is based on Poisson statistics of the number of fired pixels and on a contribution from the beam energy spread. The fit is typically well behaved and returns the mean value of the single electron peak

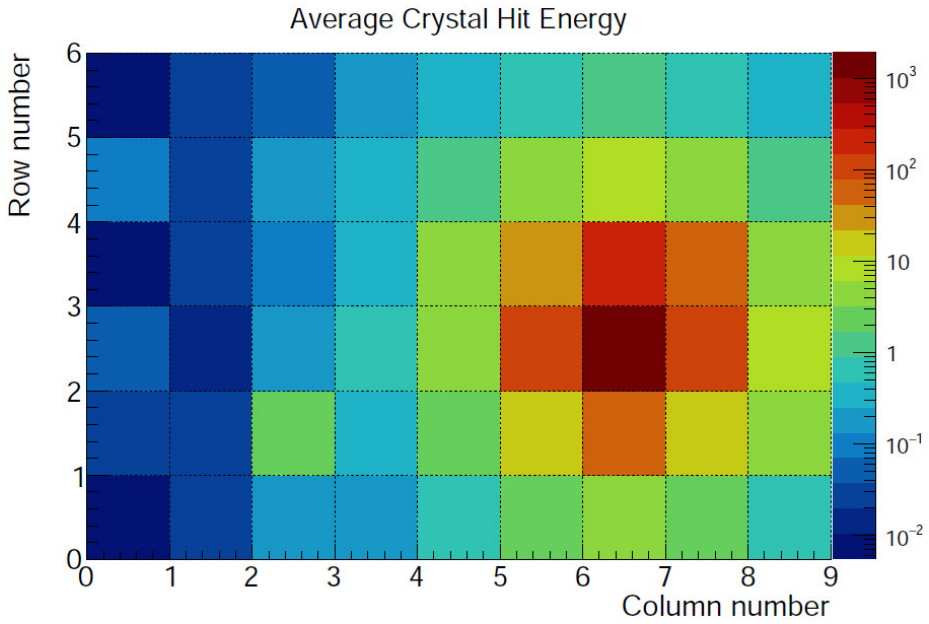

Figure 6.19: Distribution of the energy of a 3 GeV electron beam across the whole 54 crystals calorimeter.

in ADC counts. Dividing this value by the value obtained by the calibrations and by the beam energy the results is the average number of photoelectrons (p.e.)/MeV; the result is 0.9 p.e./MeV for the black wrapping which is consistent with the result presented in [140] and also confirmed in the 2016 test beam at SLAC, see Fig. 6.21, that shows the linearity of calorimeter at various beam energy, plotting fits of the reconstructed energy spectrum with a Gaussian function, for the corresponding electron beam energy varing from 2.5 to 5 GeV. The energy resolution achived was 3% at 2 GeV, less than 5% of that required for the experiment [107].

Luminous energy of the laser

Using the open position of the filter wheel it is possible take advance from the emitted laser energy to simulate positron events, providing to relate this

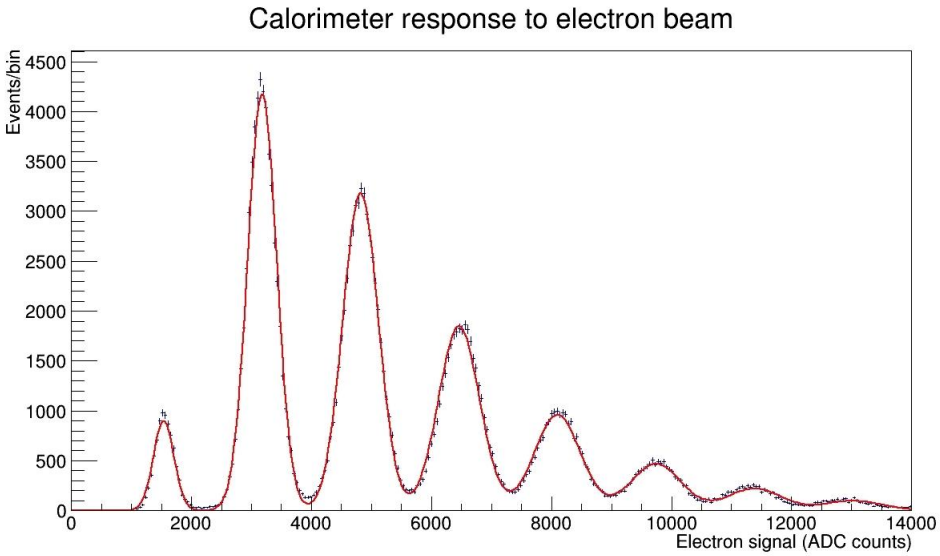

Figure 6.20: Calorimeter response showing single and multiple electron peaks, together with fitted curve.

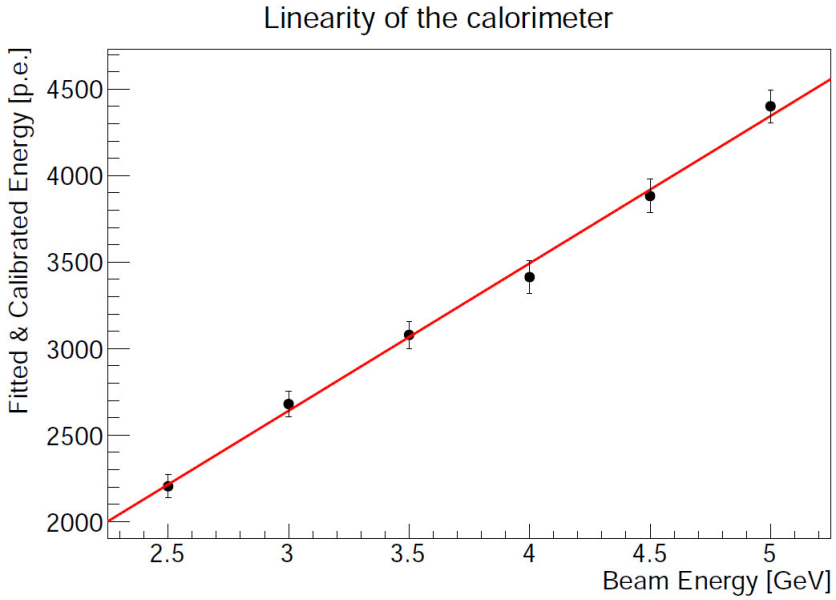

Figure 6.21: Linearity of the calorimeter.

value to the beam energy and the single electron mean. During test beams values obtained are around 800 MeV, which corresponds to a measured light power before the filter wheel of 11.2±1.1 pJ. This value can be scaled to the laser power predicted in the final full calorimeter system, expected to be 141 pJ before the filter wheel. With this value the equivalent maximum energy seen by the calorimeter would be 800 MeV × 141/11.2 pJ ∼ 10 GeV . This calculation assumes an initial laser power of 1 nJ but, since the manufacturer of our laser heads guarantees a maximum power between 0.6 and 1.0 nJ, this prediction should be scaled with the maximum power available in the practice. In any case this light yield is well matched to the 3.1 GeV maximum electron energy expected in the calorimeter from muon decays in the muon g−2 experiment.

Stability, monitoring and corrections

One of the task of the test beams is to measure the stability of the monitoring system developed for the experiment. In fact the energy of the electron incident on the calorimeter recorded by the SiPMs is expected to be affected by source of fluctuations; mainly temperature variations and also small bias voltage and SiPM responce variations. Only by monitoring these variations through the response of the SiPMs to the laser pulses during data taking it is possible to provide the necessary corrections thanks to the right accuracy of the monitoring system. In mathematical term the response of a SiPM to the electron beam during time is given by

$$r_{el}^{SiPM}(t) = R_{el}^{SiPM} \times f_{gain}^{SiPM}(t), \tag{6.4}$$

where R_{el}^{SiPM} is the SiPM response assuming a constant gain starting at time t = 0 and $f_{gain}^{SiPM}(t)$ are the time-dependent fluctuation in the SiPM's

gain. The corresponding response to the laser pulses is given by

$$r_{laser}^{SiPM}(t) = R_{laser}^{SiPM}(t) \times f_{gain}^{SiPM}(t), \tag{6.5}$$

where $R_{laser}^{SiPM}(t)$ is the laser light received by the SiPM and is due by:

$$R_{laser}^{SiPM}(t) = R_{laser}^{SiPM}(t=0) \times f_{laser}(t) \times f_{distr-chain}(t), \tag{6.6}$$

where $f_{laser}(t)$ and $f_{distr-chain}$ are determined respectively by the Source and Local Monitors. Therefore the corrected electron beam signal for a given time is:

$$R_{el}^{SiPM} = \frac{r_{el}^{SiPM}(t)}{f_{gain}^{SiPM}(t)} = r_{el}^{SiPM}(t) \times \frac{R_{laser}^{SiPM}(t=0) \times f_{laser}(t) \times f_{distr-chain}(t)}{r_{laser}^{SiPM}(t)}, \tag{6.7}$$

The result of the correction procedure used in the test beam at Frascati is shown in Fig. 6.22 where the variations, relative to the first point, in the raw electron data after four continuously running hours are shown before, with a positive drift of about 1.2%, and after correction (see Fig. 6.22 description for details) [141]. The corrected electron data correspond to the temperature dependent raw electron data, in anti-correlation with SiPM tempearature blue line, divided by the corresponding laser data after correction for laser intensity and light distribution stability. Each data points represent data averaged over approximately 23 minutes of running.

All these variations taken into account for corrections are shown inf Fig. 6.23, together with the environmental temperature recorded during the data-taking period.

The source monitor PiDs measured a variation of 0.2%. These data monitor laser stability with an accuracy of 0.003% per point (23 minutes of data taking, corresponding to $\sim$ 26000 events). Given the large number of photoelectrons generated in each PiD (almost 10^6/pulse) the expected statistical uncertainty

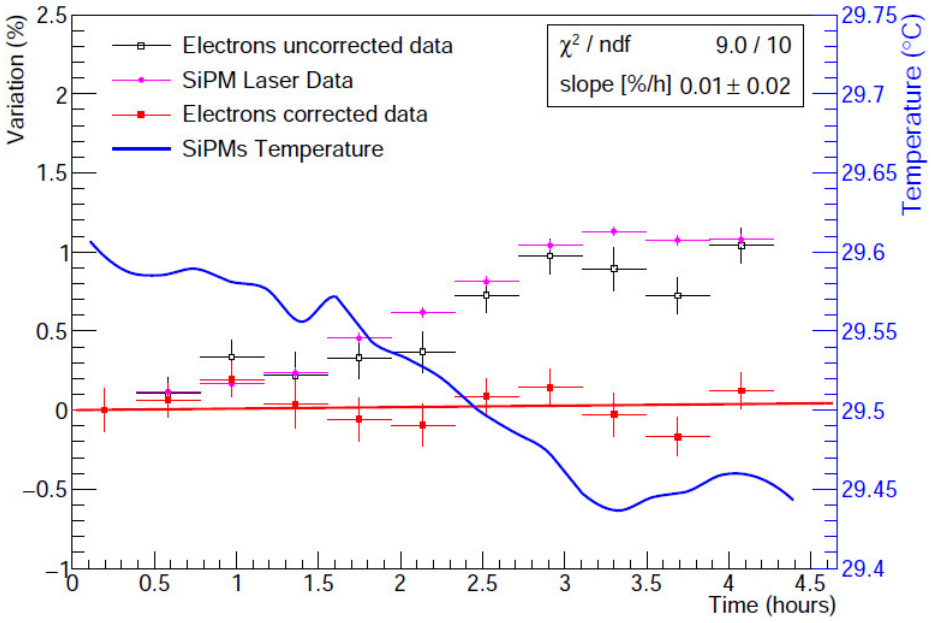

Figure 6.22: Variations in the measured energy of the electron beam and of the laser signals during four hours of data acquisition. The black (magenta) open circles show the gain fluctuations in the raw electron (laser) data while the full-red circles are the same data after the laser-based calibration correction has been applied. The SiPM temperatures recorded during the same period are represented by the blue line.

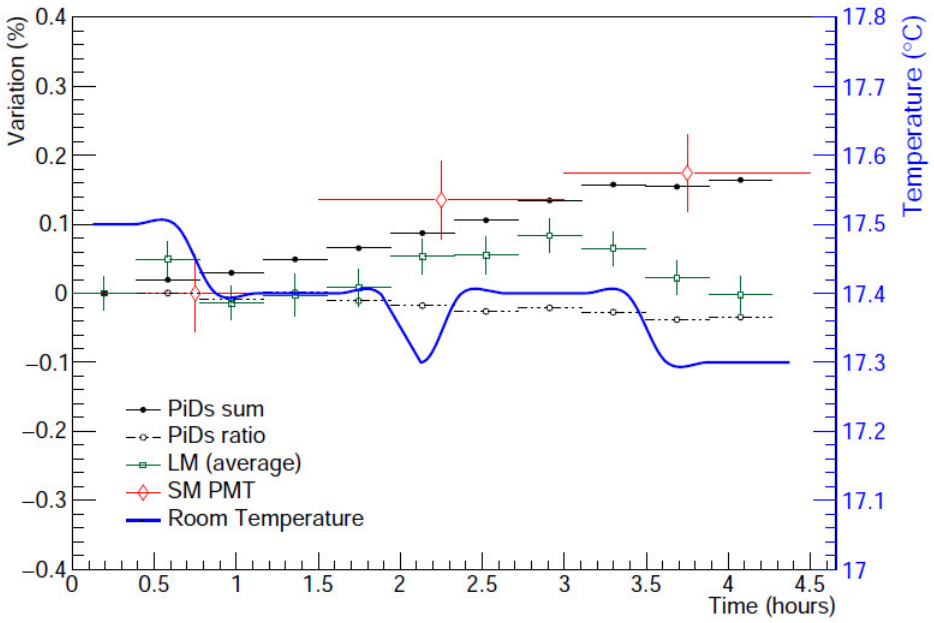

Figure 6.23: Stability of the laser calibration system. Solid black circles show the variations in the laser intensity as measured by the Source Monitor (SM) whereas the open squares represent the fluctuations in the laser light after distribution as recorded by the Local Monitor (LM). The red diamonds are the corrected SM PMT data. The ratio between the two PiDs of the SM is also shown (black open squares). The environmental temperature recorded during the same period is shown by the blue line.

per pulse is $< 0.1\%$ per pulse or 0.0006% for the 26000 pulses collected. The much larger statistical error observed indicates that it is most likely driven by the noise introduced by the prototype of the shaping amplifier used. This result is improved using the final version of the dedicated electronic used in the experiment.

Since environment temperatures variations were small, in Fig. 6.23 a large effect on PiD is not expected, on the basis of the temperature dependence (0.1%°C at 400 nm) [148, 141]. The variation of the PiD response reported in 6.22 reflected true variations of the laser intensity. Therefore the ratio between PMT and PiDs sum shows the gain fluctuations of the PMT. The fluctuation registered was about $\sim$0.3%, as shown in Fig. 6.24. Given the very low activity of the Am-source incorporated in the pulser, a more accurate comparison requires longer periods of data-taking and those were not available during the test-beams.

The same result was confirmed at SLAC for 54 crystals calorimeter prototipe, see Fig. 6.25, where the variations and corrections are reported in photoelectrons.

Preliminary tests on INFN DAQ monitoring system

At SLAC was also tested the performance of the INFN custom monitoryng DAQ system. it was possible to have a good separation of the asyncronous Am-241 signal from laser pulses, as shown in Fig. 6.26. Moreover the source monitor's signal acquired from INFN DAQ by the integration of laser pulses, in different mode respect to WFD system, resulted in optimal agreement with the Riders signal, as shown in Fig. 6.27.

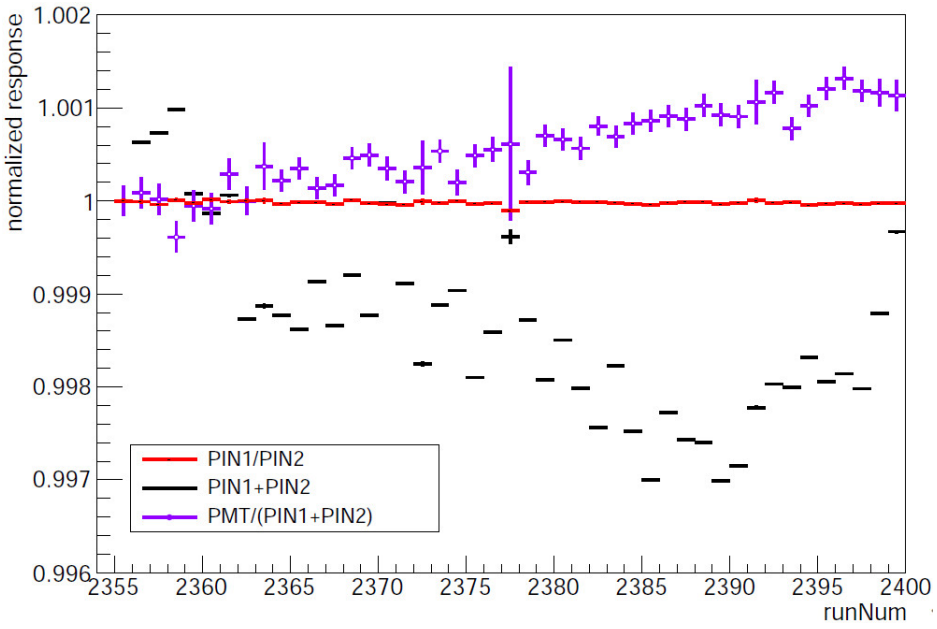

Figure 6.24: Stability of the laser registerd by the Source Monitor. The ratio between PMT and PiDs sum shows the gain fluctuations of the PMT.

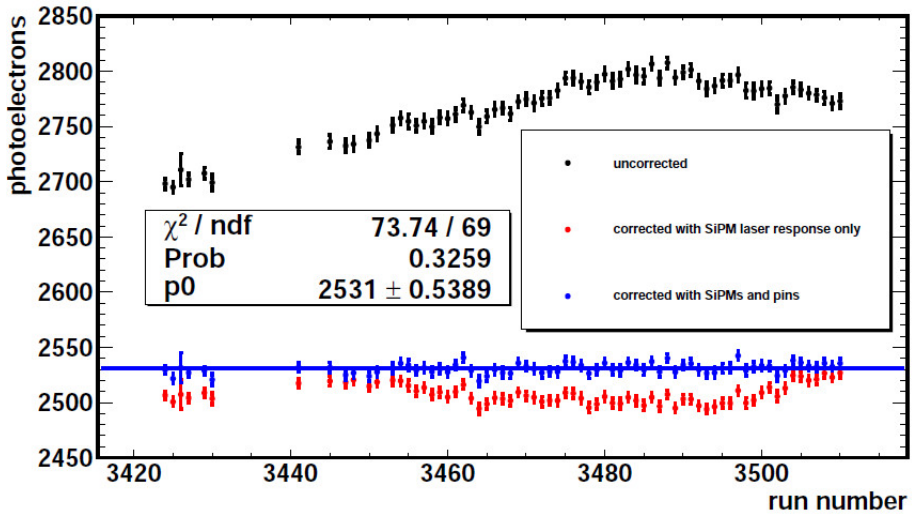

Figure 6.25: Stability of the energy scale and laser correction at SLAC.

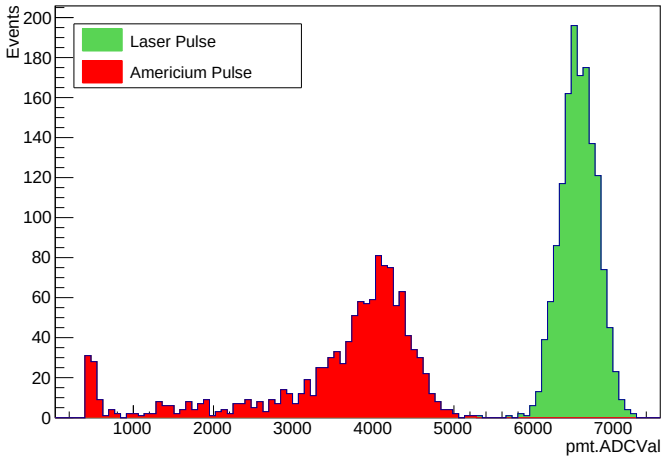

Figure 6.26: The INFN monitoring system, tested at SLAC, can also identify at the same time the sincronous signals and the 241-Am source signal of the Source Monitor system.

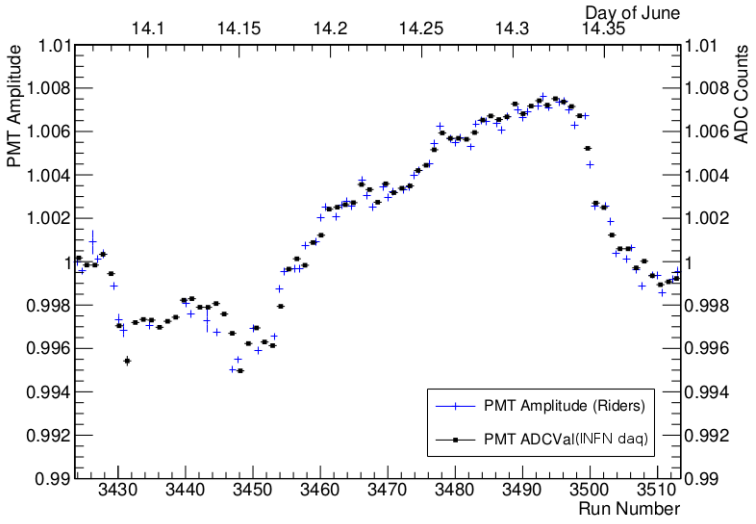

Figure 6.27: Comparision in time of Source Monitor signals at SLAC: The one acquired in a different mode, by the integration of laser pulses, from INFN monitoring system and the other digitized by WFD are in perfect accord.

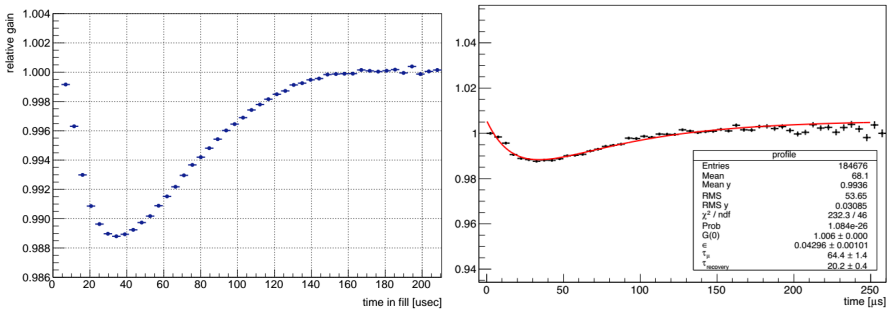

(a) (b)

Figure 6.28: Average gain as a function of time. (a) Previous test with initial rate of 2.1 MHz, 1500 photoelectrons (n.p.e.) pulses [154]. (b) Test at SLAC, 96 average number of pulses and each of them has an energy of 1100 n.p.e. The rate of the flight simulator is proportional to $e^{-\frac{t}{\tau}}$ with time constant $\tau = 64$ μs. The integrated current drawn is higher by a factor of 10 than that we expect in the Muon $g-2$ experiment, for the hottest crystal.

Study of the short term gain drift

During the test beam physics event simulation with laser pulses fired into the calorimeter has been tested. This has been achieved using the Laser Control Board in "flight simulator" mode (see Chapter 5), triggering the laser according to the exponentially decreasing time function, $e^{-t/\tau}$, as expected in the experiment due to muon decay. The slight droop and subsequent recovery of the gain (see Fig. 6.28), observed in previous tests [154] is due by a combination of the bias voltage supply and the buffer capacitance.

In order to measure experimentally any rate-dependent we analyzed the correlation between the charge and the hit time within the fill using the data collected with two different configuration of the filter wheel: one with no attenuation of the laser intensity and one with an attenuation of the 65%. In Fig. 6.28 the saturation effect in the gain followed by a recovery process be-

comes evident. The profile was fitted according to the function

$$G(t) = A - \epsilon \left(e^{-t/\tau_\mu} - e^{-t/\tau_r}\right), \tag{6.8}$$

A, a, τ_μ and τ_r being the free parameters determined by the fit. In this situation the average number of pulses produced by the simulator is 96 and each of them has an energy of 1100 number of photoelectrons (n.p.e).

In the experiment the positron energy follows the Michel distribution described in Eg. 4.13 whose mean value is around 250 MeV. Using the conversion factor calculated from the Frascati test beam, i.e.$\approx 0.86\ \frac{n.p.e.}{MeV}$, corresponding to ≈210 n.p.e and, assuming linear scaling along with some numbers from simulation, we can extrapolate the expected average gain drop for a full calorimeter. Considering:

- Total flight simulator n.p.e delivered per pulse: 80000;
- Average number of flight simulator pulses per fill: 96;
- Full calorimeter acceptance ($E > 100$MeV) $\epsilon = 0.0191$ and number of stored muons per fill ≈16000;
- Average deposited energy per decay: 250 MeV,

we can calculate the gain drop as:

$$1.5\% \frac{250 \frac{MeV}{pulse} \cdot 0.86 \frac{MeV}{n.p.e} \cdot 300\ positrons}{80000 \frac{n.p.e}{pulse} \cdot 96\ pulses} \approx 10^{-4}, \tag{6.9}$$

where 1.5% is the drop obtained from the configuration shown in Fig. 6.28b while the average number of positrons hitting one calorimeter per fill is obtained by multiplying the number of stored muons by the full calorimeter acceptance. However, since the calorimeter is segmented into 54 parts, the crystals placed closer to the muon storage region presents the biggest rate and

as a consequence will experience a bigger drop effect than the one expected on average.

Knowledge of the full gain curve has been made at sub-per-mille precision, using a custom laser calibration system, as described over in this Chapter and Chapter 8.

Finally consideration on test beams

In the test beams at BTF and SLAC the electron-energy equivalent of the laser intensity was measured and it was found that up to 10 GeV of equivalent energy could be delivered to every single calorimeter cell. This measurement establishes that six lasers will be sufficient to calibrate all the 24 calorimeters in the E989 experiment. It was also verified that the system is presently able to monitor and correct for laser intensity variations at the 10^{-4} level with less than 1000 laser pulses. Variations in the distribution chain can be corrected by the LM at the same level on a longer timescale.

6.2 Calibration procedures with Laser System at Fermilab

The Laser System provides "correction functions" which are applied at different time scales as shown in Tab. 8.1.

The laser corrections are applied to the SiPM data during the reconstruction fase of pulses due to positrons that hits calorimeterrs in the muon fill period. In the following sub sections these procedures are described. A diagram of all calibration stages is shown in Fig. 6.29 and a timing scheme of laser pulses pattern, in and out of the muon fill, is shown in Fig. 6.30.

Time scale	Calibration method	Notes
∼20 ns	Short Term Double Pulse	check of SiPM recovery
∼20 μs	Long Term Double Pulse	check of In Fill Gain Function
<700 μs	In Fill pulses	mostly corrects gain function for "splash"
>10 s	Out of Fill pulses	mostly corrects temperature variations

Table 6.1: Summary of laser methods applied for the calorimeters signals gain corrections.

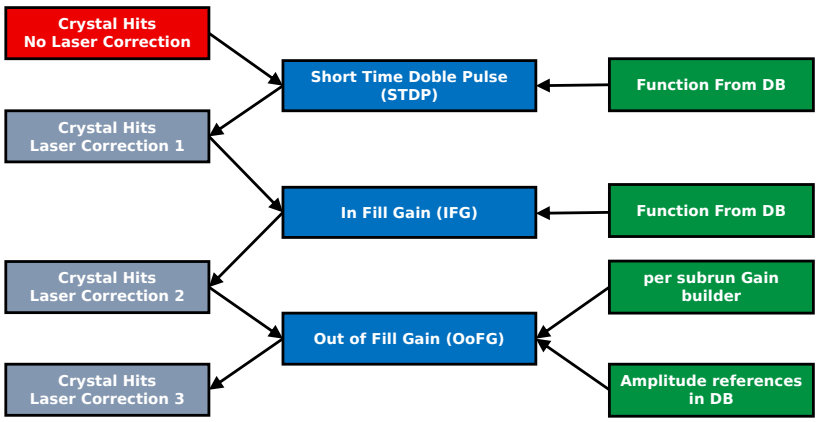

Figure 6.29: The sequence of laser corrections as applied to the reconstructed SiPM pulses. All of these corrections must be performed before the clustering stage of the data processing.

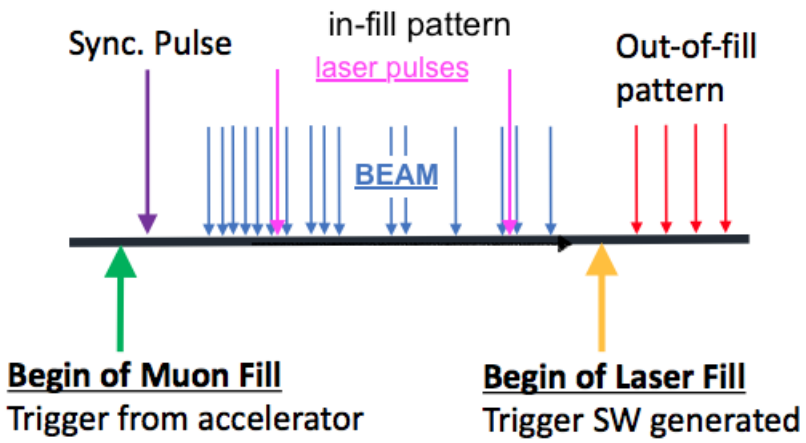

Figure 6.30: The laser pulses timing schema. the muon fill (In Fill) and Out of Fill patterns are shown.

The effects, of the laser corrections, on the ω_a determination are descibed in the Chapter 8.

6.2.1 Double pulse investigation

Short Term Double Pulse

In a SiPM the product of the pixel capacitance, 55.8 fF, and the value of the quenching resistor, 100 kΩ, sets the expected timing constant for the charge recovery of about ∼6 ns, after photons detection. Previous test has been performed to verify the charge recovery model and better understand the details of the charge recovery mechanism [154]. The results of this gain study indicated two components of the intrinsic SiPM gain recovery time response. A representative fit is shown in Fig. 6.31 where the faster component can to be compared with the expected value of ∼6 ns. The slower component (∼30 ns) is typically attributed to the bulk properties of the SiPM chip. The measured gain recovery allows us to correctly separate pileup events in the

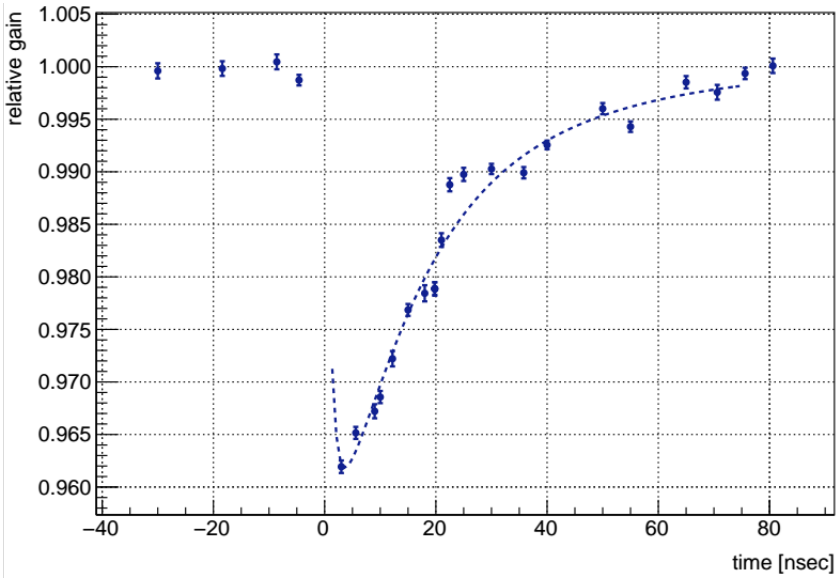

Figure 6.31: SiPM gain recovery at very short time: Relative gain of the laser pulse with respect to the reference LED pulse versus a fixed time interval between the two pulses [154].

energy domain. So the predictive drop measured can be used to correct the gains of trailing pulses in the reconstruction phase.

The effect of SiPM gain recovery at very short time scale (∼20 ns) has been also measured at Fermialb, therefore, the first correction applied to positron pulses, with the Laser Calibration System, uses the short-time double pulse (STDP) procedure. The SiPM pulse energies are corrected with the STDP model, an effect that occurs when a second pulse occurs within 60 ns or so of the previous pulse. The charge depleted in the first pulse causes a gain drop in the amplitude of the second pulse. the STPD procedure uses the Double Pulse System described in the Chapter 5. Through a set of movable and fixed mirrors, the light of laser 2 is directed into the light path of laser 1 and viceversa (see Double Pulse System schema of Fig. 5.6), testing a very Short Term time scale (∼20 ns). The even and odd subsets are completely exchanged to create the complement measurement on the opposite calorimeter

system. The delay between the triggers is controlled using a SRS DG645 [147] delay generator device.

Long Term Double Pulse

The slight droop and subsequent recovery of the gain explored during the last test beam (see Fig. 6.28) is due by a combination of the bias voltage supply and the buffer capacitance [154]. An independent check of the reconstructed energies function with time, due to the muon "splash" that occours at early time after beam injection, can be performed with the Long Term ($\sim$20 μs) Double Pulse procedure (LTDP), using the Double Pulse System described in the Chapter 5.

An initial burst mimics the muon "splash". A test pulse is sent after tens of μs. This technique allows to validate the measurements of positrons pulses in the muon fill, in a controlled environment (see next sub Section).

6.2.2 Short term (In Fill) gain calibration

The second correction applied to positron pulses is the in-fill gain (IFG) function. The function is built using laser pulses intermixed with the positron data in a subset of events in standard data-taking. The function is subsequently modeled and applied to the positrons in the dataset which was used to build the model. With this method sending a regular path of laser pulses, once every 11 fills, and evaluating the SiPM response stability using 3 pulses per fill, separated by 200 μs with a shift pattern of 2.5 μs, each subsequent fill, we obtain gain function for first 600 μs after muons injection. The laser pulses pattern schema of IFG method is shown in Fig 6.32.

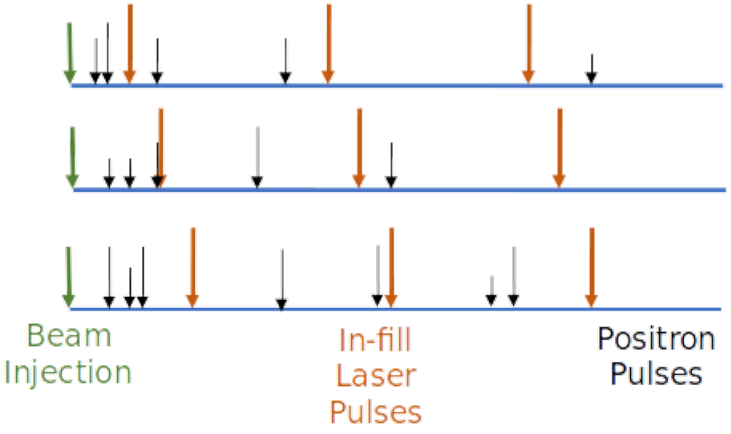

Figure 6.32: The laser pulses timing schema for the In Fill gain calibration.

6.2.3 Long Term (Out of Fill) gain calibration

After the IFG correction, the overall gain of the system receives the out-of-fill gain (OoFG) correction. The OoFG correction is realized by laser pulses occurring in the time between positron fills. The pulses are needed in order to monitor the long-time drift of the calorimetry system. The drift mostly occurs due to temperature affects in the electronics.

The out-of-fill gain correction procedures stores the correction constants applied by the next procedures where the in-fill gain pulses are normalized by the average, out-of-fill SiPM pulse amplitude. Each SiPM pulses is also corrected for fluctuations in the laser amplitude using the Source Monitor signal. With gain functions constructed for each crystal in each bunch on a full dataset, the per bunch function is fit and shifted to have a basline of unity. The bunch functions are then combined and the aggregate function is fit to define the in-fill gain parameterization.

Chapter 7

The Slow Control and Monitoring System

7.1 Slow Control System in the E989 experiment

The $g-2$ experiment is a complex system that involves many subsystems for which adequate sensoring and control during normal operation is required. The purpose of the slow controls and its associated data acquisition system is to set and monitor parameters such as voltages, currents, gas flows, temperatures, etc. These tasks are essential for the successful operation of the experiment over many months of data taking. Immediate online feedback allows the monitoring of the quality of the incoming data and opportunities to react to changes. For example, part-per-thousand gain stability for the silicon photomultiplier readout of the electron calorimeter is required to meet the systematic uncertainty budget for ω_a. While the gain stability of these photo-detectors will be monitored at the 10^{-4} level or better via Laser Calibration System, de-

scribed in Chapter 5, immediate feedback on the two parameters (bias voltage and temperature) determining the gain of these devices is achieved via such continuous monitoring. There are many of other cases where such external parameters will be useful in this high precision measurement to establish a full understanding of all systematic uncertainties.

For the setting and read-back of parameters, the slow control system provides sufficient sensors or control units which are either directly integrated into the design of subsystems or come as external devices. Most of these systems is connected to the slow control DAQ via the *MIDAS* Slow Control Bus (MSCB [157]) which is a cost-effective field bus developed at the Paul Scherrer Institute (PSI), Switzerland. This very mature system has been successfully employed in other similar experiments and allows for easy integration into the data acquisition framework *MIDAS* [133]. The slow control DAQ also includes communication interfaces to other external systems like the magnetic and cryogenic controls of the $g-2$ storage ring (iFix [158]) and the Fermilab accelerator (ACNet [159]). Other external devices like the μTCA crates [126] for the readout electronics of the electron calorimeter is interfaced and monitored.

The demand and read-back values for all parameters controlled by the slow control system is stored in a *PostgreSQL* database for easy online access and wherever possible also in the *MIDAS* data stream for later analysis. While a local copy of the database is available for online monitoring and analysis, a full copy is transferred to a Fermilab database server for long-term storage. For efficient use of the read-backs during data taking, user friendly visualization tools is developed in order to easily access the stored database information. Also a web browser based framework is developed to display the large number of different channels monitored by the system.

Preventing unsafe running conditions is required special handling of some

critical detector subsystems. Certain sensors are connected to the experiment's Programmable Logic Controller (PLC) based safety system to provide interlocks, alarms and eventually systems shutdown for such situations (see section 7.1.4).

7.1.1 Software and hardware architecture

The slow control system will comprise a variety of sensors and control units described in more detail in the following section. Some of these systems are be purchased as single units (e.g. power supplies) and interfaced via common standard protocols (e.g. RS232, TCP/IP). Other subsystems are custom-built and required an appropriate slow control interface. Instead, employ the *MIDAS* Slow Control Bus (MSCB [157]) which is a field bus developed at PSI. This system was optimized for the environment of a typical physics experiment and for cost-efficiency (typically $20 per node). In addition, it conveniently integrates into the *MIDAS* data acquisition system which is the basic design choice for the slow control computing infrastructure.

The MSCB is the default choice for all sensors and control units that are custom built for the $g-2$ experiment. The MSCB is based on the RS485 protocol which is similar to RS232 except for employing differential signals for superior noise immunity. RS485 is a multi-drop, half duplex communication standard so that many nodes can be connected to the same bus but only one can send data at a time. A single submaster facilitates the communication between the *MIDAS* host computer and up to 256 individual MSCB nodes. In fact, by employing a layer of repeaters, up to 65,536 nodes can be operated on a single bus with up to a few km long cables. The MSCB requires two signal wires for the differential signal and a ground wire. Three additional lines provide power ($+5\,\mathrm{V}$, $\pm 12\,\mathrm{V}$). The usage of a 10-wire flat ribbon cable

provides four additional digital lines for application specific usage.

The MSCB protocol is byte oriented and uses bit 9 from RS232 for addressing purposes. As this bit usually cannot be switched on and off quickly enough in the UART (universal asynchronous receiver/transmitter) of a PC, simply using RS232-RS485 converters is not sufficient. This can be overcome by employing a submaster on the computer side with a micro-controller to provide the handshake with the PC and enough memory to avoid data loss. In this scheme, bit rates of up to 42 kB/s are sustainable.

The development of the MSCB hardware at PSI had several iterations with increasingly sophisticated units. The latest generation is a general purpose unit, SCS2000 [160], as shown in Fig. 7.1(a) and is successfully employed in the MEG experiment at PSI. The SCS2000 unit has an on-board programmable logic device (CLPD, Xilinx XC2C384 [161]) which communicates with the submaster via the MSCB on one side. On the other end, there are slots for 8 independent MSCB daughter cards which are each accessed by the CLPD via a 2-lane SPI and a parallel 8-bit bus. The available daughter cards come with a multitude of different functionality and are shown in Fig. 7.1(b). The complete set of these daughter cards comprises functions like digital I/O channels, 24-bit ADCs, DACs, current sources, valve controls, and many more. Each SCS2000 unit can carry daughter cards of different functionality so that it is possible to fill up each unit to meet the various applications for $g-2$ experiment. Because the MSCB protocol and communication is handled by the central programmable logic device in the SCS2000, the daughter cards only require a simple design and the whole package offers a relatively cost-efficient solution.

Straightforward integration of MSCB-based hardware is already provided by appropriate drivers and has been developed an application specific frontend module to control the specific sensor or control unit, i.e. to set and readout

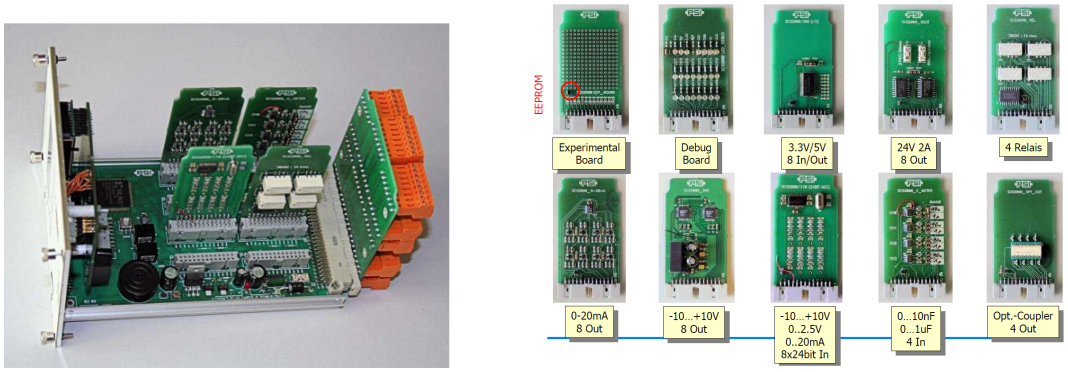

(a) (b)

Figure 7.1: (a) SCS-2000 general purpose control unit. (b) Examples of available and installed SCS200 daughter cards.

parameters of the hardware system. Setting of the parameters such as detector voltages, amplifier gains for the SiPM readout of the calorimeter or the readout rates of sensors are handled by corresponding settings in the online database (ODB) on the slow control computer. Some of these values are setted based on the readback and subsequent online analysis of slow control parameters. A backend main server handles the collection of the readout data with an adapted event builder provided in the *MIDAS* software. The assembled *MIDAS* events from all slow control subsystems are then handed off to a data logger module which stores the data in the *MIDAS* output stream and in a *PostgreSQL* database locally as well as transfer it to the Fermilab long-term storage server.

Fig. 7.2 summarizes the general components of the slow control system indicated by the solid colored boxes. A single slow control backend host (brown box) manages the communication with all MSCB nodes (blue boxes) via the MSCB submaster (green box). Non-MSCB based sensor and control nodes (purple boxes) communicate directly with the backend server via appropriate

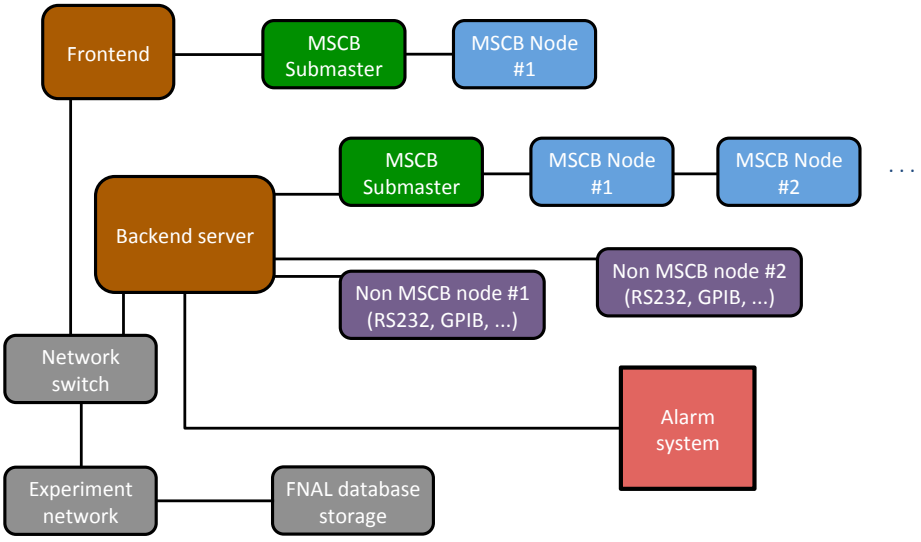

Figure 7.2: Scheme of the Slow Control System of the E989 $g-2$ experiment. See text for explanation.

interfaces (e.g. USB, serial port, ethernet, ...). Although a single main PC and submaster are sufficient to handle all MSCB nodes in the $g-2$ experiment, these additional available host computers with their MSCB submaster and nodes can be easily integrated into the slow control system. Therefore, the final implementation in E989 involved additional MSCB frontend hosts to control special subsystems. Data exchange between a frontend computer and the slow control backend computer happens via ethernet network. This scheme adds redundancy to the system in case of maintenance or failure of one of the computers since MSCB nodes and their appropriate *MIDAS* software frontend can be easily ported. The system is completed by the stand-alone alarm system (red box) to provide appropriate actions in case of unsafe operating conditions of various detector subsystems.

In the following subsections, are described the sensors and control units,

their requirements, the design of the alarm system, the backend server and the data storage.

7.1.2 Sensors and controls

The E989 $g-2$ experiment employs a variety of systems to facilitate the overall measurement of the muon anomalous magnetic moment. Fig. 7.3 displays the current functionality with respect to the slow control measurements broken down by various sub-systems. The corresponding Table 7.1 lists the actual parameters set and monitored via the slow control data acquisition where the read-back precision are best estimates. Follows here a brief description of each slow control subsystem.

For more details see Ref. [107].

Table 7.1: List of control and read-back parameters in the $g-2$ experiment handled by the slow control unit with read-back precision and rates, channel counts.

Parameter	**Read-back precision**	**Channel count**
Calorimeter		
SiPM bias voltage	∼mV	1300
SiPM amplifier gain		1300
SiPM temperature	0.1° C	1300
Laser calibration		
Laser temperature	$< 0.5\,^{\circ}$C	< 10
Output signals (enable)		< 48
Input signals		< 48
Serial laser interface	–	< 10

Table 7.1 – *Continued from previous page*

Parameter	**Read-back precision**	**Channel count**
Tracker		
HV voltage	$\sim 1\,\mathrm{V}$	54
HV current	$0.1\,\mu\mathrm{A}$	54
HV status	–	54
LV voltage	$\sim 0.1\,\mathrm{V}$	54
LV current	$\sim 10\,\mu\mathrm{A}$	54
Electronics temperature	$\sim 0.5\,\mathrm{C}^\circ$	348
Cooling temperature	$\sim 1\,\mathrm{C}^\circ$	54
Amb. pressure	few mbar	3
Amb. temperature	$< 0.5\,^\circ\mathrm{C}$	3
Amb. humidity	few %	3
Gas flow		48
Electric quadrupole		
Voltage (0-10 V)	0.1 V	5
Current (0-10 V)	0.1 V	5
HV disable / enable	–	5
Aux. detector: Fiber harps		
SiPM bias voltage	few mV	2
SiPM temperature	$0.1^\circ\,\mathrm{C}$	4
Motor control	-	4
Aux. detector: Entrance counter		
SiPM bias voltage	few mV	2
Field		
Main magnet current		1

Table 7.1 – *Continued from previous page*

Parameter	**Read-back precision**	**Channel count**
Surface coil current		200
Yoke temperature	$< 0.5\,^{\circ}\mathrm{C}$	~ 60
Hall temperature	$< 0.5\,^{\circ}\mathrm{C}$	~ 5

Calorimeter controls

As described in Section 4.3.1 the photo-readout of the electron calorimeter is based on silicon photo-multipliers. The design incorporates a surface mount SiPM on a readout board integrating the bias voltage supply and an amplification of the readout signal with adjustable gain. Since the experiment requires part-per-thousand gain stability, a stabilization and monitoring of the two external parameters that determine the SiPM gain, namely the bias voltage and temperature, is required. The bias voltage of each of the 1296 SiPM channels is set and monitored for each channel and the temperature sensors are placed on each of the amplifier boards. Compensation of changes in the gain of each channel is performing by adjustments to the variable gain setting of the differential amplifier stage.

Laser Calibration System controls

The Laser Calibration System, described in the Chapter5, need to monitor the laser intensity and the temperature of the light distribution system at several locations as explained in detail in the following section 7.2. The total number of channels required for the laser system is expected to be less than 100.

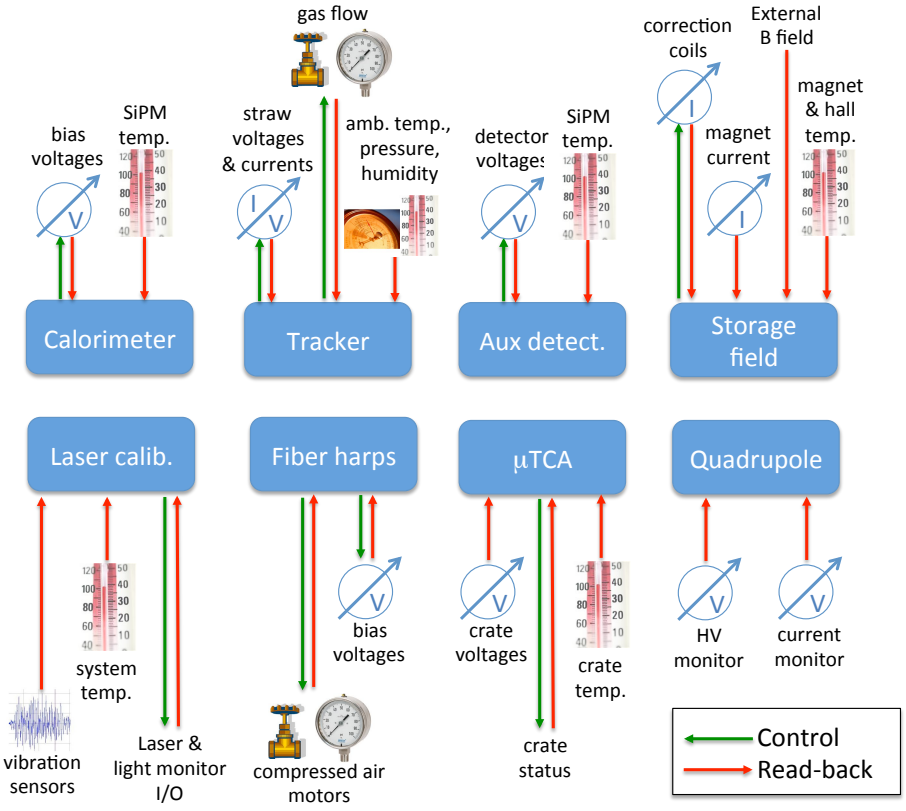

Figure 7.3: Schematic breakdown of the individual slow control nodes showing the controlled parameters and sensor read-backs.

Tracker controls

The tracker system comprises three stations of straws located inside the scallop regions of the vacuum chambers. The slow control provides readings for ambient temperature, humidity, and pressure at those three locations. It also monitors the gas flow and temperature as well as currents and voltages for both the straw high voltage and the electronics low voltage systems of each of the eight modules per station. The slow control provides the mechanism to set the high voltage demand values in addition to the read-back of the actual values. The experiment's PLC safety system (see section 7.1.4) provides interlocks for immediate shutdown of gas and HV in case of irregular running conditions.

Quadrupoles controls

The quadrupoles are supplied by five power supplies which each have two low voltage (0-10 V) outputs for monitoring of the actual high voltage and the current, respectively. The slow control incorporate 2 ADC daughter cards ($\pm$10 V range) for the SCS2000 units that accomodate the 10 channels of this low voltage measurements. A remote HV enable (2.5–15 V) / disable (0-1.5 V) signal for each unit is handled by one 8 channel digital output card for the SCS2000 unit. The quadrupole power supplies also are fast interlocked (potential free switch) by the PLC alarm system in case of bad vacuum, a storage ring magnet quench, or X-ray detection during access to the main experimental hall during operation.

Fiber harp controls

The fiber harp detectors are equipped with SiPMs as the photo-sensitive detectors. Their bias voltage power are supplied through two additional channels of the calorimeter bias supply system. As the SiPMs for the readout of the

fibers are grouped in 4 rows of 7, the monitoring of SiPM temperatures is anticipated with one probe per row. As the fiber harps are rotated into the beam by compressed air actuators, 2 control channels and read-backs are available. These are controlled by an Arduino board which has an MSCB interface.

t_0 counter controls

Beside the fiber harp, the auxiliary detectors also include the so-called t_0 entrance counter which is a Lucite Cerenkov sheet readout by two SiPMs. It requires two channels for the control and read-back of the bias voltage.

μTCA controls

The communication between the slow control DAQ and the μTCA crates has been done via software (see Section 7.1.3). The μTCA crates already have an integrated on-shelf manager that can read the status of parameters provided by the crate such as voltages or temperature.

Magnetic field controls

In the field measurement in Fig. 7.3 the slow control includes readouts of the correction coil currents and incorporates temperature sensors placed onto the magnet steel around the ring and hall temperature monitors. There are a total of <100 temperature probes for the entire experiment (mainly for the magnet steel) with a read-back precision of at most 0.1° C. Since the experiment is mostly sensitive to temperature changes, the absolute accuracy is of less importance. For the implementation of these temperature sensors, are used the above mentioned general purpose SCS2000 unit with existing 8-channel temperature daughter cards based on the Analog Device AD590 2-terminal temperature transducer. Since each channel senses the current in the

AD590, long cables of more than 10 m can be used so that the SCS2000 unit(s) may be located at the center of the ring.

7.1.3 Communication with external systems

The slow control DAQ does not only retrieve data from the various sensors described above but also communicates with other systems in the $g-2$ experiment and the Fermilab accelerator infrastructure. There are a total of three such systems:

- The main ring control system,
- the Fermilab accelerator complex,
- the μTCA crates used for the readout of the electron calorimeter stations.

The main ring control system comunication

The ring control system for the cryogenics and vacuum is based on PLC interfaces which are accessed via the human machine interface iFix [158]. The communication path between the iFix server and the slow control DAQ system is facilitated via an Object Linking and Embedding for Process Control (OPC) [162] server integrated into iFix. The communication on the slow control DAQ side is handled by an OPC client or, alternatively, the OPC server directly write into the *PostgreSQL* database.

The Fermilab accelerator complex comunication

During the $g-2$ operation, some parameters of the accelerator (like magnet currents, beam intensities, status of other beam elements) are stored in the output datastream. This information is retrieved via a data broker from the

accelerator network (ACNet). The data is stored in *PostgreSQL* [163] format and are integrated into experimental condition database.

The μTCA crates comunication

These crates typically provide internal status parameters (e.g. temperature, fan speeds, error indicators etc.) that are useful to monitor to quickly identify hardware problems or failures. System management and monitoring is achieved by means of software solutions based on the Intelligent Platform Management Interface (IPMI) [164], a standardized computer system interface. An IPMI system manager connected to an application programming interface (API) over TCP sockets has been developed for the μTCA crates employed in the CMS experiment.

7.1.4 Alarm system

The alarm system serves the purpose of allowing quick and safe shutdown of certain elements of the $g-2$ detectors. This is part of the PLC-based system handling the more critical components like the cryogens of the magnet as well as vacuum controls. There is plenty of capacity present within this PLC system. The system described here deals with detector components which are not critical in the sense of life threatening unsafe conditions. The interrupts provided by the slow control alarm system are mainly for protection of the detector components and electronics.

Hardware interlocks is provided for:

- high voltages and the non-flammable gas for the straw detectors which are located inside the vacuum,
- quadrupole power supplies in case of a bad vacuum, a magnet quench or

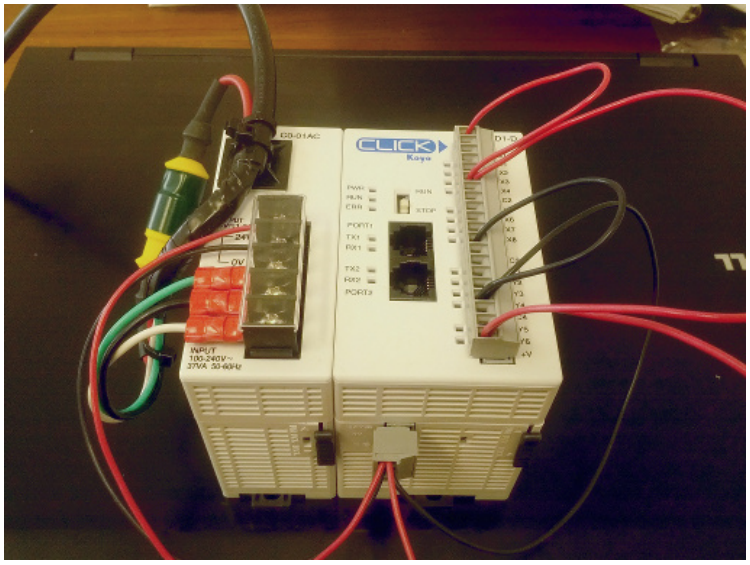

Figure 7.4: Prototype CLICK PLC for the alarm system during testing at Argonne.

X-rays from sparking plates, during person access to the $g-2$ hall,

- the laser calibration to protect the system in case of accidental opening of the optical table hat, overheating or abnormal parameters.

- SiPM bias voltages in the same scheme if the request for it arises.

The alarm system adopts a simple design, proven very successful in the MuSun experiment at PSI, using a cost-efficient CLICK PLC, as shown in Fig. 7.4.

The PLC sits at the center of the system as shown in the schematic layout in Fig. 7.5. Various input levels from other systems such as a good vacuum indicator or ring magnet status feed into the PLC. Those input levels are then used in the program running inside the PLC to determine the appropriate output levels of the interlocks for the various detectors. The implementation of this program is performed by free software on the so-called ladder logic. The slow control also includes additional switches on the input level side as

a measure to allow for bypassing of certain alarm channels. This can be very helpful during detector testing, maintenance or debugging where it is desirable to disable a specific input or output channel without interfering with all others. As the PLC is programmable, a hardcoded timeout interval could be added to automatically switch back on the bypassed channel.

Given the experience with a similar alarm system in the MuCap and MuSun experiments [165], it is to be expected that the system will expand over time because additional useful interlocks are identified during the design, testing and implementation of detector systems or even during data taking. The chosen design is ideal as new input and output modules with additional channels can be added to the single PLC.

7.1.5 Backend server

The backend server is the central computer in the slow control DAQ to communicate with the various control units and sensors and retrieve all read-backs, with a data rates less than 1 MB/s. It is equipped with interfaces (RS232, USB, MSCB) for the external devices.

The various sensors and controls can be accessed individually by independent frontend programs which run in parallel within the main *MIDAS* server. Each frontend has its specific functionality to set experimental parameters (like high voltages for each SiPM), read-back parameters, and to change read-back rates. Some hardware parameters might be set depending on the outcome of certain analyses routines. These analysis frontends can also be run on the backend server since *MIDAS* already provides for a convenient framework of an online analyzer.

For MSCB devices, necessary hardware drivers are provided by *MIDAS*. For other hardware connecting to the backend over RS232 or USB, *MIDAS* also

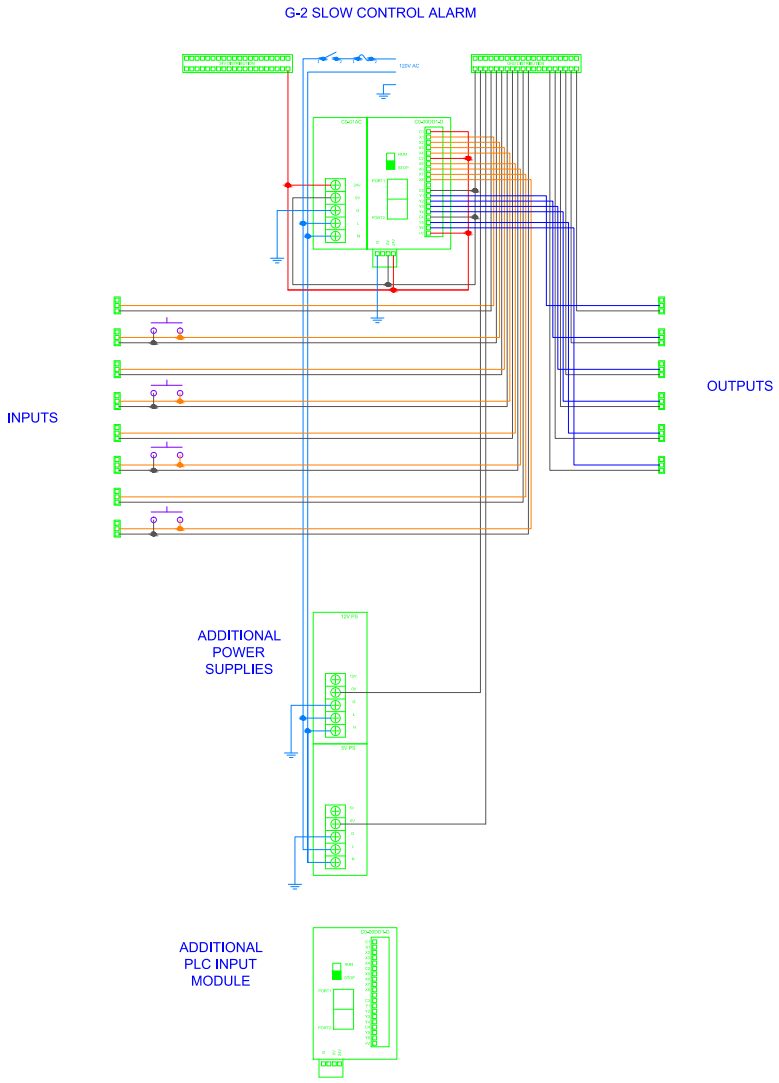

Figure 7.5: Layout for the stand-alone slow control alarm system based on a CLICK PLC.

includes software components that will make integration of these subsystems into the slow control easier. Such frontend code has been developed previously for experiments like MuLan [166] and MuCap [167] at PSI.

7.1.6 Data storage and access tools

For the data storage of slow control parameters, are used *PostgreSQL* [163] databases, with synchronization of the local database with the remote long term storage at Fermilab.

The Table 7.1 shown for the slow control a maximal of 3000 readout channels with expected rates of $\sim 1\,\mathrm{s}^{-1}$. With a recording for every single channel three float values (4 bytes) in form of a timestamp, demand, and current readback value, one can deduce a conservative upper limit of the expected data rate of 32 kB/s or 3 GB per day. Given the standard storage sizes of more than 1 TB today, the overall slow control data for the entire $g-2$ data taking period will be easily storable and does not pose any major challenge.

Based on past developments for muon precision experiments at PSI and other current Intensity Frontier experiments at Fermilab, there are a variety of user interfaces for online monitoring and the offline analysisis that are user friendly to inspect the large number of different channels, essential during data taking, as example:

- The IFbeam software tools incorporate the python based Web Server Gateway Interface and subsequent Google Charts to access and display database information in the web browser,

- the ROME software framework is well integrated into the *MIDAS* data acquisition framework and is used for online monitoring of slow controls and other data [168],

- the experiment use custom developed web browser based tools to query and display the database information as well as standalone graphics displays within the *ROOT* framework [134].

7.2 Slow Control and DQM of the Laser Calibration System

Online laser monitoring system collects real data from:

- Rider [127] to *MIDAS*(the $g-2$ online DAQ software framework) [133] to *art* (the $g-2$ offline software framework) [136] and, at end, to plot them in real time (for data quality),
- Hardware of the Laser Calibration System (slow control).

In the following sections are described these two sub monitoring systems and the software technologies chosen, developed to produce output informations, see Fig. 7.6.

7.2.1 Laser Data Quality Monitor

As described previously, the data acquisition system (DAQ) for the Muon $g-2$ experiment is based on the *MIDAS* software package. The DAQ is designed to process data from Calorimeters, Lasers, Trackers, Quads and Fiber Harps, which has been digitized in a μTCA crate. The IPbus communication protocol [169] is the standard that used to communicate with both the AMC13 [131] and the Rider [127] via ethernet. The DAQ software is modular, and has several parts working together. *MIDAS* provides the **mserver**, **mhttpd**, and **mlogger** programs that run and organize communication between the frontends, hosts a web interface, and writes the data to disk. An

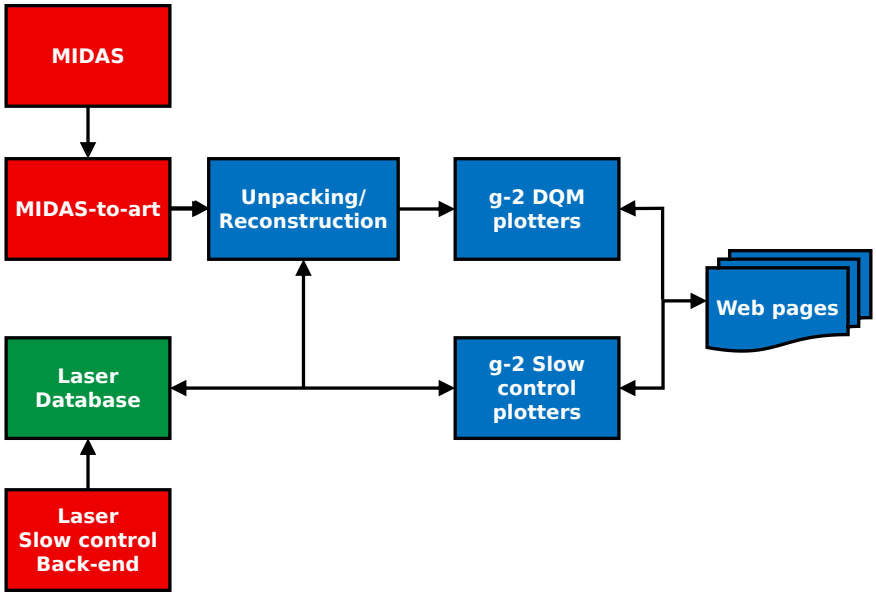

Figure 7.6: Layout of the online laser system monitoring.

event builder assembles data fragments from multiple buffers, which have been produced by the frontends. The frontend writes data in raw, histogrammed, and T and Q method formats. A frontend called MasterGM2 uses *RPC calls* to send begin and end of run signals to the other frontends, as well as triggers to any synchronous frontends.

A part of online laser monitoring system, The Data Quality Monitor (Laser DQM), collects real data from Rider [127] to *MIDAS* [133], *art* [136] and, at end, plots them in real time over ethernet with web applications. The DQM of Laser Calibration System is integrated inside the DQM system of experiment and consists of three components: 1) the *art* side, 2) the web server side, and 3) the client side, as shown in Fig. 7.6 and described in the following subsections.

The *art* based DQM presents these features:

- It uses exiting tools;
- It minimizes effort duplication using *art* modules shared with nearline

and offline frameworks;

- It uses *midas-to-art* interface and *MIDAS* API [133];
- It exerts no back pressure on *MIDAS* experiment;
- It can feed multiple real-time applications (web, paraview, etc.).

According to the data acquisition time sequence, see Fig. 5.28, the Laser DQM processes two kinds of laser signals to monitor: In fill (muon), out of fill (laser) pulses, fired respectively during and between two consecutives muon/positrons data taking.

Database access is possible from *art* job or web server and it is possible to raise *MIDAS* alarms/warnings contingent on processed data.

Triggering, waveforms and island chopping

There are different trigger types that work as follows:

Every trigger counts as an event. The main types of triggers are called muon triggers (in-fill) and laser triggers (out-of-fill). There are some other types of triggered events, like the asynchronous trigger where it possibles to read out the data from all the asynchronous riders. Besides the triggered events, there are also sometimes slow control events, which contain slow control information like temperatures. They're not really empty, but have no waveform data. In-fill pulses occur after muon triggers and out-of-fill pulses occur after laser triggers.

The way the digitizers respond to the different trigger types is defined by three parameters: waveform count, waveform length, and waveform gap. Once a digitizer receives the trigger, it will immediately acquire a waveform of length determined by waveform length, then wait for waveform gap samples, then take another waveform, repeated waveform count times. As an example, a waveform count of 4 would appear as shown in Fig. 7.7:

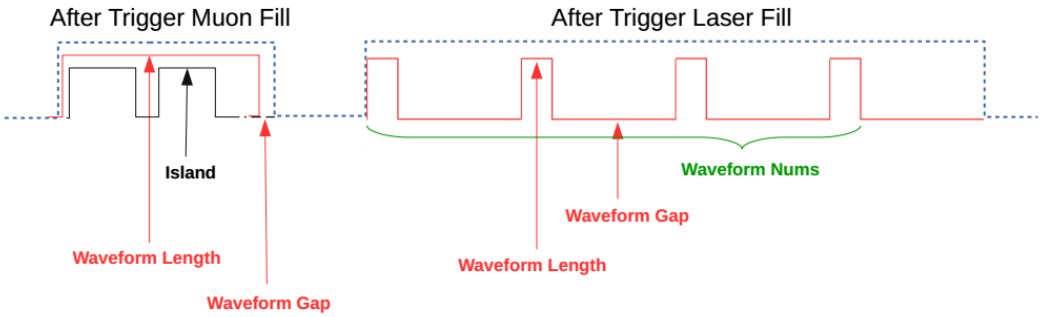

Figure 7.7: Rider acquisition pattern, defined by waveform count, length, and gap. In the muon fill trigger islands are chopped when the algorithm in the GPU finds peaks above a threshold.

The units of waveform length are "bursts", and a burst contains 8 samples. For example, 70000 means 560000 samples, which corresponds to 700 μs because one sample has 1.25 ns. The units of waveform gap are samples.

Tipically the muon trigger configuration has 1 waveform with a length of 70000 and a gap of 8. This means it acquires one waveform of 560000 samples. Because the gap comes after the waveform and the count is equal to one, the gap configuration value actually has no effect for muon triggers. This is true for any trigger type with a waveform count of 1. Islands are the result of the algorithm in the GPU that runs on muon trigger waveforms and chops out small subsections of the larger trace when it finds peaks above a threshold.

There are no islands involved in the acquisition of laser trigger waveforms. The waveforms are much shorter, 1 microsecond compared to 700 microseconds, so the DAQ is capable of saving all the raw data.

A tipical Source and Local Monitors laser traces acquired by Riders are shown in Fig. 7.8.

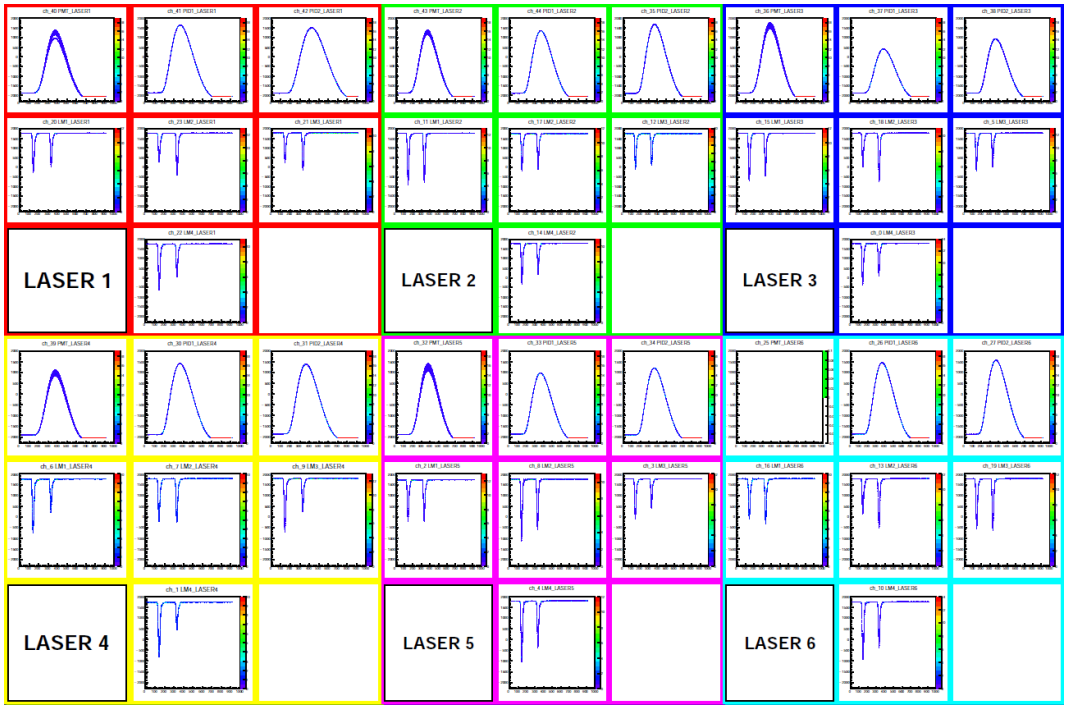

Figure 7.8: Tipical Source and Local Monitors laser traces acquired by Riders.

Data collecting

MIDAS-to-art online system has tree kinds of modules used to unpack raw data, collecting and formatting event informations: unpackers, producers and analyzers, respectively, according to the *art* structure [136]. *Midas-to-art* converts data files produce by *MIDAS* to *art* files. Both *MIDAS* and *art* are event-based frameworks, and the events are mapped 1 to 1.

The definition of a *MIDAS* event is determined by the DAQ system, and it is related to the *MIDAS* event builder. For the DAQ, an event corresponds to one fill (muon or laser). To collect event information from *MIDAS*, a special collection structure has been developed, the *midas-to-art* data product (*art* record). The *MIDAS* event format is a variable length event format. It uses "bank" as subsets of an event. A bank is composed of a bank header followed by the data, see Fig. 7.9.

Each *MIDAS* event contains data banks from DAQ detectors and software. These banks are essentially arrays of raw data words, where the data words are primitive types such as int, short, double, etc. *midas-to-art* creates *art* runs and events from *MIDAS* runs and events, and adds to each event *art* records containing the *MIDAS* bank data in *art* form (*art* record collections).

The *art* records store the detector data as vectors of chars, regardless of the type of the words in the original *MIDAS* bank, thus enabling a single *art* record to be used generically for any *MIDAS* bank. *Midas-to-art* also adds the *MIDAS* event headers to the *art* events and the Online Data Base (ODB) dumps to the *art* run. No data processing is performed by *midas-to-art*, it just converts data from one format to another. The downstream usage of the raw data such as unpacking is performed by other *art* modules (the unpackers).

There are three *art* records of interest:

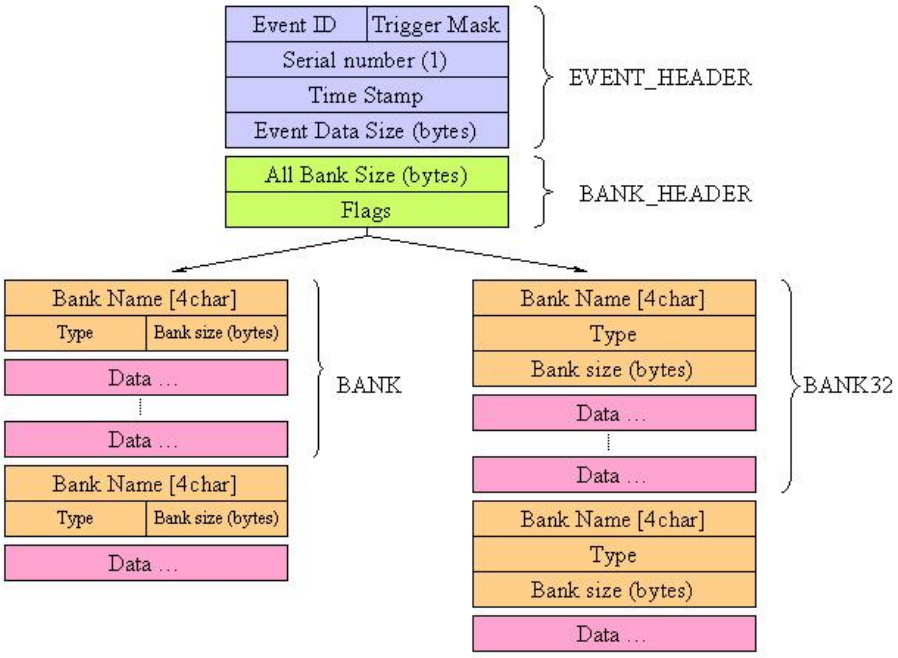

Figure 7.9: Structure of *MIDAS* event showing Event and Bank headers with data banks.

- A template class representing a *MIDAS* bank, filled once per event. It will appear in a given *art* event only if the bank was present for corresponding *MIDAS* event;
- A Container of the *MIDAS* event header information, filled once per event. Also contains a list of banks parsed in the event (as per the "requestedBanks" list provided by the user);
- A Container of the *MIDAS* ODB dump, which is stored as an XML string at the start of a *MIDAS* run.

After the raw data collecting the stages of the process are:

1. Unpacking;
2. Reconstruction;
3. Aggregation;
4. Data Quality Checks.

In the *unpacking* stage, all the raw data is converted into *art* dataproducts. Here, the dititized waveforms are unpacked into *IslandArtRecord* and *RiderArtRecord* data structures for in-fill and out-of-fill data respectively. Also in this stage, the slow control values from the database are read out on a per run basis.

In the *reconstruction* stage, waveform analysis converts the digitized traces into amplitudes and times as *LaserMonitorArtRecords*.

The *aggregation* stage uses hardware maps of the different channels and timing information to match each event with the corresponding laser monitors in a *LaserEventArtRecord*.

The final stage uses all of the linked laser data to perform *data quality checks*, ensuring that the data is sufficiently clean.

Getting data out to *art*

To get data out of the *art* process the DQM system uses *ZeroMQ* [170], a messaging library with following features:

- Supports multiple protocols (e.g., tcp, ipc, inproc, etc.);
- Bindings in many major languages;
- General tool for communicating;
- Real-time information in/out of *art* job;
- Provides convenient communication patterns.

In order to get data out of a running *art job*, analyzers *art* module use a tcp *OnlineContext* service, configured with specific sochet ports (a different one for heartbeat and publish sockets). The publish socket is typically used to send live data out *art job*, and the heartbeat socket is used to increase reliability of the system and allows for clients to confirm the presence of a running *art job*. Publish message have all its arguments serialized, starting with the header, in binary form in the order provided and send them through the subscribe socket.

As will be described more in the following section, the *Node.js* web server of the DQM is currently able to comprehend messages of the following types:

- *1d Histograms*: A histogram is an array of bin centers and an array of bin contents;
- *2D Histograms*: histogram pairs of x and y values. The data binning takes place on the *Node.js* side, unlike for 1D histograms;
- *Histories*: A history keeps track of a single value per (run, event);

- *Histogram Collections*: A histogram collection is a collection of histograms with the same number of bins and same bin content type, typically logically grouped together in some way; This is useful for example to get a histogram of pulse amplitudes for each channel of the laser crate;
- History collections: A history collection is a collection of histories.

DQM Web server

Node.js web server is a widely used *Javascript* runtime environment commonly used for real-time web applications [171]. The DQM uses *Node.js* to run a webserver that sits between the *art job* and the web-browser client that shows online plots. This web server presents the following characteristics:

- Event driven architecture;
- Asynchronous, non-blocking IO;
- Built for scalability and throughput;
- Numerous mature open source plugins and libraries (*Express.js*, *Socket.IO*, *PostgreSQL*, etc.);
- Load distribution and modularity;
- Parallelization through cluster of *Node.js* servers;
- Independently developed DQMs can be run either independently or in concert.

Many instances of *Node.js* web servers are used to data aggregation and clients communication and one of these is dedicated to the Laser System. A proxy provides single point of entry door connections to multiple clients.

The following types of online plots are available:

- *Histogram*: A basic histogram (can also be used to store any x-y scatter plot);
- *Running Average Histogram*: The data from the last event received as well as the average of data from the last n (specifiable) events received;
- *History*: The value of something for the last n (specifiable) events;
- *Histogram Collection*: A collection of histograms,
- 2D histogram: A 2D histogram, with x and y projections pre-calculated.

To show histograms it needs to declare what data structures it wants to keep track. It is also possible to register arbitrary custom data structures.

The actual rendering of the plots is done on the client side using *plotly.js* [172] as a data visualization tool with a *Javascript* library, as discussed in the following section.

Client side

The client side consists of the *Javascript* and *HTML* files that are served to users when they connect to the DQM web page. The client side code is currently the last developed. It use *plotly.js* for plot visualizzation and *socket.io* for real-time communication between the client's web browser and the *Node.js* server. An example of client side web page of Laser DQM is shown in Fig. 7.10. In order to visualize only useful informations the following pages are developed:

- *The Laser DQM muon fill (in-fill) main page*: A page with information of all Source and Local Monitors traces digitized during muon fills(see Fig. 7.10);

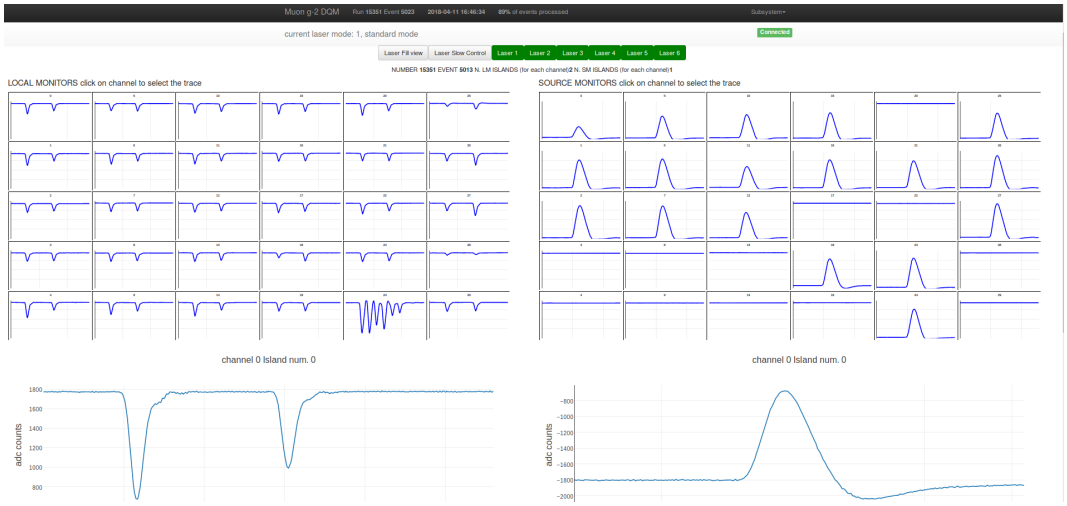

Figure 7.10: Client side main web page of Laser DQM.

- *The Laser DQM laser fill (out-of-fill) main page*: A page with informations of all Source and Local Monitors traces digitized during laser fills;

- *Single Laser chain page*: A page where a single laser chain is monitored with amplitude and pedestal histograms, time histories and trace plots of SM and LM signals (see Fig. 7.11);

- *Single Laser chain stability page*: A page where a single laser chain stability is monitored with amplitude ratio histograms, time histories and trace plots of SM and LM signals 7.10. The signals ratios that monitor the stability of the chain are:

$$\frac{PMT}{Pin1 + Pin2}, \frac{Pin1}{Pin2}, \frac{LM2}{LM1}.$$

  where PMT, Pin1 and Pin2 are respectively the amplitude of the PMT, the PIN diode 1 and the PIN diode 2 signals of the Sorce Monitor (SM) of a laser chain and LM1 and LM2 are the two signal amplitudes of

Figure 7.11: Client side of DQM that shows laser chain signals of Source and Local Monitors.

the first (from the launching fiber) and the second peak (240 ns later from returning fiber) of the Local Monitor (LM) of the same chain (see Fig. 7.12).

7.2.2 Slow control

The Laser Slow Control (LSC) is developed to monitor the hardware of the Laser Calibration System and the environment conditions. The design of the LSC considered the following hardware to be monitored:

- Source Monitor (SM) power supply bias voltages and temperatures;

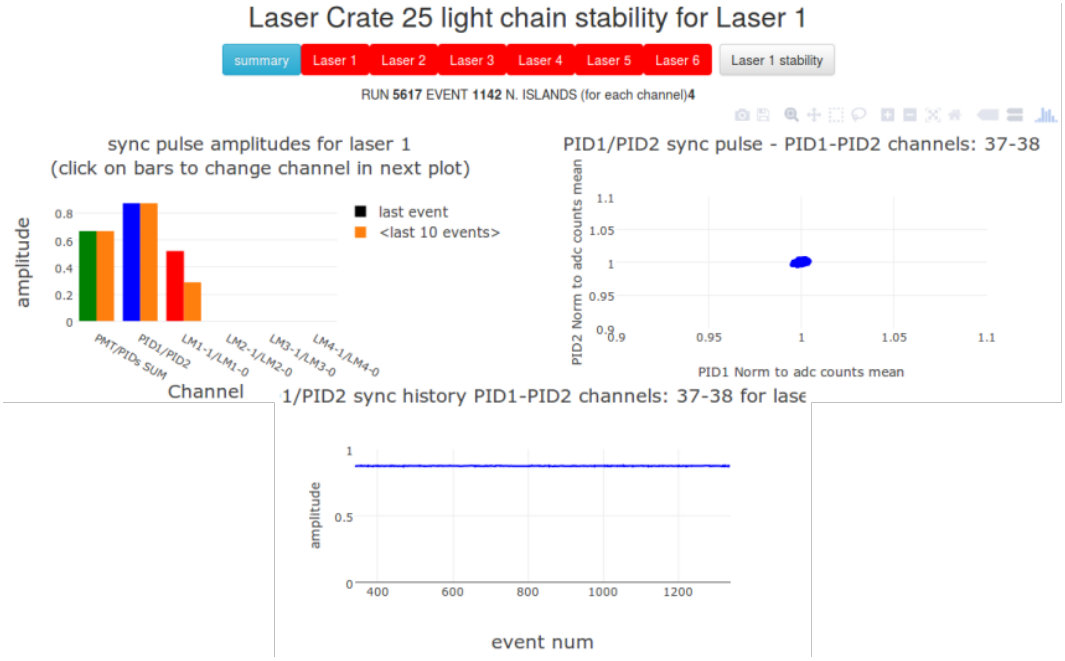

Figure 7.12: Client side of DQM that shows laser chain signals ratios to monitor the stability of Source and Local Monitors. The scatter (on the right) and history (bottom) plots are related to the PIN diodes ratio in this figure.

- Local Monitor (LM) high voltage (HV) power supply hardware parameters;
- Laser driver (Sepia II [146]) currents and interlock status;
- Network devices status;
- Filter wheels filters position;
- Flip mirrors position;
- Last day and last week laser hut room temperatures.

A developed back-end software, working on workstation inside laser hut, manage the connections with a *PostgreSQL* database and the Calibration System hardware as shown in Fig. 7.13.

This framework also provide to store the hardware status and parameters to the database, see Fig. 7.14, and to arise alarms on *MIDAS* after a quality check failed on status and data, see scheme in Fig. 7.13.

Web server side, integrated into DQM, provides a monitoring page where are shown the devices and the environment temperatures status, see Fig. 7.15.

Slow control back-end software

The back-end software, developed in C++ language under Fermi Linux distribution [173], uses the following API and software technologies to manage the hardware of the Calibration System:

- *CAEN SY5527 API* reading over socket connection to the high voltage (HV) power supply server;
- *Delay Generator status* reading over socket connection;

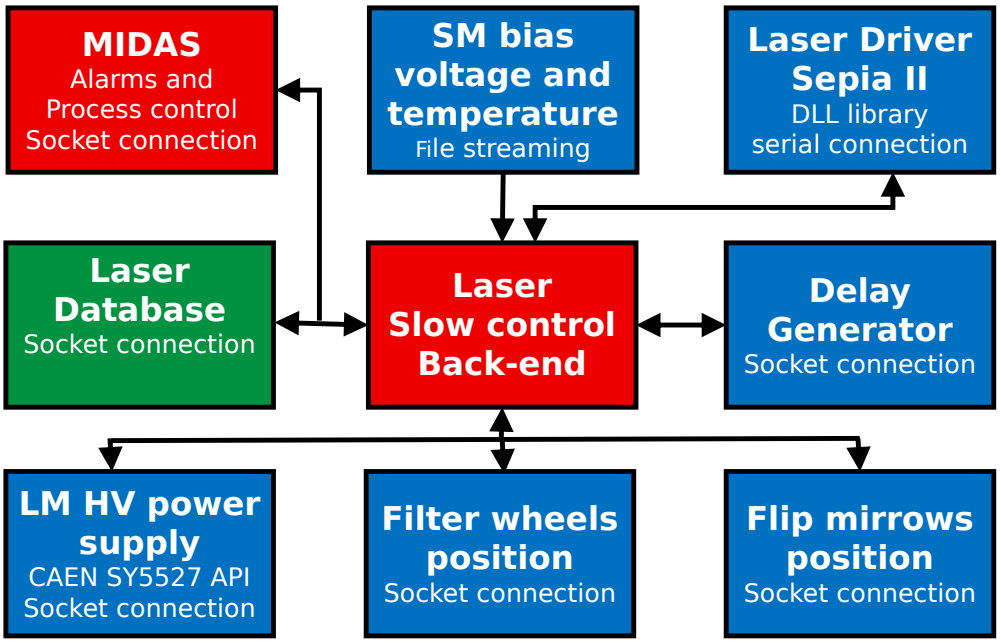

Figure 7.13: Layout of the Laser Slow Control system connections with database and hardware.

- *Filter wheels position* reading over socket connection to a server developed in Phyton;

- *Flip Mirrors position* reading over socket connection to a server developed in Phyton;

- *SM bias voltages and temperatures* reading over a file streaming;

- *SEPIA II Picoquant Laser Driver API.* Developing under linux Operating System needs to use DLL libraries interpreter.

Database of the Laser System

A relational database scheme has been designed to define what data must be stored and how the data elements interrelate, see table relationship diagram in Fig. 7.14. It involved classifying data and identifying interrelationships following the ontology theoretical representation [175]. The structure was optimized studing the organization of the application's data and the application's requirements, which included transaction rate (speed), reliability, maintainability, scalability [176].

Data relationships has been determined using the relational model approach [177, 178]. It provided a declarative method for specifying data and queries. The data has been arranged into a logical structure and mapped into the storage objects supported by the database management system. The storage objects has been corresponded directly to the objects used by the Object-oriented programming language adopted to write the slow control back-end software that manage and access the data. The relationships was defined as attributes of the object classes involved. The way the mapping is performed is such that each set of related data which depends upon a single object, whether real or abstract, is placed in a table. The list of the tables have been determined is shown in table 7.2. Relationships between these dependent objects is then stored as links between the various objects.

Specifically, each table represents an implementation of either a logical object or a relationship joining one or more instances of one or more logical objects. Relationships between tables may then be stored as links connecting child tables with parents. Complex logical relationships involves tables they have links to more than one parent, as shown in Fig. 7.14.

Finally a normalization process has been performed to ensure that the database structure is suitable for general-purpose querying and free of un-

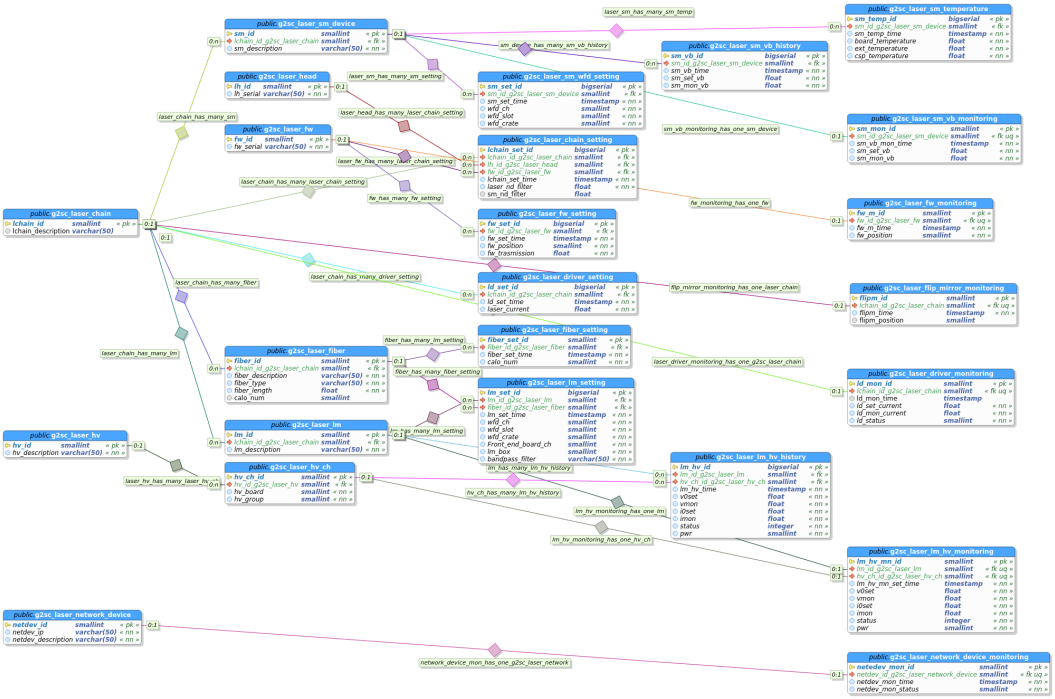

Figure 7.14: Layout of the Laser Calbration System *PostgreSQL* database.

desirable characteristics-insertion, update, and deletion anomalies that could lead to loss of data integrity.

Slow control web server and client side

Web server side of the Laser Slow Control is integrated into Data Quality Monitor web server and provides a monitoring page where are shown the devices and the environment temperatures status, see Fig. 7.15. It works in asynchronous mode respect to the DQM (runs and *MIDAS*/*art* indipendent) and read the informations of slow control, stored in the database, using *node-postgres* library [174].

The client side shows hardware parameter information using *HTML* table views and shows the laser hut temperatures behavior using plotly [172], see

Table name	Description
First level - Static informations	
g2sc_laser_chain	Laser chains definition
g2sc_laser_hv	HV device definition
g2sc_laser_network_device	Network devices definition
Second level - Quasi static informations	
g2sc_laser_sm_device	Source Monitor devices definition
g2sc_laser_lm	Local Monitor devices definition
g2sc_laser_fiber	Fibers definition
g2sc_laser_head	Laser heads definition
g2sc_laser_fw	Filter wheels definition
g2sc_laser_hv_ch	HV device channels definition
Third level - Informations with some changes in time	
g2sc_laser_sm_wfd_setting	WFD channels of Source Monitor devices settings
g2sc_laser_chain_setting	Laser chain settings
g2sc_laser_fw_setting	filter wheels settings
g2sc_laser_driver_setting	Laser driver settings
g2sc_laser_fiber_setting	fibers settings
g2sc_laser_lm_setting	Local Monitor settings
g2sc_laser_sm_vb_setting	Source Monitor vbias settings
g2sc_laser_lm_hv_setting	Local Monitor HV settings
Fourth level - informations rapidly changes in time	
g2sc_laser_fw_monitoring	Filter wheels monitoring position
g2sc_laser_flip_mirror_monitoring	Flip mirrors monitoring position
g2sc_laser_network_device_monitoring	Network devices monitoring parameters
g2sc_laser_sm_vb_monitoring	Source Monitor vbias monitoring and time history storing
g2sc_laser_lm_hv_monitoring	Local Monitor HV monitoring parameters and time history storing
g2sc_laser_sm_temperature	Source Monitor temperatures monitoring and time history storing
g2sc_laser_driver_monitoring	Laser driver monitoring parameters and time history storing

Table 7.2: List of the Laser Slow Control System database tables.

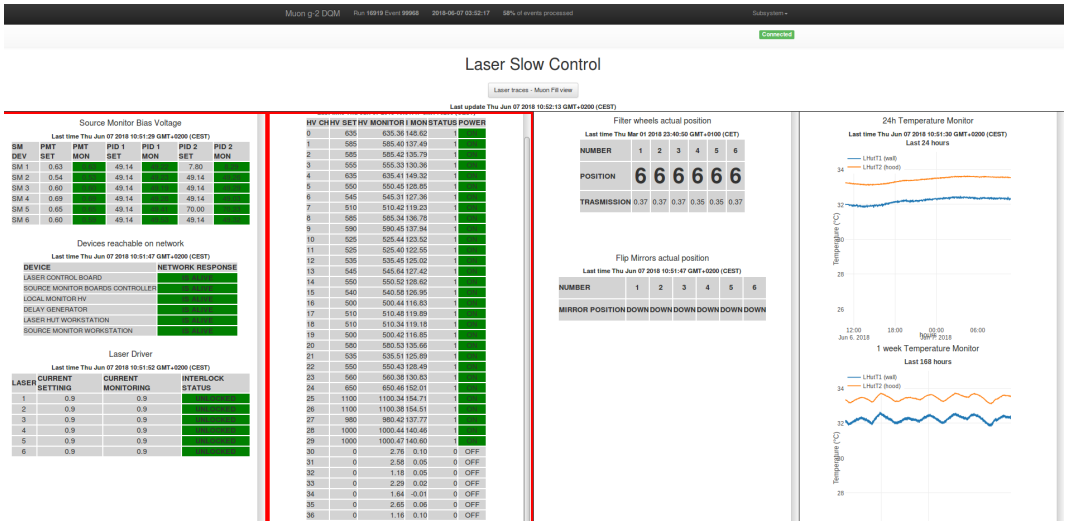

Figure 7.15: Client side web page of Laser Slow Control.

Fig. 7.15.

7.2.3 Alarms management and data quality check

MIDAS alarms interfacing

The Laser DQM and Slow Control are interfaced with *MIDAS Alarm System* [133], built-in in the $g-2$ experiment. When an alarm condition is detected, alarm messages are sent by the system which appear as an alarm banner on the status page, and as a message on any windows running clients. The *MIDAS Alarm System* includes several other features such as sequencing and control of the experiment. The alarm capabilities are:

- Alarm setting on any ODB database variable against a *threshold parameter*;
- Alarm triggered by *evaluated condition*;
- Raise alarms/warnings contingent on *processed data*;

- *Customization alarm scheme*; under a desined scheme multiple choices of alarm type can be selected;
- *Periodic Alarm* periodically activated according to a time interval:
  - Selection of Alarm check frequency;
  - Selection of Alarm trigger frequency;
- *Internal Alarm* checks run inside a process;
- *Program Alarm* triggered when a Program is not running;
- Selection of *alarm message destination* (to DB system, to system message log or to elog);
- *Alarm Alerts*: visual, audial, email, SMS.

DQM alarms

DQM Laser Monitors framework (*art* side) has been developed in order to check the quality of laser traces collected by Riders DAQ system. The Laser DQM arise an alarm to *MIDAS* if the laser traces do not pass the following data quality check:

- Pedestal check pass: The trace pedestal is greater than a predefined threshold;
- Amplitude check pass: The trace amplitude is greater than a predefined threshold;
- Saturation check pass: The trace amplitude is within a predefined range.

Collecting a prescaled amount of collected traces, an alarm is arised on *MIDAS*when it exceeds a predefined threshold.

The web server side of Laser DQM provides Visual Alarms on Laser Monitors web pages also when traces do not pass the quality control check.

Laser Slow Control alarms

The back-end Laser Slow Control system (LSC) arises the following alarms on *MIDAS* due to hardware malfunction, for example:

- Database connection fails;
- Data write to the Database fails;
- Voltages or currents supplied to Source and/or Local Monitors are out of range;
- Network devices are offline;
- Laser driver is locked or currents supplied are out of range;
- Filter wheels and/or Flip mirrors positions interrogation returns bad responces.

Also a *MIDAS Program Alarm* triggered when the slow control software is not running.

The web server side of the designed SLC system provides Visual Alarms on web pages if one of the previous conditions occurs.

7.3 Web-based big control and monitoring system

After developing specific monitoring tools for differet systems of the $g-2$ experiment, the main goal has been to design a Web-based big control and monitoring system that will collect, in the most concise way, all the informations from Slow Control and data acquisition DAQs.

Roles of Slow Control and monitoring tools in DAQ system are summarized here:

- Monitor the status of DAQ and DAQ hardware;
- Monitor physical and environmental conditions;
- Control the quality of data taken;
- Control and operate hardware equipments;
- Guarantee safety and correct functioning of whole system.

Moreover key requirements for the monitoring system are:

- Independent of particular experiment (as much as possible);
- Modular structure;
- Web-based approach.

Thanks to the modular approach, various components of the developed framework are currently used by other experiments (CMD-3 and Microbeam Radiation Therapy at Budker Institute of Nuclear Physics).

During the operations DAQ and related systems produce a lot of information for experts and people on shift that need to be monitored and taken

into account. So a unified and user-friendly access to diverse pool of monitoring/control data is needed. The key goals considered in the design of the realized high-level monitoring framework are:

- Access to real-time and archived data;
- Different focus for shifters and experts;
- Possibility to control detector subsystems;
- Various helpers (data highlighting);
- Physicist should be able to extend the interface.

The choise of web-based approach meets well these goals. Modern Web technologies offer a big set of advantages and ready to use components out of the box. Client-server architecture has scalability, reliability and extensibility (easy integration of experiment specific tools). It hide direct dependency with front-end electronics and data sources.

Web application has cross platform compatibility (no dependency to client OS), is accessible anywhere (can be even used remotely outside control room), has cost effective, rapid development (thanks to *Python* [179], *Django* [180], and plenty of open-source web packages) and it is easy customizable.

Architecture overview of sources of monitoring histograms is shown in Fig. 7.16.

Code of the developed framework (*DAQWEB*) has been organized into two different parts: a shared part (core) and a $g-2$ dedicated implementation. Thanks to this modular approach and experiment-independent architecture, parts of the system are also used for other experiments.

Available functionality to draw plots, provided by the $g-2$ monitoring framework *DAQWEB*, are:

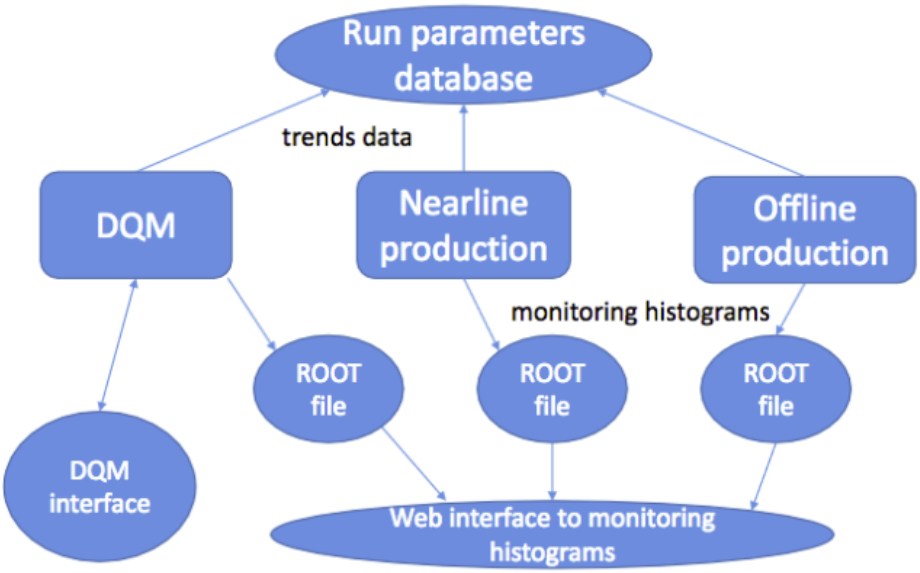

Figure 7.16: Layout of sources of monitoring histograms.

- Interactive server-side plots generation (static images) based on remote script execution:
  - using *ROOT* [134] graphic engine;
  - using whatever sources of data (database, trees, files, direct measurement if need);
  - using whatever external (custom shell) script/plot generator.
- Interactive client-side plots visualization based on *D3.js* [181] library:
  - Default visualization of time/number-based x-graphs for slowcontrol data;
  - Whatever custom sources of data (various databases, direct measurements by the frontend electronics, etc.).

Other system components included in the DAQWEB framework are:

- Update forms to change various information in databases as control (set voltage, gains) for SiPM/BK calorimeters/boards, Monitor temperatures, etc.;
- μTCA crates monitoring plots;
- Real-time monitoring using table representation;
- Overall information about runs;
- Runlog from nearline plus per-run nearline *ROOT* histogram visualization;
- Runlog for Field DAQ;
- Changes log and history of user actions made within the system.
- Custom applications for particular subsytems:
  - Hardware control modules;
  - interactive forms to configure boards (e.g. trigger settings);
  - remote execution of chain of scripts (load electronics).

Chapter 8

Calibration studies and ω_a analysis

The anomalous spin precession frequency ω_a is one of the two observables required to obtain the muon anomaly, a_μ. In order to ensure that the experiment reaches the goal of 140 ppb precision in a_μ, the error budget allows for a 100 ppb statistical uncertainty combined with equal 70 ppb systematic uncertainties from each of the ω_a and ω_p analyses. This Chapter describes the analysis steps to extract ω_a with a particular attention to the gain calibration and the lost muons correction.

8.1 Introduction to the analysis strategy

The $g-2$ E989 experiment, has at present seven independent analysis groups using four independent different reconstruction algorythms and different Fit methods. The analysis presented in this thesis is done by the "Europa" analysis group formed by italian and english institutions, each with specific competences on laser calibration (gain) and tracker reconstruction (muon

beam profile).

8.1.1 Muon decay and boost kinematics

In this Section we recall the most important aspects of the kinematics of muon decay (see [107] for details). In the muon rest frame, the angular distribution of emitted positrons from an ensemble of polarized muons is

$$dn/d\Omega = 1 + a(E)\left(\hat{S_\mu} \cdot \hat{P_e}\right), \tag{8.1}$$

where $\hat{S_\mu}$ is the muon spin direction and $\hat{P_e}$ is the positron momentum direction. The asymmetry a depends on positron energy (E) and is such that the highest-energy positrons are emitted in the direction parallel to the muon spin. To boost to the laboratory frame we define θ^* as the angle between the positron momentum and the Lorentz boost,

$$E_{e,lab} = \gamma(E_e^* + \beta P_e^* \cos\theta^*) \approx \gamma E_e^* \left(1 + \cos\theta^*\right). \tag{8.2}$$

The quantities marked with a star are those measured in the muon center-of-mass frame (CM). The magic momentum requirement fixes γ at 29.3. Due to the correlation between the muon spin and the positron momentum direction, the angle between the positron momentum and the boost direction from the CM frame to the lab frame acts as an analyzer of the muon spin. The maximum positron energy in the lab frame occurs when the positron decay energy (E_e^*) is the maximum and the positron momentum is aligned with the boost direction ($\cos\theta^* = 1$). Figure 8.1 shows the decay positron energy spectrum as a function of time for one $g-2$ period.

The modulation of the decay energy spectrum occurs at the frequency ω_a.

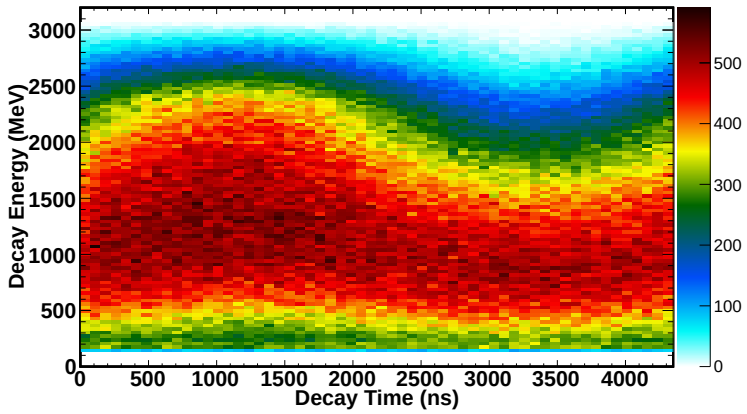

Figure 8.1: The decay positron energy spectrum as a function of time, modulo a complete 4362-ns $g-2$, period. The muon spin and momentum are aligned at $\pi/2$ and anti-aligned at $3\pi/2$ in this figure, corresponding to about 1090 and 3271 nanoseconds (ns), respectively.

8.1.2 Three methods to obtain ω_a

In general, three different methods for determining ω_a can be considered:

- *T-method (time)*: As described in previous chapters, counting the number of high energy (above the threshold) positrons along the muon momentum axis as function of time (reconstructing single positron events as Number of events in a(E,t) bin plot) gives a function that is the decay exponential modulated by the ω_a anomalous precession frequency, producing the so called "Wiggle Plot" (Fig. 4.8), where the equation used to fit this curve is, in ideally situation, the Eq. 4.13;

  - *T, E-weighted sub-method*: Each energy bin has a different asymmetry and phase value. Fitting each slice separately allows to use positrons down to 500 MeV.

- *Q-method (charge)*: It integrates all the charge, possibly with no (or minimal) threshold. Does not need to reconstruct single positrons and

it avoids cluster recontstruction;

- *R-method (ratio)*: It splits randomly half the dataset in 2 subsets shifted by ± half a $g-2$ period. By building the combinations it eliminates the exponential behaviour and leaves just a sinusoidal term.

In this Chapter will be considerd the T-method, which is used by the "Europa" analysis group.

8.1.3 ω_a statistical uncertainty

The T method fit is performed using Eq. 4.13 obtaining the relevant parameter, ω_a. The optimization of the experimental system follows from minimizing the uncertainty on that parameter, namely $\delta\omega_a$. A detailed study [182] of the statistical methods gives guidance to the statistical power of any data set built using various weighting methods. The uncertainty on ω_a can be parameterized as

$$\delta\omega_a = \sqrt{\frac{2}{N(\gamma\tau_\mu)^2} \cdot \frac{\langle p^2\rangle_y}{\langle pA\rangle_y^2}}, \tag{8.3}$$

where N is the integrated number of decay positrons in the analysis, p is the weight function and therefore is method dependent, A is the asymmetry, and $\langle f\rangle_y$ is the value of f averaged over all detected positron energies above threshold. The parameter y is the fractional decay positron energy with respect to a maximum value; therefore y ranges from 0 to 1, with $y = 1$ corresponding to approximately 3.1 GeV. Figure 8.2 shows *differential* plots of N, A, and NA^2 vs. energy for a uniform acceptance detector. This plot illustrates the importance of the higher-energy positrons (those with the greatest asymmetry). The asymmetry is negative for lower-energy positrons; thus, a single low threshold can be expected to dilute the average asymmetry. The modification of the ideal curves due to the detector acceptance is significant;

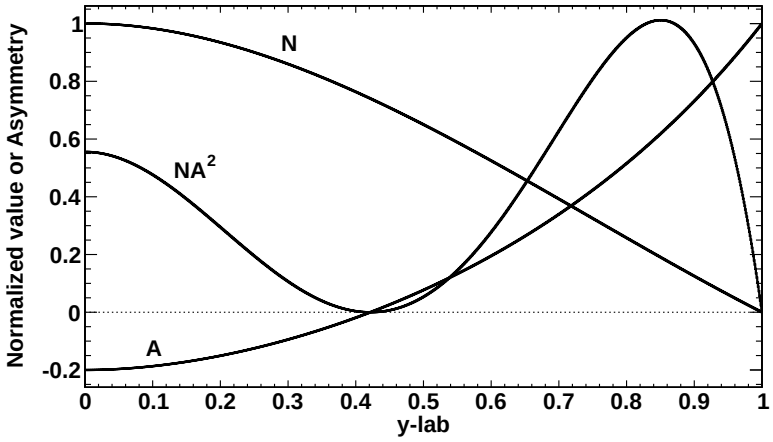

Figure 8.2: The differential distributions: normalized number of events (N), asymmetry (A), and the figure of merit (NA^2). Note, this plot assumes uniform detector acceptance across the full energy spectrum.

the detector placement has been designed to greatly favor the higher-energy events. Low energy positrons are more likely to curl between detectors and be missed. The acceptance impacts the values of N and A, which are functions of the energy-dependent detector acceptance.

In the T method, each event carries the same weight ($p = 1$) and the uncertainty $\delta\omega_a$ (Eq. 8.3) reduces to

$$\delta\omega_a = \frac{1}{\gamma\tau_\mu}\sqrt{\frac{2}{NA^2}}. \tag{8.4}$$

The figure of merit (FOM) that should be maximized to minimize $(\delta\omega_a)^2$ is NA^2. The value of the threshold that maximizes the FOM corresponds to $A \approx 0.4$ and an energy of 1.86 GeV, see Fig. 4.7. Therefore the relative uncertainty in ω_a is

$$\frac{\delta\omega_a}{\omega_a} = \frac{1}{\omega_a}\cdot\frac{\sqrt{2}}{\gamma\tau_\mu AP}\cdot\frac{1}{\sqrt{N}} \approx \frac{0.0398}{\sqrt{N}}. \tag{8.5}$$

The variable P represents the average polarization of the muons. The end-to-end beamline transport simulations project a value of 0.95 for the

stored muon polarization. For a statistical uncertainty on $\delta\omega_a/\omega_a$ of 100 ppb, $N = 1.6 \cdot 10^{11}$ fitted events will be required. The T Method is sufficient for reaching the goal of E989 and all benchmarks and estimates are based solely on this method. However there is an opportunity for additional precision by incorporating the other analysis techniques.

8.1.4 ω_a systematic uncertainties

To improve precision on ω_a measurement requires an extremely precise determination of the calorimeter crystal by crystal equalization both in term of the energy and response time. For this reason the group are studing the following calibration and reconstruction procedures (or analysis steps), see Chapter 6 or over in this Chapter:

- Fitting procedures;
- Calorimeter time calibration, clustering and energy calibration;
- Track-cluster association.

This analysis uses the method in which the data are divided into energy interval slices that are treated separately and then combined. The corrections to the functional form are identified. In this first study have been considered the following corrections (which will be described):

- Gain functions;
- Temperature;
- CBO;
- Lost muons;

- Pitch;
- Pile-up;
- Electric Field;
- Vertical Weist.

This Chapter is mostly dedicated to the calorimeter energy calibration, gain functions and lost muons corrections.

8.1.5 Fit corrections

Eq. 4.13 is the "5-Parameter Fit Function" and it represents the ideal case when muons orbits at the magic radius without any corrections (due to orbit, momentum, etc$\cdots$). In the real world we have to take in account these additional corrections to reach the high precision required by the experiment.

Gain corrections

Gain variation during the muon fill of 700 microseconds (μs) "mixes" different energies. Since phase and amplitude are energy dependent, any effect that combines together different energies within the same fill can cause a "phase shift" in Eq. 4.13.

The Laser system is the fundamental tool to reduce drastically the systematic error on ω_a determiantion, as shown in table 5.1. The gain correction will be discussed in Section 8.3.

Coherent Betatron Oscillation (CBO) correction

The beam has its own dynamics due to the magnetic and electric field applied in the storage ring by the dipoles, the kickers and the electrostatic

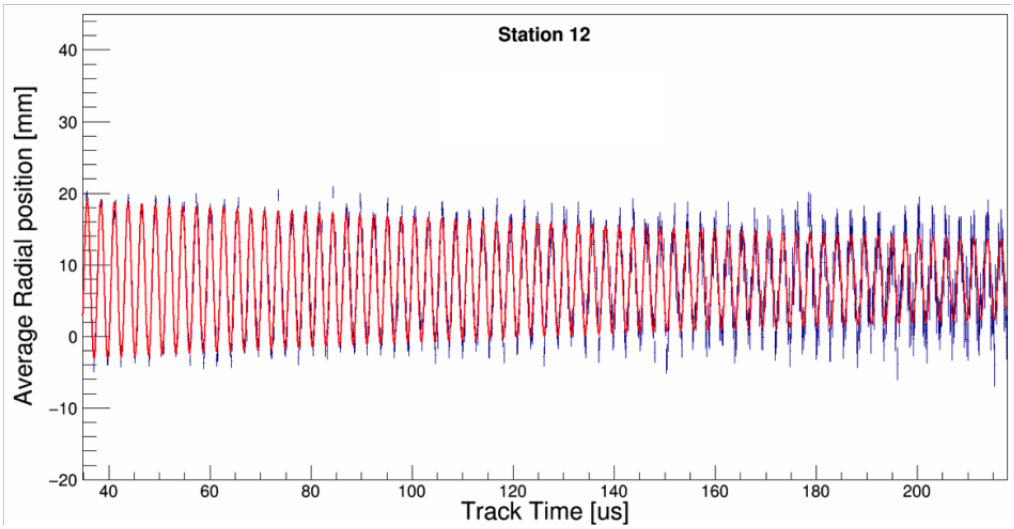

Figure 8.3: Average radial position of the beam as a function of time measured by the tracker station 12. The oscillation is due to CBO.

focussing quadrupoles. In particular it oscillates both in the radial and in the vertical directions with a typical frequency (f_x and f_y) that depends on the *field index* n, this phenomena is called Betatron Oscillation. The two frequencies can be related to the field by the following relations:

$$f_x = \sqrt{1-n} f_c \qquad f_y = \sqrt{n} f_c \ , \tag{8.6}$$

where f_c is the cyclotron frequency and n the field index. The first correction applied in this study is for CBO effect. We can define the CBO frequency as the difference

$$f_{CBO} = f_c - f_x \ . \tag{8.7}$$

This is the frequency at which a single fixed detector sees the beam coherently moving radially back and forth. In Fig. 8.3 is possible to see in one run the average radial position of the beam during the run and an oscillation of this position in time; the frequency of this oscillation is f_x.

This radial oscillation can be identified doing the FFT of the 5 Parameters

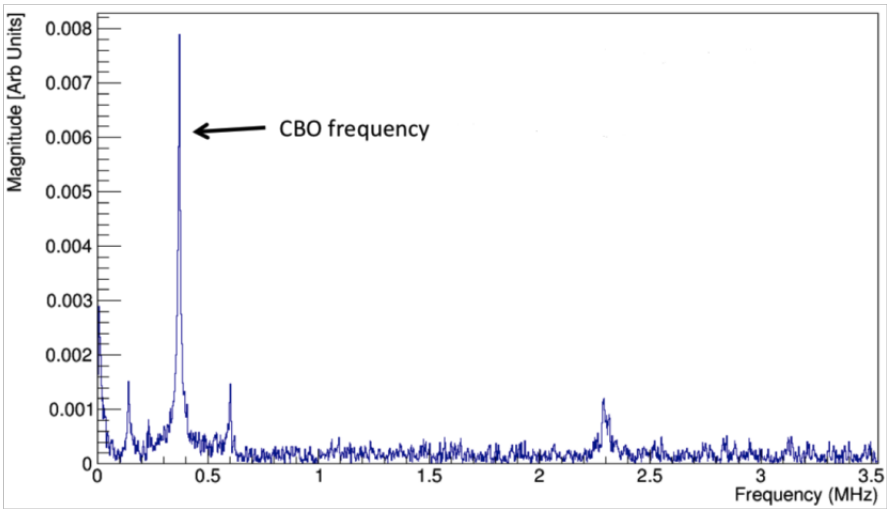

Figure 8.4: Fast Fourier Transform of the 5 Parameters fit residuals. It's possible to see a peak from the CBO frequency affecting the measure. Other peaks correspond to the $g-2$ frequency and to $f_{CBO} \pm g - 2$. The peak at ~ 2.4 MHz is the vertical waist frequency.

Fit as seen in Fig. 8.4.

CBO can affect the number of positrons hitting the calorimeter and thus introducing a systematic error on the fit ($\Delta\omega_a$). The effect can be taken into account during the fit with an additional term:

$$C(t) = 1 - A_c e^{-\frac{t}{\tau_c}} \cos \omega_c t + \Phi_c \tag{8.8}$$

where τ_c is the CBO lifetime and $2\pi \cdot \omega_c$ and Φ_c are the frequency and the phase of the oscillation. This 9 Parameters fit highly improves the measure of ω_a.

Pitch correction

It is related to the vertical oscillation of the beam. Pitch effect occours when the beam momentum is not perpendicular to the magnetic field direction. This effect reduces the ω_a and gives a ~ 0.3 *ppm* correction. The angle between momentum and field changes over time harmonically with a frequency f_y,

so the measure of vertical betatron oscillations allows to calculate the pitch correction.

Lost muons correction

It is a correction due to the muons lost in the storage ring during the time window of the measure. This loss can lower the number of positrons counts in the calorimeter and then affect the ω_a measure. The lost muons correction introduces an extra term in the fitting function (10 Parameters Fit). It will be discussed in Section 8.4.

Pile-up correction

It is related to the energy measured by calorimeters. It is possible, for two positrons, to hit the calorimeter at the same time (i.e. with a time difference below the time resolution of the detector). In this case, the energy measured by the detector is the sum of the energies of the two positrons. This produces a tail at the energy spectrum endpoint as shown in Fig. 8.5. Moreover a wrong energy measurement can lead to low energy positrons (whose spin is not related to their direction) introducing a systematic effect in the fit of ω_a. Pile-up can be reduced using faster calorimeters and photodetectors (as the ones chosen in E989), and identifying, by Calorimeter and Tracker information, the particles arrival coordinates and time.

Electric field correction

It is related to the $\overrightarrow{\beta} \times \overrightarrow{E}$ term in Eq. 4.13. This term cancels out when a muon has the magic $\gamma = 29.4$. Actually, due to the momentum spread, this term has to be considered in order to evaluate the electric field contribution to the anomalous precession frequency.

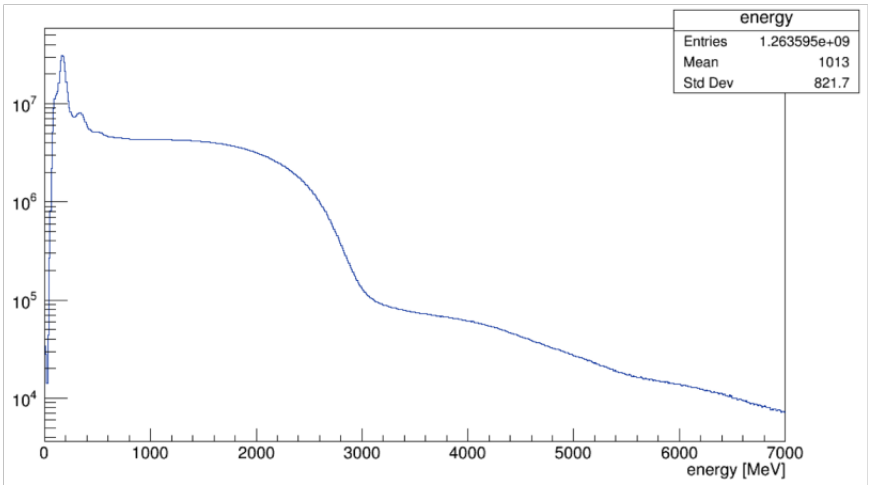

Figure 8.5: Energy spectrum measured by calorimeters. While the endpoint should be at ~ 3.1 GeV, the plot shows a long tail due to the pile-up events.

Vertical waist

It is an effect that changes the mean width of the beam. During the rotation of the beam, the mean width is observed to change with a frequency that is twice the f_y frequency. The vertical waist frequency can be defined as:

$$f_v = f_c - 2f_y. \tag{8.9}$$

So, the correction applied to the fit (14-Parameters fit) is the function:

$$V(t) = 1 - A_v e^{\frac{-t}{\tau_v}}(cos\omega_v t + \Phi_v). \tag{8.10}$$

8.2 Energy calibration

The calibration procedures of calorimeters from ADC counts to photo-electrons (p.e.) has been discussed in Chapter 5. Here will be described the calibration procedure which allows to pass from number of p.e. to the energy deposit.

In a calorimeter the charge measured in ADC is proportional to the deposited energy by a particle via the following relation:

$$Q = \Delta E(MeV) \cdot C \left(\frac{ADC}{MeV} \right), \tag{8.11}$$

where Q is the charge (integral of the pulse shape) in ADC counts, ΔE is the energy deposited (in MeV or GeV) by the particle in the material, and C is a calibration constant from ADC to MeV; C can be factorized as:

$$C = c_g \left(\frac{ADC}{n_{phe}} \right) \cdot c_e \left(\frac{n_{phe}}{MeV} \right). \tag{8.12}$$

The first term is the conversion factor between ADC counts to number of p.e. and is obtained from the laser system; the second is the number of p.e per MeV of energy deposited and obtained from the absolute energy calibration, which will be discussed in Section 8.2.2.

8.2.1 Gain factor

The gain factor is measured by the laser system sending in the calorimeter a laser pulse of a fixed intensity. The collected charge is:

$$Q = eGn_{phe}, \tag{8.13}$$

where n_{phe} is the number of photoelectrons in the SiPM, G is the gain factor and e is the electron charge. The relative error on the charge is:

$$\frac{\sigma_Q}{Q} = \frac{\sigma_G}{G} \oplus \frac{\sigma_{n_{phe}}}{n_{phe}} = \sqrt{\left(\frac{\sigma_G}{G} \right)^2 + \left(\frac{\sigma_{n_{phe}}}{n_{phe}} \right)^2}. \tag{8.14}$$

The term $\frac{\sigma_G}{G} \approx 10^{-3}$, so the dominant term in the sum is

$$\left(\frac{\sigma_{n_{phe}}}{n_{phe}} \right)^2 = \frac{1}{n_{phe}} \approx 10^{-3} \; for \; 1 \; GeV \; energy, \tag{8.15}$$

since $\sigma_{n_{phe}} = \sqrt{n_{phe}}$ (Poisson statistics). Eq. 8.14 becomes

$$\frac{\sigma_Q^2}{Q^2} = \frac{1}{n_{phe}} \tag{8.16}$$

and using the Eq. 8.13

$$\sigma_Q^2 = \frac{Q^2 eG}{Q} = c_g Q, \tag{8.17}$$

with $c_g = eG = \frac{ADC}{n_{phe}}$. So there is a linear relation (first order approximation) between the charge measured by the ADC and its variance. Changing the laser intensity (with the filter wheel) it's possible to determine the ADC to photoelectron conversion factor (see also Chapter 5).

8.2.2 Absolute energy calibration

Using a fixed energy process we can determine the energy calibration constant c_e measuring the charge in the SiPM knowing the deposited energy. There are two processes that can be used at this purpose: the endpoint of the positron spectrum (from the $\mu^+ \to e^+ \nu_e \overline{\nu}_\mu$ decay) and the MIP peak.

Endpoint

Endpoint of the energy spectrum is fixed by kinematics of the process. The momentum of the μ^+ entering the storage ring is selected at 3.1 GeV, the energy is $E_\mu = 3.102$ GeV (from the Energy-Momentum relation). This energy puts an upper limit to the energy of a decay positron. Fitting the charge of the energy spectrum endpoint, the calibration constant will be:

$$c_e^{endp}\left(\frac{n_{phe}}{GeV}\right) = \frac{Q^{endp}(ADC)}{3.1\ GeV \cdot c_g\left(\frac{ADC}{n_{phe}}\right)}. \tag{8.18}$$

MIP

A muon typically deposit MIP-like energies in a single crystal in each calorimeter as better described in the next Section 8.4.2. These particles lose a fixed amount of energy in a 14 *cm* crystal. This energy loss can be predicted with a MonteCarlo simulation of the particle traversing the calorimeter and confronted with the charge measured, so that

$$c_e^{MIP}\left(\frac{n_{phe}}{MeV}\right) = \frac{Q^{MIP}(ADC)}{\Delta E_0\ (MeV)\cdot c_g\left(\frac{ADC}{n_{phe}}\right)}. \tag{8.19}$$

8.2.3 The energy calibration procedure

For each crystal's charge Q_i (with $i = 1, 2, \cdots, 1296$), we can define:

$$\overline{Q}_i = \frac{Q_i}{c_g^i}. \tag{8.20}$$

where c_g^i is the gain factor for each crystal (determined by the laser system). The total energy deposited in the calorimeter is the sum of the single crystals energy ΔE_i:

$$\Delta E = \sum_i \Delta E_i = \sum_i \frac{\overline{Q}_i}{c_e^i}. \tag{8.21}$$

For each crystal $\overline{Q}_i$ can be calculated with the two following processes.

Endpoint

Endpoint pocedure can be used to determine an average value of all the c_e^i in the calorimeter. In order to get the positron energy spectrum, a clustering algorithm has to be applied to the hits. Eq. 8.21 can be modified as follows:

$$\Delta E = \sum_i \Delta E_i = \frac{1}{\widehat{c}_e}\sum_i \overline{Q}_i^{ep}, \tag{8.22}$$

where $\overline{Q}_i^{ep}$ is defined as in Eq. 8.20 with Q_i measured at 3.1 GeV and $\widehat{c}_e$ is an average value of the energy calibration constant (weighted on the clusters).

The $\widehat{c}_e$ approximation is correct as long as the differences between the c_e^i are smaller than $\sim 10^{-2}$.

MIP

Particles can be selected in each crystal and their energy spectrum compared with a Montecarlo simulation; each energy calibration constant c_e^i, can be then determined. This method requires, in order to know the amount of energy deposited by the MIP in the crystal, the point where the particle hits the crystal and its momentum direction.

The two methods in principle should give the same average result, this can be used as a check on the overall procedure. After the calibration, the deposited energy of each particle in the calorimeter can be determined. In the specific case of the Muon $g-2$ experiment positrons lose almost all their energy into the calorimeter[1], so the deposited energy corresponds to the total energy of the incoming positron:

$$E_{e^+} = \frac{Q(ADC)}{c_e\left(\frac{n_{phe}}{MeV}\right) \cdot c_g\left(\frac{ADC}{n_{phe}}\right)}. \tag{8.23}$$

8.3 Gain-related systematic effects on ω_a

Since phase and amplitude are energy dependent in Eq. 4.13, any effect that combines together different energies within the same fill can cause a "phase shift" as shown and in Fig. 8.32.

Gain variation during the muon fill "mixes" different energies, so any gain drifts over the short term time scale of a fill must be corrected at the analysis

[1] PbF_2 calorimeter crystal has very high density (7.77 g/cm^3), an assial dimension of $15 \cdot X_o$ radiation length($X_o = 9.3 - mm$) and designed as positrons absorber [124].

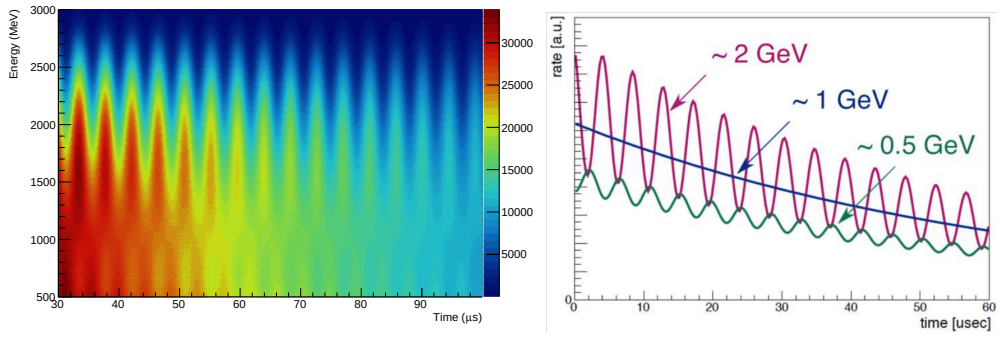

(a) (b)

Figure 8.6: The plot shows as combining together different energies within the same fill can cause a "phase shift".

Time scale	Correction	Method	Notes
>10 s	Long term	Out of Fill pulses	mostly corrects temperature variations
<700 μs	Short term	In Fill pulses	mostly corrects gain function for splash
~20 μs	Short term	In Fill Long Term Double Pulse	check of In Fill Gain Function
~20 ns	Very short term	In Fill Short Term Double Pulse	check of SiPM recovery

Table 8.1: Summary of laser methods applied for the calorimeters signals gain corrections.

stage, event by event for each calorimeter station and crystal. The gain correction function must be constructed using the known laser calibration pulses and evaluating the time stability of the overall energy spectrum, pileup-corrected. Figure 8.7 shows the perturbation of ω_a to be expected based on the value of the Gain variation.

To reach the goal of 20 ppb, the laser system provides "correction functions" which are applied at different time scales as shown in Tab. 8.1. In the following sub sections are shown the magnitude of gain variations monitored and the relative reduction, after the correction, performed by the Laser Calibration System. The steps staged to apply the laser corrections are described in the

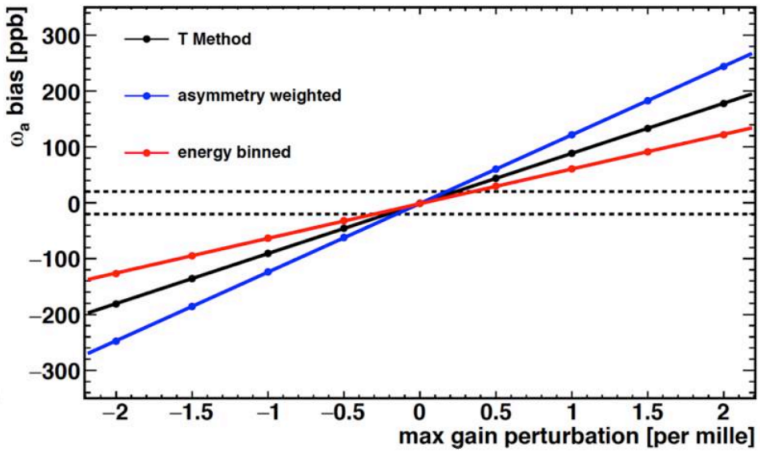

Figure 8.7: Perturbation of ω_a to be expected based on the value of the Gain variation. The colors show the different methods applied to obtain ω_a. The vertical scale is the size of the systematic shift in ω_a. The dashed lines delimit the region of the 20 ppb error acceptance.

previous Chapter 6.

8.3.1 Long term gain variation

In a time scale of 10 seconds or more the SiPM response varies mostly due to temperature variations.

Gain equalization

As described in previous chapters, the SiPM response is affected by the temperature of the device itself. To ensure a uniform response across the calorimeter, the 54 SiPM gains must be equalized as well as possible. Uncorrected temperature gradients across the calorimeter housing can cause gain differences between SiPMs in different positions. In order to take in account this effect, the SiPMs are separated into four groups based on their position within the calorimeter and each of these groups is connected to an independent bias supply. Additionally, each individual SiPM amplifier board contains

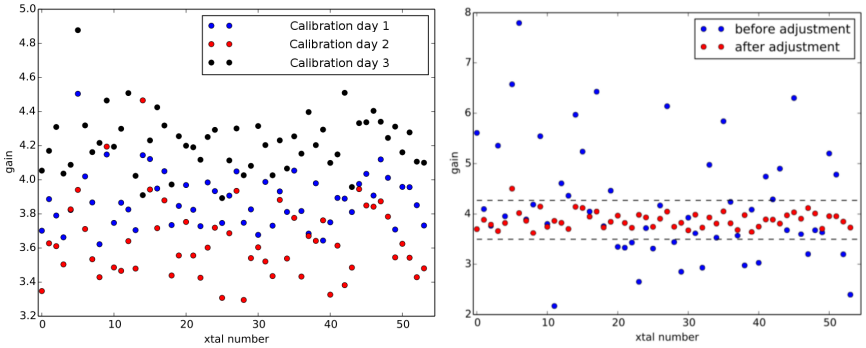

(a) (b)

Figure 8.8: (a) Example of the SiPM gains distribution in a calorimeter for three different days. (b) Gains distribution before and after adjustment.

a programmable gain amplifier (PGA) with an indipendent adjustable amplification range. The equalization process is iterative and consists of alternating laser calibrations (see Chapter 6 for details) and adjustments to the gains and bias voltages. The objective is to equalize the value of pulse-integral/p.e. for each segment. After several iterations, equalization of the order of 10% has been achieved (an example is shown in Fig. 8.8). Limits to the procedure are due to the statistics and the discrete gain scale of the PGA.

Out of Fill correction

The SiPM's Gain fluctuations, due to temperature variations, can be corrected by firing laser pulses between muon fills (out of these fills), named "Out of Fill" pulses (out-of-fill). The correction factor, applied for each of 1296 crystals of the $g-2$ calorimeter, in each bunch of a full dataset, is the following:

$$C^{OoF} = \frac{G}{G_0} = \frac{L}{L_0} \cdot \frac{SM_0}{SM}, \tag{8.24}$$

where the muon fill (in-fill) gain pulses are normalized by the average out-of-fill SiPM pulse amplitude L. L_0 is the SiPM average pulses amplitude of

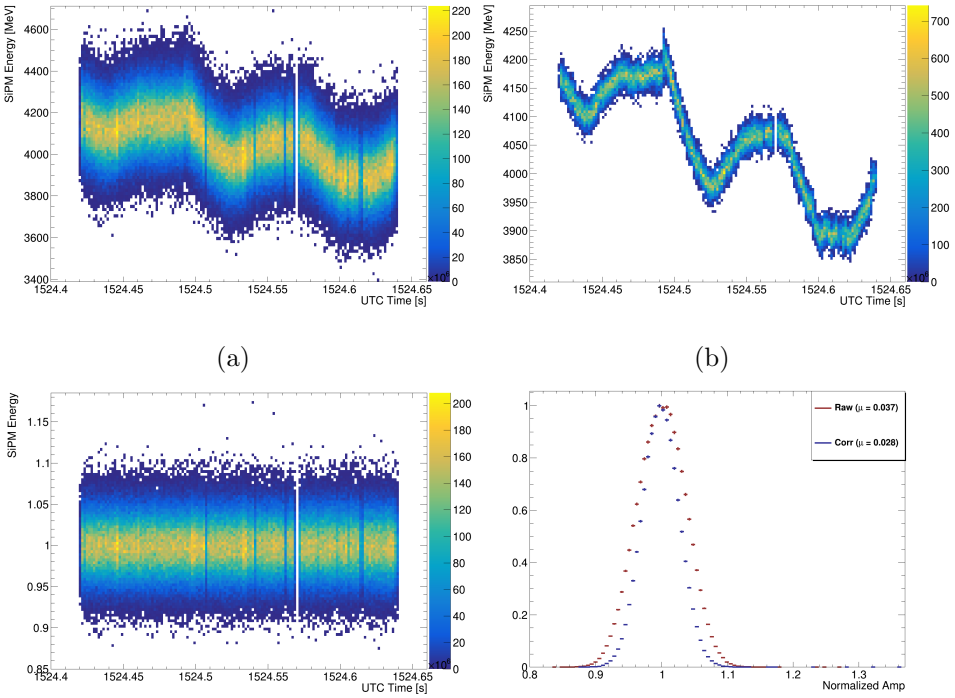

Figure 8.9: The results of the out-of-fill correction. (a) The SiPM amplitude not corrected. (b) The out-of-fill correction. (c) The SiPM amplitude corrected. (d) The comparision of SiPM energy distribution width before and after the out-of-fill correction.

a refence run (the same run is used for the energy calibration, see previous Section 8.2.2). Each SiPM pulses is also corrected for fluctuations in the laser amplitude using the Source Monitor signal SM[2]. The results of the out-of-fill correction, applied at dataset used in the analysis described in this Chapter, are shown in Fig. 8.9, where the absolute correction as large as few % and the SiPM, energy distribution width, before and after this correction is 3.7% and 2.8%, respectively.

[2]Note that this expression does not include effects due to light transmission that has to be studied separately with Local Monitors.

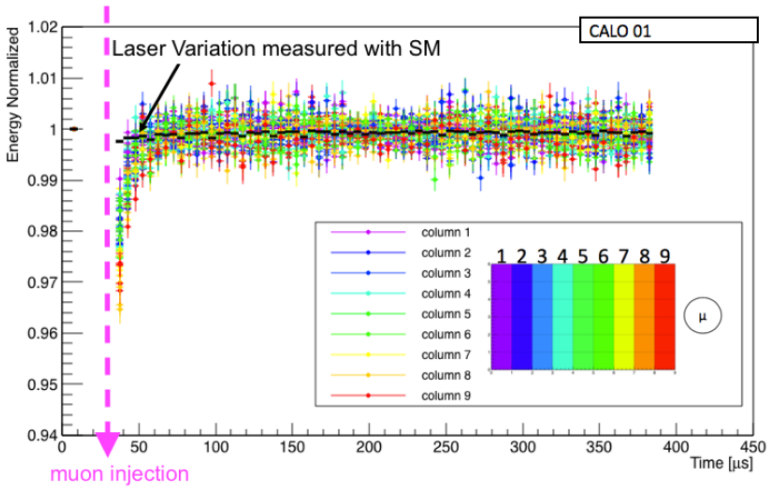

Figure 8.10: Gain variation of SiPM during the muon fill. As shown it is higher at early-time and in the calorimeter's side near the ring, calorimeter crystal column 9 in figure.

8.3.2 Short term gain variation

The gain variation of SiPM, during the muon fill (in-fill), is caused by the positron rate (higher at early-time, the so colled "splash" and in the calorimeter's side near the ring) and by the power supply recovery time, as shown in Fig. 8.10.

In Fill correction

An uncorrected variation of the SiPM response during the muon fill has immediate repurcussions on the ω_a fit. Therefore the most relevant correction applied to positron pulses is the in-fill gain (IFG) function. The function is built using laser pulses intermixed with the positron data in a subset of events, once every 11 fills (prescaling), in standard data-taking. The IFG function is built based on the following equation:

$$G_{IFG}(t_i) = \frac{SiPM_{in-fill}}{SM_{in-fill}} \cdot \frac{SM_{out-of-fill}}{SiPM_{out-of-fill}}. \tag{8.25}$$

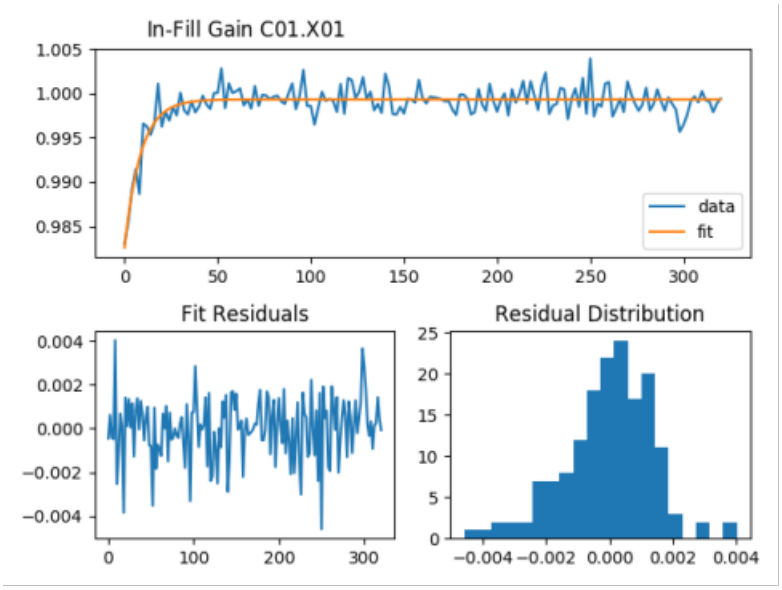

Figure 8.11: Example of IFG function for one calorimeter crystal, built using laser pulses intermixed with the positron data, in a subset of events in standard data-taking. the IFG is modeled by an exponential function.

The IFG function is subsequently modeled and applied to the positrons in the dataset which was used to build the model. The IFG is modeled, at present, by the following simple exponential decay function:

$$f(t) = g \cdot \left(1 – a \cdot e^{-\frac{t-t_0}{\tau}}\right), \tag{8.26}$$

where results $\tau \sim 6$ μs in a range of 2-8 μs, for different dataset. The IFG is stable across runs and, starting from 30μs after injection, the residuals of IFG are within $\sim 4 \cdot 10^{-4}$, as shown in Fig. 8.11.

As preliminary results, the effect of IFG on ω_a fit is shown in Fig. 8.12 where we obtain ΔR ~30ppb (at this stage fit procedure is not optimized: $\chi^2/ndf \approx 1.27$).

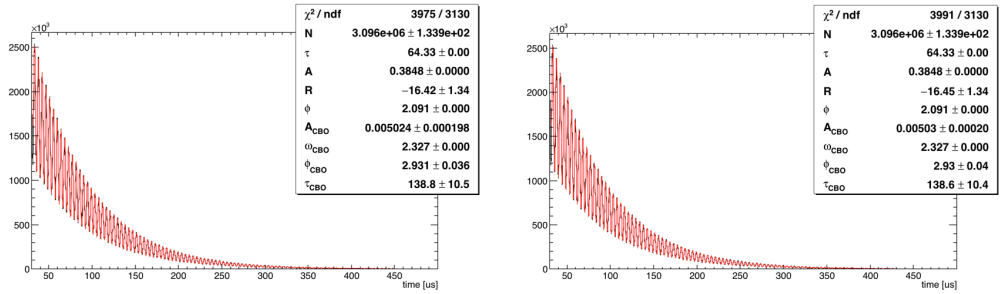

(a) Without IFG correction. (b) With IFG correction.

Figure 8.12: The effect of IFG on ω_a fit. Before (a) and after (b) the IFG correction shows difference on residuals ∼30ppb.

In Fill "Long Term" Double Pulse investigation

An independent check of the IFG function can be performed with the Long Term (∼20 μs) Double Pulse procedure (LTDP) described in the Chapter 6, using the Double Pulse System described in the Chapter 5.

An initial burst mimics the muon "splash". A second test pulse is sent after tens of μs. This technique allows to validate the IFG measurements in a controlled environment.

At present the LTDP is still under definition. The SiPM response is parametrized with an exponential fit function similar to that of Eq. 8.26, used to model IFG function.

$$G(t) = N_0 \cdot \left(1 – a \cdot e^{-\frac{t}{\tau}}\right), \tag{8.27}$$

Preliminary results shows a decay time of ~ 6.6 μs, as observed in IFG.

The LTDP allows to build an analitical model of the initial muon "splash" as a burst of N pulses of known height to which the SiPM respond with an exponential gain function. The convolution of the SiPM response function with the initial burst is under study. It should provide an analytical function to be compared with IFG function.

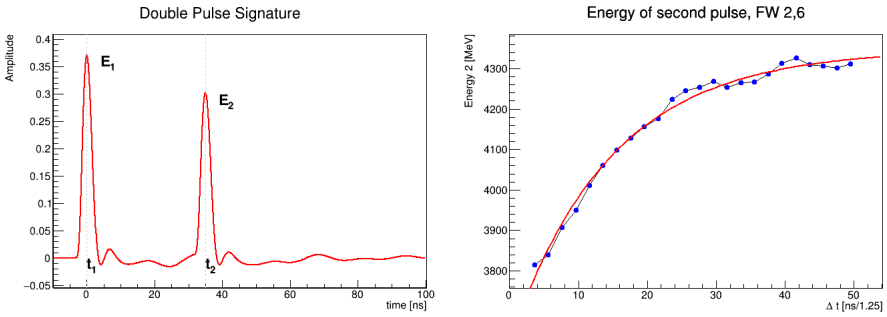

(a) (b)

Figure 8.13: (a) Example of double pulses digidized. A special pulse fitting procedure has been used for double pulse events. (b) The effect of a first pulse in lowering the second pulse energy. In the STDP tests have been used the filter wheel 1 and 2 setted respectivily in position 2 (trasmission 79%) and 6 (trasmission 36%).

8.3.3 Very short term gain variation

As described in Chapter 6 (see Fig. 6.31), a first light pulse in the calorimeter crystals, causes a systematic reduction in the size of a second pulse, due to charge depletion in the capacitive components of the system's electronics. If the gain response is well understood, the effect can be corrected in the positron events. In a very short term (∼20 ns) time scale two pulses are sent with tens of nsec time difference (see Fig. 8.13a) and the gain measured is fitted as an exponential function, as shown in Fig. 8.13b:

$$G(\Delta t) = N_0 \cdot \left(1 – a \cdot e^{-\frac{\Delta t}{\tau}}\right). \tag{8.28}$$

Differently from individual laser templates on a per SiPM basis were needed to extract precise pulse amplitudes [140, 154], in STDP procedures has been used a double pulse algorithm, defined in the Eq. 8.29. The fitting routine allows all 5 input parameters to float with reasonable initial guesses and the

result is shown in Fig. 8.13a.

$$f_{STDP}(b, a_1, t_1, a_2, t_2) = a_1 \cdot f_{pulse}(t_1) + a2 \cdot f_{pulse}(t_2) + b. \tag{8.29}$$

An estimation of the effect on ω_a of the STDP correction has been done by using a constant value of $a = 0.1$ and $\tau = 12$ ns. Preliminary result, reported in Eq. 8.31, says that the STDP correction has more effect at early fill times, see Fig. 8.14:

$$\Delta\omega_a \sim 230ppb \ (t_0 = 32 \ \mu s) \tag{8.30}$$

$$\Delta\omega_a \sim 50ppb \ (t_0 = 40 \ \mu s) \tag{8.31}$$

The STPD correction is still under study and at least three arguments must be better understood:

- Fit parameters $a(E_1, E_2, i)$ and $\tau(E_1, E_2, i)$ are function of the positron energy and of the cristal number i. Therefore, the STDP test runs are under data-taking, with different position of the filter wheels 1 and 2, to study the effect of two pulses sequence at the very short time scale.

- We observe an oscillation of the gain respect to the fitting with a simple exponential after $\sim$30 μs, see Fig. 8.13b. It is possible that this effect is due to an inaccurate template fit for the double pulse: The amplitude of the second pulse is affected by the ringing by the first pulse echo. This oscillation effect vanishes when the ratio E_2/E_1 is higher. This artifact is therefore in the order of $< 1\%$ of the gain in any case additional studies are in progress.

- Time distribution of Double Pulse. The STDP correction function is currently defined in the time interval [6.25, 75] ns. Above 75 ns the

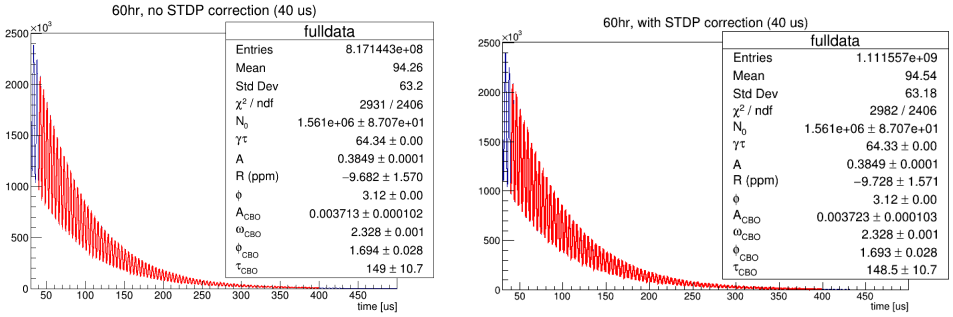

(a) Without STDP correction.

(b) With STDP correction.

(c) Without STDP correction.

(d) With STDP correction.

Figure 8.14: The effect of STDP correction on ω_a fit. Before (a) and after (b) the STDP correction shows difference on residuals ∼50ppb. Starting the fit from 32 μs, before (c) and after (d) the STDP correction shows difference on residuals ∼230ppb.

effect seems to be negligible ($7 \cdot 10^{-4}$ correction at 75 ns). Below 6.25 ns there is a transition region which requires some specific analysis which involves also pile up corrections.

8.3.4 Summary

The laser system allows to calibrate the calorimeter at different time scales. The laser pulses, taken within and outside the muon fill, are currently used to correct SiPM response and this correction may be as large as 20%.

The Long Term Double Pulse system allows to cross check in-fill Gain corrections and the initial STDP tests made it evident that the double pulse gain response function must be considered for each crystal/SiPM pair. Further STDP tests will explore the space of the gain functions with different amplitudes for the first and second pulses in the test. This can easily be achieved using the filter wheels in the laser system.

8.4 Lost muons correction study

During their travel into the storage ring part of the muons can be lost mainly due to the interaction with collimators or because their injection angle is different from the that of design one. The probability for a muon to be lost is not constant in time, as the muons at the outer boundary of the phase space are lost preferentially at early times. The lost muons are expected to have a different average spin polarization than the stored muons due to muons being created at different points in the muon production beamline, so that a shift is also expected in ω_a. The relative number of lost muons needs to be minimized and quantified. As reported in the table 5.1, a new collimators system in the E989 experiment has been designed to reduce the systematic error due to lost

muons to the limit of 30 ppb. The E989 goal is to keep the relative muon losses at or below 10^{-4} per muon lab frame lifetime (τ).

Monte Carlo (MC) simulation studies of the E989 muon storage ring have been used to evaluate the lost muons and to optimize the storage of the muon beam by estimating the operating parameters for the inflector magnet, kicker, surface coils, and electrostatic quadrupole system [183]:

- The inflector magnet provides an almost field free region to transport the beam into the storage region while minimizing perturbations to the storage ring magnetic field;

- The muons injected into the storage ring are off the central orbit, and the kicker uses a magnetic field to "kick" them into the storage ring acceptance;

- The surface coils are used to adjust the storage ring magnetic field during operations;

- The electrostatic quadrupole system uses electric fields to provide weak vertical focusing.

The lost muons contribution to the systematic effect on the ω_a measure, must to be measured and accounted for in the final fit.

Starting from the case of a perfect exponential decay where no muons are lost from the storage ring, the number of muons that decay dN_μ in a time period dt is proportional to the number of muons in the storage ring N_μ. This is the definition of exponential decay, where the proportionality constant is commonly defined as $1/\tau$,

$$\frac{dN_\mu}{dt} = -\frac{N_\mu}{\tau}. \tag{8.32}$$

Note that since we are talking about the number of muons stored, there is no $g-2$ modulation. Eq. 8.32 is a first-order ordinary differential equation (ODE), which is easily solved through separation of variables,

$$\int_{N_{\mu 0}}^{N_\mu} \frac{1}{N'_\mu} dN'_\mu = -\int_{t_0}^{t} \frac{1}{\tau} dt', \tag{8.33}$$

$$N_\mu(t) = N_{\mu 0} e^{-\frac{t-t_0}{\tau}}. \tag{8.34}$$

$N_\mu(t)$ in Eq. 8.34 describes the number of muons still stored at a time t given that a total of $N_{\mu 0}$ existed at t_0. However, in addition to decay, we know that at any specific instant in time muons are being lost from the storage ring due to scattering. Only a fraction c of the total lost muons $L(t)$ at a time t can be observed and is given by $cL(t)$ .Adding the additional loss mechanism to the original differential Eq. 8.32 yields

$$\frac{dN_\mu}{dt} = -\left(\frac{N_\mu}{\tau} + cL(t)\right). \tag{8.35}$$

The solution to this differential equation has been derived through two different approaches [105]. In the traditional solution, Eq. 8.35 is once again treated as a separable ODE,

$$\int_{N_{\mu 0}}^{N_\mu} \frac{1}{N'_\mu} dN'_\mu = -\int_{t_0}^{t} \left(\frac{1}{\tau} + \frac{cL(t')}{N_\mu(t')}\right) dt'. \tag{8.36}$$

In order to remove the $N_\mu(t)$ from the integrand on the right of Eq. 8.36, it is assumed that the muon losses are small enough that the approximation,

$$N_\mu(t) \approx N_{\mu 0} e^{-\frac{t-t_0}{\tau}}, \tag{8.37}$$

is valid when used in the denominator of the loss term. Making the substitution yields,

$$\int_{N_{\mu 0}}^{N_\mu} \frac{1}{N'_\mu} dN'_\mu \approx -\int_{t_0}^{t} \left(\frac{1}{\tau} + \frac{c}{N_{\mu 0}} L(t') e^{\frac{t'-t_0}{\tau}}\right) dt', \tag{8.38}$$

which is then easily solved by integration to give,

$$N_\mu(t) \approx N_{\mu 0} e^{-\frac{t-t_0}{\tau}} \left[exp\left(-\frac{c}{N_{\mu 0}} \int_{t_0}^{t} L(t') e^{\frac{t'-t_0}{\tau}} dt' \right) \right]. \tag{8.39}$$

Expanding the solution in a Taylor series we obtain,

$$N_\mu(t) \approx N_{\mu 0} e^{-\frac{t-t_0}{\tau}} \left[1 - \frac{c}{N_{\mu 0}} \int_{t_0}^{t} L(t') e^{\frac{t'-t_0}{\tau}} dt' + \cdots \right]. \tag{8.40}$$

If only the first two terms from the Taylor expansion in Eq. 8.40 are used, decay positrons can then be inferred rewriting the Eq. 4.13, with $N_0(E_{th}) = A_{e^+}(E_{th}) N_{\mu 0}$, as follows:

$$N(t, E_{th}) = N_0(E_{th}) e^{-\frac{t-t_0}{\tau}} \Lambda(t) [(1 + A(E_{th}) \cos(\omega_a (t - t_0) + \phi(E_{th}))], \tag{8.41}$$

where the multiplicative factor $\Lambda(t)$ is:

$$\Lambda(t) = 1 - \frac{c}{N_{\mu 0}} e^{-\frac{t_0}{\tau}} \int_{t_0}^{t} L(t') e^{\frac{t'}{\tau}} dt' = 1 - K_{LM} \int_{t_0}^{t} L(t') e^{\frac{t'}{\tau}} dt', \tag{8.42}$$

where $L(t)$, as defined before, is the number of lost muons as function of time in the fill window ($t \in [0, 700 \mu s]$), $\tau = \gamma \tau_0 = 64.4 \mu s$ is the decay constant and $K_{LM} = \frac{c}{N_{\mu 0}} e^{-\frac{t_0}{\tau}}$ is an acceptance factor. The constant K_{LM} can be extracted from the fit of the ω_a. A Montecarlo simulation of the ring can give an estimation of K_{LM} value. To find the function $L(t)$, a way to identify lost muons in the calorimeters must be found.

8.4.1 Source of backgrounds

The muon loss signal is expected to be embedded in a much higher background of decay positrons. The decay positrons contribute to two different types of backgrounds: *Uncorrelated* two low energy e^+ backgrounds (random coincidences) and *correlated* single e^+ background. The random coincidences

occurring when two independent decay positrons or a second lost muon are randomly detected in the coincidence time window Δt. *Correlated* background is due to a single e^+ that can pre-shower and deposit MIP-like energies in two consecutive calorimeters. A cut-based analysis has been performed to reduce the correlated in-time-window backgrounds.

The analysis presented in this Section has a timing cut of $t > 30\mu s$. This cut is applied to exclude the so-called beam "splash", that's the high number of lost particles right after the beam injection into the ring. This effect can produce fake signals in the calorimeters.

8.4.2 Muon's energy deposition and clustering

Muons with momentum 3.1 GeV behave in matter as a minimum ionizing particles, so they deposit in the crystals a reasonably fixed amount of energy according to the Bethe-Bloch formula [184]. For muons in Lead Fluoride the energy loss per unit of length is $dE/dx = 1.55\ MeV cm^2 g^{-1}$ [44], so we can estimate the mean energy deposit in a single 14 cm crystal ($\rho = 7.77\ g/cm^3$):

$$E_{dep} = dE/dx \rho x \approx 169\ MeV. \tag{8.43}$$

A Geant4 [185] simulation of 3.1 GeV muons in a single P_bF_2 crystal shows that the peak of energy is around 170 MeV in agree with the calculation in Eq. 8.43, as shown in Fig. 8.15.

The muons as MIP-like particles, produce a Landau-like energy distribution in the E989 calorimeters, as described in the following [186, 187, 188]. However the spectrum can be distorted by side effects like leftover positrons counted as coincidences. The collision theory introduce a parameter, k, as the ratio between the mean energy loss by a particle during the process (ξ) and the

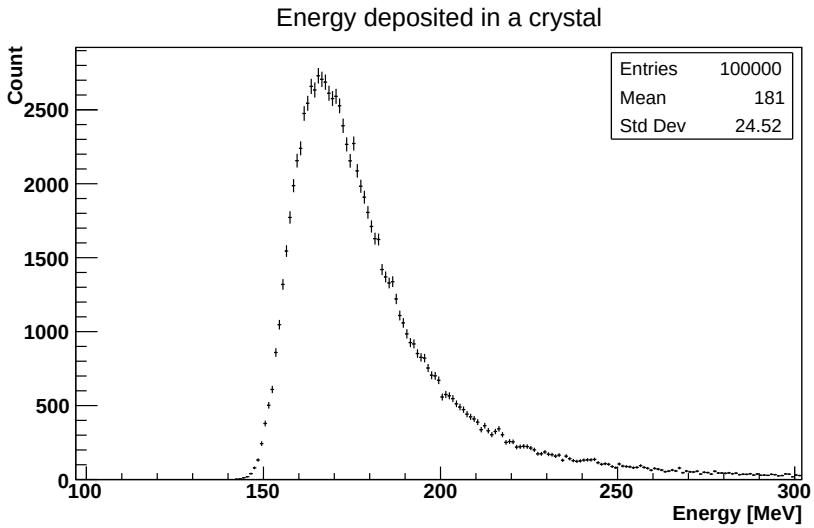

Figure 8.15: Geant simulation with an azial muon that hit a sigle calorimeter crystal.

maximum energy that the particle can exchange during a collision:

$$k = \frac{\xi}{E_{max}}. \tag{8.44}$$

This parameter is used to characterize the large fluctuation that can occour in the energy loss by a particle during a ionisation process. The maximum allowed energy transfer during a collision is given by:

$$E_{max} = \frac{2m_e\gamma^2\beta^2}{1 + 2\gamma\frac{m_e}{m_x} + \frac{m_e}{m_x}^2}, \tag{8.45}$$

where $\gamma = \frac{E}{m_x}$ is the Lorenz's factor of the incident particle, E it's energy, β it's speed in units of c, m_x it's mass and m_e is the electron's mass. In case $m_x >> m_e$, Eq. 8.45 can be expressed as:

$$E_{max} \approx 2m_e\gamma^2\beta^2. \tag{8.46}$$

From the Rutherford's scattering cross section, ξ can be defined as:

$$\xi = \frac{2\pi z^2 e^4 N_{Av} Z\rho\delta x}{(4\pi\varepsilon_0)^2 m_e\beta^2 c^2 A}, \tag{8.47}$$

where z is the charge of the incident particle in units of e and β it's speed in units of c; Z, ρ, A and δx are the charge, density, atomic number and thickness of the material transversed by the particle; finally N_{Av} is the Avogadro's constant and m_e the electron mass. All the variables used are in SI units [3]. With all the constants set, Eq. 8.47 becomes:

$$\xi = 1.534 \cdot 10^{-6} \frac{z^2 Z}{\beta^2 A}, \rho \delta x [MeV] \tag{8.48}$$

the parameter k becomes smaller for thin[4] materials and for relativistic particles ($\beta \to 1$). Two regimes can be identified depending by the value of k:

- $k > 10$, the gaussian regime, is when the mean energy loss is greater than the maximum energy transfer for a single collision. It occours when all or most of the energy is deposited by the particle in a large number of small collisions (each with its probability function); since the number of collisions is large, central limit theorem can be applied and the overall energy loss distribution becomes gaussian. This case applies to non relativistic particles in a thick[5] material;

- *Small k* applies to relativistic particles in thin materials, and to electrons under any condition. For $0.01 < k < 10$ the energy distribution follows the Vavilov distribution, for $k < 0.01$ it follows the Landau distribution.

In our experiment:

$$E_{max} = 875.35 \ MeV, \tag{8.49}$$

with $\rho = 3.1 \ GeV$ and, using for the P_bF_2: $\rho = 7.770\dot{1}0^3 kg/m^3$, $Z = 100$, $A = (246)\dot{1}0^{-3}$ mol kg and $\delta x = 0.14 \ m$; Eq. 8.47 gives

$$\xi = 6.79 MeV \tag{8.50}$$

[3] A is usually given in $g \cdot mol^{-1}$ units, needs to be scaled in kilograms.

[4] Its radiation lenght is much greater than thickness of the material.

[5] Its radiation lenght is comparable or less than thickness of the material.

The k parameter then is:

$$k = 7.76 \cdot 10^{-3}, \tag{8.51}$$

so the deposited energy distribution for 3.1 GeV muons in a 14 cm P_bF_2 crystal is a Landau distribution.

Reconstruction

As it will be shown afterwards, a muon deposits most of its energy in one crystal, with only 4% of cases with the energy shared between neighboring crystals. A clustering algorithm has been developed by calculating a logarithmic energy-weighted position and time (as given by Eq. 8.53) of the crystal hits in a calorimeter [156]. It groups together calibrated crystal hits and gives as output an arbitrary number of reconstructed decay parameters, called "clusters".

$$\begin{aligned} X &= \left(\sum W_{crystal} \cdot X_{crystal}\right) / \sum W_{crystal} \\ Y &= \left(\sum W_{crystal} \cdot Y_{crystal}\right) / \sum W_{crystal} \\ t &= \left(\sum W_{crystal} \cdot t_{crystal}\right) / \sum W_{crystal}. \end{aligned} \tag{8.52}$$

where $W_{crystal}$ is chosen as

$$W_{crystal} = max\left\{0, \left(W_0 + log\frac{E_j}{\sum_j E_j}\right)\right\} \tag{8.53}$$

with the free parameter W_0 derived empirically.

The sequence of steps in this algorithm is applied in the following order:

- First: Time partitioning sort fit results from a given island of pulses by time group;
- Second: After, cluster spatial separation runs on positron hits pulses grouped by time. It is based on finding peaks in E/E_{max} far from max crystal;

- Third: Finally iterative procedure find arbitrary number of separate clusters energy partition, according to $3x3$ sums surrounding cluster centers, scaled to match overall total energy.

Following are listed the improvements in the reconstruction due to the clustering algorithm:

- Spatial resolution of 2 mm at 2 GeV;
- Time partitioning with $\Delta T <\sim 5\ ns$;
- 75% of overthreshold pileup events resolved.

8.4.3 Coincidence analysis

There are different ways to identify lost muons. Muons that get kicked out by the collimators punch through calorimeters as minimum ionizing particles (MIPs), where the calorimeters are located every 15° around the storage ring. Muon deposits ∼170 MeV into a calorimeter crystal when passing through it, unlike the decay positrons which typically produce an electromagnetic shower that deposits almost all of the energy into the calorimeter. These two distinct behaviors and the detector's geometry that permit to consider double and triple coincidences in the calorimeters allow for the isolation of lost muons. In fact a muon exiting the orbit curls inside the ring. Due to their nature, muons can cross matter without stopping in the calorimeter, so the trajectory can cross two or more calorimeters, as shown in Fig. 8.16.

Selection cuts

In this analysis the lost muons algorithm finds a hit (signal) in one calorimeter (let's call it n) with the request that this hit fires less than three crystals

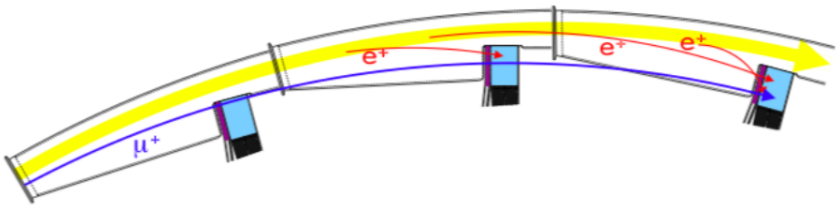

Figure 8.16: Lost Muon triple coincidence event scheme. The yellow arrow represents the beam, the blue one the muon.

(ionization due to muons is almost localized in one crystal). If a positive hit is found the algorithm looks for a signal in the $(n+1)$ calorimeter and calculates the time $\Delta t_{21} = t_{n+1} - t_n$. There is a double coincidence if:

- Time separation: $5\ ns \leq \Delta t_{21} \leq 7.5\ ns$;
- Energy difference: $\Delta E = abs(E_{n+1} - E_n) \leq 100\ MeV$;
- MIP-like energy events $50 < E < 500\ MeV$.

For a triple coincidence we look also for hits in the $(n+2)$ calorimeter. In this case we will also have $\Delta t_{32} = t_{n+2} - t_{n+1}$ and $\Delta t_{31} = t_{n+2} - t_n$, so that:

- Time separation: $5ns \leq \Delta t_{32} \leq 7.5\ ns$ and $10\ ns \leq \Delta t_{31} \leq 15\ ns$;
- Energy differences:
  $\Delta E_{32} = abs(E_{n+2} - E_{n+1}) \leq\ 100\ MeV$
  $\Delta E_{31} = abs(E_{n+2} - E_n) \leq\ 100\ MeV$;
- MIP-like energy events $50 < E < 500\ MeV$.

Consecutive calorimeters $(n+1$ and $n+2)$ don't have any restriction to the number of crystals fired. Using triple coincidences helps to reduce the positrons' background improving the muons identification (on the downside triple coincidences loose some of the statistics).

Timing cuts can be justified by the following consideration:

A muon with $\gamma = 29.3$ has a speed $v = 0.99942c$, and takes about 6.2 ns to cover the distance between two calorimeters ∼1.8 m. Fig. 8.17a shows the time difference between two consecutive calorimeters in a double coincidence. The plot shows a sharp peak at 6.2 ns as expected. In order to measure the peak a gaussian fit is applied to the histogram. The fit shows a mean value of $(6.22 \pm 0.40\ ns)$ that is used for the double coincidence cuts, within $\sim 3\sigma$. Similarly, in Fig. 8.17b are plotted the time differences between two consecutive calorimeters (the second and the first and, the third and the second) and the two non consecutive calorimeters (the third and the first), in a triple coincidence. The plot shows three sharp peaks, two in the region of 6.2 ns and one in the region of $2\Delta t \approx 12.4\ ns$ as expected. A gaussian fit is applied to all three peaks and the mean values (compatible with the double coincidences) are used to define cuts for the triple coincidences, within $\sim 3\sigma$. The results are:

- $\Delta t_{21} = (6.22 \pm 0.40)\ ns$;
- $\Delta t_{32} = (6.22 \pm 0.41)\ ns$;
- $\Delta t_{31} = (12.36 \pm 0.43)\ ns$.

The energy cuts are justified by the following consideration:

As described in the previous Section 8.4.2 muons at 3.1 GeV behave like Minimum Ionizing Particles (MIPs), so they deposit a fixed (∼170 MeV, see next sub Section) amount of energy in the crystal they cross, so we can reasonably expect that an energy cut for E >50 MeV will redeuce low energy deflected muons. As shown in Fig. 8.18 absolute energy differences ΔE_{21} spectrum in double coincidences are centered at zero and have a flat tail over ∼

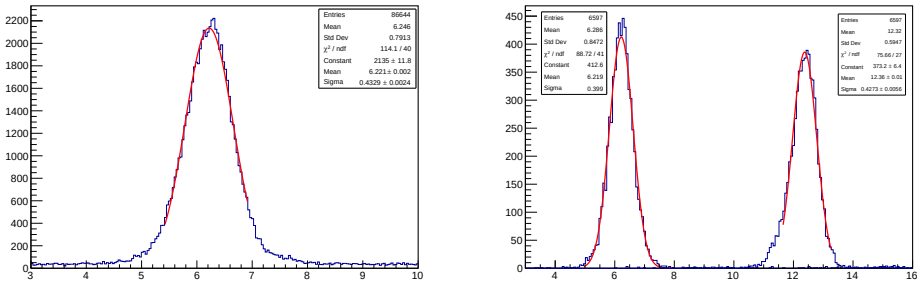

(a) Double coincidences. The plot shows a peak at 6.24 ns as expected

(b) Triple coincidences. The plot shows peaks at 6.2 ns and 12.4 ns as expected.

Figure 8.17: Time differences between calorimeters in the double and triple coincidences. The fit applied is gaussian (see text). (a) Time difference $\Delta t_{21} = t_{n+1} - t_n$ between two consecutive calorimeters in the double coincidences. The plot shows a peak at 6.24 ns as expected. (b) Time difference between consecutive and non consecutive calorimeters in triple coincidences. calorimeter$_i$-calorimeter$_j$ is the time difference between calorimeters i and j ($\Delta t_{ij} = t_i - t_j$).The plot shows peaks in two regions: 6.2 ns and $2 \cdot 6.2$ ns = 12.4 ns as expected.

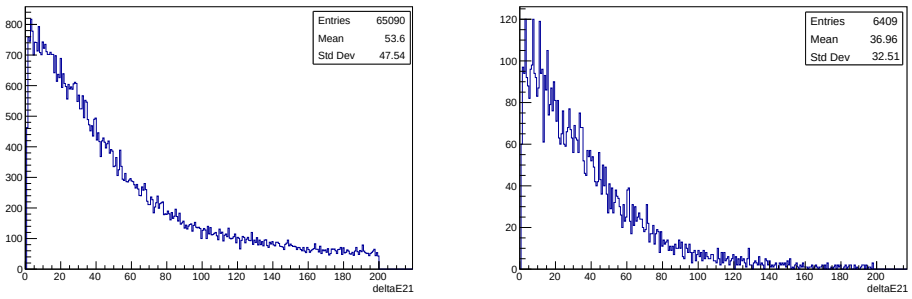

(a) Double coincidences ΔE_{21} spectrum. (b) Triple coincidences ΔE_{21} spectrum.

Figure 8.18: Lost muons ΔE_{21} energy spectrum in the calorimeter identified with double and triple coincidences. A long flat tail of backgroun is present over 100 MeV (a) the tail is extremily reduced in triples lost muons ΔE_{21} energy spectrum (b).

100 Mev, not present in triple coincidences ΔE_{32} or ΔE_{31} spectra. So an additional cut over ΔE_{21} was applied in double coincidences, also kept in triples, to remove background from these random coincidences.

The improvement on χ^2 Landau fit of double coincidences energy spectrum is shown in Fig. 8.19.

The search for coincidences is done from calorimeter 1 to calorimeter 24 (for the 24^{th} calorimeter $n+1=1$ and $n+2=2$ in a triple coincidence) to find the number of lost muons crossing the calorimeters during the whole run. The time distribution of the lost muons is the function $L_i(t)$, where $i=2,\ 3$ is an index to identify if the distribution is from double or triple coincidences. The $L_i(t)$ is then used to calculate the $\Lambda(t)$ function and this correction is applied, together with the CBO correction, to fit the wiggle plot with the 10-Parameters function and in order to obtain the measure of ω_a.

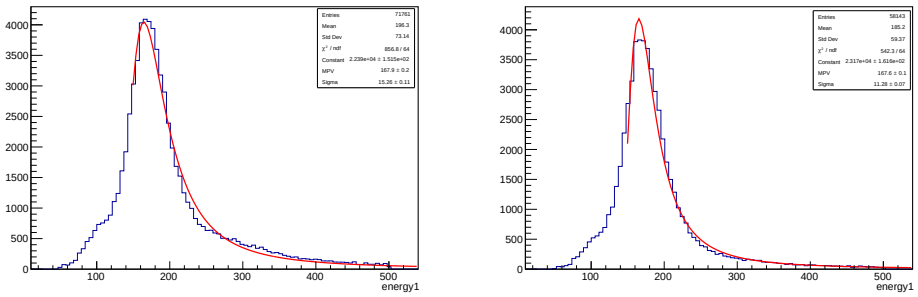

(a) Double coincidences energy spectrum without ΔE_{21} cut.

(b) Double coincidences energy spectrum with ΔE_{21} cut.

Figure 8.19: Lost muons energy spectrum in the calorimeter identified with double coincidences. Both curves show a maximum in the $\sim$ 170 MeV region as expected form the MIP behaviour of the muons in P_bF_2 crystals. In (b) the χ^2 Landau fit of double coincidences energy spectrum is better than in (a).

8.4.4 Track identification

As shown in Fig. 8.20, the tracker, in association with the calorimeters, can be used to identify particles, in particular muons, cutting on the energy and the momentum. The cuts used for the track identification are:

- $2.3\ GeV < p < 3.0\ GeV$ (from the tracker);
- $50\ MeV < E < 500\ MeV$ (from the calorimeter).

These cuts select the region of the Fig. 8.20 with low energy E and high momentum p of the reconstructed tracks.

Identifying lost muons with the tracker can be useful to check if the coincidences algorithm is correct and to justify some of the cuts on the coincidences. Tracker stations are present just in front of calorimeters number 13 and 19, so this check can be done just for two calorimeters losing some of the statistics. In Fig. 8.21 is plotted the number of crystals fired by a muon event measured by the tracker. The number of events with hit number greater than

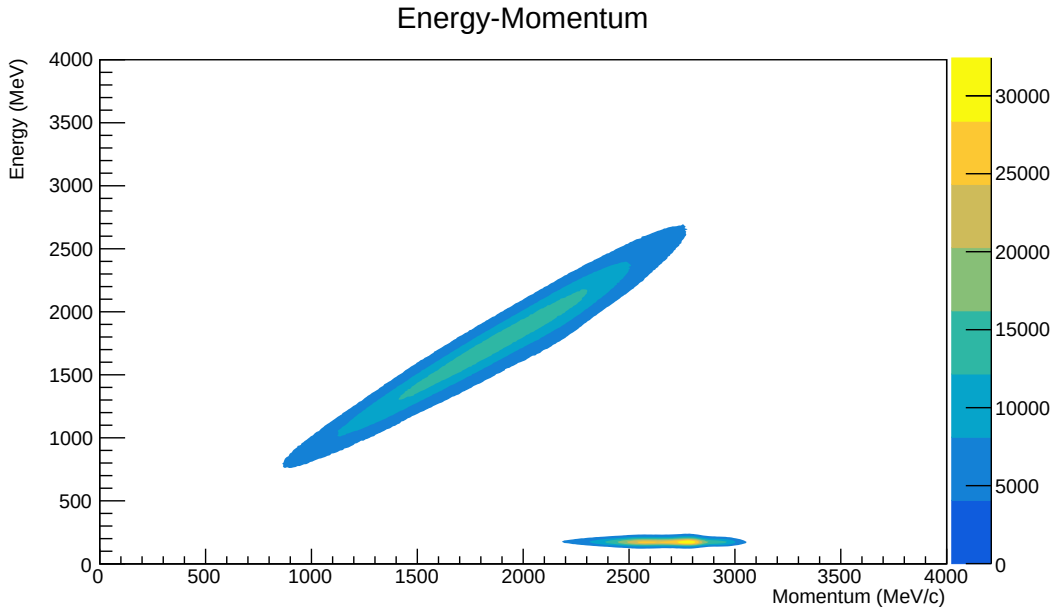

Figure 8.20: Energy-Momentum plot measured by the tracker and the calorimeters (Calo-Track Matching). Positrons events can be identified on the diagonal ($E \approx pc$) and muons on the peak at high momentum and low energy.

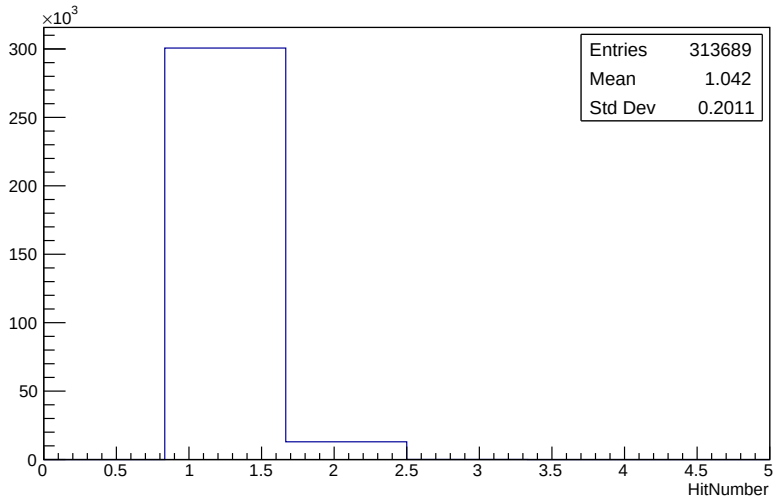

Figure 8.21: Number of crystals fired by a muon identified by the tracker. The number of events with hits greater than 1 is negligible ($\sim 4\%$) compared to the total number of muon events.

one ($nHit > 1$) are about 4% of the total number of events. This plot suggests that muons behave as MIP particles with a very localized ionization path, and only a small part of them enters the calorimeter with a big angle causing more than one crystal to have signal. This justifies the cut of a single crystal hit for the double and triple coincidences.

8.4.5 Results

All the results presented in this Chapter refer to the data acquired in the period of April-May 2018. Data quality cuts are applied to ensure the uniformity of the runs conditions. Same quadrupoles and kickers settings are used to keep the same conditions for all the dataset. In Fig. 8.22 the number of lost muons normalized to the total events for each run is shown. The variation during the whole dataset is small, so these runs will be analysed together.

In the following sections the results are presented both for double and triple

Figure 8.22: Number of lost muons double coincidences normalized to the total events per run. The number is stable, so all the runs can be processed in the same dataset.

coincidences. Tracker results will be used whenever possible to compare the distributions.

Energy spectrum measured by calorimeters

Plots in Fig. 8.23a and 8.23b show the energy spectra for double and triple coincidences. Both spectrum has a peak in the right energy region around 170 MeV as expected from the simulation, however the double coincidences peak shows a shoulder at small energies.

This shoulder can be caused by positrons or even muons going through the last column of crystals in the calorimeter. Those particles fire up just one crystal and deposit a smaller amount of energy into the calorimeter. This effect doesn't appear in the triple coincidences. Triple coincidences show a narrower peak with maximum at $\sim 162\ MeV$ (obtained by a gaussian fit around the peak). The mean value shows a little discrepancy (few MeV) with the double coincidences one. This difference can be caused by different shapes of the two curves, but can also be due to the path the particle takes into the crystal, different from double to triple coincidences[6].

The energy spectrum determination is important, besides the lost muons identification, for the calorimeters calibration during the runs using a physical process, as described in previous Section.

Spatial distribution

The segmented structure of the calorimeters allow to measure the position of a particle into the calorimeter itself. In this Section will be presented both the double and triple coincidence signals. In all the plots shown here the ring

[6]This effect is probably due to the different trajectory the particle has in double and triple coincidences.

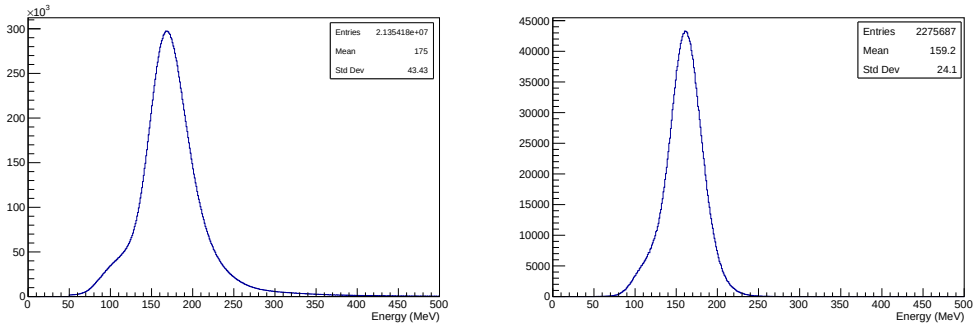

(a) Double coincidences spectrum.

(b) Triple coincidences spectrum.

Figure 8.23: Lost muons energy spectrum in the calorimeter identified with double and triple coincidences. Both curves show a maximum in the ~ 170 MeV region as expected form the MIP behaviour of the muons in P_bF_2 crystals. The Landau-like tail is largely depressed with full statistics on all the calorimeters.

is on the left side of the calorimeter ($X < 0$), so the lost muons (and also the positrons) curl inside the ring going towards positive X values. The length on the X and Y axes are in units of crystals, each crystal is 2.5 *cm* both in vertical and horizontal directions.

Fig. 8.24 shows the distribution of the lost muons double coincidences on the calorimeters. As the plot shows, lost muons mostly hit the calorimeter on the region near the ring (Fig. 8.24a) and curl inside due to the residual magnetic field in the calorimeters' region. So the trajectory is on a plane horizontal to the calorimeters and points toward the inner radius of the ring as expected.

Fig. 8.25 shows the spatial distributions (substantially horizzontally) on three consecutive calorimeters in a triple coincidence and is possible to see a progressive shift of the hit point away from the ring region. The first hit is near the ring (Fig. 8.25a), the second one is at a distance of $\sim$2 crystals, and the third is at the inner edge (furthest column from the ring) and bend

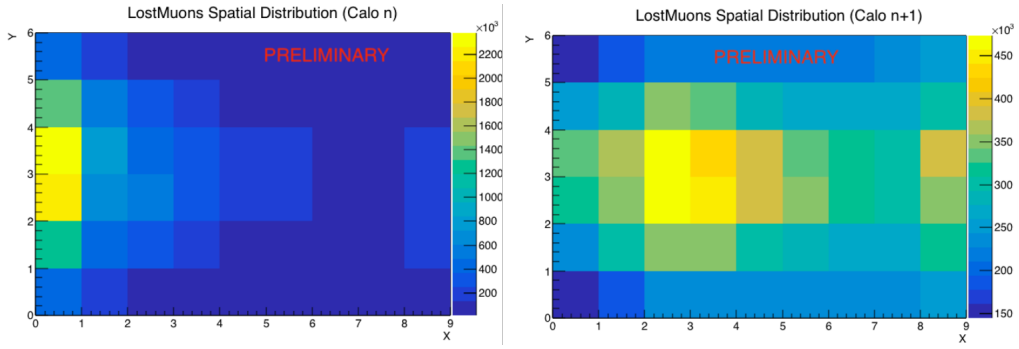

(a) First calorimeter in the coicidence. (b) Second calorimeter in the coicidence.

Figure 8.24: Spatial distribution of lost muons (double coincidences) on the calorimeters. The ring here is on the left side. Lengths are in crystal units.

inside. The trajectory is less curved than the double coincidence one due to the request of a third coincidence that limits the trajectory geometry.

Construction of the loss function

The correction function $L(t)$ in Eq. 8.42 is the time distribution of the lost muons during the 700 μs measure window. This distribution is obtained selecting events with the lost muons cuts presented in the previous Section. The result is shown in Fig. 8.26, for double and triple coincidences. Both curves show an exponential-like decay and two different slopes can be identified, before and after 100 μs due to the fact that muons at the edge of the phase space (wrong injection angle, momentum different from the magic one etc.) are most likely to be lost at early times. The integral of the $L_i(t)$ function, according to the Eq. 8.42, is the lost muons correction applied to the wiggle plot's fit in order to obtain the ω_a value. In Fig. 8.26a is presented the comparison between $L_2(t)$ and $L_3(t)$. Both functions have area normalized to 1. From the plot is possible to see a similar trend in the first 100 μs for the two curves and then a different behaviour in the later times region. This difference can be caused by

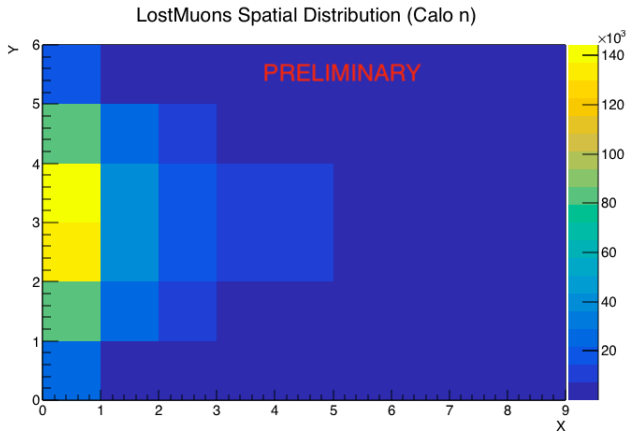

(a) First calorimeter in the coicidence.

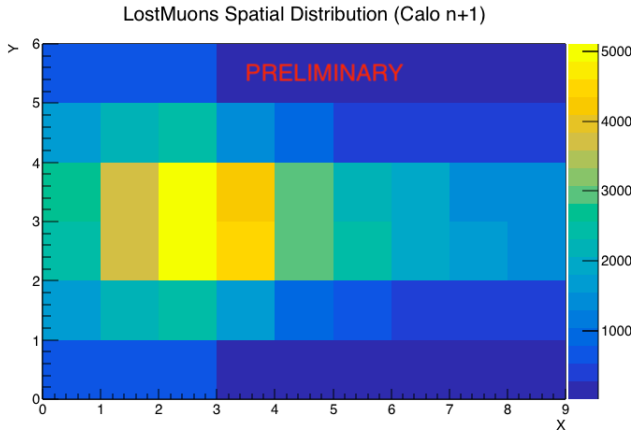

(b) Second calorimeter in the coicidence.

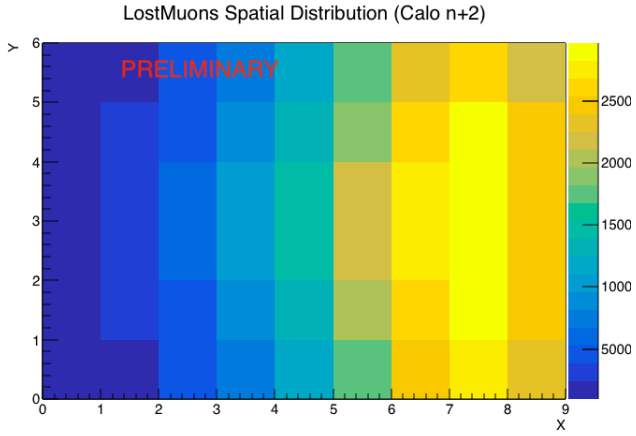

(c) Third calorimeter in the coicidence.

Figure 8.25: Spatial distribution of lost muons (triple coincidences) on the calorimeters. The ring here is on the left side. Lengths are in crystal units.

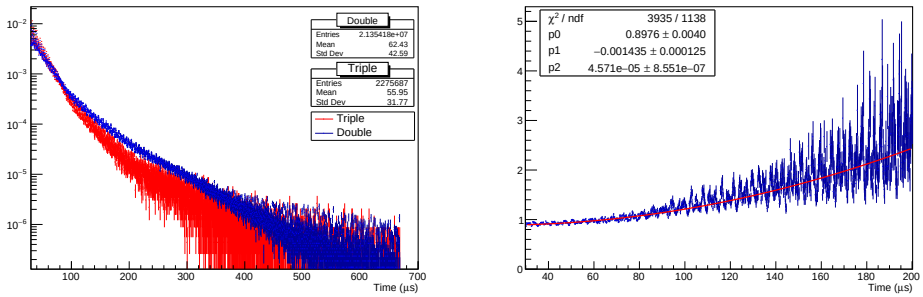

(a) L(t) comparitions between double and triple coincidences.

(b) Bin ratio $\frac{L_2 t)}{L_3(t)}$. The curve show a rising trend increasing with time.

Figure 8.26: (a) Comparison between lost muons time spectrum double ($L_2(t)$ function) and triple ($L_3(t)$ function) coincidences. Two different slopes can be identified in the curves. Each function is normalized to its integral. Higher fluctuations after 300 μs are due to the low statistics of triple coincidence in that region of time. (b) Is plotted the ratio of the two functions.

false double coincidences: leftover positrons or coincidences between positrons and muons which can mimic the double coincidence signal, but not the triple one. The difference between the two functions can introduce a systematic effect in the ω_a fit, so the right function has to be chosen in order to correctly fit the wiggle plot. One way to check if the lost muons function is correct is to use a Montecarlo simulation. Another way is to use the tracker, which will be presented in a next Section. In Fig. 8.26b the ratio between the two curves shows a rising trend increasing with time with a quadratic term p_2 of $\sim 5 \cdot 10^{-5}$.

Lost muons distribution along the ring

The number of lost muons along the ring varies because of the different materials the beam goes through into the vacuum chamber. Fig. 8.27 shows the integral of the $L_3(t)$ function for each calorimeter. This gives the distri-

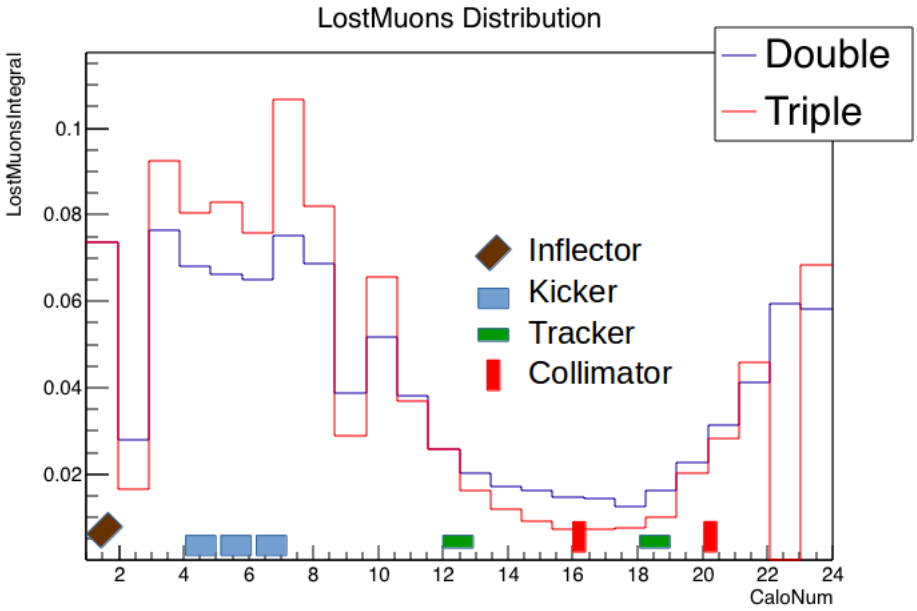

Figure 8.27: Integral of the lost muons function for each calorimeter. The distribution of lost particles along the ring depends on the material through the vacuum chamber.

bution along the ring of the lost muons. Most of the muons are lost in the first half of the ring, that's because, right after the injection, all the particles with momentum and injection angle outside the machine acceptance are lost (inflector is between calorimeters 1 and 2 and kickers are before calorimeters 7, 8 and 9). In the second half of the ring, the remaining particles have the momentum to be in a stable orbit, moreover quadrupoles provide focusing in that region. However collimators in the last quarter of the ring rise up again the number of lost particles.

Lost muons function and track matching

The tracker combined together with the calorimeters, allows to identify a particle by its energy and its momentum. So lost muons events from the tracker can be used to check the double/triple coincidences. In Fig. 8.28a the

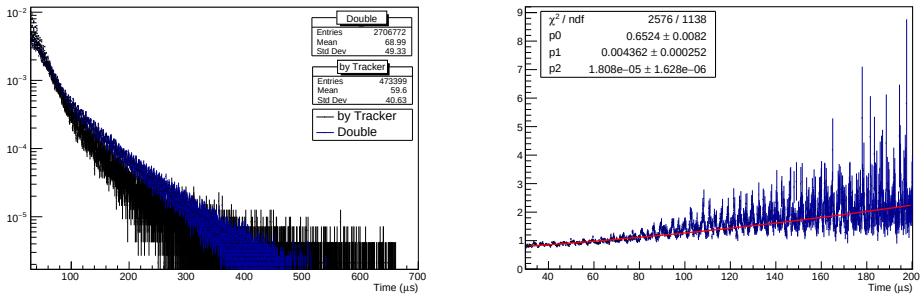

(a) Time distributions. Each function is normalized to area 1.

(b) Bin ratio $\frac{L_2 t)}{L_{trk}(t)}$. The curve show a rising trend increasing with time.

Figure 8.28: (a) Comparison between the $L_2(t)$ function (blue) and the time distribution using tracker matching algorithm(black). (b) Is plotted the ratio of the two functions.

double coincidences time distribution, obtained as the distribution in Fig. 8.26 cutting on the calorimeter number and the time distribution of the muons identified with the tracker, is plotted. The behaviour of the curves is the same for the first 50 μs and becomes different after that point. In Fig. 8.28b the ratio between the two curves shows a rising behaviour increasing with time with a slope at per mill level. The higher number of double coincidence can be caused by leftover positrons found in coincidence.

Triple coincidence curve Fig. 8.29 matchs the tracker distribution with a more restrictive selection on energy ($130\ MeV < E < 220\ MeV$) imposed with the calo-tracker algorithm. The ratio, apart from fluctuations, has an average flat distribution, though it has a slow decreasing behaviour (with a slope at sub per mill level) that can be caused by the low triple coincidence events found later in time. The previous energy selection with $50\ MeV < E < 500\ MeV$, used for omogeneity energy selection in double coincidence, produces in this last case a negative slope of $\sim$3 per mill for the ratio $\frac{L_3 t)}{L_{trk}(t)}$. The plots in Fig. 8.29 however suggest that the $L_3(t)$ function is the right candidate for the

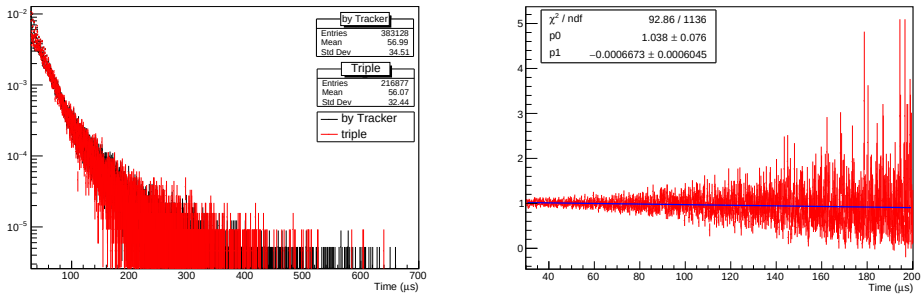

(a) Time distributions. Each function is normalized to area 1.

(b) Bin ratio $\frac{L_3 t)}{L_{trk}(t)}$. The curve show a rising trend increasing with time.

Figure 8.29: Comparison between the $L_3(t)$ function (red) and the time distribution using tracker matching algorithm(black). On the left is plotted the ratio of the two functions.

lost muons correction.

In Fig. 8.30b the energy spectra of double (blue) and triple (red) coincidences (shown in previous Section) and the tracker spectrum (green), normalized to area 1 for comparison, of all calorimeters, are plotted. In Fig. 8.30a only calorimeters 13 and 19 have been analyzed with the Tracker. All the three curves show the peak in the expected region and the mean values are consistent within the errors. Energy spectrum of double conicidences for all calorimeters, Fig. 8.30b, presents a peak very close to the curve obtained by trackers. In both cases of Fig. 8.30 is evident the shoulder at small energy ($50\ MeV < E < 120\ MeV$), described in a previous Section and still present (although reduced) in triple coincidences energy spectrum, that could be removed by a better restriction in the energy selection cuts. However is also visible a slight difference (few MeV) between the energy of the triple coincidences and the other two spectra. Triple coincidences are well fitted by gaussian curve in a wide range around the peak but, the presence of the shoulder and the gaussian behavior before the peaks and the Landau like after, are

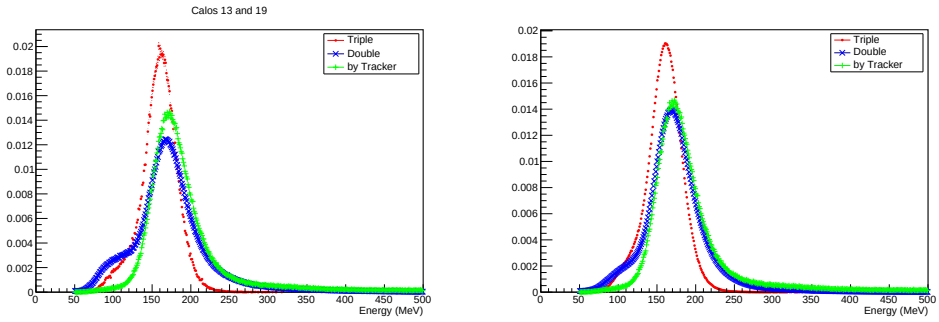

(a) Comparison with calorimeters 13 and 19.

(b) Comparison with all calorimeters.

Figure 8.30: Energy spectra from the double and triple coincidences and from the tracker events. All three curves are normalized to have area 1. The maximum value of the peak is compatible with the 170 MeV region expected.

still to be investigated in double coincidences.

Wiggle function 10-parameters fit

Finally, after the identification of lost muons and the construction of the $L_i(t)$ functions, is possible to calculate the $\Lambda(t)$ function, according to equation 8.42, and to add the lost muons correction to the wiggle plot's fit. In Fig. 8.31 are shown the curves to construct the correction function $\Lambda(t)$. Both plots show in black the time distribution for double and triple coincidences. In red the function

$$L_{exp}^{(i)} = L_i(t)e^{\frac{t}{\tau}}, \tag{8.54}$$

where $\tau = \gamma\tau_0 = 64.4\mu s$ is the muon lifetime in the laboratory frame of reference[7]. Lastly the blue curve is the integral of $L_{exp}^{(i)}$:

$$J_i(t) = \int_0^t L_{exp}^{(i)} = \int_0^t L_3(t)e^{t'\tau}dt'. \tag{8.55}$$

[7]The pattern at the end of the spectrum is due to the low statistics of the $L_i(t)$ function in that region.

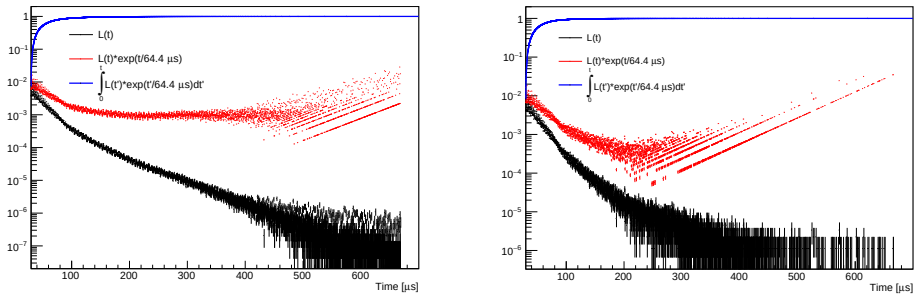

(a) Double Coincidences. (b) Triple Coincidences.

Figure 8.31: Lost muons correction for double ($i = 2$) and triple ($i = 3$) coincidences: in black the $L_i(t)$ function; in red the function $L_{exp}^{(i)} = L_i(t)e^{\frac{t}{\tau}}$; in blue the integral of $L_{exp}^{(i)}$.

The correction

$$\Lambda(t) = 1 - K_{LM} \cdot J_i(t) \tag{8.56}$$

has to be applied to the wiggle plot fit in order to calculate the K_{LM} value from the fit and to better fit the ω_a.

In Fig. 8.32 is shows the time distribution of positrons with energy $E_{e+} > 1.7\ GeV$ from the chosen dataset. The fit applied is a 10-Parameter fit, so takes into account the standard 5-Parameters fit plus the CBO, the pile up and the lost muons correction. The fit shows a little χ^2 and residuals on improvements going from the 9-Parameter fit to the 10-Parameter one better for the lost muons correction $L_3(t)$ that matches better with the tracker distribution too.

This suggest that the triple coincidence method goes in the right direction. The fitted constant K_{LM} for the given dataset is:

$$K_{LM} = (6.283 \pm 0.121) \cdot 10^{-11} \tag{8.57}$$

The values related to ω_a in the fit are both hardware and software blinded for the duration of the analysis, so this wiggle plot doesn't provide explicitly

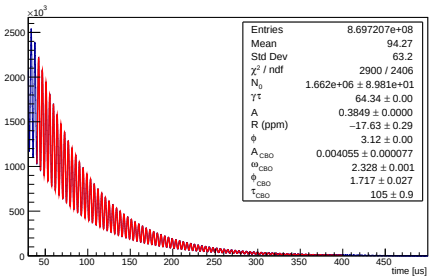

(a) 9-parms fit function.

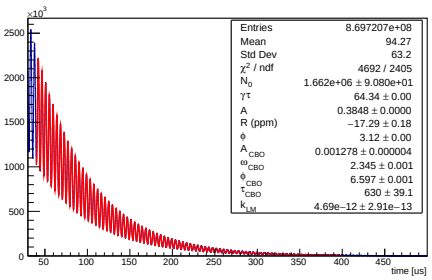

(b) $L_2(t)$ integral correction.

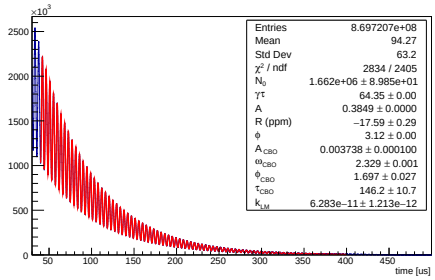

(c) $L_3(t)$ integral correction.

Figure 8.32: Time spectrum of positrons with energy $E_{e+} > 1.7\ GeV$ from the chosen dataset. The fitting function is the 10-Parameter fit and it includes the CBO, pile up and Lost Muons correction. Note: the fit is blinded, so there is not an explicit ω_a value. (a) 9 parameters fit function with CBO correction. (b) 10 parameters Fit with CBO and $L_2(t)$ integral function corrections. (c) 10 parameters Fit with CBO $L_3(t)$ integral function corrections.

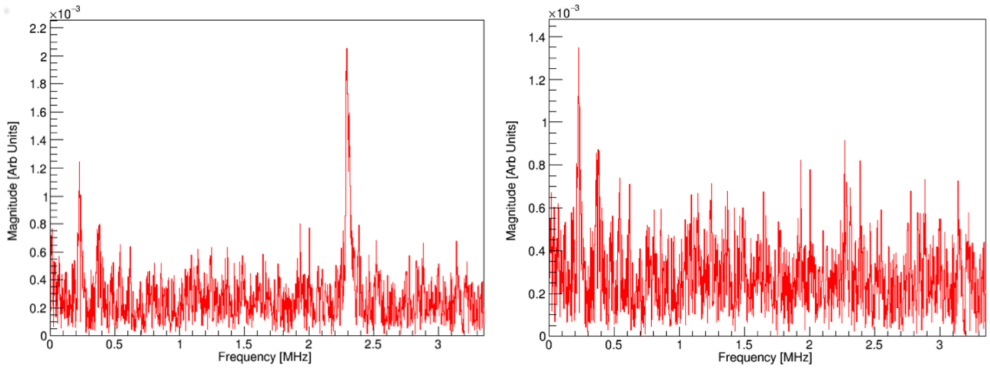

(a) 9 Parameters fit without lost muons correction.

(b) 10 Parameters fit with lost muons correction.

Figure 8.33: Residuals FFT before and after the lost muons correction. The plot shows a reduction of the low frequency peak caused also by lost muons. Here is also applied the vertical CBO correction in order to remove the $\sim$ 2.4 MHz peak.

a value to calculate a_μ. Fig. 8.33 shows the residuals FFT before (a) and after (b) the Lost Muons correction (pile up correction is applied). The plot shows a reduction of the low frequency peak after the correction and also suggests that the method improves the ω_a fit.

8.4.6 Summary

Among the corrections applied to the fitting function to extract the ω_a value (CBO, Electric Field, Pitch, etc.), the lost muon analysis done with double and triple coincidences is described in this Section. Results show that the analysis with triple coincidences should be preferred for the final fit correction. An encouraging preliminary fit of the ω_a function has been computed independently by the Europe working group, and the fit shows a χ^2 and residuals improvements using the triple coincidences (together with the other) correction.

This analysis is still under studying and we need to better understand

behaviour lke the drop in the muon loss fit parameter, K_{LM}, that has been observed at high energies. This effect is not statistically significant indeed. The high energy bin fits yield good χ^2 values when K_{LM} is fixed to the T-Method result, but it may indicate residual uncorrected effects in the high energy bins.

This first studies show that gain perturbations cause surprisingly large time-dependent effects at the high-end of the energy spectrum.

Particularly, gain perturbations cause a large reduction in counts at early times. This is opposite to the muon loss effect, which causes a relative gain of counts at early times, and therefore gain perturbations could be contributing to the instability of the K_{LM} term at high energies.

Two powerful tools for identifying the presence of small, time-dependent, gain perturbations are under study: the properly normalized ratio of the late-time energy spectrum to the early-time energy spectrum, and the measurement of K_{LM} versus energy.

Conclusion

The muon anomaly a_μ was measured in the late 1990s–early 2000s at Brookhaven National Laboratory (BNL) in the USA [106]. These measurements were combined together and showed a 3.4σ discrepancy with the Standard Model's value. The discrepancy can be hint of new physics (SUSY, Dark Matter, etc.) contributing to the $g-2$ value. In order to investigate this discrepancy and confirm (or disprove) the BNL result, a new Muon $g-2$ experiment at Fermilab (E989) aims to measure a_μ with an uncertainty of 0.14 ppm. To reach the precision required for this experiment, a precise measurement of the anomalous precession frequency is needed (together with a precision measurement of the field inside the ring).

The work presented in this thesis documents the development and the results obtained in the design, construction, test and installation of the Laser Calibration System for the new E989 experiment.

Several laboratory tests were performed, in order to find the best solution for a system which should be the first of its generation, with a total accuracy requested by the experiment of one order of magnitude better than the existing laser calibration system.

This calibration system has been developed and tested in 4 years, from the beginning of 2012 to 2016, installed at Fermilab starting from second half of 2016 up to may 2017, where has been commissioned. In the last year and half

the system has been continuously operated.

During this time it was verified that the calibration system is presently able to monitor and correct for laser intensity variations at different time scales. The laser pulses, taken within and outside the muon fill, are currently used to correct SiPM response and this correction may be as large as few %. It has been also proven that 6 lasers are enough to illuminate all 24 calorimeters with an equivalent energy of as maximum 10 GeV per laser pulse. The Double Pulse procedures of the Laser Calibration System result to be a powerful tool to investigate the calorimeters gain function at different time scale inside the muon fill.

All these results proved that the calibration system satisfies the main goal of the experiment and the project specifications: to monitor the gain fluctuations of the SiPM with a 0.04% statistical accuracy and at 0.01% systematic one in the $700\mu s$ time window.

During this time the Italian group[8] has also designed and developed the software frameworks necessarily to the real time data taking and monitoring of the laser calibration system in Fermilab and has started to manage the slow control of all $g-2$ E989 experiment (All this work have been presented in this thesis).

During the last years, the italian group has been and is currently involved in the analyses of calorimeters gain correction and the ω_a determination studies, together with other european istitutions. This work has been documented in the last three chapters of this thesis.

The E989 experiment has collected in July 2018, at the end of Run 1, almost two times the statistics of BNL and is starting Run 2 again with significant improvements both on hardware and software sides. We are all looking forward

[8]Whose activitely have been funded by the National Scientific Committee 1 of INFN.

to the next years to complete the analysis and to the first results hoping that this measure could bring us a step further in the knowledge of how the universe works.

Bibliography

[1] D. Griffiths, "Introduction to Elementary Particles", 1st ed. John Wiley and Sons, New York (1987).

[2] W. Gerlach and O. Stern, Zeitschrift für Physik **9**, 353 (1922).

[3] T. Phipps and J. Taylor, Phys. Rev. **29**, 309 (1927).

[4] R. Kronig, in"Theoretical physics in the twentieth century; a memorial volume to Wolfgang Pauli", edited by M. Fierz, Interscience Publishers, New York (1960).

[5] F. Halzen and A. D. Martin,"Quarks and Leptons: an introductory course in modern particle physics", John Wiley and Sons, New York (1984).

[6] L. Foldy, Phys. Rev. **87**, 688 (1952).

[7] J. Chadwick, Nature **129**, 312 (1932).

[8] C. Anderson, Phys. Rev. **43**, 491 (1933).

[9] Sin-itiro Tomonaga, "The Story of Spin", translated by Takeshi Oka, U. Chicago Press (1997).

[10] R. Frisch and O. Stern, Z. Phys. **85**, 4 (1933), and I. Estermann and O. Stern, Z. Phys. **85**, 17 (1933).

[11] I. Estermann, O. Simpson and O. Stern, Phys. Rev. **52**, 535 (1937).

[12] Luis W. Alvarez and F. Bloch, Phys. Rev. **57**, 111 (1940).

[13] J.E. Nafe, E.B. Nelson and I.I. Rabi Phys. Rev. **71**, 914 (1947).

[14] D.E. Nagel, R.S. Julian and J.R. Zacharias, Phys. Rev. **72**, 971 (1947).

[15] P. Kusch and H.M Foley, Phys. Rev **72**, 1256 (1947).

[16] P. Kusch and H. Foley, Phys. Rev. **74**, 250 (1948).

[17] J. Schwinger, Phys. Rev. **73**, 416 (1948), and Phys. Rev. **76**, 790 (1949).

[18] Hans A. Bethe and Edwin E. Salpeter, "Quantum Mechanics of One- and Two-Electron Atoms", Springer-Verlag, p. 51 (1957).

[19] P. J. Mohr, D. B. Newell and B. N. Taylor, Rev. Mod. Phys. **88** no.3, 035009 (2016).

[20] D. Hanneke, S. Forgwell and G. Gabrielse, Phys. Rev. Lett. **100**, 120801 (2008).

[21] B. C. Odon, D. Hanneke, B. D'Urso and G. Gabrielse, Phys. Rev. Lett. **97**, 030801 (2006).

[22] D. Hanneke, S. F. Hoogerheide and G. Gabrielse, Phys. Rev. A **83**, 052122 (2011).

[23] Richard H. Parker *et al.*, Science **360**, Issue 6385, pp. 191-195 (2018).

[24] T. Kinoshita and M. Nio, Phys. Rev. Lett **90**, 021803 (2003).

[25] M. Kecht, "The anomalous magnetic moment of the muon: A theoretical introduction", [hep-ph/037239] (2003).

[26] G. F. Giudice, P. Paradisi and M. Passera, "Testing new physics with the electron g-2", JHEP **1211**, 113 (2012).

[27] T. Aoyama, T. Kinoshita, and M. Nio Phys. Rev. D **97**, 036001 (2018).

[28] R. VanDyck, P. Schiwinberg and H. Dehmelt, Phys. Rev. Lett. **59**, 26 (1987).

[29] D. Hanneke, S. Fogwell, and G. Gabrielse Phys. Rev. Lett. **100**, 120801, 26 (2008).

[30] See Figure 5 in Paul Kunze, Z. Phys. **83**, 1 (1933).

[31] Carl D. Anderson and Seth H. Neddermeyer, Phys. Rev. **50** 263 (1936), and Seth H. Neddermeyer and Carl D. Anderson, Phys. Rev. **51**, 844 (1937).

[32] J.C. Street, E.C. Stevenson, Phys. Rev. **52**, 1003 (1937).

[33] Y. Nishina, M. Tekeuchi and T. Ichimiya, Phys. Rev. **52**, 1198 (1937).

[34] M.M. Jean Crussard and L. Leprince-Ringuet, Compt. Rend. **204**, 240 (1937).

[35] RL. Garwin, DP. Hutchinson, S. Penman, G. Shapiro, Phys. Rev. **118**, 271 (1960).

[36] J. Bailey, *et al.*, Phys. Lett. 28B:287 (1968). Additional details can be found in J. Bailey, *et al.*, Nuovo Cimento. A **9**, 369, and references therein (1972).

[37] J. Bailey, *et al.*, Nucl. Phys. B **150**, 1 (1979).

[38] M. Davier, "in Advanced Series on Directions in High Energy Physics", Vol. **20** *Lepton Dipole Moments*, eds. B. L. Roberts and W. J. Marciano, World Scientific, chapter **8** (2010).

[39] T. Kinoshita and M. Nio, Phys. Rev. D **73**, 013003 (2006).

[40] F. Jegerlehner, A. Nyffeler: The Muon g-2, Physics Reports Volume **477**, Issues 1 3, Pages 1 110, June (2009).

[41] P. J. Mohr, B. N. Taylor and D. B. Newell, CODATA Group, Rev. Mod. Phys **84**, 1527 (2012).

[42] R. Bouchendira *et al.*, Phys. Rev. Lett. **106**, 080801 (2001).

[43] R. Jackiw and S. Winberg, Phys. Rev. D **5**, 2396 (1972).

[44] Particle Data Group: Phys. Rev. **38**, 090001 (2015).

[45] J. P. Miller, E. de Rafael and B. L. Roberts, Rept. Prog. Phys. **70**, 795 (2007). JHEP **0403**, 035 (2004).

[46] A. Czarnecki, B. Krause and W. J. Marciano, Phys. Rev. Lett. **76**, 3267 (1996).

[47] A. Czarnecki, W. J. Marciano and A. Vainshtein, Phys. Rev. D **67**, 073006 (2003), Erratum-ibid. D **73**, 119901 (2006).

[48] C. Gnendiger, D. Stöckinger and H. Stöckinger-Kim, Phys. Rev. D **88** 053005 (2013).

[49] M. Knecht, S. Peris, M. Perrottet and E. de Rafael, JHEP **0403**, 035 (2004).

[50] C. Bouchiat and L. Michel: J. Phys. Radium **22** (1961).

[51] F. Jegerlehner, arXiv:1511.04473.

[52] M. Davier *et al.*, EPJ C **71**, 1515 (2011).

[53] Hagiwara *et al.*, JPG **38**, 085003 (2011).

[54] A. Aloisio *et al.*, hep-ph/0312056.

[55] BESIII Collaboration, arXiv:1507.08188.

[56] B. Krause, Phys. Lett. B **39**, 392 (1997).

[57] A. Kurz, T. Liu, P. Marquard and M. Steinhauser,"Hadronic contribution to the muon anomalous magnetic moment to next-to-next-to-leading order", arXiv:1403.6400 [hep-ph] (2014).

[58] J. Bijnens, Phys. Rept. **265**, 369 (1996).

[59] E. de Rafael, Phys. Lett. B **322**, 239 (1994).

[60] M. Knecht, A. Nyffeler, M. Perrottet and E. de Rafael, Phys. Rev. Lett. **88**, 071802 (2002).

[61] K. Melnikov and A. Vainshtein, Phys. Rev. D **70**, 113006 (2004).

[62] J. Prades, E. de Rafael and A. Vainshtein, Adv. Ser. Direct. High Energy Phys. Vol.**20** *Lepton Dipole Moments*, 303 (2010).

[63] E. Eichten, K. D. Lane and M. E. Peskin, Phys. Rev. Lett. **50**, 811 (1983).

[64] P. Mery, S. E. Moubarik, M. Perrotet and F. M. Renard, Z. Phys. C **46**, 229 (1990).

[65] S. J. Brodsky and S. D. Drell, Phys. Rev. D **22**, 2236 (1980).

[66] S. P. Martin, hep-ph/9709356.

[67] J. Wess, B. Zumino: Nucl. Phys. B 70 39, 1974; R. Haag, J. T. Lopuszanski, M. Sohnius: Nucl. Phys. B **88**, 257 (1975).

[68] U. Chattopadhyay and P. Nath, hep-ph/0208012.

[69] A. Czarnecki and W. J. Marciano, Phys. Rev. D **64**, 013014 (2001).

[70] A. Czarnecki, W. J. Marciano and A. Vainshtein, Phys. Rev. D **67**, 073006, [hep-ph/0212229] (2003).

[71] T. Appelquist and B. A. Dobrescu, Phys. Lett. B **516**, 85, [arXiv:hep-ph/0106140] (2001).

[72] M. Blanke, A. J. Buras, B. Duling, A. Poschenrieder and C. Tarantino, JHEP **0705**, 013, [arXiv:hep-ph/0702136] (2007).

[73] M. Pospelov, Phys. Rev. D **80**, 09500 (2009).

[74] B. C. Allanach *et al.*, in "Proc. of the APS/DPF/DPB Summer Study on the Future ofParticle Physics (Snowmass 2001)", ed. N. Graf, Eur. Phys. J. C **25** (2002), 113, eConf C **010630** P125 (2001).

[75] N. Arkani-Hamed, G. L. Kane, J. Thaler and L. T. Wang, JHEP **0608**, 070 (2006).

[76] M. Endo, K. Hamaguchi, S. Iwamoto and T. Yoshinaga, arXiv:1303.4256 [hep-ph].

[77] H. Baer, V. Barger, P. Huang and X. Tata, JHEP **1205**, 109 (2012).

[78] Adam C, Kneur J -L, Lafaye R, Plehn T, Rauch M, Zerwas D. *Eur. Phys. J. C* **71**, 1520 (2011).

[79] M. Alexander, S. Kreiss, R. Lafaye, T. Plehn, M. Rauch, and D. Zerwas, Chapter **9** in M. M. Nojiri *et al.*, "Physics Beyond the Standard Model: Supersymmetry", arXiv:0802.3672 [hep-ph].

[80] P. Renton, "Electroweak Interactions", 1st ed. (Cambridge University Press, Cambridge) (1990).

[81] B. Roe, "Particle Physics at the New Millennium", 1st ed. (Springer-Verlag, New York) (1996).

[82] T. Lee and C. Yang, Phys. Rev. **104**, 254 (1956).

[83] C. Wu *et al.*, Phys. Rev. **105**, 1414 (1957).

[84] R. Garwin, L. Lederman and M. Weinrich, Phys. Rev. **105**, 1415 (1957).

[85] D. Hutchinson *et al.*, Phys. Rev. Lett. **131**, 1315 (1963).

[86] W. Louisell *et al.*, Phys. Rev. **91**, 475 (1953).

[87] F. Farley and E. Picasso, "The muon g-2 experiments, in Quantum Electrodynamics", edited by T. Kinoshita, pp. 479–559, World Scientific, Singapore (1990).

[88] H. Eland, Phys. Lett. **21**, 720 (1966).

[89] D. Kawall, "Statistical and Systematic Errors in fitting ω_a", Muon $g-2$ Internal Note No. **322** (1998).

[90] F. Farley, "Proposed high precision (g-2) experiment", CERN Intern. Rep. No. NP/**4733** (1962).

[91] J. Aldins *et al.*, Phys. Rev. Lett. **23**, 441 (1969).

[92] M. Gourdin and E. de Rafael, Nucl. Phys. B **10**, 667 (1969).

[93] V. Auslander *et al.*, Phys. Rev. **91**, 475 (1953).

[94] J. Augustin *et al.*, Phys. Lett. B **28**, 517 (1969).

[95] K. Crowe *et al.*, Phys. Rev. D **5**, 2145 (1972).

[96] T. Kinoshita, B. Nizic and Y. Okamoto, Phys. Rev. Lett. **52**, 717 (1984).

[97] G. Charpak, *et al.* Phys. Rev. Lett. 6:28 (1961), Nuovo Cimento. 22:1043 (1961), Phys. Lett. 1:16 (1962), and G. Charpak *et al.*, Nuovo Cimento Soc. Ital. Fis. **37**, 1241 (1965).

[98] J. Bailey *et al.*, Nuovo Cimento Soc. Ital. Fis. A **9**, 369 (1972).

[99] CERN Muon Storage Ring Collaboration, J. Bailey *et al.*, Phys. Lett. B **67**, 225 (1977).

[100] R. M. Carey *et al.*, Phys. Rev. Lett. **82**, 1632 (1999).

[101] Muon g-2 Collaboration, H. N. Brown *et al.*, Phys. Rev. D **62**, [hep-ex/0009029], 091101 (2000).

[102] Muon g-2 Collaboration, H. N. Brown *et al.*, Phys. Rev. Lett. **86**, [hep-ex/0102017], 2227 (2001).

[103] Muon g-2 Collaboration, G. W. Bennett *et al.*, Phys. Rev. Lett. **89**, [hep-ex/0208001], 101804 (2002) and Phys. Rev. D **73**, 072003 (2006).

[104] F. E. Gray, Jr.,"A Measurement of the anomalous magnetic moment of the positive muon with a precision of 0.7 parts per million", Illinois U., Urbana, UMI-30-86067, FERMILAB-THESIS-2003-54 (2003).

[105] C. C. Polly, "A Measurement of the anomalous magnetic moment of the negative muon to 0.7 ppm", Illinois U., Urbana, UMI-31-99116 (2005).

[106] Muon g-2 Collaboration (G. W. Bennet *et al.*), Phys. Rev. D **73**, 072003 (2006).

[107] Muon g-2 Collaboration, arXiv:1501.06858 (2015).

[108] T. P. Gorringe, D. W. Hertzog, *Precision Muon Physics*, arxiv:1506.01465v1 (2015).

[109] O. Rifiki, "The muon anomalous magnetic moment: a probe for the Standard Model and beyond", Report approved for the H.L.Dodge Department of Physics and Astronomy (2014).

[110] A. Anastasi *et al.*,"The calibration system of the new g-2 experiment at Fermilab", Nucl. Instrum. Meth A **824**, 716-717 (2016).

[111] D. Hertzog, "Next Generation Muon g-2 Experiment", arxiv:1512.00928v1 (2015).

[112] R. Carey *et al.*, FERMILAB PROPOSAL-0989 (2009).

[113] L. H. Thomas, Nature **117** (1926).

[114] V. Bargmann, L. Michel, V. L. Telegdi, Phys. Rev. Lett. **2**, 435 (1959).

[115] G. W. Bennet *et al.*, Phys. Rev. D **80**, 052008 (2009).

[116] E. J. Konopinski, Ann. Rev. Nucl. Sci. **9**, 99 (1959).

[117] X. Fei, V. Hughes and R. Prigl, Nucl. Inst. Meth. Phys. Res. A **394**, 349 (1997).

[118] A. Abragam, in "Principles of Nuclear Magnetism", p. 173-178, Oxford U. Press (1961).

[119] P. J. Mohr, B. N. Taylor, and D. B. Newell, Rev. Mod. Phys. **84(4)**, 1527 (2012).

[120] W. D. Phillips *et al.*, Metrologia **13**, 179 (1979).

[121] J. L. Flowers, B. W. Petley and M. G. Richards, Metrologia **30**, 75 (1993).

[122] Mohr PJ, Taylor BN, Newell DB (CODATA recommended values). *Rev. Mod. Phys.* **80**, 633 (2008).

[123] W. Liu et al., Phys. Rev. Lett. **82**, 711 (1999).

[124] A. A. Savchenko *et al.*, "Geant4 simulations of the lead fluoride calorimeter", Nucl. Instrum. Meth. B **402**, 256 (2017).

[125] G. W. Bennett *et. al.* (Muon $g-2$ Collaboration) Phys. Rev. D **80**, 052008 (2009).

[126] VadaTech VT895 "μTCA Data Sheet", *https://www.vadatech.com/media/VT895_VT895 Datasheet.pdf.*

[127] A. Chapelian,"Development of the electromagnetic calorimeter waveform digitizers for the Muon $g-2$ experiment at Fermilab", PoS, EPS-HEP2015, **280** (2015).

[128] M. Pesaresi *et al.*,"The FC7 AMC for generic DAQ & control applications in CMS", JINST **10**, no. 03, C03036 (2015).

[129] Timing, "Trigger and Control Systems for the LHC", *http://ttc.web.cern.ch/TTC/intro.html.*

[130] B. Taylor, "TTC Distribution for LHC Detectors", IEEE Trans. Nuclear Science, Vol. **45** (1998).

[131] AMC13 development project, *http://www.amc13.info*.

[132] E. Hazen *et al.*, "The AMC13XG: a new generation clock/timing/DAQ module for CMS MicroTCA", JINST **8**, C12036 (2013).

[133] E. Frlez *et al.*, Nucl. Instrum. Meth. A **526**, 300 (2004). see also *http://midas.psi.ch/* and TRIUMF MIDAS homepage, *http://midas.triumf.ca* (2018).

[134] R. Brun and F. Rademakers, "ROOT - An Object Oriented Data Analysis Framework", Nucl. Inst. Meth. in Phys. Res. A **389**, 81-86 (1997). See also *http://root.cern.ch/*.

[135] *https://developer.nvidia.com/cuda-zone*.

[136] C. Green, J. Kowalkowski, M. Paterno, M. Fischler, L. Garren and Q. Lu, The art framework, J.Phys. Conf. Ser. **396**, 022020 (2012).

[137] A.Anastasi *et al.*, Nucl. Instrum. Meth. A **788**, 43-48 (2015).

[138] V. Tischenko *et al.*, Phys. Rev. D **87**, 052003 (2012).

[139] A. Ghigo *et al.*, Nucl. Intrum. Meth. A **515**, 524 (2003).

[140] A. T. Fienberg *et al.*, Nucl. Instrum. Meth. A **783**, 12-21 (2015).

[141] A. Anastasi *et al.*, "Electron Beam Test of Key Elements of the Laser-Based Calibration System for the Muon g− 2 Experiment", Oct 11, 2016. 6 pp. Published in Nucl.Instrum.Meth. A **842**, 86-91 (2017).

[142] M. E. Biagini *et al.*, Brussels 1995, High energy Physics, 377-379 (1995).

[143] Picoquant, "Picosecond Laser Diode Heads datasheet", *https://www.picoquant.com/images/uploads/downloads/ldh_series.pdf*.

[144] A. Anastasi *et al.*, "The laser control of the muon g-2 experiment at Fermilab", Nov 9, 2017. 15 pp. Published in JINST **13**, no.02, T02009 (2018).

[145] S. Mastroianni,"The Readout Controller for the Calibration System of the Muon g-2 Experiment", in IEEE Transactions on Nuclear Science, **vol. 65**, no. 4, pp. 1033-1039 (2018).

[146] Multichannel Picosecond Diode Laser Driver PDL 828 "Sepia II" datasheet, *https://www.picoquant.com/images/uploads/downloads/pdl828_sepiaii.pdf.*

[147] SRS Digital Delay Generator, *https://www.thinksrs.com/products/dg645.html.*

[148] Hamamatsu Si PIN Photodiode Datasheet, *http://www.hamamatsu.com/resources/pdf/ssd/s3590-08-kpin1052e.pdf.*

[149] Beagle board microprocessor: *http://beagleboard.org/BeagleBoard-xM.*

[150] A. Anastasi,"The Calibration System of the E989 Experiment at Fermilab", FERMILAB-THESIS-2017-07 (2017).

[151] Shanghai SICCAS High Technology Corporation, 1295 Dingxi Rd., Shanghai 200050, China *http://english.sic.cas.cn/rh/em/tcg/.*

[152] Hamamatsu. Multi-Pixel Photon Counter Model number S12642-4040PA-50 *MPPC Selection Guide* (2014).

[153] *Eigen: A C++ linear algebra library, http://eigen.tuxfamily.org/.*

[154] J. Kaspar *et al.*,"Design and performance of SiPM-based readout of PbF_2 crystals for high-rate, precision timing applications", JINST **12**, no. 01, P01009 (2017).

[155] W. Gohn,"Data Acquisition for the New Muon g-2 Experiment at Fermilab", Journal of Physics: Conference Series **664**, 082014 (2015).

[156] T.C. Awes *et al.*,"A simple method of shower localization and identification in laterally segmented calorimeters", Nucl. Inst. Meth. A **311**, 130-138 (1992).

[157] *http://midas.psi.ch/mscb/.*

[158] *http://www.ge-ip.com/products/proficy-hmi-scada-ifix-5-5/p3311.*

[159] *http://www-bd.fnal.gov/controls/consoles/userguide.html.*

[160] *https://www.psi.ch/ltp-electronics/WwwDocumentsEN/Datasheet_SCS2000_0-2.5mA_0-25mA.pdf.*

[161] *https://www.xilinx.com/support/documentation/data_sheets/ds095.pdf.*

[162] *https://opcfoundation.org.*

[163] *https://www.postgresql.org/.*

[164] *https://www.intel.com/content/www/us/en/servers/ipmi/ipmi-home.html.*

[165] V. A. Andreev *et al.* [MuSun Collaboration], arXiv:1004.1754 [nucl-ex].

[166] V. Tishchenko *et al.*, Phys. Rev. D **87**, 052003 (2013).

[167] V.A. Andreev *et al.*, Phys. Rev. Lett. **110**, 012504 (2013).

[168] *http://midas.psi.ch/rome/.*

[169] *http://ohm.bu.edu/ chill90/ipbus/ipbus_protocol_v2_0.pdf.*

[170] *http://zeromq.org/.*

[171] *https://nodejs.org/en/.*

[172] *https://plot.ly/.*

[173] *http://www.scientificlinux.org/at-fermilab/.*

[174] *https://node-postgres.com/.*

[175] G Budin, "Ontology-driven translation management", in Helle V. Dam, Knowledge Systems and Translation, Jan Engberg, Heidrun (2005).

[176] T. Teorey, S. Lightstone, and T. Nadeau, H.V. Jagadish, "Database Modeling and Design: Logical Design", Morgan Kaufmann Press (2011).

[177] E.F. Codd, "Derivability, Redundancy, and Consistency of Relations Stored in Large Data Banks, Research Report", IBM (1969).

[178] E.F. Codd, "A Relational Model of Data for Large Shared Data Banks", Communications of the ACM. Classics. **13** (6), 377–87 (1970).

[179] *https://www.python.org/.*

[180] *https://www.djangoproject.com/.*

[181] Data-Driven Documents *https://d3js.org/.*

[182] G. W. Bennett *et al.* [Muon G-2 Collaboration], "Statistical equations and methods applied to the precision muon (g-2) experiment at BNL", Nucl. Instrum. Meth. A **579**, 1096 (2007).

[183] J. Crnkovic, S. Ganguly, W. Morse and D. Stratakis,"Lost Muon Study for the Muon g-2 Experiment at Fermilab", IPAC WEPIK119 (2017).

[184] H. Bethe und J. Ashkin in Experimental Nuclear Physics, ed. E. Segré, J. Wiley, p. 253, New York (1953).

[185] J. Allison et al., "Recent developments in Geant4", in Nuclear Instruments and Methods in Physics Research A, vol. **835**, pp. 186-225 (2016).

[186] L. Landau, "On the Energy Loss of Fast Particles by Ionization", J. Phys. USSR **8**, 201 (1944).

[187] P.V. Vavilov, Sov. Phys. JETP **5**, 749 (1957).

[188] H. Bichsel, Rev. Mod. Phys. **60**, 663 (1988).